IGNITION, TOPOLOGY, AND GROWTH OF TURBULENT PREMIXED FLAMES IN SUPERSONIC FLOWS

A Dissertation
Presented to
The Academic Faculty

By

Bradley A. Ochs

In Partial Fulfillment
of the Requirements for the Degree
Doctor of Philosophy in the
School of Aerospace Engineering

Georgia Institute of Technology

December 2019

IGNITION, TOPOLOGY, AND GROWTH OF TURBULENT PREMIXED FLAMES IN SUPERSONIC FLOWS

Approved by:

Prof. Suresh Menon, Advisor
School of Aerospace Engineering
Georgia Institute of Technology

Prof. Devesh Ranjan
School of Mechanical Engineering
Georgia Institute of Technology

Prof. Jerry Seitzman
School of Aerospace Engineering
Georgia Institute of Technology

Prof. Wenting Sun
School of Aerospace Engineering
Georgia Institute of Technology

Prof. Robert Pitz
Department of Mechanical Engineering
Vanderbilt University

Dr. Campbell Carter
Air Force Research Laboratory
Wright Patterson Air Force Base

Date Approved: October 16, 2019

To my wife, Jessica and children, Melody, Logan, and Annabelle.

ACKNOWLEDGEMENTS

First I'd like to thank my advisor, Professor Suresh Menon for giving me the opportunity to work on this fascinating topic and for his many valuable inputs along the way. I especially appreciate his encouraging me to explore numerical simulations which have proved very valuable in this problem. Many thanks also go to my committee for their time reading this thesis and for their comments and suggestions to improve it.

I'd also like to thank my combustion lab colleagues who have engaged in great conversations throughout the years. In particular, Chris Ballance and David Scarborough offered invaluable technical and life advice and this work would not be the same without their presence. I should also mention the many great students I've worked with over the years including Miad Karimi, Steven Roth, and Sam Majidi to name just a few.

This acknowledgment would not be complete without mentioning my family. Thanks to my parents, Bob and Georgia Ochs, who gave me an amazing start in life, I am forever grateful for your love, to my brother, Rob, for amazing conversations, to my children Melody, Logan, and Annabelle who keep me on my toes, watching you grow is one of the most rewarding things in my life, and most importantly to my wife, Jessie, who has been infinitely patient and loving throughout this process.

Finally, thanks to the Air Force Office of Scientific Research who supported this work under grants FA9550-12-1-0107 and FA9550-15-1-0512 (Dr. Chiping Li, program manager). The computational resources provided by the US AFRL DSRC centers of the DOD HPCMP are equally appreciated.

TABLE OF CONTENTS

LIST OF TABLES

LIST OF FIGURES

SUMMARY

Supersonic combustion ramjets (scramjets) are currently the most efficient combustor technology for air breathing hypersonic flight, however, lack of fundamental understanding and numerous engineering challenges hinder regular deployment of these devices. This work addresses scramjet-relevant knowledge gaps in supersonic turbulent premixed combustion, including laser ignition, numerical modeling, and flame-compressibility interaction. One of the main contributions of this work is introduction of a new turbulent premixed flame arrangement where flame-compressibility interaction can be systematically explored: flame kernels in an expanding flow field. The scramjet flow path is replaced by a simplified channel geometry with a well characterized mean flow acceleration that mimics flow field expansion typically imposed on scramjet combustors to avoid thermal choking. Spherically expanding flames are created via laser ignition and subsequent flame growth and morphology are investigated using combined physical and numerical experiments. Pressure-density misalignment due to flame-compressibility interaction produces vorticity at the flame surface through baroclinic torque, i.e. flame-compressibility interaction acts like a turbulence source. The flame ultimately evolves into a reacting vortex ring that increases the flame speed and enhances reactant consumption. To explore the relative importance of turbulence and compressibility on flame dynamics, the Mach number ($M = 1.5, 1.75, 2$), equivalence ratio ($\phi = 1.0, 0.9, 0.8, 0.7$), and root-mean-squared turbulent velocity ($u' = 3.98, 4.14, 4.45$ m/s) are varied systematically.

This work also introduces flame kernels in an expanding flow field as a canonical numerical validation test case for flame-compressibility interaction. Inaccuracies in simulation results are easily identified due to high flow velocity and simplicity of the problem. The numerical setup and models are scrutinized to minimize errors. Using the appropriately verified numerical models, simulation results show very reasonable agreement with experimental data. Validated simulations are instrumental in enhancing understanding of

the underlying physics of supersonic flame kernels.

Laser ignition studies in supersonic flows have historically focused on ignition of non-premixed fuels within cavity flame holders. This work introduces a far simpler and more tractable problem: laser ignition of a fully premixed supersonic gas. Ignition experiments with a range of laser settings are performed to determine supersonic breakdown and ignition probabilities, length of time the ignition event influences flame growth, and Mach number influence on the ignition process. The ignition event has a long-lasting effect on kernel growth, but the influence can be minimized by properly selecting the laser energy. Mach number has a minimal impact on the ignition process, but does affect the initial kernel shape due to flow field variations with Mach number. Kernel growth matches low speed studies closely at early times, but deviates at later times due to vortex ring topology.

It is not obvious how the turbulent flame speed will scale for flows with mean compressibility. Therefore, the combined physical and numerical experiments are leveraged to explore this question. The vortex ring causes significant errors in the line of sight-measured burned volume, hence correction factors to convert from line of sight to volumetric measurements are presented. Conditions for displacement and consumption speed equivalency are shown to depend heavily on the particular diagnostic used; which progress variable isocontour is measured and where it is measured within the flame brush must be considered carefully during interpretation of experimental data. Scaling with the RMS turbulent velocity cannot collapse these flame speed data, i.e. previously established flame speed scalings are inappropriate for flames interacting with compressibility. Drawing motivation from vortex ring literature, a new flame speed scaling based on the ring propagation velocity is proposed. The proposed scaling collapses the data and produces a nearly linear scaling regime, which suggests turbulence plays a secondary role to the hydrodynamic instability created by flame-compressibility interaction. In summary, flame kernels are a new and effective canonical configuration for exploring flame-compressibility interactions in supersonic flows.

CHAPTER 1
INTRODUCTION AND BACKGROUND

In 1949, the upper stage of a modified V-2 rocket reached Mach 5 and became the first man-made object to reach hypersonic speeds. Slightly more than a decade later, the first manned aircraft broke the hypersonic flight regime. Since this time, countless more manned and unmanned craft achieved hypersonic flight for a variety of reasons. These vehicles were almost entirely powered by solid or liquid rocket engines. The rocket engine, while able to produce a sizable thrust, has suffered from low specific impulse ($Isp \approx 150 - 600$) due to carrying both fuel and oxidizer on board. For hypersonic flight within Earth's atmosphere, air-breathing propulsion systems are a more efficient option, having specific impulses several times larger ($Isp \approx 700 - 1200$) than that of the typical rocket engine. The main propulsion system candidate for air-breathing hypersonic flight is the supersonic combustion ramjet (scramjet) combustor. This system is unique from other air-breathing systems in that fuel/air mixing and combustion occur at speeds faster than the local speed of sound. For vehicles traveling at flight Mach number 4-6, the combustor Mach number is around 1.8-2.8. The scramjet engine has been flight demonstrated on several occasions and is likely the desired propulsion technology for future hypersonic flight. Despite that promise, the scramjet presents a number of technical challenges and has exposed a lack of fundamental understanding in the areas of combustion and fluid dynamics at compressible conditions. This work attempts to address supersonic combustion related technical challenges in the areas of ignition, numerical modeling, and flame-compressibility interaction.

In order to explore these technical challenges, a series of simplified experiments are performed. The scramjet flow path is isolated from the inlet and thrust nozzle, and the combustor is replaced by a simplified channel geometry. A well characterized mean flow acceleration is imposed on the baseline channel flow by diverging the tunnel walls. This

mimics a flow field expansion that is typically imposed on scramjet combustors to avoid thermal choking due to heat release, but more importantly, it enables systematic exploration of flame-compressibility interaction. Finally, the stabilized flame of the scramjet is replaced by the canonical premixed spherically-expanding flame kernel. Kernels are point-initiated via laser ignition and then convect downstream, interacting with mean flow expansion. Upon interaction, the kernels morph into reacting vortex rings that are difficult to observe with experimental data. Combining experiments and well validated simulations yields additional insights that are not available from either experiments or simulations alone. Turbulent consumption speed scaling in this problem allows prediction of the consumption speed in supersonic combustors operating in a premixed mode with similar expansion strength assuming flame structure is also similar.

This chapter gives a literature overview of laser ignition, premixed turbulent flames, and combustion in supersonic flows, and discusses the specific objectives of this work. The remainder of this thesis is organized as follows. Chapter 2 discusses the experimental and numerical methods, Chapter 3 gives laser ignition results and discussion, Chapter 4 discusses experimental observations of supersonic kernels in a mean expansion and numerical validation, and Chapters 5 and 6 discuss the morphology and flame speed analysis of supersonic kernels, respectively. Conclusions and suggestions for future work are given in Chapter 7.

1.1 Supersonic Combustors

Combustion at supersonic conditions is a relatively old endeavor dating back to post World War 2 goals of hypersonic flight. The Hypersonic Research Engine (HRE) test program began in 1964 with the aim of ground testing a number of conceptual supersonic combustor configurations [1]. Following nearly two decades of ground testing, the National Aerospace Plane program (1987-1995) planned to produce a flight test demonstration of scramjet technology but never succeed in producing a feasible prototype [2]. During this time, the first

scramjet combustor was flight tested in a captive-carry rocket test in Russia in 1991. A free-flight scramjet would have to wait till 2002 when the HyShot scramjet program produced the first free-flight scramjet [3]; although the flight was meant as a demonstration test and the vehicle did not produce self-propelling thrust. The Hyper-X program (1996-2007) produced the X-43A in 2004, the second flight of which achieved greater than Mach 9 flight [2]. The more recent self-powered X-51A waverider combines a scramjet engine with a lifting body design. The X-51A achieved Mach 5 flight for over three minutes, the longest duration air-breathing hypersonic flight. Today, hypersonics is a very active area of interest with numerous flight vehicles on the horizon from several competing groups.

The scramjet engine is an essential part of all air breathing, self-propelled hypersonic vehicles. The scramjet consists of an inlet diffuser, fuel injection section, supersonic combustor, and diverging nozzle. The diffuser slows the inlet air, increasing the static temperature to greater than 1000 K. Fuel injection is accomplished by a number of techniques such as jet in crossflow or ramp injectors. The combustor typically has a ramp, strut, or cavity flame holder behind which a main flame is stabilized in a subsonic flow. Finally, the nozzle diverges to accelerate the reacting flow. During off-design, lower flight Mach number conditions, or if an adverse pressure gradient exists, a shock-train may form upstream of the combustor. The shock-train may move upstream and cause an unstart of the supersonic core [4], so an isolator is typically used. The isolator anchors the shock-train upstream of the fuel injection but downstream of the inlet. Dual-mode scramjets [5] employ an isolator which produces a subsonic core for flight below Mach 5 but a supersonic core during hypersonic flight.

Nearly all of the premixed flame research has been conducted on flames traveling in low speed, incompressible flows. The extension of this behavior to flows with mean compressibility is not well understood. In fact, nearly all the research effort has been limited to the flamelet regime in relatively low velocity flows. However, high velocity is not a sufficient condition to consider a flow compressible. After acceleration, supersonic flows

are solenoidal and hence incompressible in the core region of the flow (away from boundaries). Compressibility effects are felt through mean compressible features such as Mach, expansion, and shock waves or when the characteristic velocity fluctuation or difference is on the same order as the local speed of sound (such as in high intensity, compressible turbulence or a supersonic boundary layer). There have been very limited studies of fundamental premixed turbulent flame behavior when these compressible features exist. Compressible turbulence has not been experimentally achieved so far, although there have been attempts to generate it in the past [6, 7, 8]. Expanding classical turbulent premixed flame studies into the compressible regime will enhance the understanding of fundamental physical processes applicable to scramjet combustion technology.

Supersonic combustors typically have several compressible mixing layers due to fuel injection, cavities or struts. Even a fully premixed combustor has a mixing layer between the flame-holding device and the core flow. It should be expected that as flow speed increases from subsonic to supersonic, compressibility effects will change the nature of the fine-scale structures of turbulence [9]. For example, suppression of mixing efficiency has been observed for highly compressible shear layers. Also, the presence of eddy shocklets have been identified in DNS of high intensity (compressible) turbulence [9]. How the flame will respond to these flow features on the small scales is an important and unexplored topic within supersonic combustion [10, 11]. In order to investigate these questions a canonical flame configuration in a supersonic expanding flow field is created via laser energy deposition. The remainder of this chapter discusses background on laser ignition, premixed turbulent flames, and flame-compressibility interaction.

1.2 Laser-Induced Breakdown Ignition

The supersonic combustor presents a unique environment in which to ignite a flame. Generation of shock waves, large aerodynamic loads, large rates of heat and radical dissipation and high velocities make the use of traditional spark electrodes unfavorable for supersonic

combustors. Homogeneous ignition via autoignition provides the benefit of having no intrusive elements within the flow; however, autoignition presents other challenges. For example, autoignition delay times are often on the same order as the flow time, meaning specialized fuel injection, mixing devices and long combustors are needed to fully burn the fuel. Also, autoignition is not useful for studying the evolution of freely propagating flame kernels. Point energy deposition via a laser-induced plasma creates a compact volume of hot gas that can ultimately form a self propagating flame kernel without creating a major flow disturbance [12]. In addition, laser ignition has already been shown to compare favorably to the more traditional electrode spark ignition experiments in terms of minimum ignition energy and initial flame shape [13, 14]. Laser ignition has been demonstrated for scramjet combustors [15], supersonic flame kernels [16, 17, 18] and hypersonic flows [19]. Here, a distinction is made between the *ignition event* and *transition* to a self-propagating flame. The ignition event includes the laser pulse, dieletric breakdown, and flame front generation, all of which occur within the first several hundred microseconds after the laser pulse. Depending on the specifics of the laser wavelength used and species ignited, the ignition event can also have a long lasting effect on the emergent flame due to an overdrive in the flame speed (discussed below). Therefore, transition to a fully self-propagating flame may be a long process and must be investigated prior to flame speed measurements. While there is some understanding on the laser ignition event in low speed flows, the ignition mechanism and driving parameters in supersonic flows are not well understood. It may be speculated that the ignition event in supersonic flows is similar to subsonic flows if the time scale for energy deposition is much shorter than the flow through time, but these details have yet to be investigated. Ignition studies using variable laser power and flow field parameters are needed to measure the propensity for ignition and to ascertain any long lasting memory of the ignition event.

During laser ignition, a focused beam creates a plasma, leading to a self-sustaining flame. There have been several theoretical explanations as to how the focused laser gener-

ates heat, pressure and/or radicals as well as several explanations for how the self-sustaining flame front is formed (see, for example ref. [20]). However, the ignition process generally proceeds as follows. First, photons from a high peak power laser generate free electrons via ionization (electronic absorption). Impurities in the gas can also contribute to initial ionization. Free electrons then absorb energy via inverse bremsstrahlung and will eventually ionize other molecules in the gas leading to dielectric breakdown. The plasma generated has many excited species that act as the ignition source. Finally, the chemically seeded gas undergoes a transition to a self sustaining flame. The last step may or may not generate temperatures above the adiabatic flame temperature and a large pressure spike. These are primarily decided by the laser ignition type. In laser-induced photochemical ignition, the beam chemically interacts with fuel or oxidizer species, breaking them down and forming radicals [21]. A chemically seeded gas is generated with very little overpressure and, unlike in spark ignition, no shock wave. In laser-induced thermal ignition, the beam excites the vibrational mode of the gas at the focal point [12, 14]. Then, the rapid increase in temperature and pressure ionizes the gas. The plasma formed in this way is optically dense and readily absorbs the remaining laser radiation via the inverse bremsstrahlung process (inverse radiative breaking) [14]. The result is a strong shock wave reminiscent of a blast wave with a large increase in temperature and pressure. In laser-induced spark ignition, dielectric breakdown (plasma formation) occurs when the atomic species of the gas absorb a sufficient number of photons, thereby exciting and ionizing them. If the laser wavelength is tuned just right, resonant two-photon absorption can occur. In this case, the plasma forms and leads to a successful ignition without a blast wave. For example, an ultraviolet laser interacts with oxygen (225.6 nm) or hydrogen (243 nm) leading to atomic radicals of those species with relatively low irradiance from the laser [22, 23]. The irradiance is so low that the inverse bremsstrahlung is relatively weak (i.e., there is not enough energy absorption to cause a significant overpressure). More generally, non-resonant absorption occurs over a wide range of wavelengths [23]. This multi-photon absorption has low efficiency, meaning

that a very large irradiance is needed to cause breakdown. Once breakdown occurs, the inverse bremsstrahlung process will rapidly ionize the gas supporting a strong detonation wave back towards the laser source, once again leading to a large temperature and pressure increase and the audible crack of spark ignition. Laser-induced spark ignition is the most general and commonly used form of laser ignition and therefore is the focus of these studies.

For laser-induced spark ignition via non-resonant breakdown, ignition is accompanied by a strong supersonic shock wave. In addition, pressure, temperature, and intermediate radicals achieve larger values than would normally been seen in the flame, a phenomena commonly referred to as ignition overdrive. All of these features are responsible for transition to a self-propagating flame. In one theory, the blast wave rapidly heats the surrounding gas to autoignition temperatures. As the blast wave travels away, a reaction zone forms immediately behind it. For non-detonable mixtures or low ignition energy, the reaction zone decouples from the blast wave and propagates as a flame [12]. The blast wave has a cylindrical shape because of the initial shape of the plasma [14]. After some time, the shock strength deteriorates and the flame propagates into relatively unperturbed gas. Taylor blast wave theory is relatively successful at predicting the evolution of the spark kernel out to several tens of microseconds after the spark for both experiments and numerical simulations [24, 25, 26, 27, 28, 29]. After 30-50 microseconds, the kernel shape is driven by a different phenomena. As the gas expands behind the cylindrical blast wave, conservation of momentum forces an inflow along the laser axis resulting in an initially torus-shaped flame kernel [27]. The torus shape may last for several hundred microseconds. One other effect may influence the initial shape of the flame kernel: plasma back-streaming [28]. Once breakdown occurs, the plasma is optically dense and therefore preferentially absorbs the laser energy on the side facing the incoming beam, i.e. the plasma streams back towards the laser source. For strong overdrives, this will lead to the formation of a third lobe in the initial flame kernel [14].

The torus and third lobe are particularly challenging features for turbulent flame speed measurements because they impart a memory effect on the flame shape for some time after ignition. The strong pressure and temperature overdrives also complicate these measurements because of their effect on the flow field and laminar flame speed. For example, the blast wave causes an over expansion of the kernel which will later shrink [14]. Also, the inflated temperatures induce flame speeds that are greater than the laminar, unstretched flame speed; this occurs even for fuel/air combinations where large stretch rates should drastically reduce the flame speed (i.e. rich methane/air at early growth times [28]). These flame shape effects and ignition probability have not been fully investigated as a function of ignition energy and flow velocity. In addition, the effect of seeding particles on spherical kernel initiation is unknown. These dependencies must be resolved prior to performing flame speed measurements.

While there is some evidence that unfueled kernels begin to dissipate after approximately 250 μs [30] (see Figure 1.1), it is unclear how long the ignition event affects flame growth in supersonic flames. In order to answer this question, it will be necessary to evaluate the dependence of the flame growth, which is related to the rate of change of the kernel radius, on the deposited laser energy (E_d). Of critical importance is to identify the time when flame growth becomes independent of E_d, termed the independence time (τ_{ind}), and the minimum ignition energy (E_{ign}). Here, E_{min} could be thought of as the minimum energy required for ignition. However, it is more useful to define E_{ign} as the minimum deposited energy that should be used to minimize the influence of the ignition event on flame speed measurements. Therefore, τ_{ind} and E_{ign} are two critical parameters that should ideally be identified before flame speed measurements are made. The influence of the mean flow Mach number (M) and equivalence ratio (ϕ) on the ignition event should also be established. Chapter 3 investigates these questions and others related to laser ignition in supersonic flows.

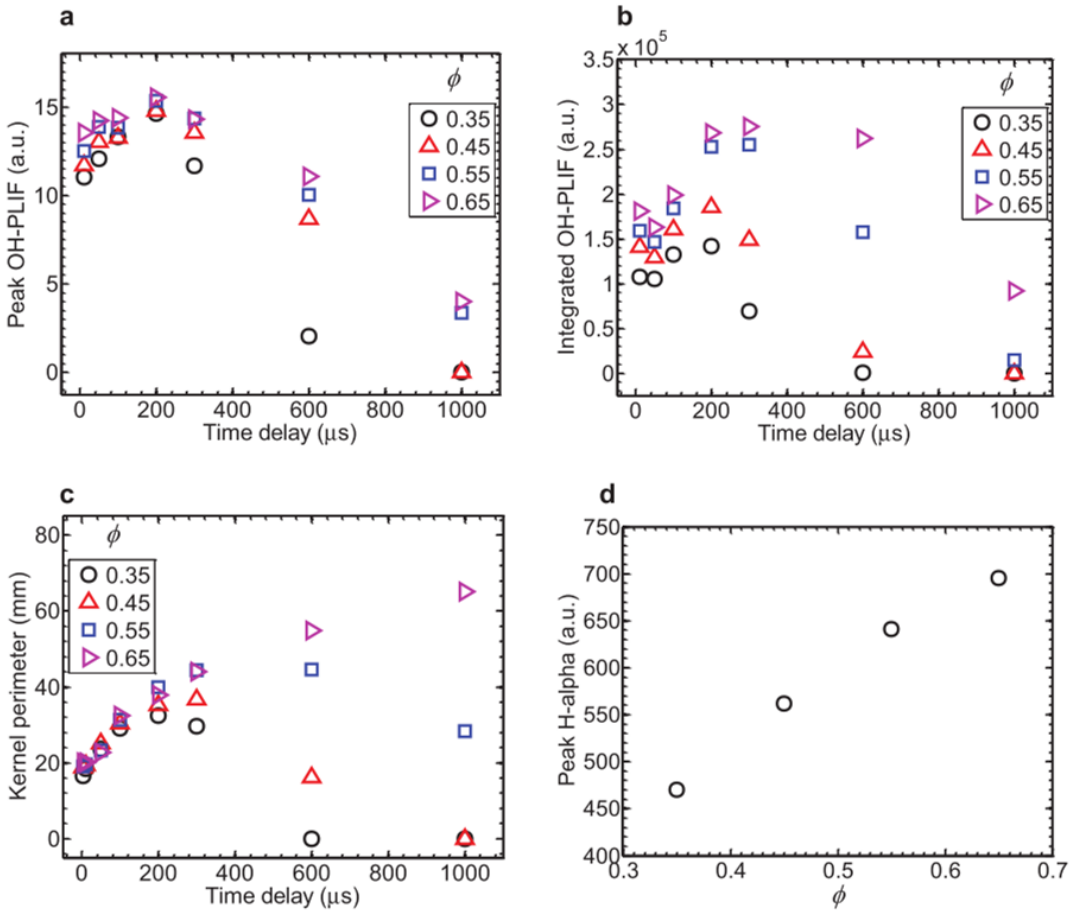

Figure 1.1: Ignition kernel evolution data from Mulla *et al.* [30] for a 128 mJ pulse showing the effect of equivalence ratio on (a) peak PLIF intensity, (b) spatially-integrated PLIF intensity, (c) flame-kernel perimeter, and (d) H-alpha emission intensity at 280 ns after the laser pulse.

1.3 Premixed Turbulent Flames

Premixed turbulent flames are a particularly challenging topic because the underlying mechanisms of turbulence are unsolved. Turbulent flames are usually studied in a time-averaged sense because the instantaneous realizations are chaotic, meaning it's nearly impossible to recreate the conditions at any given instant. Therefore turbulent flames, like turbulence, are highly amenable to statistical analysis. Two main effects of turbulence are a wrinkling of the flame front with associated increase in the instantaneous flame area, and penetration and broadening of the preheat zone. These effects lead to an increase in the reactant consump-

tion rate and are quantified by a change in time averaged quantities. One such quantity is the turbulent burning velocity S_T, which is rigorously defined in Section 1.4. Other mechanics that lead to a modification of these parameters include flame stretch through hydrodynamic or thermo-diffusive effects and chemistry. The former causes a local modification of the burning velocity, which ultimately results in an averaged flame surface change while the later affects the entire flame. Previous studies (described below) have attempted to collapse all three effects (turbulence-flame interactions, stretch, and chemistry) into solitary correlations for desired quantities, such as S_T. A new scaling for supersonic kernels exposed to mean expansion is one of the main goals of this work.

Four canonical flame configurations have been used for premixed turbulent flame studies. These are the so-called envelope flames (Bunsen burners), oblique flames (V or bluff-body flames), flat flames (diffusion, low swirl, and counter-flow burners), and spherical flames (flame bombs and freely-flowing flames)[31]. The first three configurations are advantageous in that they create stationary flames for long term measurement. However, they are also problematic due to the difficultly in decoupling the effect of large-scale strain from true turbulence-flame interactions. For example, in Bunsen flames S_T has been shown to vary along the flame length due to flow field development, i.e. the flame is affected by the "memory" of large-scale structures [32]. Other issues related to flame holding that contaminate results include heat loss due to heat transfer to the injector face and the influence of pilot burners that are needed to stabilize high speed flames in those configurations. In this work, spherical flames are used to avoid these problems. In addition, it is impossible to create stabilized flames in supersonic flows without creating regions of highly variable properties. For example, the cavity flame holder imposes an enormous range of scales and large scalar dissipation rates on the flame, making fundamental studies of the turbulent flame speed in scramjets tenuous.

Studies of low-speed, turbulent premixed flames have established that an increase in the turbulence intensity, or more specifically u'/S_{L0}, results in a modification of the fundamen-

tal structure and behavior of the flame [33, 32, 34]. Here, $u' = \sqrt{1/3\left(u_1^2 + u_2^2 + u_3^2\right)}$ is the average RMS of the turbulent velocity fluctuation in each direction and acts as a measure of the turbulence intensity, S_{L0} is the unstretched laminar flame speed determined by the mixture chemistry. As the turbulence intensity increases, the nature of the flame wrinkling changes and the resulting flames fit broadly into several flame regimes. Flames within a weakly turbulent flow field are observed to behave like a laminar flame with superimposed wrinkles: wrinkled laminar flamelets regime. An increase in the turbulent intensity results in a corrugated, or strongly wrinkled flame front: corrugated flamelets regime. A further increase results in a flame front that is very highly contorted, often with pockets of unburned reactants or products but still maintaining a thin/discrete flame front: thin reaction zone regime (TRZ). Flames within all of these regimes are considered flamelets because the reaction zone exists over a compact spatial region and vorticity does not enter the reaction zone. In the TRZ, turbulent fluctuations enter the preheat zone enhancing transport of heat and species, ultimately increasing the flame speed but leaving the structure of the reaction zone mostly unaffected. Experimental evidence supports the notion of preheat zone broadening in the TRZ and several different diagnostics (e.g. simultaneous OH/CH_2O planar laser-induced flourescence (PLIF) [35], simultaneous particle image velocimetry(PIV)/Rayleigh scattering [36], and simultaneous PLIF/Rayleigh scattering measurements [37]) have shown this broadening effect. There is a large literature base on the behavior of weakly turbulent flames, but some more recent studies have also focused on the thin reaction zone [38, 39, 40, 41, 42, 43]. The wide range of behaviors from laminar flamelets to thin reaction zones (TRZ) is well documented in the premixed turbulent flame literature [34, 44, 45, 46].

In the limit of extreme turbulence (turbulent time scales on the same order as the chemical time scale), the turbulent eddies may be small enough and strong enough to enter the reaction zone. Summerfield *et al.* [47] coined this scenario the distributed reaction zone (DRZ). In this situation, the flame does not behave as a flamelet. They noted that a high

speed, specifically ramjet flame may fall within this regime. Some experimental evidence of distributed or broken reactions is available [38, 48, 37] but the existence of this regime, and the ability to achieve it experimentally, is still an active area of research. There are considerable variations in the local properties within supersonic combustors; therefore, it is not surprisingly that realistic supersonic flames span several flame regimes. However, the conditions in this work were set so that all of flames are in the thin reaction zone.

Macroscopic turbulent properties, such as u' and the longitudinal integral scale L_{11}, are used to completely describe the flame regimes of turbulent premixed flames through regime diagrams. Two primary regime diagrams exist: one that uses the length and velocity scales directly, known as the Borghi-Peters diagram [49, 50], and one that uses the length and velocity scales to produce the large eddy Reynolds and Damkohler numbers, known as the Williams diagram [51]. For example, Figure 1.2 shows the Borghi-Peters diagram. These flame regime diagrams are advantageous because, in theory, flames of a similar configuration can be compared if they fall within in the same flame regime. It is not clear how compressibility plays into the flame regime diagram. If and how these flame regime diagrams should be modified for supersonic flames exposed to mean expansion is an interesting and unexplored question.

A consistent definition of S_T is required to compare across experiments and/or numerical simulations. Indeed, inconsistency in the definition of S_T caused a large scatter and much confusion in initial experimental data [31]. In order to be more precise about the definition of S_T, we must acknowledge that there are several measures of the turbulent flame speed. These are:

$$\text{Local Displacement Speed} = S_{TD,L} = \left(V_{FLAME} - V_{GAS}\right)_{LE} \cdot \boldsymbol{n}_{LE} \tag{1.1}$$

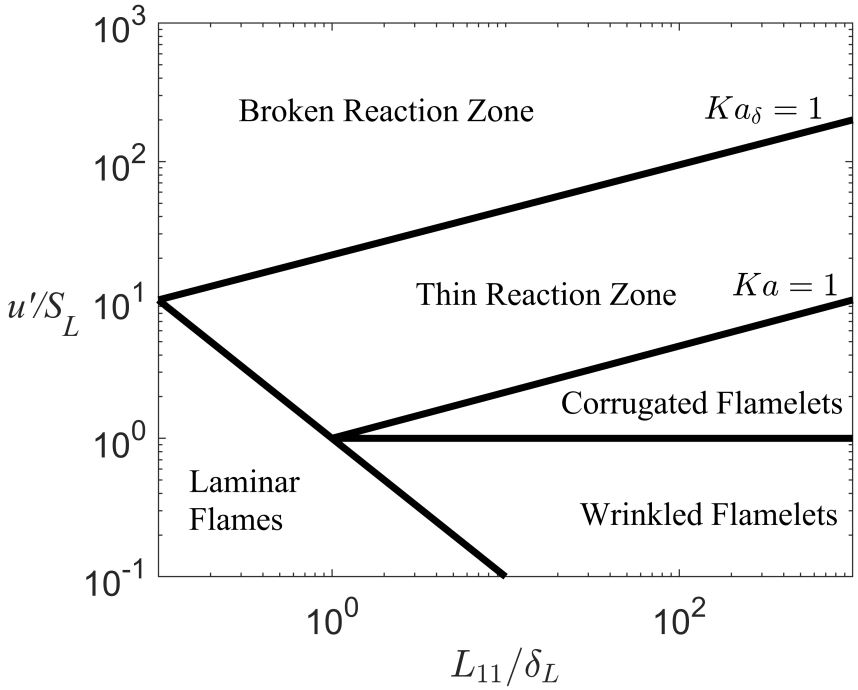

Figure 1.2: Borghi-Peters diagram [49, 50].

$$\text{Global Displacement Speed} = S_{TD,G} = \frac{\rho_1}{\rho_0} \cdot \frac{d\langle R \rangle}{dt} \tag{1.2}$$

$$\text{Local Consumption Speed} = S_{TC,L} = S_{L0} I_0 \int_{-\infty}^{\infty} \Sigma \, d\eta \tag{1.3}$$

$$\text{Global Consumption Speed} = S_{TC,G} = \frac{\dot{m}_R}{\rho_R \, A_{c=0.5}} \tag{1.4}$$

Here, V_{FLAME} and V_{GAS} are the observed flame velocity and gas expansion velocity at the leading edge (LE) of the flame. The subscripts 0 and 1, for example on the gas density ρ, are meant to convey that the property is evaluated at the reactant and product side of the flame, respectively. The instantaneous spherical flame radius is denoted R, and the $\langle \, \rangle$'s indicate ensemble averaging. The stretch factor, denoted I_0, is the the ratio of the local flamelet consumption speed to the unstretched laminar flame speed, Σ is the flame surface

density, and c is the progress variable. These flame speed definitions are universally applicable to any flame configuration with the exception of the global displacement velocity; this formulation is specific for spherically expanding flames and the reason behind it's definition will become apparent in Section 1.4. For any given configuration, one formulation may be more or less appropriate. For example, the global consumption speed depends on the reactant mass flow rate which is hard to measure in experiments of freely expanding spherical flames. On the other hand, premixed jet flames are ideally suited to measure the global consumption speed; hence Bunsen burner-type studies often present that flame speed measurement. In this work, only global measures of the turbulent flame speed are considered. Therefore the subscripts L and G are dropped in the remainder of this work.

Bradley *et al.* [52] derived a relatively simple equation for S_{TD} of a turbulent flame kernel under the restriction where the flame radius is such that the volume of burned gas inside the radius is equal to the volume of unburned gas outside it. In this simplifying case, S_{TD} is a function only of $d\langle R\rangle/dt$ and the unburned to burned density ratio ($\Theta = \rho_0/\rho_1$):

$$S_{TD} = \frac{1}{\Theta}\frac{d\langle R\rangle}{dt} \tag{1.5}$$

Specifying the location within the flame brush where $\langle R\rangle$ is defined is crucial because outward reactant expansion causes differing values of $d\langle R\rangle/dt$ depending on the definition of $\langle R\rangle$ [53, 54]. Chaudhuri *et al.* [54] derived an expression for the flame speed that accounts for this gas expansion effect:

$$S_{TD} = \frac{2}{\Theta + 1}\left(\frac{\langle R\rangle}{\langle R_{c=0.5}\rangle}\right)^2\frac{d\langle R\rangle}{dt} \tag{1.6}$$

where $\langle R\rangle^2/\langle R_{c=0.5}\rangle^2$ is the ratio of the mean flame radius (measured using schlieren data in their work) to the radius where the progress variable attains a value of 0.5 ($c = 0.5$). Using simultaneous Mie scattering and schlieren data, the ratio was measured by Bradley *et al.* [53] as a function of $\langle R_{c=0.5}\rangle/\delta_T$ (δ_T is the turbulent flame brush thickness). The ratio is

approximately 4/3 for statistically spherical expanding turbulent flames at all but the earliest times measured in their study. The S_{TD} definition above is strictly only valid for flames that have infinitely thin reaction zones and hence are only weakly wrinkled by isotropic turbulence and do not deviate heavily from a spherical shape. These assumptions limit the applicability of S_{TD} expressions to the laminar flamelet regime [55]. However, outside this regime the same expressions are used because there are currently no generally accepted better alternatives. Equations (1.5) and (1.6) are derived more rigorously in Section 1.4.

Some of the earliest premixed turbulent flame studies focused on predicting S_{TD} as a function of turbulence characteristics and fuel properties [56, 57]. In his seminal work on the topic, Dahmköhler suggested that the turbulence-flame interaction depends on the nature of the turbulent field [56]. He proposed two distinct scenarios of turbulence-flame interaction [56]: (a) "coarse-body" (large scale) turbulence characterized by large spatial fluctuations that wrinkle and distort the flame and (b) "fine-body" (small scale) turbulence characterized by small scale fluctuations that can penetrate the flame zone itself. These conditions would later become known as the corrugated flamelets and TRZ flame regimes [58], as previously discussed. For corrugated flamelets, he derived:

$$\frac{S_{TD}}{S_L} \propto= \frac{u'}{S_L} \tag{1.7}$$

Dahmköhler derived a different expression for flames within the TRZ [56]. In this scenario of fine scale turbulence, the main role of turbulence is to increase the rate of heat and mass transfer in front of the flame surface. For this situation he derived:

$$\frac{S_{TD}}{S_L} \propto Re_T^{1/2} \tag{1.8}$$

where Re_T is the turbulent Reynolds number, and S_L is the stretched laminar flame speed. Using broadband chemiluminescence photography, he showed the theoretically derived scalings in Equations (1.7) and (1.8) matched experimental results for Bunsen-burner flames.

Figure 1.3 shows a collection of normalized turbulent burning velocities plotted versus normalized turbulent intensity from many sources [59]. At low turbulent intensity, the data are roughly linear as predicted by Dahmköhler; although the slope is higher than predicted. Equation (1.7) is fairly simple but appears to capture the experimental observations at low turbulence intensity. At higher turbulence intensities, however, the correlation begins to fail and the turbulent flame speed no longer increases linearly with turbulence intensity (for example, see Figure 1.4 [60]). The reason for these differences is not fully established. Effects such as flame surface self-annihilation (two cusps joining in the flame sheet) or stretch, both of which modify the flame speed, are partially responsible for the differences.

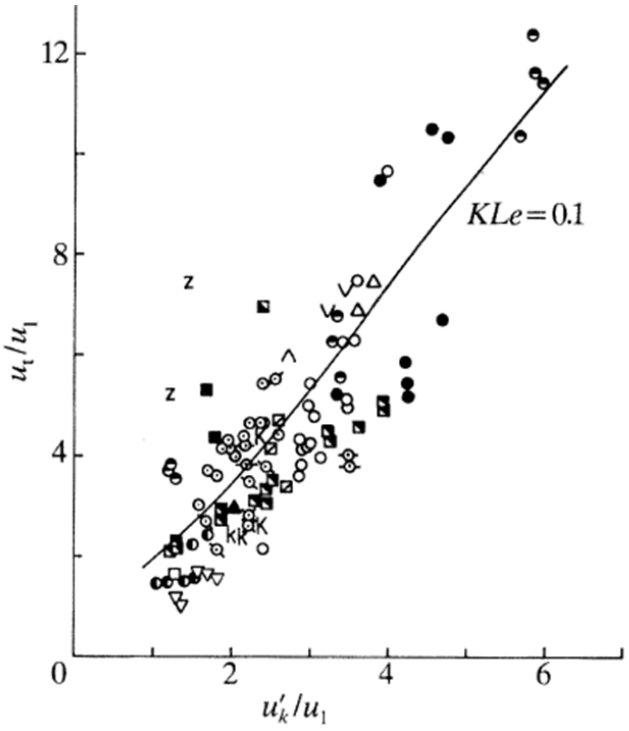

Figure 1.3: Turbulent burning velocity as a function of turbulent intensity from many sources presented by Bradley *et al.* [59]. In their nomenclature, u'_k is the RMS turbulent velocity fluctuation, u_l is the laminar flame speed, and u_t is the turbulent flame speed.

The non-linear behavior above has encouraged new correlations and many turbulent flame speed scalings have been proposed [32]. For example, Bradley empirically developed Equation (1.9), and showed that it collapsed his data quite well [61]. This relation correlates the burning velocity with ${Re_T}^{0.5}$ similar to Dahmköhler's fine-scale turbulence

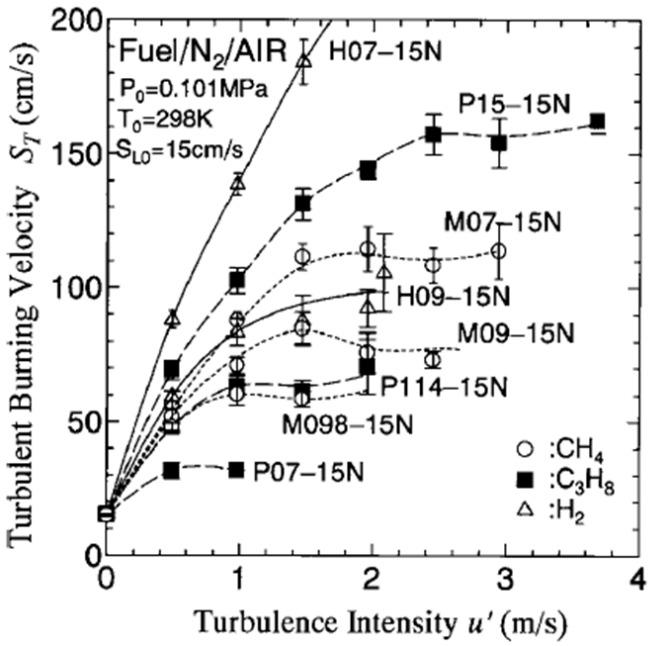

Figure 1.4: Turbulent burning velocity as a function of turbulent intensity from many sources presented by Kido *et al.* [60].

scaling but also attempts to account for thermo-diffusive stretch through inclusion of the Lewis number. The factor of 0.95 and the exponent are selected to fit experimental data of that particular work. Correlations of this type have provided useful comparisons to simulation, however their accuracy is limited by significant scatter of historical data and because different definitions of the flame speed have been used. In the limit of extreme turbulence all of these correlations fail; hence, extreme turbulence levels are avoided in this work in order to make reasonable comparisons to some of these canonical results.

$$\frac{S_T}{S_L} = 1 + 0.95 Le^{-1} \left(\frac{u'}{S_L} \frac{L_{11}}{\delta_L} \right)^{0.5} \tag{1.9}$$

Dahmköhler's simple $Re^{1/2}$ scaling can also be achieved when applying a spectral closure to the G equation [62, 63]. Following this approach, Chaudhuri *et al.* [63] arrived at a turbulent flame speed scaling law for low speed flame kernels that looks remarkably

similar to Dahmköhler's original $Re^{1/2}$ scaling:

$$\frac{S_{TD}}{S_{L0}} \propto \left[\frac{u'}{S_{L,1}} \frac{\langle R \rangle}{\delta_L} \right]^{\frac{1}{2}} \tag{1.10}$$

where δ_L is the laminar flame thickness and is defined as $\delta_L = (T_1 - T_0)/(dT/dx)_{max}$, T is the gas temperature and the subscripts 1 and 0 again refer to products and reactants, respectively. In this scaling, u' and $\langle R \rangle$ are hydrodynamic scales and $S_{L,1}\delta_L$ is related to the thermal diffusivity. In their later work, Chaudhuri *et al.* [64] replaced δ_L with $\delta_{M,b}$, the burned Markstein length, which accounts for the effect of flame stretching on the flame speed: $S_{L,b} = S_{L0,b}(1 - \delta_{M,b} \cdot \overline{\kappa})$ [65]. Here, $S_{L0,b}$ is the unstretched laminar flame speed measured with respect to the burned products and $\overline{\kappa}$ is the mean curvature.

For a spherical flame geometry, $\overline{\kappa}$ is the reciprocal of the flame radius ($\overline{\kappa} = 1/\langle R \rangle$) and is positive when the flame is convex to the reactants. It is worth nothing that a factor of two is sometimes included in fluid mechanics and flames literature ($\overline{\kappa} = 2/\langle R \rangle$) [66], however $\overline{\kappa} = 1/\langle R \rangle$ is used in this work. Abdel-Gayed *et al.* replaced u' with an effective RMS velocity u'_{eff}, which removes the portion of the 1D turbulent kinetic energy spectra (E_{11}) that is too large to affect the flame [67]. Here ${u'_{eff}}^2 = \int_{\nu_{\langle R \rangle}}^{\infty} E_{11} d\nu$ and $\nu_{\langle R \rangle} = \pi/\langle R \rangle$ is the smallest wavenumber (largest motion) that influences the flame. The procedure is further refined by introducing a high wavenumber limit related to the Gibson scale (smallest turbulent scale that can interact with the flame, $l_G = {S_L}^3/\epsilon$)[68, 53]. The hydrodynamic scale is the ensemble mean kernel radius, $\langle R \rangle$. Equation (1.10) is similar to $Re^{1/2}$ where the diffusion coefficient in the denominator, $S_{L,b}\delta_L$, is related to the thermal diffusivity.

Equation (1.10) was developed for thermodiffusively neutral flames, but then extended to thermodiffusively stabilizing conditions by taking the mean stretch into account in $S_{L,b}$ [64]. Hence, Chaudhuri *et al.* [64] were able to collapse S_T/S_L for a wide range of thermodiffusively neutral and stabilizing flame kernels within the corrugated flamelets and thin reaction zones. Figure 1.5 shows the collapse for a broad range of conditions that span lean CH_4-air flames at varying pressure (circles), rich H_2-air flames (stars), stoichiometric

C_2H_6-air flames at varying pressure (squares), and rich C_2H_4-air flames at varying pressure (triangles). It is not clear whether this scaling holds for supersonic flame kernels, or if some other parameter, perhaps the Mach number, should be added to the scaling for supersonic flames. Hence, the relevance and accuracy of this scaling is investigated for the case of supersonic flame kernels exposed to a mean flow expansion and a direct comparison to the data of Chaudhuri *et al.*[64] is made.

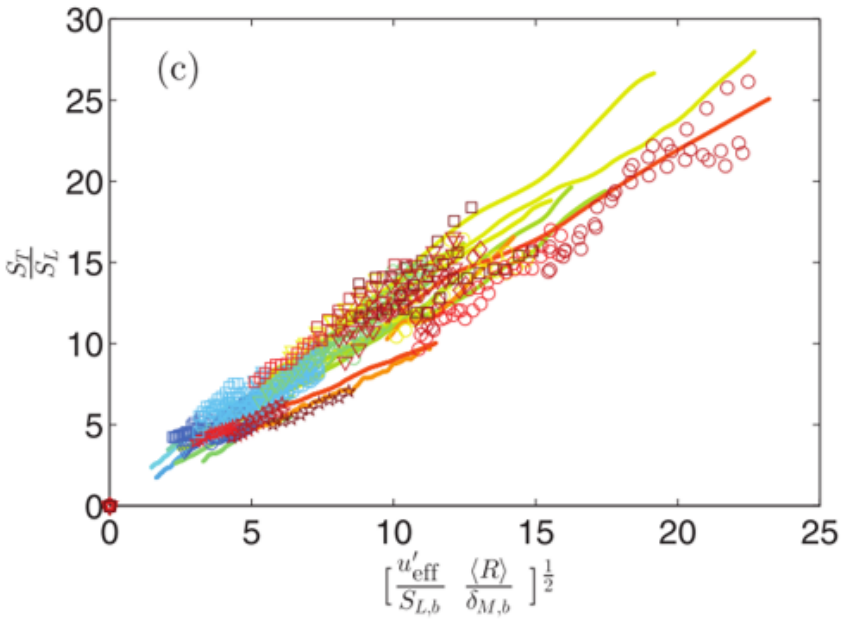

Figure 1.5: Turbulent flame speed scaling presented by Chaudhuri *et al.* [64] showing collapse for turbulent premixed flame kernels spanning several fuel types, equivalence ratios, pressures and turbulence conditions.

1.4 Definition of Turbulent Burning Velocities

There are generally two turbulent flames speeds used in literature: the turbulent displacement and consumption speeds. To derive these we start with a generic form of mass conservation through the flame on a flame-centered reference frame. The approach is similar to one performed by Bradley *et al.* [52], except that a distinction is made between the consumption and displacement speeds, both of which depend on the flame front specification.

The production rate of burned mass is:

$$\dot{m}_b = \rho_I A_{f,I} S_I = \rho_{II} A_{f,II} S_{II} \tag{1.11}$$

where ρ is the density, A_f is the flame surface area, and S represents the velocity. The subscripts I and II are used to denote variables evaluated at different progress variable contours, defined as $c = \frac{Y_F - Y_{F,0}}{Y_{F,1} - Y_{F,0}}$. Y_F is the fuel mass fraction and the subscripts 0 and 1 denote the unburned and the burned values.

For an unstretched laminar flat flame evaluated at the $c = 1$ and 0 contours, this relationship simplifies to the well known relation: $\Theta S_1 = S_0 \rightarrow \Theta S_L = S_{L,b}$, where S_L is the laminar flame speed, $S_{L,b}$ is the so-called burned laminar flame speed and $\Theta = \rho_0/\rho_1$ is the gas expansion ratio. In a lab-centered frame with a zero burned gas velocity boundary condition, $S_{L,b}$ is the observed flame front propagation velocity due to the combined effects of flame propagation and gas expansion. For an unstretched flame, S_L defined in this way is equivalent to the unstretched laminar flame speed, S_{L0}. However, stretching of the flame surface and the differences in the thermal and the mass diffusivity of the mixture can cause S_L to differ from S_{L0} [65]. Turbulent flames, having a distribution of curvature (κ) along the flame surface, will have an additional distribution of the local flamelet velocity along the flame surface.

Markstein's classic linear relation, $S_L = S_{L0}[1 - \delta_M \kappa\,]$, can be used to calculate the local flamelet velocity in turbulent flames by using the local κ. Here, δ_M is the Markstein length. Unfortunately, it is impractical to measure the curvature over the entire 3D turbulent flame surface experimentally. Instead, an ensemble-averaged global curvature $\left(\langle \kappa_g \rangle = \frac{1}{\langle R \rangle}\right)$ based on an ensemble-averaged 2D flame shape is usually employed to produce an average flamelet velocity, which is referred to as S_L by many authors. However, it is not hard to imagine that $\langle \kappa_g \rangle$ would differ from the flame surface average of κ because: 1. the ensemble averaging process acts like a low pass filter, removing large κ content and, 2. PDF's of κ are known to be skewed [55, 69]. In this situation, S_L (as previously defined)

is not equivalent to the flame surface average of the local flamelet velocity, in general. This discrepancy is a limitation that is hard to overcome in experimental works. In numerical simulations, the entire 3D solution is known, and therefore the local flamelet velocity or its average over the flame surface (a quantity termed $\overline{S_L}$), can be calculated directly. This is a superior quantity to use for flame speed scaling because it automatically considers skewness in κ, whereas the flame speed based on $\langle \kappa_g \rangle$ does not.

Turbulent flame speeds are derived from the evolution of the ensemble averaged burned volume. Ensemble averaging over statistically spherical flames yields a nearly spherical average flame volume with an associated spherical flame area $\langle A \rangle$. A distinction is made here between $\langle A \rangle$ and the ensemble averaged flame area, $\langle A_f \rangle$. Because of the presence of wrinkles, $\langle A_f \rangle > \langle A \rangle$. Only in the case of a laminar spherical flame does $\langle A_f \rangle = \langle A \rangle$. It is difficult to measure volumetric flame information directly in spherical flame experiments due to diagnostic constraints. In many situations only 2D flame images (such as OH PLIF, schlieren, or Mie scattering) are attainable. Therefore, it is customary to estimate the average 3D flame volume from 2D images by fitting a radius to the average 2D cross sectional area, $\langle A_{2D} \rangle$:

$$\langle R \rangle = \sqrt{\langle A_{2D} \rangle / \pi} \tag{1.12}$$

In the following discussion it will be useful to define a spherical flame area estimate, $\langle A \rangle = 4\pi \langle R \rangle^2 = 4 \langle A_{2D} \rangle$. The result of this 2D→3D conversion depends heavily on the diagnostic used, whether those diagnostics yield line of sight (LOS) or planar measurements, and what progress variable isocontour is measured. Three typically used diagnostics and corresponding c are: 1. planar OH PLIF ($c \approx 0.25$ [70]), 2. LOS schlieren ($c \approx 0$ [71, 72]), and 3. planar Mie scattering ($c \approx 0.5$ [53]). Bradley *et al.* [53] reported that radii derived from schlieren images were $\approx 33\%$ larger than those derived from Mie scattering images [53], which could influence flame speeds drastically.

The ensemble averaged mass burning (consumption) rate evaluated at the $c = 0$ con-

tour is given by: $\langle \dot{m}_b \rangle = \rho_0 \langle A_{f,0} \rangle \overline{S_L}$, where the subscript 0 refers to the progress variable isocontour. Equation (1.11) is also valid for turbulent flames, however, it is customary to evaluate the turbulent flame speed at $\langle A \rangle$, which is readily available from experiments. The mass burning rate is constant, therefore $\langle \dot{m}_b \rangle = \rho_0 \langle A_0 \rangle S_{TC,0}$. Here, $S_{TC,0}$ represents the turbulent consumption speed evaluated at the $c = 0$ isocontour, which is picked for consistency with the definition of $\overline{S_L}$ (however S_{TC} could be evaluated at any c). Combining these equations yields the well known relation:

$$\frac{S_{TC,0}}{\overline{S_L}} = \frac{\langle A_{f,0} \rangle}{\langle A_0 \rangle} \tag{1.13}$$

Some authors prefer to evaluate S_{TC} at the $c = 0.5$ contour [53, 54]. This becomes slightly more complicated when using experimental schlieren data because the derived flame area corresponds to the $c = 0$ isocontour. In this case it is useful to evaluate $\rho \langle A \rangle S_{TC}$ at the $c = 0.5$ contour. Then rearranging, taking $\rho_{0.5}$ to be $0.5(\rho_0 + \rho_1)$, and solving for $S_{T,0.5}$ yields:

$$\frac{S_{TC,0.5}}{\overline{S_L}} = \frac{2\Theta}{\Theta + 1} \frac{\langle A_{f,0} \rangle}{\langle A_{0.5} \rangle} \tag{1.14}$$

The quantity $\langle A_{f,0} \rangle$ requires the full 3D flame topology which is not readily available from experimental data. Additionally, the product production rate (reactant consumption rate) is not measurable in spherical flame experiments. Therefore, it is impossible to directly evaluate Eqs. 1.13 or 1.14 using experimental data. One approach to resolve this limitation has been to assume that the burned mass production rate is equivalent to the displacement rate of the burned volume times the burned density:

$$\langle \dot{m}_b \rangle^* = \rho_1 \frac{d\langle \mathcal{V}_0 \rangle}{dt} \tag{1.15}$$

where $\langle \mathcal{V}_0 \rangle$ represents the ensemble averaged burned volume. In Equation (1.15), the star is used to indicate that the mass burning rate estimated from the burned volume displacement

may differ from $\langle \dot{m}_b \rangle$. Here, $\langle \mathcal{V}_0 \rangle$ is evaluated at the $c = 0$ contour for consistency with previous work, but this choice and the definition of $\dot{m}_b$ are critically important. Equivalence between $\langle \dot{m}_b \rangle^*$ and $\langle \dot{m}_b \rangle$ implies equivalence between the consumption and displacement speeds. However, these two would differ if the flame is not infinitely thin, which allows for ambiguity in the burned volume and density definitions [73]. Indeed, this ambiguity is at least partially responsible for the large spread in turbulent flame speed measurements from experiments [73, 31]. This distinction is explored for supersonic flame kernels in this work.

Assuming a spherical flame, normalizing by $\overline{S_L}$, and equating Equation (1.15) with $\rho_0 \langle A_{f,0} \rangle \overline{S_L}$, one can arrive at:

$$\frac{S_{TD,0}}{\overline{S_L}} = \frac{1}{\overline{S_{L,b}}} \frac{d\langle R_0 \rangle}{dt} \tag{1.16}$$

where $S_{TD,0}$ is the turbulent displacement speed evaluated at the $c = 0$ isocontour. The assumption of average sphericity is valid for Galilean invariant, point ignited flames propagating outward into a homogeneous and isotropic turbulent field. If the flame speed referenced to the $c = 0.5$ contour is desired, then one can arrive at the expression [54]:

$$\frac{S_{TD,0.5}}{\overline{S_L}} = \frac{2\Theta}{\Theta + 1} \frac{1}{\overline{S_{L,b}}} \frac{\langle R_0 \rangle^2}{\langle R_{0.5} \rangle^2} \frac{d\langle R_0 \rangle}{dt} \tag{1.17}$$

1.5 Combustion in Supersonic Flows and Expansion-Flame Interaction

One specific problem of interest to supersonic combustors is the interaction of a flame with mean flow dilatation, which takes the form of expansion and/or compression waves. This problem is of interest because it is guaranteed that scramjets will experience a flame-compressibility interaction somewhere within their operating envelope. This interaction process produces vorticity on many different scales and greatly increases the chemical energy conversion rate for some time immediately after the flame passes through the expansion or shock. For example, the energy release rate can increase by 20-30 times for a single,

strong normal shock wave due to pressure/temperature rise and increased flame surface area [74]. In fact, multiple shock-flame interactions have been observed prior to a deflagration to detonation transition (DDT). Because supersonic combustors have short residence times, these compressibility interactions may enable a shorter (and lighter) combustor. Shock-flame interaction would be a useful method to increase the reactant consumption if the rapid increase in energy conversion was not counterbalanced by stagnation pressure loss. Expansion-flame interaction, while weaker in general, may actually be a more useful mechanism to increase the consumption rate because it does not suffer from the entropy losses associated with shock waves. Therefore the expansion-flame interaction merits additional study.

The interaction roughly follows a 3 step process [75]. In the first step and prior to the interaction, the flame is considered a sharp interface between low (burned) and high (unburned) density fluid. As the expansion fan contacts the flame surface, the density discontinuity causes reflection, refraction and transmission of the expansion. In the second step, the transmitted expansion travels faster through the high temperature fluid creating a velocity difference between the burned and unburned fluid. This acceleration creates large scale vorticity which stretches the flame surface on a large scale. In addition, at the flame surface density-pressure misalignments feed the Richtmyer-Meshkov instability, creating motion on many different scales through the action of baroclinic torque. This increase in velocity fluctuation occurs faster than reactions can smooth the surface leading to an increase in the flame surface density. In the third step, which is relevant to strong expansion/shocks, the thickened flame reacts as a partially distributed flame with an increased heat release rate. The highly convoluted flame may produce further destabilizing pressure waves before finally relaxing to the original burning velocity. For weaker expansions, the flame surface is wrinkled but remains intact. A review of the available literature on this topic follows.

While the underlying processes are similar, the vast majority of flame-compressibility

interaction work has focused on shock-flame interactions, rather than expansion-flame interactions. The investigation of shock-flame interactions had its origins in shock tube studies with a number of papers written by Markstein in the 1950's [76, 77, 78]. Prior to this, Chu described mathematically the conditions under which pressure disturbances were generated by a 1D flame [79]. For example, a flame propagating into a change in flame speed, heat release rate, reactant temperature or composition, or velocity generates a pressure wave in response to the discontinuity. In an open flame these pressure fluctuations propagate away from the flame, having a negligible effect on the flame itself. However, in duct flows these pressure waves can couple with the natural duct acoustics or further interact with the flame surface, leading to a significant modification of the burning rate or, at the very least, additional pressure fluctuations [77]. This analysis and the observation of deflagration to detonation transition set the stage for the more general investigation of strong pressure waves with a flame kernel. Markstein performed one of the first shock-flame kernel studies using a shock tube [77]. One of his major conclusions was the proposal of a two step interaction process. Markstein observed that the shock was partially reflected and partially transmitted through the kernel with little change in the flame structure. Then after some time, he observed that there was a significant distortion in the flame surface due to the accelerating products. An increase in the energy conversion rate followed.

With the experimental foundation laid, Rudinger [80] attempted an algebraic analysis of the shock-flame interaction. His analysis was too numerically complicated to perform at the time but did lead to the need for experimental studies of flame and turbulence interaction. Following this, Salamandra [75] performed additional shock tube experiments and proposed the three step interaction process discussed earlier. Next, Laderman *et al.* [81] suggested that the observed increase in heat release rate post (strong) shock was due to the breakup of the flame surface into a distributed reaction zone. Picone *et al.* [82] expanded on this description by expounding the role vorticity in the post shock flame. They suggested that the increase in energy release led to pressure and density disturbances which interact to

produce vorticity. The vorticity further increases mixing, leading to additional heat release. Haas and Sturtevant [83] proposed that the Richtmyer-Meshkov instability was responsible for the vorticity generation via baroclinic torque during the shock-flame interaction. Ju *et al.* [84] performed numerical analyses of H_2-air shock-flame interactions. They confirmed that the Richtmyer-Meshkov instability was responsible for the growth of the flame surface and burning velocity. Thomas *et al.* [85] studied shocked ethylene-air flame kernels and suggested that chemi-acoustic interactions, gas dynamic effects and thermal autoignition chemistry were responsible for the combustion enhancement. They concluded that a better understanding of the combined processes of diffusion, thermally initiated reactions and turbulence was necessary. Shocked methane-air flame kernels were studied by Gui *et al.* [86] with similar results.

The compressibility-flame interaction leads to increased flame stabilization and energy conversion rates and is therefore very important for supersonic combustion. For example, several studies have dealt with shock flame interactions in scramjets [87, 88, 89, 90, 91]. However, the shock-flame phenomena is likely not well captured by current numerical models because it combines finite rate chemistry with non-equilibrium turbulence (production of motion at many different scales through baroclinic torque) which violates Kolomorov's [92] first and second hypotheses. For example, in the numerical simulation of Dong *et al.* [93], the large scale effects are well captured but the fine scale velocity and chemistry effects at the flame are not well resolved. These results are potentially due to the strong discontinuity of shock waves. In this work, an expansion-flame interaction is studied because similar (but opposite) pressure change can be achieved more gradually with an expansion, avoiding some of the numerical problems discussed above. This will be important because numerical simulations are utilized in this work to enhance the description of the interaction. Previous experimental investigations on this topic have been mostly qualitative and did not include detailed flame and velocity data needed to formulate flame speed correlations. Therefore, there is a need to collect these data within practical supersonic

combustors that include expansion-flame interactions.

The flame kernel is an ideal choice for supersonic flame studies because it is free of large scale strain imposed by combustor geometry and hence can be used to isolate the effect of mean compressibility on the flame. In addition, there is a comprehensive low speed database that can be used for comparison. These include kernels studied in fan-stirred bombs [67, 53, 94, 54, 64] and shear-free subsonic ducts [39, 95, 96, 97, 98, 99]. The flame bomb is a heavily studied, canonical flame-turbulence problem and results from various groups are well established and reasonably collapse when scaled appropriately (Equation (1.10) for example). In order to lend credibility to the supersonic studies, the results will be anchored to flame bomb data at low speed (M < 0.1). Then, modeling the differences at high speed may be as simple as adding a constant to Equation (1.7) or modifying the exponent in Equation (1.9) or (1.10). A key goal of past experiments is to assess if a universal scaling or regime-specific scaling for S_T can collapse data over a wide range of operating conditions and experiments and this remains a goal of this work.

How spherically expanding flames propagate in low speed flows is fairly well understood. The flamelet structure and flame speed are well documented and universal flame speed scalings mentioned previously are successful at collapsing flame speeds for low to moderate turbulence intensity. On the contrary, premixed flame kernels propagating in a supersonic flow are unexplored and present unique challenges with many open experimental questions. Of particular interest is whether the flamelet behavior in supersonic flames is consistent with observations in subsonic flames. It is unclear whether supersonic flame regimes and their associated flamelet descriptions are consistent with the interpretation in subsonic flows. Whether the presence of compressibility affects the flame structure and hence the growth is also an open question. If compressibility has an impact on the small or large scale flame structure and growth, then S_T may fail to collapse onto well established scalings. In this scenario, turbulence may play a secondary role to the flame-compressibility interaction. New concepts of supersonic flamelets may be needed with

new scalings that depend, perhaps, on the Mach number. In order to assess the effects of compressibility, this work uses a supersonic channel with a mean velocity acceleration accomplished by diverging the tunnel walls. It will be shown that this mean expansion interacts with the flame to generate local velocity fluctuations akin to turbulence, which ultimately modifies the turbulent flame speed.

When a flame interacts with the compressibility, the evolution is substantially altered compared to the constant (or zero) velocity case [18]. The physical problem is similar to the reacting shock-bubble interaction [100, 101]. As the flame interacts with compressibility, vorticity is produced whenever the density gradient across the flame is misaligned with the pressure gradient because of baroclinic torque $\left(\frac{\nabla P \times \nabla \rho}{\rho^2}\right)$:

$$\frac{D\boldsymbol{\omega}}{Dt} \approx (\boldsymbol{\omega} \cdot \boldsymbol{\nabla})\boldsymbol{u} - \boldsymbol{\omega}(\boldsymbol{\nabla} \cdot \boldsymbol{u}) + \frac{\boldsymbol{\nabla}\rho \times \boldsymbol{\nabla} P}{\rho^2} \tag{1.18}$$

Here it is assumed that the change in vorticity due to viscous dissipation and body forces are negligible. The remaining terms on the right hand side represent the change in vorticity due to: (a) vortex stretching, (b) dilatation, and (c) baroclinic torque. Baroclinic torque is negligible for subsonic flames with minimal confinement. Also, dilatation acts to reduce vorticity across the flame, but is otherwise irrelevant for flames in an incompressible flow. On the contrary, both dilatation and baroclinic torque are significant for flames exposed to mean flow compressibility. Vorticity deposition due to these effects imposes additional multi-scale motion, which drastically affects the kernel shape and its growth. Figure 1.6 shows simulation results from Niederhaus *et al.* [102] for a RC22 bubble interacting with a Mach 1.22 shock. Upon interaction with the shock, many small vortices are formed on the bubble surface. The small vortices eventually coalesce into a larger scale over-turning motion. Both of these features are important because the flame will interact with the large and small scale content differently. Small scale vortical motion at the kernel interface may penetrate/interrupt the flame surface while the larger scale motion could contort the entire flame surface. For interactions with expansion waves, the small scale motion may be less

prevalent because the vorticity deposition is more gradual. However, if present, these small scale vortices could be difficult to observe because the schlieren diagnostic may not have sufficient resolution to identify them, or the flame may smooth them out as quickly as they are formed.

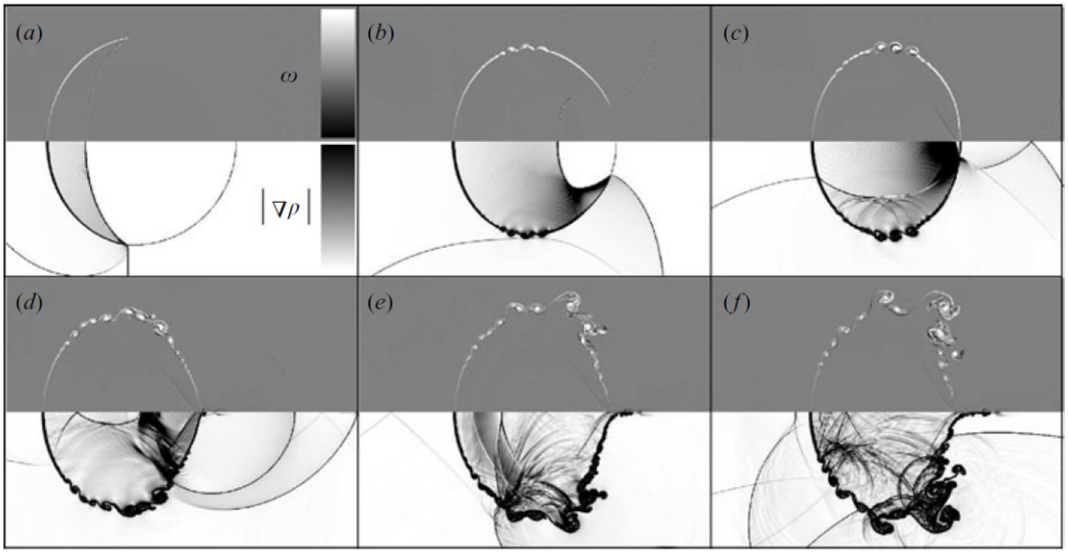

Figure 1.6: Simulated evolution of a R22 bubble in air interacting with a Mach 1.22 normal shock as shown by Niederhaus *et al.* [102].

When the bubble density is lower than the surroundings, as would be the case for flame kernels, the expansion accelerates the kernel with respect to the reactants. After some time, the initially spherical bubble evolves into a vortex ring. A similar evolution was shown in the classical shock-bubble work of Haas and Sturtevant [83]. Figure 1.7 from their work shows a helium bubble evolving into a vortex ring. This case is similar to the reacting vortex rings of this work because the Atwood number and pressure change are similar. The vortex structure of supersonic flame kernels exposed to mean expansion is a previously unexplored topic that is probed using new experiments and validated numerical simulations in this work.

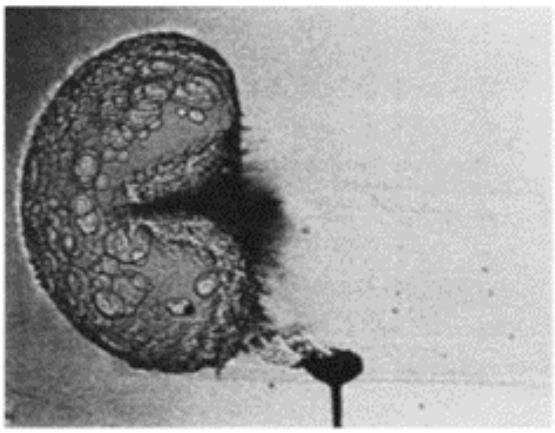

Figure 1.7: Shock-bubble interaction presented by Haas and Sturtevant [83]. Image was captured 510 μs after interaction of a Mach=1.1 shock with a helium bubble in air.

1.6 Overall Objective/Impact of the Study

The overall goal of this thesis is to advance the understanding of premixed flames in supersonic flows and to explain how those flames interact with mean compressibility. The interaction of the flame front and pressure wave, resulting in vorticity generation and motion over many scales, is a key interest in this work. This interaction is explored for the relatively simple case of a premixed flame kernel traveling in a supersonic channel flow with mean expansion. Whether previously established flame speed scalings are sufficient for this problem or if simple modifications of those scalings can be conducted are two important questions addressed. How the kernel morphology evolves in the expanding flow field is also of interest. An emphasis is placed on predictive ability with these studies, and hence this work should be useful for the experimental high speed combustion community as well as scramjet numerical modeling endeavors.

Specific Objectives of the Study

1. **Experimental facility development and evaluation.**

   While premixed flames have been studied in scramjet-like ground test experiments, there remains a need to study these flames under less general, more well-defined

supersonic conditions. For example, the typical scramjet combustor uses a cavity or ramp stabilizer which introduces a large range of scales in a highly non-uniform compressible region. The compression and expansion waves modify the growth and surface area of the flame and, if not taken into consideration, can produce flawed statistics. This objective aims to isolate the supersonic combustor, producing a channel that is nominally free of shocks, suitably optically accessible, designed with a nearly uniform flow expansion, and superimposed with well characterized turbulence. This new canonical configuration allows a systematic exploration of flame-compressibility interaction. However, it is not immediately obvious whether flame kernels could be generated in this environment nor whether a self-propagating flame front can be created. These design/construction tasks and research questions must be answered before a detailed exploration of the flame-compressibility interaction can be conducted. Chapter 2 shows the design of the facility and Chapter 4 shows that creating self-propagating flame kernels is possible with LIP of premixed fuel and air in a supersonic channel.

(a) Produce a mechanical design that is shock-free and optically accessible.

(b) Show feasibility of producing supersonic turbulent premixed flame kernels.

(c) Show feasibility of performing PIV, schlieren, OH* and PLIF measurements.

(d) Develop/characterize new turbulence generation grids for the supersonic flow.

2. **Ignition system development and laser ignition memory evaluation.**

The ignition process imposes a memory upon the emerging flame kernel. This memory effect takes the form of an overdrive in the species, temperature, and pressure that causes inflates flame growth for some time. The shape of the plasma discharge may also impart a memory on the flame shape which can persist well beyond the useful measuring size of the kernel. While these phenomena have been studied independently, their effect on propagating/growing supersonic flame kernels is not known.

This work contributes to the laser ignition community by performing premixed laser ignition studies in supersonic flows where the long term effects (or lack thereof) of the ignition event and dependence on the Mach number are explored. If a memory of the ignition process exists, then the duration and strength of that memory should be evaluated before meaningful kernel topology and flame speed measurements can be conducted. To answer these research questions, kernel images are collected using phase-locked schlieren photography while varying the ignition power. A deposited laser energy measurement system (shown in Chapter 2.1.4), calibration procedures, and best practices are developed. The kernel size versus time and deposited energy is evaluated for different equivalence ratios and Mach numbers. Chapter 3 shows how the ignition process effects kernel growth and provides recommendations and guidelines for optimal LIP settings for supersonic channel flows.

(a) Develop a laser ignition system which can measure the deposited laser energy.

(b) Perform ignition studies to investigate the supersonic laser ignition process.

(c) Investigate the transition to free flame growth.

(d) Isolate effect of equivalence ratio and Mach number.

3. **Numerical simulation evaluation.**

It is uncertain a priori if numerical simulations will yield results capable of enhancing the understanding of the supersonic flame kernel problem. A major goal of this work is to show that simulations can reproduce the experimental observations. Thereby, the supersonic flame kernel problem is demonstrated to be a robust flame-compressibility validation test case for CFD. The simulations are anchored to the experimental data using three key experimental observables: flow field velocity statistics, flame growth, and the kernel topology. Chapter 2 discusses the numerical methods including model and grid considerations and Chapter 4 shows validation of the numerical results against experimental data. The overall goal of this thesis is

understanding the physics of supersonic flame kernels rather than numerical model development and evaluation. Therefore, the simulations are only utilized as a well validated tool that enhances understanding of the experimental observations.

(a) Perform evaluation studies to assess numerical models and grid resolution.

(b) Compare experimental and numerical results for velocity statistics, flame growth, and flame topology.

4. **Investigation of flame kernel morphology and the reacting vortex ring.**

This chapter discusses previous shock-bubble and shock-flame interaction studies. Flame kernels in expanding supersonic flow likely have similar features to these classical problems, but this has not yet been demonstrated. Of specific interest is whether a reacting vortex ring forms. Numerical simulations are utilized to show without a doubt that the reacting vortex ring develops due to the flame-compressibility interaction. One of the goals of this work is to give a thorough description of the flame kernel topology evolution during the flame kernel-expansion interaction. Initial experimental observations are given in Chapter 4 followed by investigation of the baroclinic torque term and numerical observations in Chapter 5.

(a) Investigate direction and magnitude of the baroclinic torque term to develop a theory for kernel response to mean flow expansion.

(b) Evaluate the theory above using 2D experimental data.

(c) Using the validated 3D numerical data, show that the kernel morphs into a reacting vortex ring.

5. **Evaluation of supersonic flame speed correlations.**

The flame surface wrinkles and contorts in response to the local velocity field. Previous shock-flame studies have shown that flow field compressibility modifies the

flame surface, enhancing the burning rate, and increasing the turbulent flame speed. This is a crucial process to understand because in every practical supersonic combustor flames interact with compressibility. This phenomena likely occurs for supersonic flame kernels exposed to mean expansion, but this has not yet been tested/observed. How the interaction effects the flame speed is of particular interest. This work aims to establish the relative importance of turbulence versus compressibility on the flame speed and whether previously used, incompressible flame speed scalings are appropriate for supersonic flame kernels exposed to mean expansion. These results could then be extended to more general supersonic combustion problems where the flame operates in a premixed mode within the thin reaction zone. Chapter 6 shows how these low speed correlations perform and offers a new correlation appropriate for impulsively accelerated supersonic flames.

(a) Establish an experimental database of schlieren images for a variety of Mach numbers, equivalence ratios, turbulence intensities, and ignition time delays.

(b) Process experimental data into flame speed statistics.

(c) Perform numerical simulations for select experimental conditions.

(d) Evaluate subsonic flame speed correlations using combined experimental and numerical data.

(e) Propose and evaluate a new supersonic flame speed correlation, if needed.

CHAPTER 2
EXPERIMENTAL AND NUMERICAL METHODS

Experiments are conducted in a blow-down reacting wind tunnel capable of completely premixing fuel into air at equivalence ratios up to $\phi = 1.5$. Kernels are ignited using a focused Nd:YAG laser beam and PIV and schlieren are used to probe the flow field. The details of the experimental facilities and diagnostics arrangements are discussed here. Large eddy simulations are used to further explore supersonic flame kernels. Details about the simulation methodologies and problem setup are presented. Exploration of the accuracy of numerical schemes used for this problem are also discussed.

2.1 Experimental Methods

2.1.1 Flow Facility

Experiments were conducted at the Ben T. Zinn Combustion Laboratory in Supersonic Test Cell 1 (SSTC1), designed and built as part of this thesis work. A schematic of SSTC1 is shown in Figure 2.1 and a picture of the facility is shown in Figure 2.2. High pressure, preheated air is supplied by a blow-down type air storage system and an in-direct natural gas-fired heater. The air travels through supply piping into a vertical stagnation tank, designed to improve homogeneity in the experimental air by drastically slowing the air velocity. The stagnation pressure (P_0) is measured in the stagnation tank using a pressure transducer with a standoff pipe to avoid excess temperatures. The stagnation temperature (T_0) is also measured in the stagnation tank using a k-type thermocouple immersed in the flow. The temperature and pressure conditions are variable from $T_0 = 300 - 650$ K and $P_0 = 0.3 - 0.6$ MPa. Stagnation conditions are varied to achieve constant static temperature ($T_s \approx 335$ K) and pressure ($P_s \approx 73,000$ Pa) within the test section across all Mach

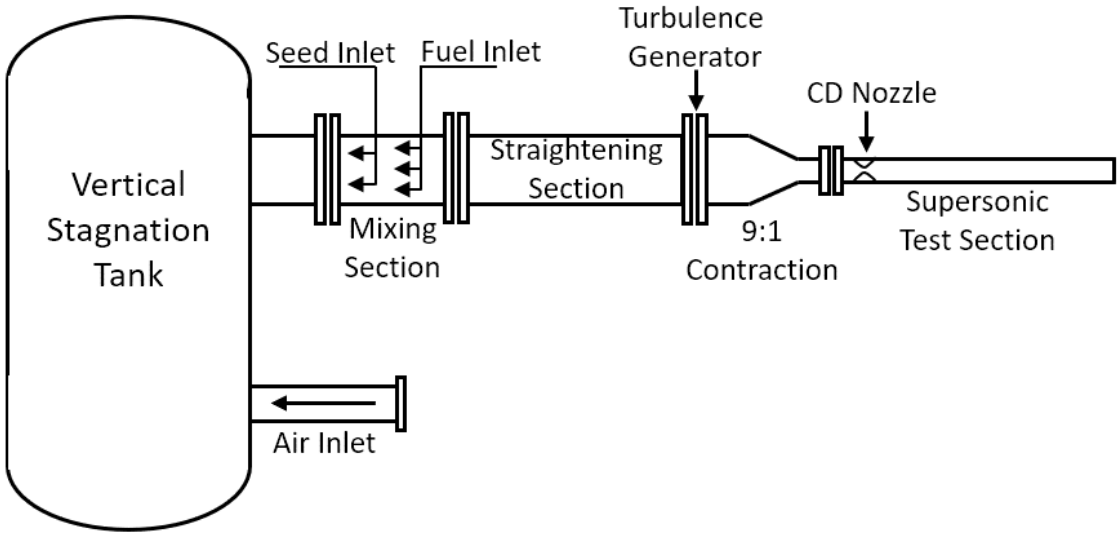

Figure 2.1: Schematic of flow facility facility.

number conditions tested. The air flow rate is metered using a choked flow calculation at the facility nozzle.

Natural gas with $> 98\%$ CH_4 is injected into the air stream through an array of counter-flowing jets in the mixing section. The fuel flow is controlled by increasing the facility supply pressure and gas is directed into the mixing section by opening a LabView-controlled isolation valve. The fuel flow rate is metered by a choked flow calculation at the injection orifices as well as by a sub critical orifice further upstream. The flow rate can be varied to achieve an equivalence ratio in the range $\phi = 0, 0.12 - 1.4$, with typical runs between $0.7 - 1$. The fuel/air mixture then flows through the horizontal straightening/homogenizing section, which is sized sufficiently long to achieve complete mixing and uniform velocity. Premixedness in the mean was verified by traversing an extractive sampling probe and analyzing the samples using an online infrared absorption gas analyzer. Variation in the cross-stream air-fuel ratio is less than 5% at the end of the straightening section. The hot/premixed mixture then travels through a turbulence generator, into a 9:1 area contraction, through the facility nozzle, and finally into the supersonic test section. A schematic of these components is shown in Figure 2.3. The 9:1 area contraction was included to re-

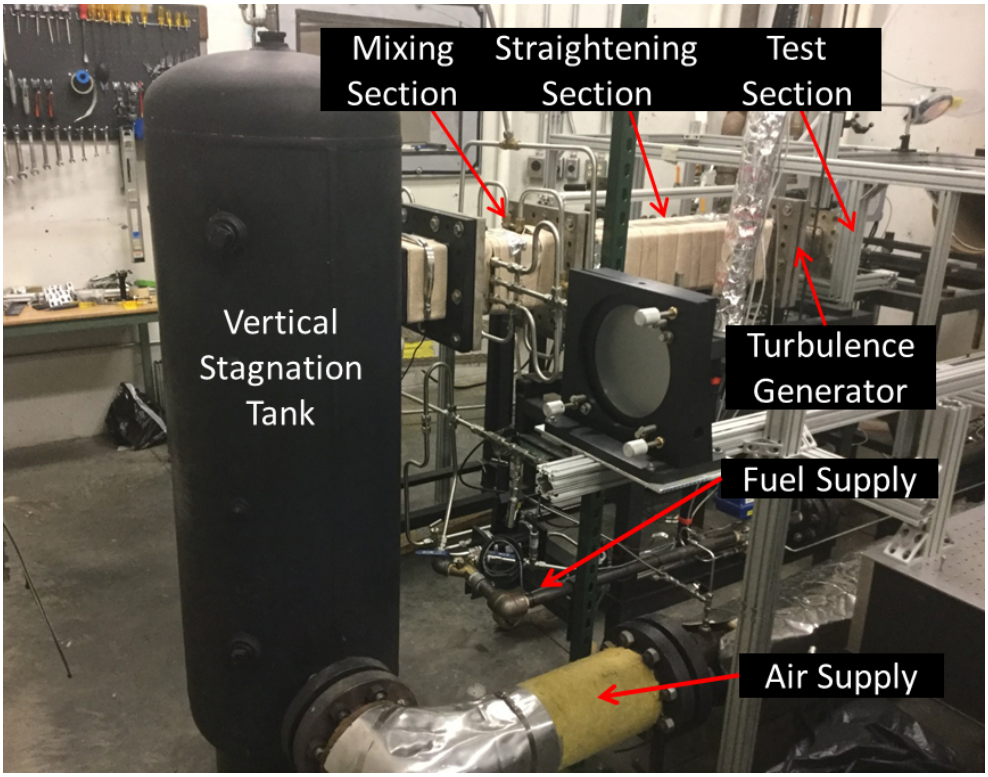

Figure 2.2: Air and fuel delivery system. Shown with test section not installed.

duce the upstream velocity, which improves premixedness and velocity uniformity. Three different throat geometries ($M = 1.5$, 1.75, or 2.0) are designed using a minimum length method of characteristics code developed as part of this work. Appendix A shows the nozzle designs and coordinates. The turbulence generators and test section are discussed in the following sections.

2.1.2 Turbulence Generation

Turbulence is added to the base flow by means of two different turbulence generating plates installed upstream of the 9:1 area restriction, at the exit of the horizontal flow straightener. The plates utilized in these studies are: 1. a planar grid of uniform holes (Figure 2.4 left), and 2. a biplanar grid of rods (Figure 2.4 right). The former is referred to as the hole grid while the later is simply the biplanar grid. The base flow, without a turbulence generator, is referred to as the no-grid condition. The hole grid has an array of 8.89 mm holes with

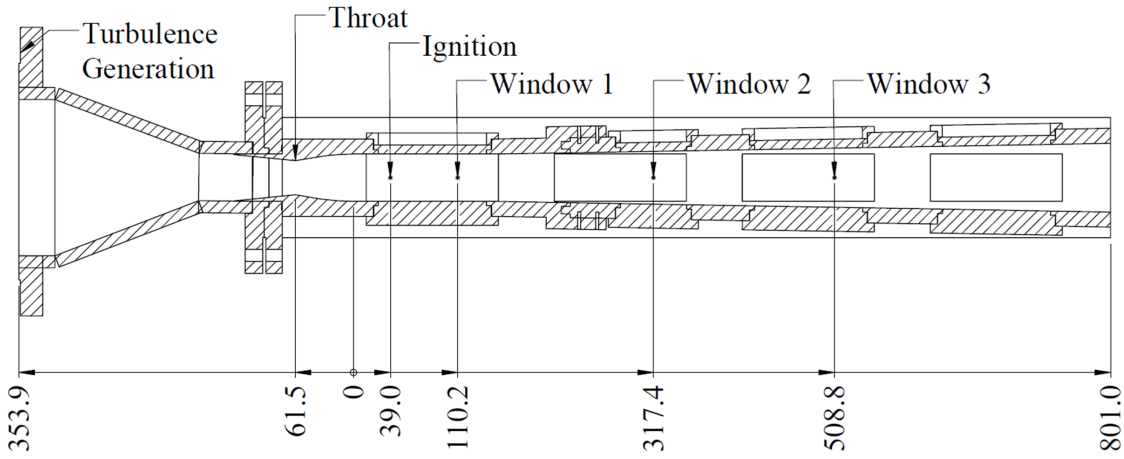

Figure 2.3: Schematic of the optically accessible diverging tunnel shown with $M_0 = 1.75$ nozzle installed. Distances are millimeters from the C-D nozzle exit.

33% solidity with a hexagonal pattern machined into a 3.2 mm stainless steel plate. The biplanar-grid has two perpendicular grids of 4.76 mm stainless rods separated by 19.58 mm. The horizontal and vertical rods are arranged on two different planes, separated by 7.83 mm.

For $M = 1.75$, no grid, biplanar grid and hole grid are used. For $M = 1.5$ and 2.0, only the hole grid is used. Turbulence properties for the various arrangements are collected using particle image velocimetry (PIV) at each window. Inflow properties at the first window are shown in Table 2.1, and turbulent velocity and isotropy trends are shown in Chapter 4. The RMS turbulent velocity (u') does not vary significantly downstream, which is not surprising considering the eddy turn over time is quite long when compared to the flow through time. For example, the eddy turn over time for the large, energy containing motions is $\tau_e = L_{11}/u' \approx 2.2$ ms. This number is quite large when compared to the flow through time, which is $\tau_f \approx 0.8$ ms for $M = 1.75$. Therefore, it would seem that the large scale motions only weakly evolve throughout the test section. Additional turbulence generation through interaction of existing fluctuations with compressible features yields a flow field with nearly constant turbulent statistics.

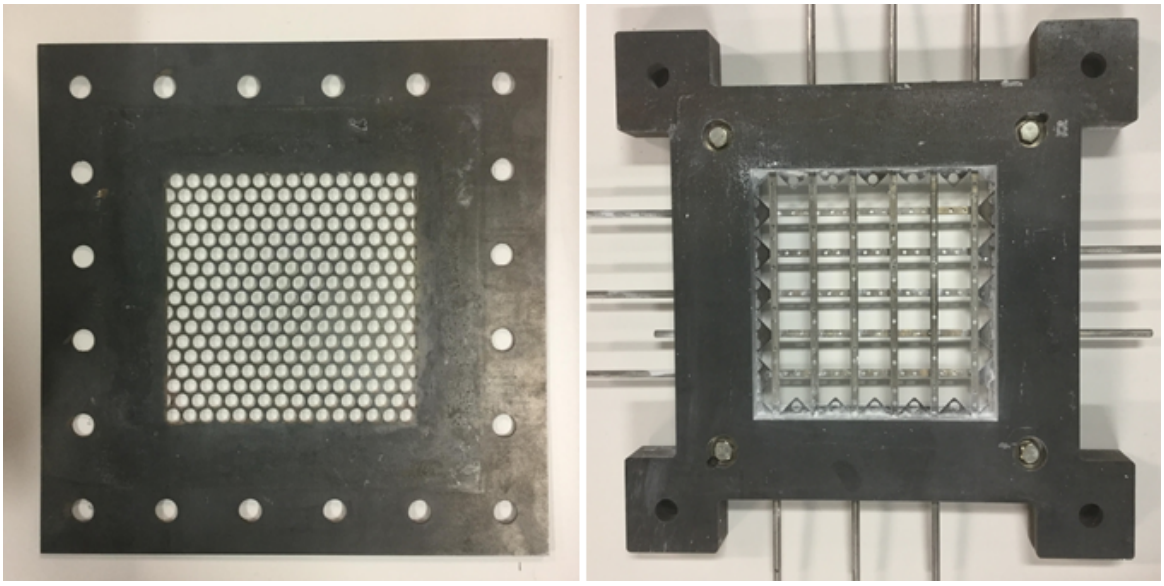

Figure 2.4: Hole grid (left) and biplanar grid (right) turbulence generators.

Table 2.1: Turbulence generator properties measured at position 1, approximately 75 mm downstream of the ignition point.

Turbulence Generator	M_0	u' (m/s)	u_1/u_2	L_{11} (mm)	$Re_{L_{11}}$
1. No Grid	1.75	3.98	0.42	11.43	1,691
2. Biplanar Grid	1.75	4.15	0.45	10.9	1,681
3. Hole Grid	1.50	3.96	0.43	10.3	1,584
4. Hole Grid	1.75	4.45	0.41	10.2	1,663
5. Hole Grid	2.00	2.99	0.65	16.81	1,712

2.1.3 Supersonic Test Section

A schematic of the test section internal geometry is shown in Figure 2.5, with the CFD domain superimposed in gray shading. The supersonic tunnel is a $\approx$ 800 mm $\times$ 50 mm $\times$ 50 mm channel, whose top and bottom walls diverge with a 1° angle. The fuel-air mixture enters from the left, passes through the converging-diverging (CD) facility nozzle and exits at the design Mach number. Three minimum-length facility nozzles are available for three exit Mach numbers: $M = 1.5, 1.75,$ or 2.0. The design and geometry of these facility nozzles is given in Appendix A.

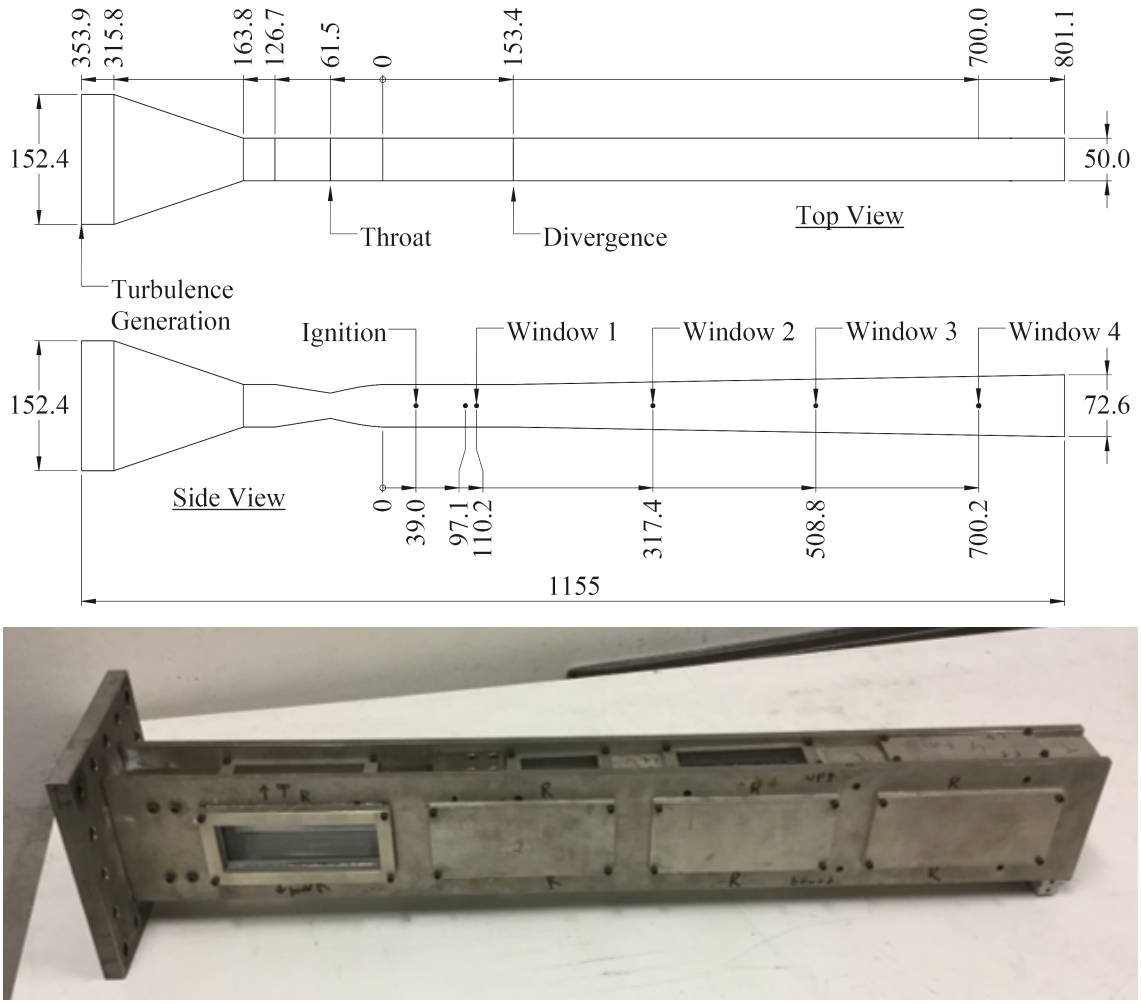

Figure 2.5: Top and side views of the internal flow geometry and picture of the as-built tunnel. Flow is from left to right. Units are in millimeters.

At the CD nozzle exit, the test section has a 50×50 mm^2 square cross-section. Approximately 140 mm downstream of the nozzle exit, the tunnel walls abruptly diverge at $1°$, creating expansion waves that reflect indefinitely downstream (see Figure 2.6). This arrangement mimics a scramjet geometry, where divergence is added to avoid frictional and thermal choking and to generate thrust surface. The $1°$ divergence was chosen because early studies indicated the boundary layer grew at about $0.5°$; a significant expansion above this is required to generate a sizable flame-compressibility interaction. At $1°$, the mean flow field experiences an acceleration with a pressure gradient of $\nabla P \approx -30,000$ Pa/m across all cases. Increasing the expansion above $1°$ would result in a flow field which cools too rapidly for flame studies.

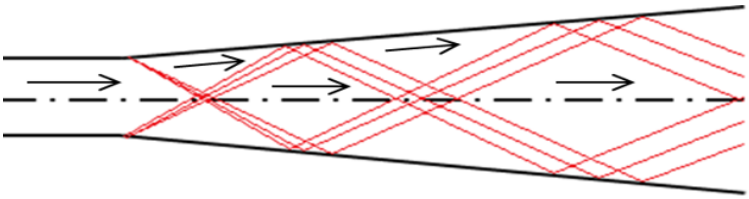

Figure 2.6: Cartoon of expansion waves emanating from turning corners and reflecting indefinitely downstream.

The supersonic test section has four axial viewing locations. At each axial location, there are four windows: two on the top/bottom walls, and two on the side walls. Experimental data are collected at the first three viewing locations and blanks are installed at the furthest downstream location. To avoid shock waves, the windows are designed with a step that interlocks with the tunnel walls, ensuring a smooth transition from metal to glass. Hence, the windows are set glass on metal and externally sealed with a graphite gasket. The window size was selected to allow full orthogonal viewing of the top and bottom walls at the first viewing location. Both side windows are utilized for schlieren photography and, for laser diagnostics, all four windows are utilized. The ignition laser also passes through either the side or top/bottom windows.

2.1.4 Laser Ignition

Laser ignition and deposited energy measurement system

A schematic of the ignition laser and deposited energy measurement systems is shown in Figure. 2.7. Flame kernels are ignited with a Q-switched frequency-doubled (532 nm) Continumm Powerlite Nd:YAG laser. The laser enters the test section through either the first top window (ignition studies) or the first side window (flame kernel studies). The laser pulse energy can be varied (without changing the laser settings) by rotating the polarization using a half-wave plate (Thorlabs WPMH05M-532). The unwanted energy is sent to a beam dump using a polarizing beamsplitter plate (Thorlabs PBSW-532). The laser energy is measured using two calibrated photodiodes (the calibration procedure is discussed below). For the incident energy, a beam sampler (Thorlabs BSF20-A) is used to extract a small amount of energy for measurement. The sampled beam travels through a one inch opal diffuser glass (Edmund Optics 43-717) then through one of several different absorptive neutral density filters (kit from Thorlabs- NEK01) selected based on the incident energy and is finally measured using a photodiode (Thorlabs DET25K). The diffuser, filter, and photodiode are mounted using a Thorlabs one inch rail carriage system.

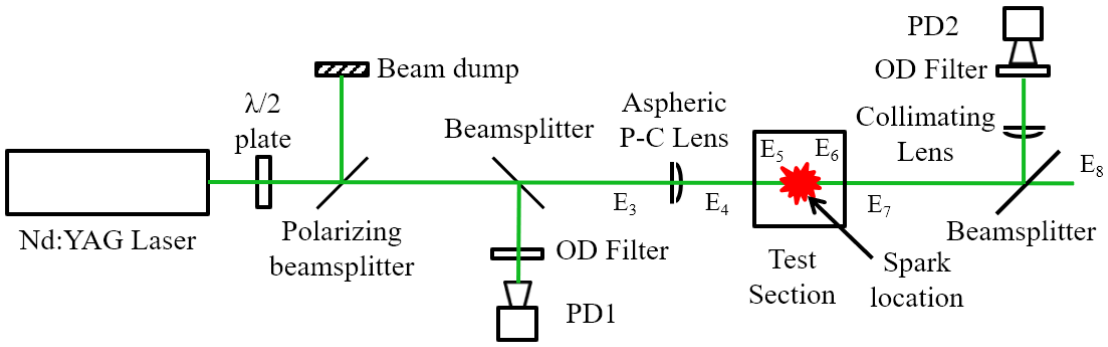

Figure 2.7: Schematic of ignition and laser power measurement system.

The incident energy is focused using a 100 mm plano-convex ashperic lens (Thorlabs AL50100) then travels through the test section windows where, if the energy is high

enough, breakdown occurs. Some of the incident energy is deposited into the kernel, the rest is transmitted through the kernel and exits the test section. The transmitted light is partly scattered by the optical lensing effect of the dense plasma formed during breakdown. The transmitted/scattered light travels to a 50:50 beam splitter (Thorlabs BSW42-532), after which it is measured using a diffuser/filter/photodiode arrangement that is identical to the one discussed for the incident light measurement.

Calibration of the laser energy measurement system

Before discussing the calibration procedure, it will be necessary to define terminology for the energy measured at various locations and to define transmission coefficients across the various optics and windows. Referring to Figure 2.7, E_3 is the energy immediately before the Aspheric P-C Lens, E_4 is the energy after the Aspheric P-C Lens and before Tunnel Window 1, E_5 is the energy after Tunnel Window 1 and before breakdown, E_6 is the energy after breakdown and before Tunnel Window 2, E_7 is the energy after Tunnel Window 2 and before the beamsplitter, and E_8 is the energy after the beamsplitter. Typical values for $E_3 - E_8$ are shown later in Figure 2.10. The energy deposited into the flame kernel is calculated through a subtractive technique, $E_d = E_5 - E_6$. The transmission across the Aspheric Lens is calculated by measuring the mean energy in front and behind the lens using a Coherent LabMax-TOP laser power meter with a J-50MG-YAG sensor head. The transmission coefficient across this lens is $\epsilon_l \approx 0.9$ across all incident laser energy levels. Similarly, the transmission across the tunnel windows is $\epsilon_{w1} = \epsilon_{w2} \approx 0.928$ ($\sigma_{\epsilon_w} = 0.00136$), which was determined with new/clean windows. The value can be quite a bit lower with old/dirty windows ($\epsilon_w = 0.858$ was measured with a 10 run-hour old window), therefore new windows are used whenever laser energy measurements are conducted.

Scattering of transmitted light due to the strong optical lensing of the plasma causes some of the transmitted light to spill over the beamsplitter, and therefore miss the transmitted photodiode. The scattering angle is small enough that a negligible amount of the

transmitted energy is lost when the sensor head is located at the tunnel window. Unfortunately, the sensor cannot be located here because 1. during hot calibration the sensor head becomes overheated, and 2. space limitations demand it be placed further away. Therefore, the amount of lost energy must be measured. The $\%$ light lost due to scattering can be calculated by measuring the mean energy (E_7) at the tunnel wall and then measuring the mean energy past the 50:50 beamsplitter (E_8). The ratio of these two, $\epsilon_s = E_7/E_8$, is the amount by which E_7 is reduced due to scattering and the 50:50 beamsplitter. The transmitted photodiode is directly calibrated against E_8, and therefore ϵ_s is the only piece of information needed to back-calculate E_7. The value of ϵ_s is relatively independent of the incident energy (when breakdown occurs), therefore an average value of $\epsilon_s \approx 0.3601$ was calculated and then used for all cases. This number can be in error if the scattering is intermittently less than expected, such as when breakdown doesn't occur or is very weak, which may happen when the incident energy is very low. In this case, E_7 will be overestimated. Fortunately, the transmitted energy is also quite low in this case, and therefore the error is small. The overestimation of E_7 will make the deposited energy appear negative at the lowest energy levels. This low energy error is a fundamental limitation of this system because the energy in the scattered light cannot be directly measured given the thermal and physical constraints.

The values of E_5 and E_6 are given by:

$$E_5 = \epsilon_l \, \epsilon_{w1} E_3 \tag{2.1}$$

$$E_6 = \frac{E_8}{\epsilon_s \epsilon_{w2}} \tag{2.2}$$

The incident and transmitted photodiodes are calibrated against the laser power meter to yield E_3 and E_8, respectively. Both photodiodes are calibrated prior to every test. For the incident energy, the power meter is placed immediately in front of the ashperic igni-

tion optic. The laser energy is measured for 1000 pulses while the incident photodiode (PD1) voltage is simultaneously recorded on a Teledyne Lecroy HDO6104 oscilliscope in sequence sampling mode. An example time trace of the PD1 voltage is shown in Figure 2.8. For the transmitted energy, the calibration procedure is identical except that the power meter is placed behind the last beam splitter when calibrating the transmitted photodiode (PD2).

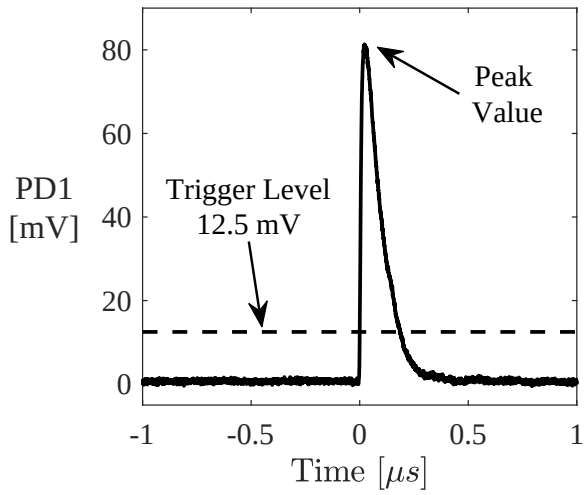

Figure 2.8: Time sequence of incident photodiode signal.

Given the simultaneous photodiode and laser power measurements, the information within the photodiode trace can be correlated to the measured power. Two obvious observables to use for this correlation are the peak voltage or the area under the trace. Both the peak and area have strong correlations to the laser energy measurement, with correlation coefficients greater than 98%. The area has a slightly larger correlation coefficient but the correlation curve is non-linear, causing a strong error if extrapolation off the curve is needed. Alternatively, the correlation based on the peak is linear (and less computationally expensive). Therefore, the peak-based correlation was deemed superior. An example calibration curve for PD1 with an average incident energy $\langle E_3 \rangle \approx 35$ mJ is shown in Figure 2.9.

Calculating the energy at each of the various locations is a simple matter once PD1

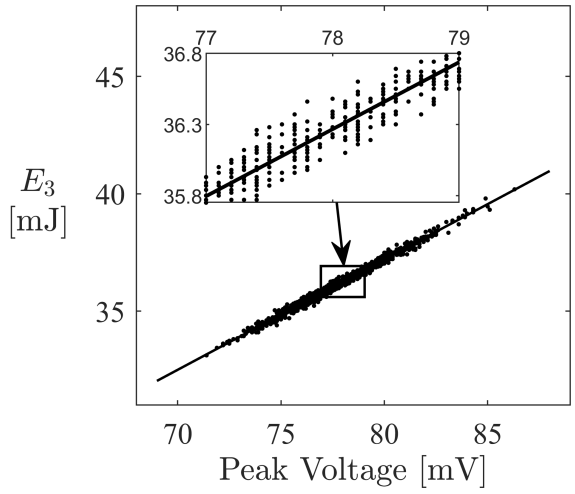

Figure 2.9: Calibration of photodiode peak voltage with laser energy measurement.

and PD2 are calibrated. Figure 2.10 shows a sequence of 950 laser pulses. Clearly the incident energy drops as it passes through the ignition optic and tunnel windows. About 70% of E_5 is deposited into the kernel while $\approx$ 30% is transmitted. The coefficient of variation (standard deviation divided by mean) of E_3 is a weak function of E_3 increasing from 2.45% to 3.34% as E_3 increases from approximately 15 to 55 mJ.

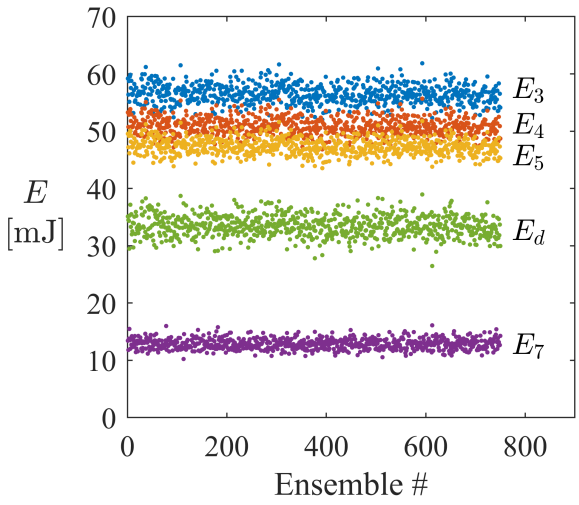

Figure 2.10: Laser energy at various locations.

Most of the analyses in Chapter 3 utilize a kernel size versus energy or time plot. The accuracy of these scatter plots depend on the fidelity of the edge detection algorithm em-

ployed. Noise in the detected edge, due to weak edges in schlieren images or overlapping of signal (kernel) with other features (shocks) in the flow can cause an error in the detected edge. Two steps are taken to mitigate these errors. First, a Fourier-based shock-removal process is employed to remove shocks in images. This step takes advantage of the fact that lines in physical space are also (rotated) lines in Fourier space. The image is converted to Fourier space and a mask is applied to the lines, then the original image is reconstructed via an inverse Fourier transform, resulting in an image with the shocks almost entirely removed and the kernel mostly unaffected. Figure 2.11 shows this process for a $M = 1.75$, $\phi = 1.0$ kernel at $\Delta t_{ign} = 30$ μs. Next, a progressive trend-based outlier detection and removal algorithm is used to remove outlier points. The goal here is to focus in on kernels that look similar, and to discard kernels that have a drastically larger or smaller width, perimeter, or area than the rest. A trend (area versus energy for example) is formed, then ensembles 3.5 standard deviations away are removed. A similar process is followed for the width and perimeter. The entire process is repeated, forming new trends on each repetition, until no more ensembles are removed. The critical standard deviation is then decreased and the entire process repeated. Finally, kernels 1.9 standard deviations away from their respective trends are retained. About 150-350 kernels out of 750 are retained.

2.1.5 Diagnostics

A number of laser and optical diagnostics are used to derive flow, velocity, and flame statistics. Velocity vectors are calculated using planar and stereo-PIV and flame edges are visualized using schlieren photography. Evidence is provided to show that, despite their advantages, OH PLIF and OH* chemiluminescence are not very useful for supersonic flame kernels.

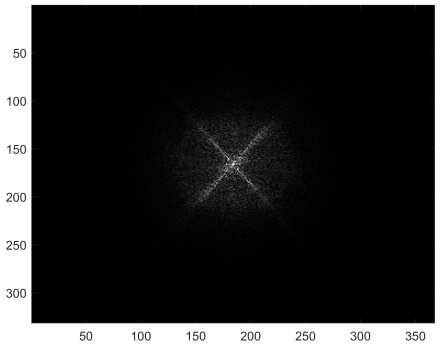

(a) FFT without mask.

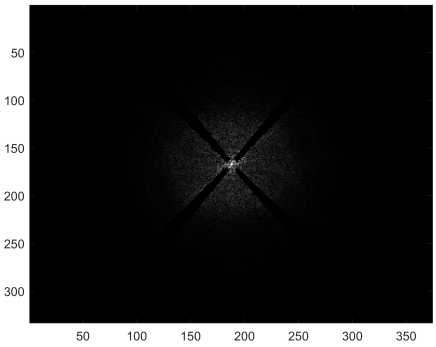

(b) FFT with mask.

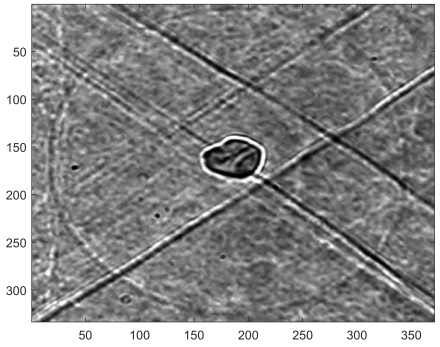

(c) Raw image without mask.

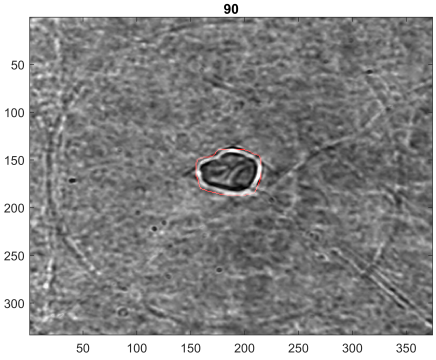

(d) Raw image with mask.

Figure 2.11: Fourier-based shock removal algorithm.

Schlieren Visualization

Schlieren is an optical technique for extracting refractive index differences within a transparent media. Schlieren is particularly useful for fluid flows because variation in fluid density results in a change in the refractive index. Also, most fluids of engineering interest satisfy the requirement that the fluid be transparent. Famous examples of schlieren images span a wide range of applications from the visualization of strong density variations (such as shock waves [103]) to weak density fluctuations (such as the heat plume from ones hands [104]). Schlieren events occur naturally so it is likely that no one person ”invented” schlieren. However, much of the modern scientific use of schlieren has its origins with the pioneering work on Toepler [105]. In these studies, two schlieren setups are used, both of

which are adapted from Settles [106]. For flame growth studies, the schlieren system is a folded lens system and for ignition studies a Z-type mirror setup is used. These systems are discussed below.

For flame growth studies, a modified dual-field-lens LOS schlieren system [107] is used. A schematic of the arrangement is depicted in Figure 2.12. The light source is a High-Speed Photo-Systeme Nanolite KL-L flashlamp with 18 ns flash duration, which is a sufficiently short pulse to freeze the supersonic flows in these studies. A 150 mm diameter, 750 mm focal length plano-convex lens is used to collimate the light. The collimated light passes through the test section before being refocused by a 150 mm diameter, 1000 mm focal length plano-convex lens. The focused light falls on a horizontally oriented knife edge and images are captured using an Imperx Bobcatt 29 MP CCD camera, a $2\times$ teleconverter, and a 200 mm macro lens. The ignition laser, arc flashlamp, and camera are synchronized using a BNC 575 digital delay generator, all operating at 1 Hz. A MATLAB Canny algorithm [108] is used for edge detection with some manual corrections made in post processing. The flame images are processed into the ensemble mean 2D flame area, $\langle A_{2D} \rangle$, from which from which the ensemble mean radius, $\langle R \rangle$ is calculated as discussed in Chapter 1.4 and Appendix B.1. Typically, 200 phase-locked images are recorded but, owing to low variability in the data, only 30 images are processed per dataset resulting in ± 0.2 mm confidence interval on the radius measurement (see Section 2.1.6).

For ignition studies, a higher sensitivity folded Z-type mirror schlieren system is used. A schematic of the arrangement is depicted in Figure 2.13. The light source is a High-Speed Photo-Systeme Nanolite KL-L flashlamp with 18 ns flash duration. A 200 mm diameter, 2 m focal length parabolic mirror is used to collect/collimate the light. The collimated light passes through the test section before being refocused by another 200 mm diameter, 2 m focal length parabolic mirror. The focused light falls on a horizontally oriented knife edge and images are captured using a Photron SA-Z camera and a Sigma 50-500 mm telephoto lens. The ignition laser, arc flashlamp, and camera are synchronized using a BNC 575

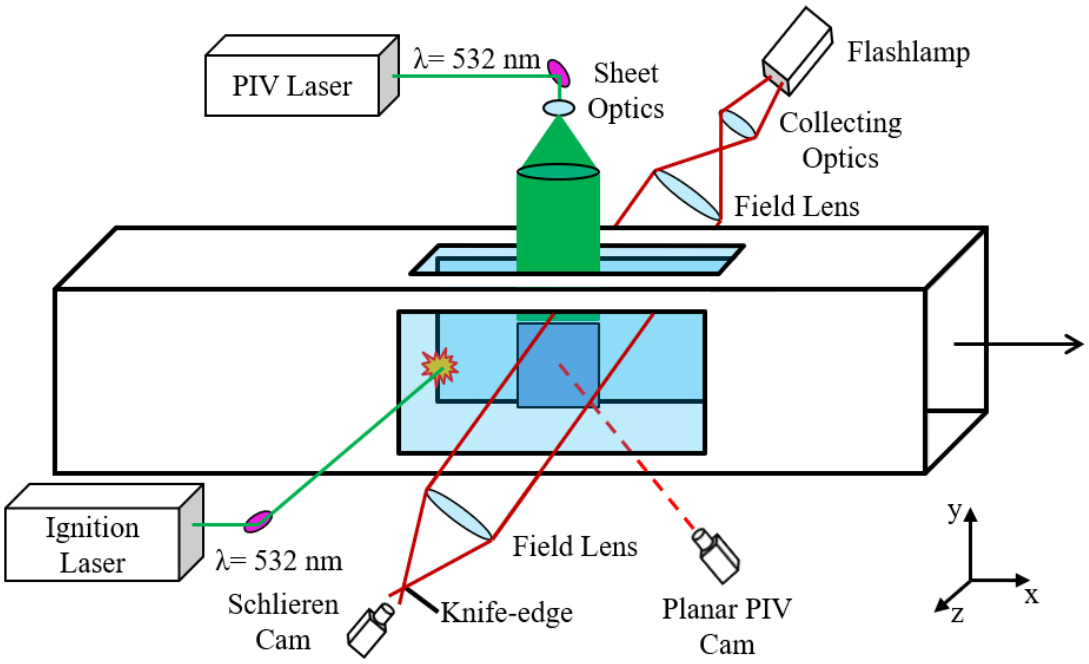

Figure 2.12: Schematic of schlieren and PIV arrangement for flame growth studies. The ignition laser and schlieren pass through the side windows. The PIV sheet enters through the top of the test section and is viewed through the test article side windows.

digital delay generator, all operating at 10 Hz. Once acquired, the images are processed in a similar manner as discussed above.

A very limited set of high speed schlieren cinematography is recorded, primarily in an attempt to investigate the vortex ring. For those studies, high speed images are collected at 50 kHz with a 300 ns exposure using a Photron SA-Z. The folded Z-Schlieren arrangement is used with a Lightspeed HPLS-36DD18B high speed LED light source. The camera is triggered in Random-50 mode, i.e. it is set to capture 50 frames with every TTL trigger signal from the delay generator.

Sample phase-locked schlieren images are shown in Figure 2.14 at three different measurement locations. An example high speed sequence is shown in Figure 2.15.

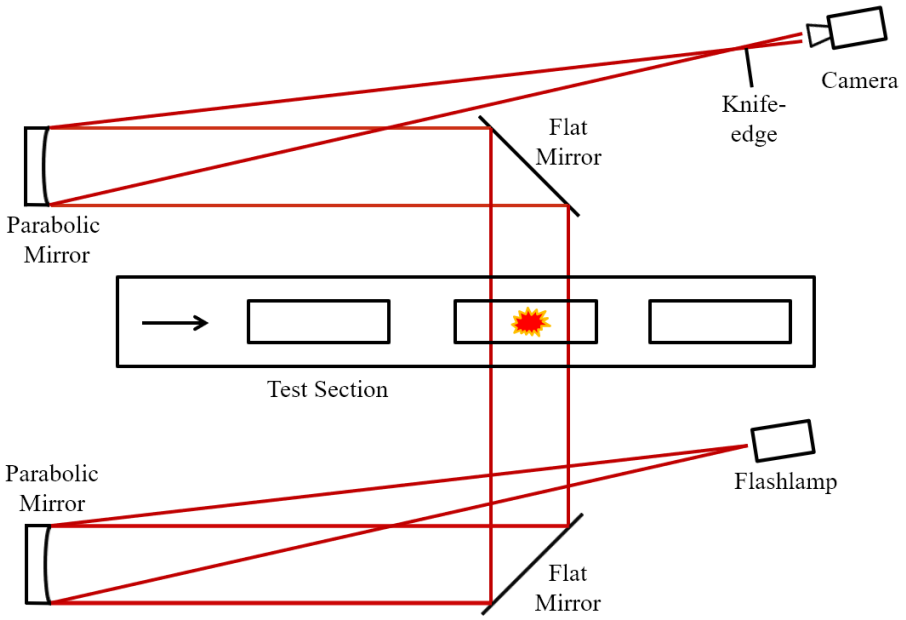

Figure 2.13: Schematic of Z-Schlieren arrangement for flame growth studies. The ignition laser passes through the top window and schlieren passes through the side windows.

Planar Laser Induced Fluorescence

Schlieren imaging has several disadvantages that merit exploration of other diagnostics. For example, schlieren imaging overestimates the flame volume because the measurement uses line of sight information. Further, the schlieren edge corresponds roughly to a temperature rather than a chemical species. To address these deficiencies, OH planar laser induced fluorescence (PLIF) was attempted. In this Section, it will be shown that while PLIF works well for low speed flows, it proved problematic in this high speed environment.

Before discussing the PLIF results, a quick note is made about flame edge detection. Najm *et al.* [109] suggest that OH alone is an inadequate marker of the flame front. They show that the formyl radical (HCO) more accurately represents the flame edge and heat release zone. However, HCO is hard to detect experimentally. An alternative to HCO is the simultaneous measurement of the OH and CH_2O radicals [110, 111]; the pixel by pixel product of OH and CH_2O representing the flame zone. Unfortunately, simultaneous

OH/CH_2O is a difficult diagnostic unto itself. Therefore, despite these limitations it is not surprising that OH PLIF has been used extensively/successfully for flame edge detection in experimental works involving low speed flows [99]. With this knowledge, an attempt was made to use OH PLIF for the supersonic flame kernel problem.

A Lambda Physik Scan Mate dye laser pumped by a frequency doubled Spectra Physics Quanta-ray Nd^{+3}:YAG is used to induce fluorescence in the OH radical. The output is frequency doubled and tuned to $\sim$ 283 nm. The frequency is swept for the strongest fluorescence peak using a torch prior to testing. A plano-concave and two plano-convex lenses form a 50 mm wide by 0.5 mm thick sheet (measured by the knife-edge technique). A NAC GX-3 camera and HiCatt intensifier with 1 μs gate capture the OH PLIF images. With this arrangement, the PLIF system has an overall spatial resolution of 0.5 mm, driven by the sheet thickness. Images are collected at 10 Hz (synced with the BNC Model 575 digital pulse generator) and approximately 1000 kernels are imaged per dataset. Figure 2.16 shows example PLIF results for the no grid and passive grid at $M = 1.75$, $T_s = 335$ K, and $P_s = 75$ kPa. A threshold intensity was applied to the raw images to detect the flame area, from which flame sizes were calculated.

Extreme kernel motion and deformation make c-map generation difficult. Large scale lateral motions convect the kernels in the y and z directions and the kernels move far enough off the laser plane that a significant portion of them are only partially intersected by the sheet. In fact, a non-negligible portion also miss the laser sheet entirely. If the kernel size is extracted from these flawed measurements, then flame statistics will be significantly biased. In an attempt to correct for these biases in post processing, a histogram of the kernel diameter was used to remove the unwanted images and improve the statistical convergence. A threshold diameter was picked by hand and all kernels with a smaller diameter were discarded. Kernels larger than the threshold are averaged to yield the mean flame area. This technique appeared to improve the results, but the settings were ad hoc, requiring a different manual tuning for every dataset. One further problem with the OH PLIF measurement was

that the kernels appeared very stretched and broken in many of the images and it was difficult to interpret the progress variable maps generated. Therefore, it was determined that OH PLIF is of questionable merit for the supersonic flame kernel problem and was abandoned for the simpler and more reliable schlieren diagnostic. However, the internal structure does reveal some interesting features that schlieren imaging alone cannot.

Particle Image Velocimetry

Velocity measurements in supersonic flows present a particular challenge due to the difficulty of properly time resolving measurements. In addition, achieving faithful particle tracking within the flow field is difficult due to high mean flow momentum and reduced time scales. Despite these challenges, previous studies have demonstrated several techniques for accurate velocity measurements in supersonic flows including: laser Doppler velocimetry [112], Doppler shift laser induced fluorescence[113], and particle image velocimetry [114]. In these studies, a limited set of stereoscopic PIV is utilized to show cross-stream homogeneity and justify use of a more extensive planar 2D PIV diagnostic.

Velocities are measured using either a standard stereoscopic or a two-component planar PIV system. The main challenge in adapting these systems to this supersonic flow is in achieving a small enough interframe delay on the camera, which was relatively easy on the cameras used. Planar two-component PIV is used to measure velocity statistics at Windows 1, 2, and 3, while stereo-PIV is used only at Window 1. Additionally, reacting PIV data are collected for the baseline case ($M_0 = 1.75$, $\phi = 1.0$) at Windows 1, 2, and 3. A schematic of the planar 2D PIV system is shown in Figure 2.12. In both systems, a dual headed, frequency doubled Big Sky Nd^{+3}:YAG laser provides particle illumination. For planar PIV, an Imperx Bobcatt 29 MP CCD camera captures the image pairs, whereas two Photron SA-5 CMOS cameras were used for stereo-PIV. The laser and camera(s) are synchronized at 1 Hz with a $4\,\mu$s delay between laser pulses. A BNC Model 575 delay generator provides timing for the lasers and camera. The sheet is formed using a 50 mm plano-concave lens to

spread the beam, one 500 mm plano-convex lens to collimate, and a final 750 mm plano-convex lens to control the sheet thickness. The sheet width is approximately 50 mm and the sheet thickness is approximately 1.0 mm (calculated by the scanning knife edge technique). The sheet enters the test section through the top window and is imaged from the side. The images cover approximately a 30 x 30 mm^2 area within the test section. Total beam power is ≈ 80 mJ/pulse upstream of the sheet forming optics.

Instantaneous velocity vectors are calculated using a cross-correlation algorithm [115] for each interrogation volume. A multi-pass approach [116] is used with 512 x 512 (64 x 64) pixel interrogation volumes on the first pass and 48 x 48 (24 x 24) pixels on the final pass for the 29 MP Bobcatt camera (Photron SA5). Two-dimensional Gaussian weighting and sub pixel interpolation are used [115], and interrogation volumes are 75% overlapped to decrease the vector spacing. The resulting vectors are spaced approximately 250 μm apart and have a wavenumber resolution of about 6,300/m. Velocity vectors 5σ outside the mean or with a correlation value under 0.7 are discarded in post processing. Additionally, vectors with a difference to the mean $2\times$ larger than the RMS of it's neighbors are removed in post processing [117]. Lavision's DaVis 8.3 is used to perform the above calculations. Details of the calculation of turbulent statistics: mean (U_i), standard deviation (u_i), autocorrelation (R_{ii}), longitudinal and lateral integral length scales (L_{11} and L_{22}), and 1D energy spectra (E_{ii}) are discussed in Appendix B.1.

A fluidized bed seeding system is used to mix a separate air stream with alumina (Al_2O_3) seed particles. A manual control valve is used to vary the flow rate. The seeded air is then mixed with the main air via injection through counter-flowing jets located in the mixing section (immediately upstream of the horizontal homogenizing section), which ensured a homogeneous mixture of seeding particles. The seed medium is 300 nanometer Alpha Alumina from Mark V Laboratory. The particle size and material are picked to maximize the particle response time while limiting particle agglomeration and seeding difficulties, as well as for its resistance to combustion temperatures. The particles are suf-

Table 2.2: Variance of the statistic estimators and typical values for the 95% confidence interval from a sampling distribution with N independent observations. Units are [m/s] for velocity and [mm] for length.

Stat.	$s_x^2 \times N$	95% CI
U_i	$\langle u_i'^2 \rangle$	± 0.224
u_i	$\frac{\langle u_i'^4 \rangle - \langle u_i'^2 \rangle^2}{4\langle u_i'^2 \rangle}$	± 0.254
$u_i u_i$	$\langle u_i'^2 u_i'^2 \rangle - \langle u_i' u_i' \rangle^2$	$\pm 0.908^2$
$\langle R \rangle$	$\langle R'^2 \rangle$	± 0.2

ficiently small to resolve motion with spectral content under $\approx$ 28 kHz (determined via Stokes number analysis [118]).

2.1.6 Error Estimates and Resolution of Experimental Observables

The random error for a statistic *X* can be calculated from it's estimator variance (s_x^2). Benedict and Gould [119] discussed the convergence of turbulent statistics from time series data of independent random variables. They gave estimator variances for higher order statistics such as mean, standard deviation, and auto covariance, which are shown in Table 2.2, along with a typical value for the confidence interval (CI). The CI is defined as $\pm 1.96(s^2/N)^{0.5}$ where 1.96 corresponds to the 95% confidence level of a normal distribution. Also shown in Table 2.2 is s_x^2 for the ensemble mean flame radius, $\langle R \rangle$, and its CI, formed using the Student's t-distribution with $30 - 1 = 29$ degrees of freedom. All of the statistics converge as $N^{-0.5}$ where N is the number of independent samples and is ≈ 250 for PIV and 30 for schlieren. Error bars are omitted in plots due to insignificant size.

It should be noted that the actual confidence intervals are likely higher than the values quoted in Table 2.2. This is a well known artifact of collecting turbulence data via PIV and comes from several factors of the PIV analysis including image quality, failure to reject bad vectors and dependence on and associated problems with sub-pixel interpolation. PIV measurements require more samples for convergence then the sampling theorem would

Table 2.3: Summary of flame kernel measurements conducted. The turbulence conditions identifier refers to the turbulence generator number in Table 2.1.

Case	1	2	3	4	5	6	7	8
Symbol	◯	◊	□	◯	◊	★	△	▽
M_0	1.75	1.75	1.75	1.5	2.0	1.75	1.75	1.75
ϕ	1.0	1.0	1.0	1.0	1.0	0.9	0.8	0.7
$T_s\ [K]$	332.8	337	334	337.3	334.3	334.6	344.7	350.6
$P_s\ [kPa]$	73.1	73.1	73.1	76.3	69.7	73.1	73.1	73.1
Turb. Cond.	1	2	4	3	5	3	3	3
$\Theta = \rho_u/\rho_b$	6.77	6.69	6.75	6.69	6.57	6.44	5.88	5.35
$S_{L,0}\ [m/s]$	0.592	0.605	0.596	0.598	0.633	0.545	0.482	0.370
$\delta_L\ [mm]$	0.475	0.473	0.475	0.459	0.487	0.511	0.568	0.679
$\delta_{M,b}\ [mm]$	1.24	1.23	1.24	1.21	1.26	0.967	0.822	0.809
$u'/S_{L,0}$	6.23	6.78	7.52	6.63	4.69	8.22	9.30	12.10
L_{11}/δ_L	24.0	23.1	21.4	22.4	34.5	19.9	17.9	15.0

suggest. For example, Lavoie *et al.* [120] suggested 300 samples to converge the mean, over 2000 for second order moments, and tens of thousands for third order moments. This suggests that the confidence interval on the second order moment may be higher than the numbers quoted in Table 2.2.

2.1.7 Experimental Test Conditions

Eight cases are investigated spanning several nozzle exit Mach numbers (M_0), equivalence ratios (ϕ) and turbulence generators. Conditions for each case are shown in Table 2.3. The turbulence grid refers to the grid information in Table 2.1. T_s and P_s are produced using the 1D model discussed in Chapter 4. $S_{L,0}$, δ_L and Θ are calculated using Cantera. $\delta_{M,b}$ is calculated using a curve fit to data in Gu *et al.* [121], which is discussed later in Chapter 4.

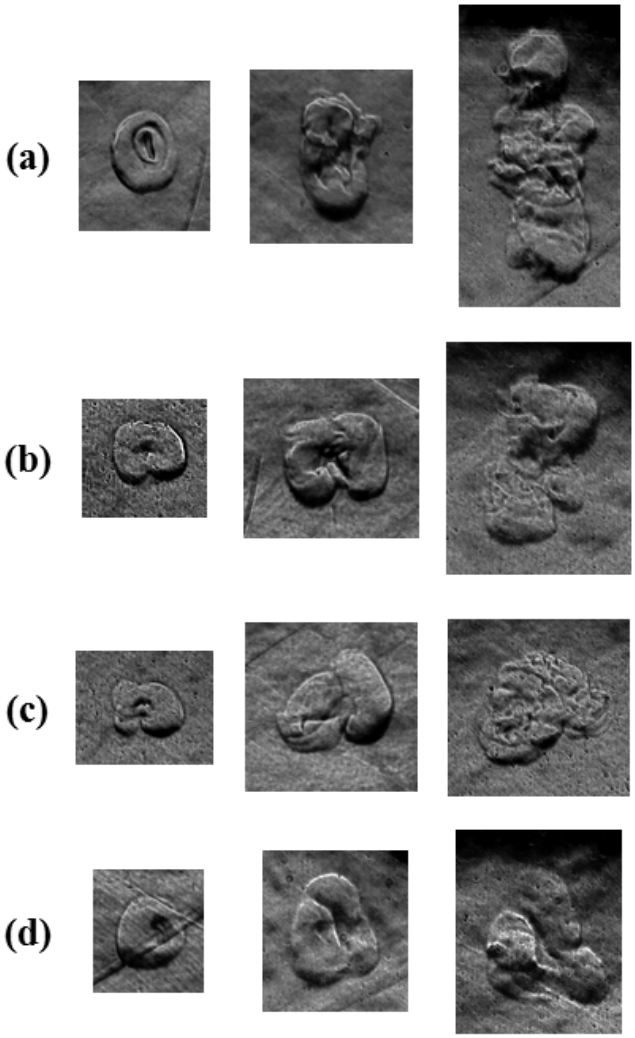

Figure 2.14: Schlieren snap shots for a. case 4 ($M_0 = 1.5$, $\phi = 1.0$), b. case 3 ($M_0 = 1.75$, $\phi = 1.0$), c. case 8 ($M_0 = 1.5$, $\phi = 0.7$), and d. case 5 ($M_0 = 2.0$, $\phi = 1.0$) at (left) Window 1 ($\Delta x_{ign} \approx 0.11\ m$), (middle) Window 2 ($\Delta x_{ign} \approx 0.32\ m$), and (right) Window 3 ($\Delta x_{ign} \approx 0.51\ m$).

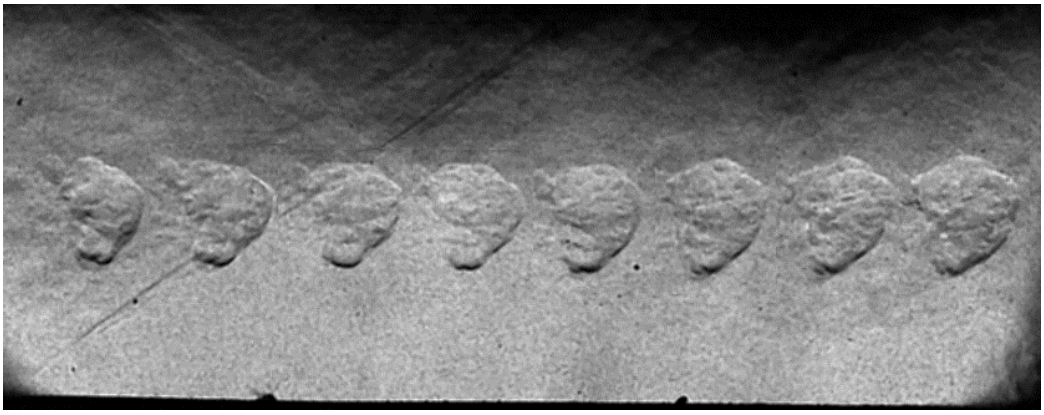

Figure 2.15: High speed schlieren sequence of case 3. Image sequence is collected with a high speed LED and Photron SAZ camera at 50 kHz.

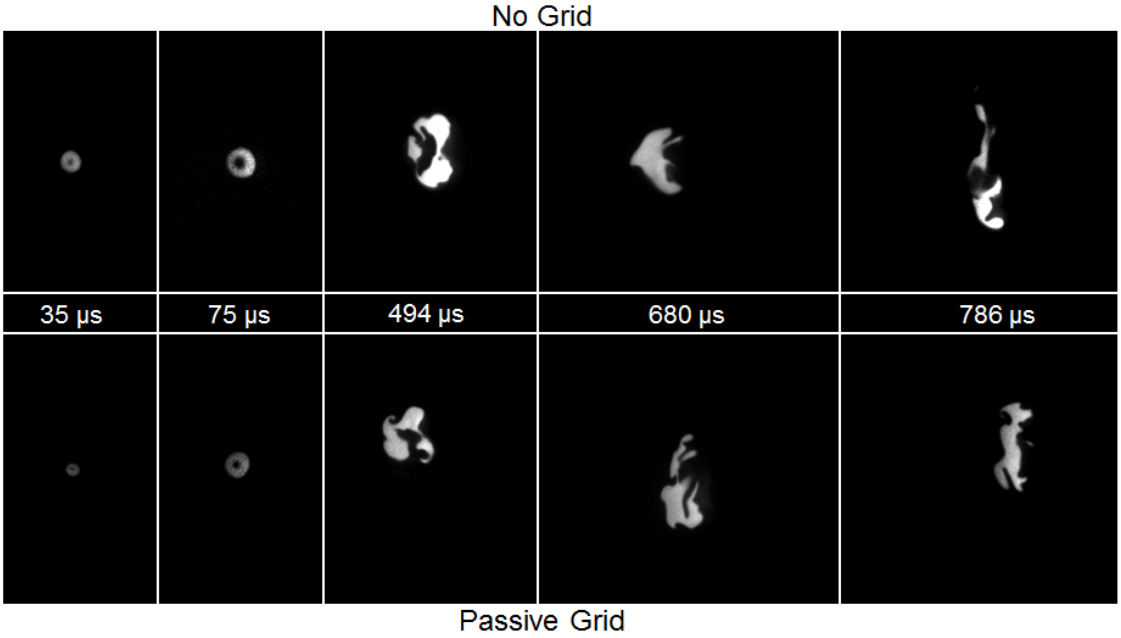

Figure 2.16: OH PLIF snap shots for (top) case 1: $M_0 = 1.75$, $\phi = 1.0$, no grid and (bottom) case 3 $M_0 = 1.75$, $\phi = 1.0$, passive grid at various time delays from ignition.

2.2 Numerical Methods

2.2.1 Numerical Domain

The computational domain closely resembles the experimental test section but includes several small differences that reduce computational cost and minimize variability in initial conditions between the various cases. The domain is a nominally rectangular channel; however, the geometry is modified to 700 mm $\times$ 50 mm $\times$ 35 mm with a 0.5° divergence on the $(+y)$ and $(-y)$ walls. Figure 2.17 shows a comparison between the experimental and numerical domains; the numerical domain is highlighted in the schematic. Supersonic inflow and outflow boundary conditions are used, and slip walls are specified on the transverse boundary surfaces. The divergence starts at $x = x_{\mathrm{d}} = 153.4$ mm.

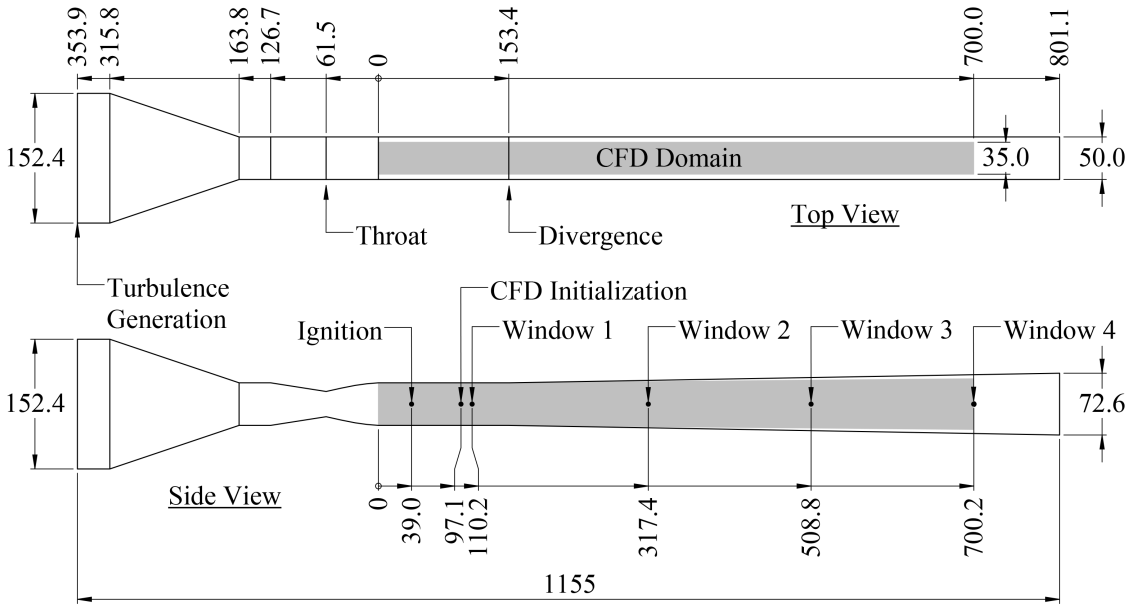

Figure 2.17: Top and side views of the internal flow geometry with experimental domain outlined and numerical geometry shaded. Flow is from left to right. Units are in millimeters.

Two differences between the experimental and numerical setup are: 1. a reduction in the domain size, and 2. slip walls are employed in the computations. For these changes to be valid, flame kernels should have minimal interaction with the walls. This assumption

is because the maximum transverse flame area is less than 17% of the transverse area of the channel. Further, the maximum transverse extent of the kernel is less than 53% of the channel width, which is sufficiently small to avoid significant confinement effects [122]. Finally, the boundary layer is only a few millimeters thick at the channel exit [18], therefore it is reasonable to assume that the flame kernel has minimal interaction with the walls and hence slip walls are reasonable.

In experiments, the boundary layer grows downstream which effectively restricts the cross-sectional area. This effect is not captured with slip walls so the boundary layer thickness should be subtracted from the computational domain. Experimental results indicate that boundary layer growth can be estimated by a line oriented $\approx 0.5^\circ$ to the axial direction (see Chapter 4). Therefore, the divergence in the computational domain is reduced from 1° to 0.5°. The accuracy of this assumption is shown to be quite reasonable (in Chapter 4.5) by comparing the mean axial velocity between experiments and simulations.

One further difference is related to the way results are analyzed in experiments and simulations. In experiments, multiple realizations are obtained for each case and then the quantities of interest are obtained via ensemble averaging. Variability in initial/boundary conditions, the ignition process, and the turbulent fluctuations are accounted for during ensemble averaging. However, to make computations tractable, only one simulation is performed for each case. Compared to the experiments, simulation variability only occurs in the turbulence specification at the inflow boundary, and therefore, the comparison can still be considered reasonable. This is also apparent from the experimental-numerical comparison performed in Chapter 4.5. Further discussion and justification for the use of a single ensemble is given in Section 2.2.4.

2.2.2 Numerical Methodology

The numerical methodology is discussed in detail in Ochs *et al.* [123]. The Favre-filtered LES equations for mass, momentum, energy and species mass conservation are solved

using a parallel solver for the compressible multi-species Navier-Stokes equations. A modification to the well-established finite-volume solver, LESLIE [124], has been performed to incorporate a higher-order-accurate scheme by casting the governing equations in a conservative finite-difference form [125]. This higher-order finite-difference version, LESLIE-HOFD, has a wide range of available spatial discretization and time integration schemes, and the solver has been extensively validated for accuracy and convergence on well-established test problems [126]. In these studies, a higher-order-accurate numerical scheme is required because of large advection velocities and interaction of the flame with expansion waves.

A priori simulations of 3D laminar flame kernel evolution in a high speed straight channel flow are performed to examine the flame shape and vorticity field across the flame-brush region using different numerical schemes. Galilean invariance of the Navier Stokes equations requires that the flame grow spherically; non-spherical evolution being the result of computational errors. Figure 2.18 shows a comparison between WENO, MUSCL, and hybrid MUSCL/MacCormack flux schemes on two grids: the first with one cell per thermal flame thickness (1x) and the second with three cells per thermal flame thickness (3x). Two conclusions are immediately apparent: 1. the MUSCL and Hybrid schemes perform poorly on this simple problem and 2. the flame structure and shape are significantly improved on the higher resolution grid.

Another test case is performed to investigate the subgrid-scale (SGS) flame model, initialization, and grid resolution. Here, a laminar spherical flame kernel is allowed to grow in a 2D periodic box to examine the flame shape and growth rate using three different closure models: 1. thickened flame model, 2. algebraic partially-stirred reactor mode, and 3. finite rate chemistry. Initial simulations used a hotspot initialization, with the species and temperature inside the hotspot set by the equilibrium solution. Using this setup, it was observed that $\phi = 0.7$ kernels grow faster than $\phi = 1.0$ kernels, which is counter intuitive. It was assumed that the difference was due to the much higher temperature gradient in the

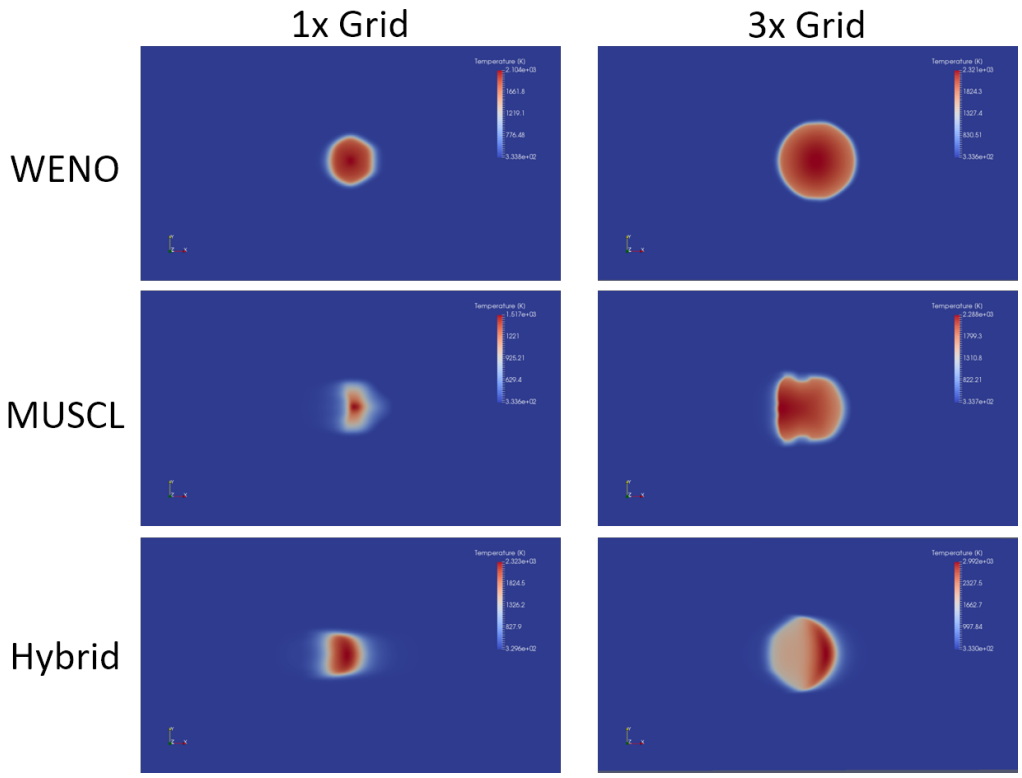

Figure 2.18: Comparison of flux computation schemes for a 3D laminar spherical flame test case in a $M = 1.75$, $\phi = 1.0$ straight channel flow.

$\phi = 1.0$ case that caused the flame to grow more slowly as the flame structure rearranged to the laminar solution. To investigate this further, the 2D box is used with three cases: 1. $\phi = 1.0$ with hotspot initialization, 2. $\phi = 0.7$ with hotspot initialization, and 3. $\phi = 1.0$ with 1D laminar flame initialization. The results are shown in Figure 2.19. It is immediately obvious the initialization has a strong affect on the kernel evolution. The flame structure in the hotspot cases take some time to rearrange to the proper laminar flame solution, which slows the growth. The $\phi = 0.7$ appears to be less affected by this rearrangement, most likely because the temperature gradient is not as extreme in that case. Given enough time, the $\phi = 1.0$ case with hotspot initialization eventually attains the same growth rate (slope) as the case with the 1D laminar flame initialization. Clearly the laminar flame initialization should be used to avoid non-physical growth behavior.

Initial simulation results suggested that the flame model and/or grid resolution may

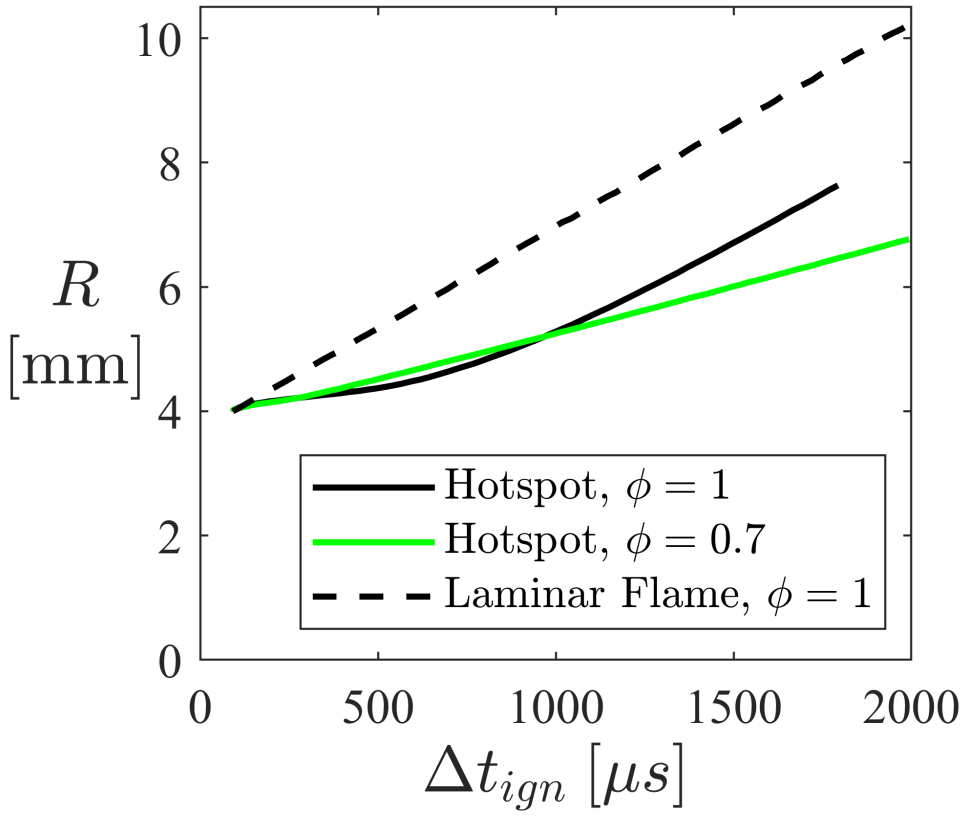

Figure 2.19: Comparison of flux computation schemes for a 3D laminar spherical flame test case in a $M = 1.75$, $\phi = 1.0$ straight channel flow.

need to be improved. To investigate these issues, the 2D box is used. Figure 2.20 shows the results, which compare the laminar chemistry and thickened flame solutions, as well as the grid resolution. As the grid resolution increases, the laminar chemistry solution becomes independent of the grid. At 3x resolution (i.e. three hexahedral cells per laminar flame thickness, $\approx$(116 μm)^3 per cell), the radius is roughly 4.2% larger than the 10x case. The simulation grid size at 3x resolution is $\approx$300 million cells, which is quite large, which means the 3x resolution is the practical limit for grid refinement. At 1x resolution, the solution is significantly in error and actually crashes the simulation due to the creation of a super heated spot due to numerical error. At 3x resolution the thickened flame model underestimates the laminar chemistry solution by 11.4% and is significantly in error at smaller resolutions. The PaSR model is not shown in these plots because the model only activates

when subgrid-scale kinetic energy is present and these are laminar solutions. However, the PaSR solution will be more appropriate than laminar chemistry when subgrid-scale kinetic energy is present in the simulation. Given these observations, a 3x grid with PaSR is used in the simulations.

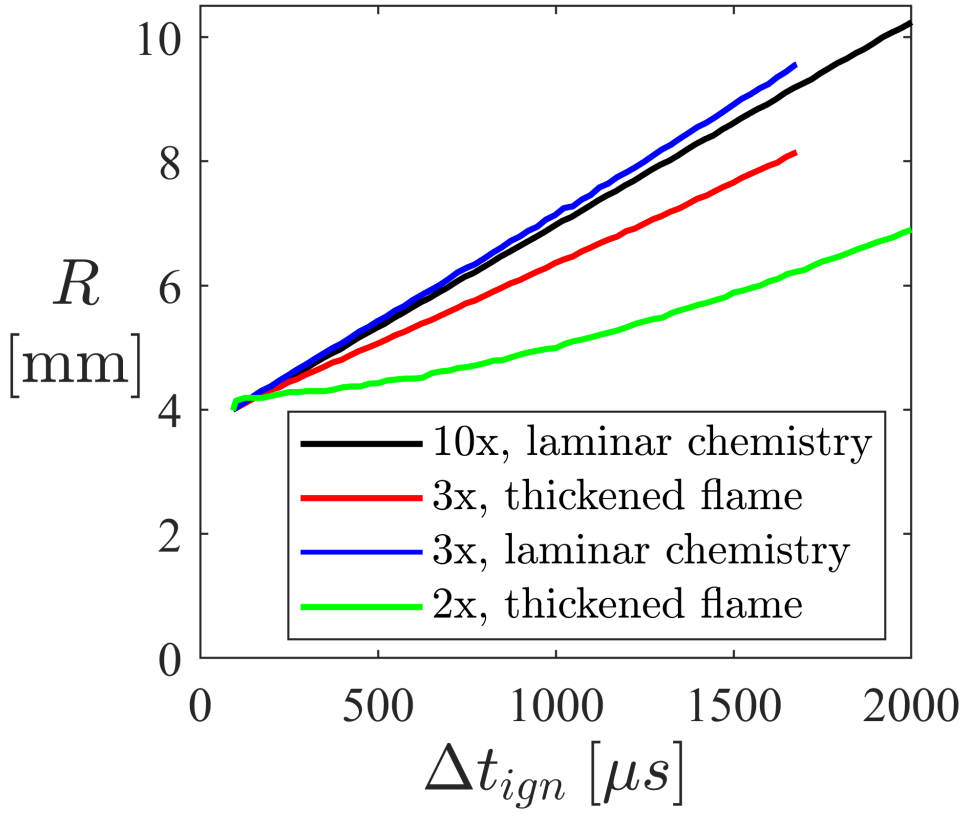

Figure 2.20: Comparison of flux computation schemes for a 3D laminar spherical flame test case in a $M = 1.75$, $\phi = 1.0$ straight channel flow.

Based on the above results, a formally fourth-order-accurate explicit scheme is selected (see Section 2.2.3), where the inviscid flux is discretized using a ninth-order-accurate WENO scheme [125], and a fourth-order-accurate central scheme is used for the viscous terms. The time integration is performed using a low-storage version of the explicit fourth-order-accurate Runge-Kutta scheme. The SGS momentum and energy fluxes are closed using a subgrid eddy viscosity (ν_t) model, which is obtained using the local grid filter Δ and the subgrid kinetic energy k^{sgs} through: $\nu_t = C_\nu \sqrt{k^{\text{sgs}}} \Delta$. Here, C_ν is a model co-

Case	M	ϕ	u'/S_{L0}	L_{11}/δ_L	$S_{L0}\ [m/s]$	$\delta_L\ [m]$
3n	1.75	1.0	7.42	20.8	0.60	4.8E-4
4n	1.50	1.0	7.42	20.8	0.60	4.8E-4
5n	2.00	1.0	7.42	20.8	0.60	4.8E-4
8n	1.75	0.7	13.0	14.3	0.34	7.0E-4

Table 2.4: Simulation parameters for the cases considered in this study.

efficient and k^{sgs} is obtained by solving an additional transport equation. The localized dynamic evaluation procedure is used to obtain C_ν and all other model coefficients [127, 128]. The SGS scalar fluxes are closed using an eddy-diffusivity ($D_t = \nu_t/Sc_t$, with Sc_t being the turbulent Schmidt number) based approach. The SGS turbulence-chemistry interaction is modeled using the algebraic partially stirred reactor (PaSR) [129]. Further details of the LES equations, numerical method, and the SGS closures are presented in several previous works [124, 125, 126, 127, 128, 129, 130, 131]. A reduced four-step, eight-species methane-air mechanism [130, 131] is used to account for finite-rate kinetics. The mixture-averaged transport properties, the finite-rate kinetics source terms, and the thermally perfect gas based thermodynamic properties are obtained using Cantera [132].

Table 2.4 summarizes the numerical cases simulated in this study. Case numbers are chosen for consistency with the experimental cases. The domain is discretized using approximately 308 million cells on a stretched/structured grid (see Figure 2.21). The hexahedral cells are nominally $\sim$153 μm cubes at the inflow boundary, which yields a resolution of approximately three cells per laminar thermal flame thickness. The simulations are performed in three stages. First, non-reacting flow is simulated for 2 advective flow through times to establish the mean flow field. Next, Kraichnan inflow turbulence [133] ($u' = 4.45$ m/s, $L_{11} = 10$ mm) is specified at the upstream boundary and allowed to develop for an additional flow through time. Finally, a spherical flame kernel of radius $R_0 = 4$ mm is placed in the channel at $(x,\ y,\ z) \equiv (97.1\ \text{mm}, 25\ \text{mm}, 17.5\ \text{mm})$ by mapping a 1D lami-

nar premixed flame solution to spherical coordinates. The kernel size is slightly larger than is observed in experiments at this location ($\approx$ 3.5 mm) in order to guarantee free flame growth. Then, LES of the reacting flow is performed for a final flow through time, after which the kernel exits the computational domain. Experimental and simulation data are presented with respect to physical channel dimensions or the time elapsed from ignition, Δt_{ign}. This quantity is directly measured in experiments, but is derived in simulations by adding the elapsed time to a hypothetical elapsed time before the kernel arrives at $x = 97.1$ mm, i.e. $\Delta t_{ign} = 0.0971/U + \Delta t$. The quantity $0.0971/U$ varies with Mach number. The computational cost of one reacting flow through time in the lowest Mach number case is approximately 450,000 CPU hours using an Intel E5 Haswell 2.6 GHz processor on DOD HPCMP's ARL:Centennial and AFRL:Thunder supercomputers.

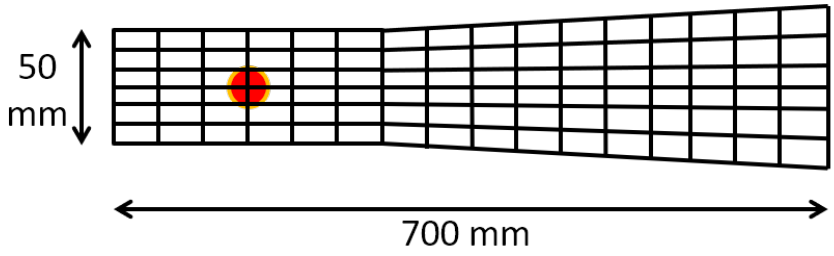

Figure 2.21: Schematic of stretched/structured grid used in these studies.

2.2.3 Accuracy of Numerical Schemes

The conservative higher-order-accurate finite-difference scheme for the spatial discretization of the inviscid terms [125] used in these studies is formally higher-order-accurate in multi-dimensions (3D), as shown through several examples in [126]. Ochs *et al.* [123] show two canonical 2D test-cases which demonstrate the higher-order accuracy of the WENO scheme: 1. the linear Euler system [134], and 2. the isentropic vortex convection [135]. The first test case is a particular condition, when the inviscid Euler equations are linear, while the second case is a nonlinear problem. For both cases, the time-integration is performed using the low-storage fourth-order-accurate Runge-Kutta scheme, and the calor-

ically perfect gas equation of state with constant specific heat ratio, $\gamma = 1.4$.

For the first test case, a doubly periodic square computational box of size 2 units along each direction is considered. The initial conditions are given by:

$$\rho(x, y, t = 0) = 1 + \frac{1}{2}\sin[\pi(x + y)], \quad u(x, y, t = 0) = v(x, y, t = 0) = 1, \quad P(x, y, t = 0) = 1. \tag{2.3}$$

With these initial conditions, the exact analytical solution is given by:

$$\rho(x, y, t) = 1 + \frac{1}{2}\sin[\pi(x + y - 2t)], \quad u(x, y, t) = v(x, y, t) = 1, \quad P(x, y, t) = 1. \tag{2.4}$$

The simulations are performed for $t = 0.2$ s, and L^2 error norm is computed for the density field.

For the second test case, again a doubly periodic square computational box of size 20 units along each direction is considered. The initial conditions are given by:

$$u(x, y, t = 0) = 1 - y\frac{\epsilon}{2\pi}\exp\left[\frac{1}{2}\left(1 - (x^2 + y^2)\right)\right], \tag{2.5a}$$

$$v(x, y, t = 0) = 1 + x\frac{\epsilon}{2\pi}\exp\left[\frac{1}{2}\left(1 - (x^2 + y^2)\right)\right], \tag{2.5b}$$

$$T(x, y, t = 0) = 1 - \frac{(\gamma - 1)\,\epsilon^2}{8\gamma\pi^2}\exp\left[1 - (x^2 + y^2)\right], \tag{2.5c}$$

where $\epsilon = 5$. The simulation is performed for one convective flow through time when the initial vortex convects back to its original location at $t = 20$ s. Similar to the first test case, the error assessment is performed for the density field.

Table 2.1: L^2 error norm and the convergence rate of the WENO scheme for the two test problems.

Linear Euler			Isentropic Vortex		
h	Error	Order	h	Error	Order
2/20	7.67×10^{-6}	-	20/40	4.20×10^{-3}	-
2/40	2.90×10^{-8}	8.1	20/80	9.15×10^{-5}	5.5
2/80	1.12×10^{-10}	8.0	20/160	6.40×10^{-7}	6.3
2/160	5.60×10^{-12}	6.8	20/320	1.66×10^{-9}	7.1

Table 2.1 and Figure 2.22 show the L^2 error norm and the rate of convergence of the scheme for the two canonical 2D test cases. Higher-order-accuracy is achieved in both cases. A reduction in the formal order of accuracy of higher-order-accurate WENO schemes is typically associated with the adaptive stencil used by these schemes, which has a particularly strong effect in nonlinear problems [125]. These results demonstrate that the formal order of accuracy of the spatial discretization when both inviscid and viscous terms are considered is fourth-order-accurate in 3D, as already mentioned in Section 2.2.2.

2.2.4 Justification for Single Ensemble Statistics

The validity of single ensemble statistics is investigated here. Data from two different realizations (initial conditions) of case 3n are compared in order to quantify the variation of important statistics. Figure 2.23 shows the evolution of numerical schlieren for both realizations of case 3n and it is clear that the solution, while similar at early times, is quite different at late times. Despite this qualitative difference, there is a relatively small variation in the derived statistics between the realizations, suggesting that the key conclusions drawn from flame speed statistics would hold even if additional simulations are performed.

Turbulence is apparently a small driver of flame growth in this problem (see Chapters 4 and 6). Therefore, flame growth should be a weak function of the initialization. Figure

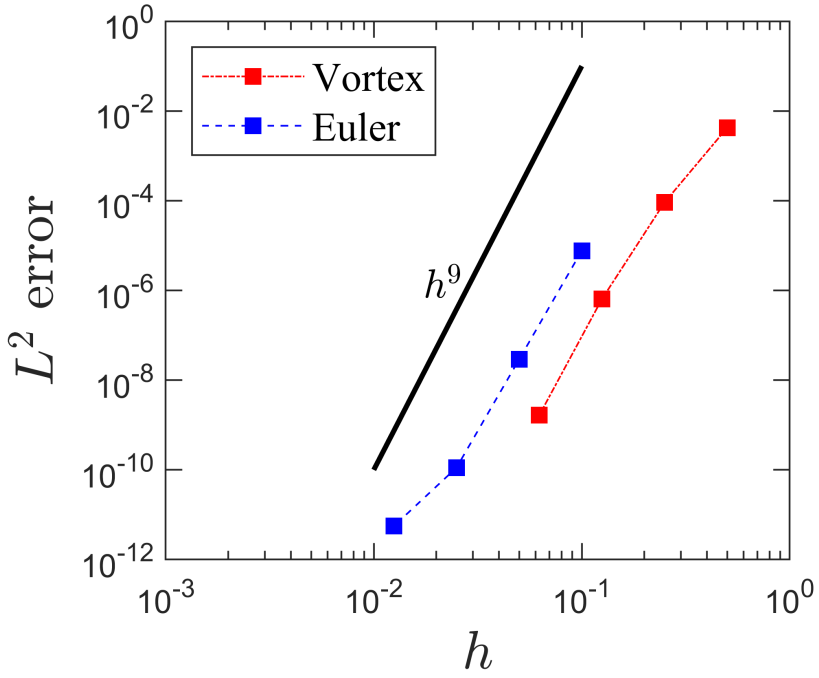

Figure 2.22: Spatial order of accuracy of the WENO scheme for two test cases.

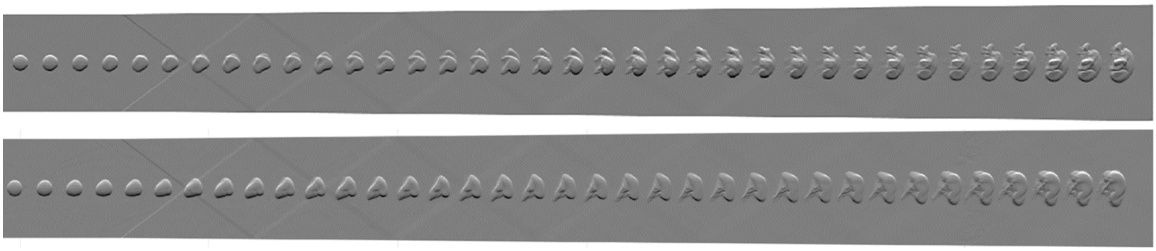

Figure 2.23: Numerical schlieren for case 3n, repetitions 1 and 2.

2.24 shows the effective flame radius derived from numerical and experimental schlieren images. There is nearly no difference in the radii of the two numerical realizations and both match the experimental data quite well at all except the earliest times when the ignition overdrive strongly affects growth in the experimental case. Similar results are seen in the burned volume and flame area evolution, which are shown in Figure 2.25. There is slightly more variation in $A_{f,0,05}$ at later times, but both $A_{f,0,05}$ and $\mathcal{V}_{0.05}$ are very similar between realizations. Since the flame radii, ratios of radii, line of sight comparisons, and flame speeds are all derived from the $A_{f,0,05}$ and $\mathcal{V}_{0.05}$, we should expect that these quantities are

quite close as well.

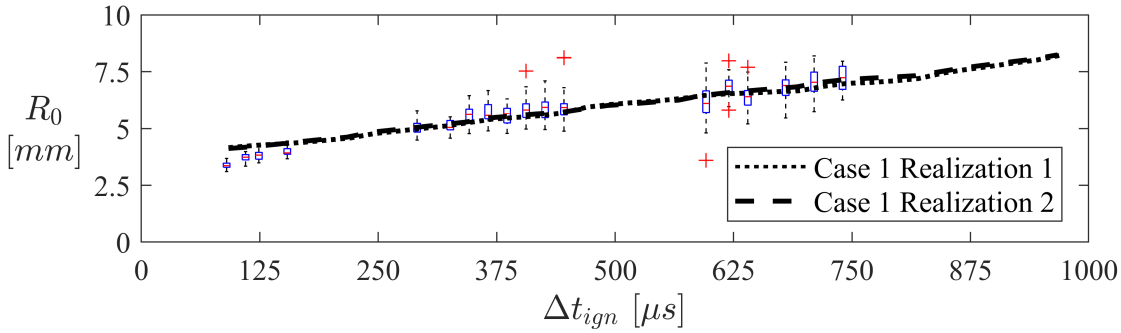

Figure 2.24: Time trend of effective kernel radius derived from schlieren images for case 3n: numerical realizations 1 and 2 compared to experimental box plots. Plus symbols correspond to outlier data points where the deviation is greater than 1.5 times the interquartile range.

Table 2.2 shows the maximum and average normalized variation between various statistics calculated from case 3n realization 1 and 2 (as a % of the mean value). Indeed $\mathcal{V}_{0.05}$, $A_{f,0.05}$, $R_{l,0.05}$, and $R_{v,0.05}$ vary by only a very small amount, $< 6\%$ of the measured value at a maximum. Similar results are seen for the ratio of radii and $S_{TC}/\overline{S_L}$. The maximum deviation of S_L between realization is large in Table 2.2, however this difference occurs at early times when the flamelet structure is rearranging to a spherical orientation. The difference is negligible within the window of interest for flame speed measurements (after 250 μs), which is why the mean difference is low in comparison to the maximum.

Even if the deviation between realizations is small, convergence (or proximity to it) of desired statistics is not guaranteed. In order to investigate the convergence of the desired statistics, a confidence interval analysis of the $S_{TC}/\overline{S_L}$ scaling and S_{TD}/S_{TC} follows. Each point on the scaling/evolution is considered an independent random variable with N=2 ensembles. The Student's T distribution with 1 degree of freedom is used to construct the 80% confidence interval (CI). This is an unforgiving statistical analysis because the T-score at one degree of freedom is very large, which can make the CI quite large even if the difference between realizations is small. The CI's are shown in Figure 2.26 for $S_{TC}/\overline{S_L}$ and S_{TD}/S_{TC}. Surprisingly, and owing to the overall similarity between realizations, the

Table 2.2: Maximum and mean % deviation of various quantities.

Quantity	Maximum	Mean
$\mathcal{V}_{0.05}$	5.83	2.44
$A_{f,0.05}$	5.01	2.41
$R_{l,0.05}$	2.43	1.29
$R_{v,0.05}$	1.95	0.81
U_T	24.7	7.57
$\overline{S_L}$	25.2	8.88
δ_L	13.1	6.34
$\frac{R_{l,0.05}}{R_{v,0.5}}$	3.91	2.15
$\frac{R_{l,0.05}}{R_{v,0.05}}$	2.18	0.99
$\frac{R_{v,0.05}}{R_{v,0.5}}$	2.25	1.67
$\frac{S_{TC}}{S_L}$	3.52	1.11
$\frac{S_{TD}}{S_{TC}}$	16.1	4.92

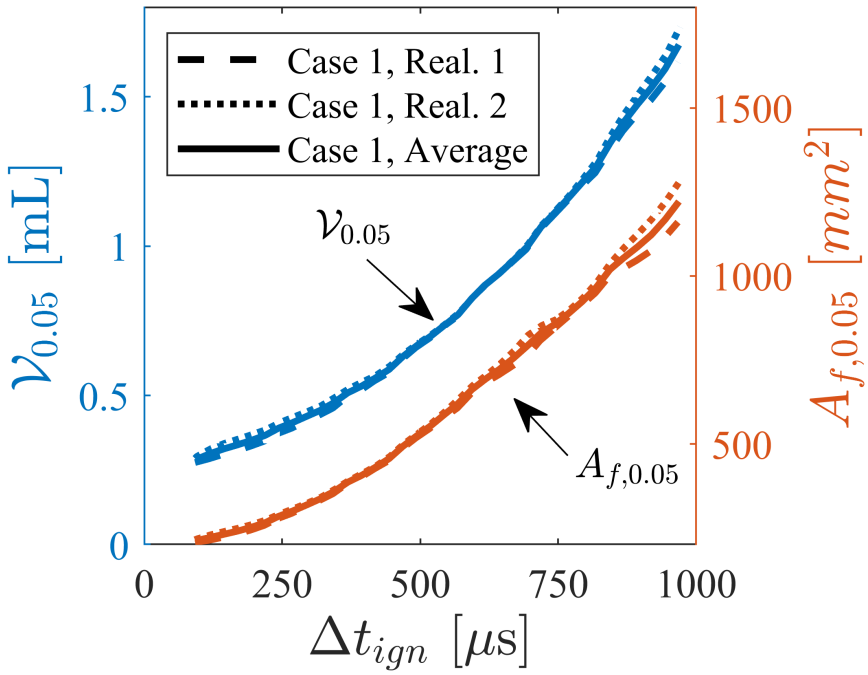

Figure 2.25: Evolution of $\mathcal{V}_{0.05}$ and $A_{f,0.05}$ for case 3n, realizations 1 and 2.

CI's are tight within the region of interest ($\gtrapprox 250\,\mu s$). The nearly linear trend of $S_{TC}/\overline{S_L}$ is maintained in Figure 2.26a and the range of S_{TD}/S_{TC} is between 0.7 and 0.9 for most of the useful part of the dataset in Figure 2.26b. Variation of the statistics between the realizations does not significantly alter the conclusions, which suggests that the conclusions discussed above would continue to hold even if more realizations are added. Therefore, the single ensemble estimates for the presented statistics appear usable for the purposes of this work.

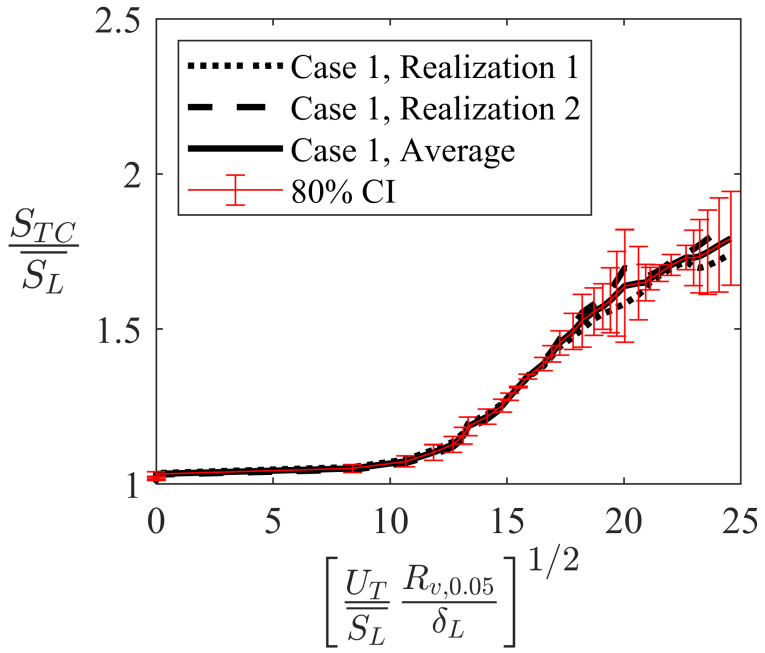

(a) Turbulent consumption speed scaling

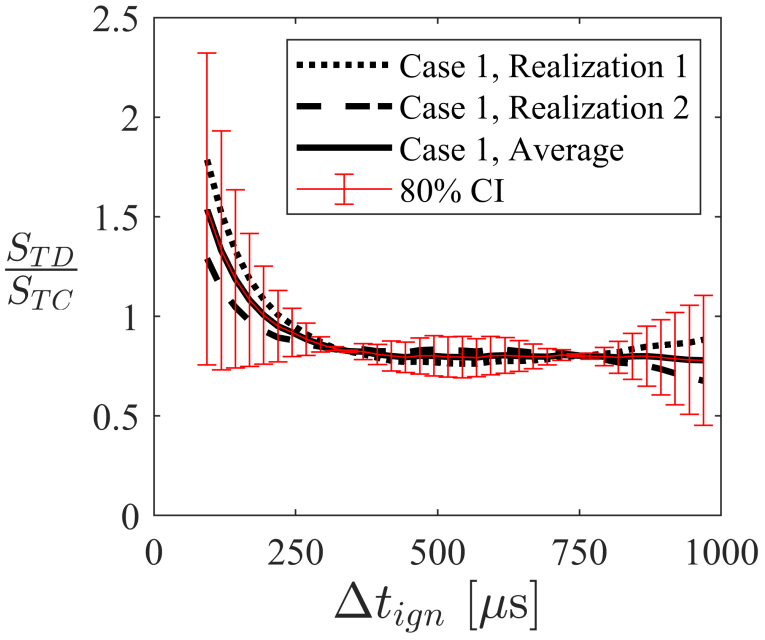

(b) Comparison of turbulent displacement (c=0.05) and consumption speeds

Figure 2.26: Confidence interval of selected statistics at 80% confidence level.

CHAPTER 3

LASER IGNITION OF SUPERSONIC FLAME KERNELS

The primary goal of this chapter is to evaluate how long the ignition process affects the flame. The laser ignition process is non-resonant laser ignition, which is characterized by a strong ignition overdrive, i.e. more energy than is necessary for breakdown is absorbed by the plasma. The additional energy results in an over pressure/temperature condition, after which the kernel rapidly expands. When observing the kernel edge, this expansion can easily be mistaken for flame growth. Therefore, a specific goal of this work is to determine how long the ignition event memory influences flame growth. There have been numerous laser ignition works, and some even discuss kernel radius/area trends and transition to self-propagation for laminar spherical flames [28]. However, a laser ignition study whose specific goal is to investigate when the turbulent flame from a laser ignition kernel transitions to a fully self-propagating flame has not been performed, especially for supersonic flames. Identifying the independence time for flame speed studies utilizing laser ignition will be a significant contribution for both the turbulent premixed flame and laser ignition communities. Several other goals of this chapter are to establish the breakdown and ignition probability for supersonic flows, and to identify if/how the breakdown process is affected by the Mach number and equivalence ratio. This chapter starts with a comparison of quiescent breakdown results to previous work then discusses the laser ignition process in supersonic flow, transition to a self-propagating flame, and investigates Mach number and equivalence ratio dependencies. First, however, several details of the experimental facility and key terms are revisited below.

The laser ignition and deposited energy measurement systems have already been discussed in Chapter 2, therefore only a few key details are repeated here. The laser pulse is provided by a water-cooled frequency doubled Nd:YAG (532 nm), which has an oscillator

stage and an amplifier stage. An air-cooled laser was also used in this work, but could not deliver repeatable results for the incident laser power or ignition probability because the cooling system interacted with the environmental cooling system in the room. The pulse energy from the laser is tuned to the desired energy/pulse by rotating the polarization and dumping the unwanted portion of polarized light. Therefore, the laser energy can be tuned without having to change the voltage applied to the oscillator or amplifier flash lamps, nor having to modify the Q-switch timing on either stage. This detail is very important because the cavity quality and mode depend heavily on the flash lamp power and Q-switch timing. The laser settings are held where the full range of desired pulse energies can easily be achieved throughout the testing campaign, which took place over several weeks. Additional care was taken to maintain the cleanliness/quality of the ignition optics. The aspheric plano-convex lens, which had to be replaced once during the test campaign, is especially sensitive because back reflections from the tunnel window can damage the optic. The incident beam is focused into the supersonic tunnel from above and the breakdown/ignition kernel are viewed from the side.

Several key terms are redefined here for reference. When breakdown occurs, some amount of the incident energy is deposited into the kernel, some is transmitted and scattered, and the remaining amount is radiated visibly and acoustically. Schwarz et al. [136] measured the scattered energy in laser breakdown to be less than 3% using an integrating sphere. Time elapsed from the ignition laser pulse is defined as Δt_{ign}. A distinction is made between the elapsed time (Δt_{ign}) and the amount of elapsed time required for transition to a self-propagating flame or the amount of elapsed time required for the flame to become independent of the ignition process (τ_{ind}). The deposited ignition energy (E_d) is the amount of the incident energy (E_5) that is deposited into the kernel. The transmitted and scattered energy is measured and the radiated energy is usually small. Therefore, E_d is calculated using a subtraction technique: $E_d = E_5 - E_6$, where E_6 is the sum of the transmitted and scattered energy. The ignition energy, E_{ign} is defined as the minimum deposited energy

that will result in a self propagating flame that has the additional late-time properties of being independent of the ignition process and having high ignition probability. Therefore, $\Delta t_{ign} \geq \tau_{ind}$ and $E_d \geq E_{ign}$ are necessary conditions for flame speed measurements to be independent of the laser ignition process. It should be noted that E_{ign} is not the minimum ignition energy E_{min}, which is usually defined as the minimum energy required to produce a self-propagating flame. The requirement $E_d \geq E_{ign}$ is more restrictive than $E_d \geq E_{min}$, because the flame speed must also be independent of the ignition event. The breakdown probability, BP, is the $\%$ of kernels which breakdown at early times and the ignition probability, IP, is the $\%$ of flame kernels that result in self-propagating flames at late times. Both BP and IP depend greatly on the ignition laser make/model and flash lamp and Q-switch settings.

3.1 Laser Breakdown Observations

Previous quiescent laser breakdown results of are used to anchor the experimental procedures, which forms a foundation for the remainder of this chapter. Comparisons are made with qualitative results, such as the visual appearance and evolution of the kernel, and with quantitative results, such as trends in the kernel perimeter. The results presented here correspond to kernels produced within the supersonic tunnel but without flow. Additional observations about laser breakdown in a quiescent environment (outside the tunnel), including characterization of the blast wave velocity and kernel size are presented in Appendix C.

Fuel-free breakdown within the tunnel establishes a baseline free of turbulence, mean flow, and fueling effects. Figure 3.1 shows snapshots of these quiescent laser breakdown kernels, as well as flowing and fueled kernels for comparison. The rows represent different operating conditions; the top row corresponds to the quiescent condition. Four time delays from ignition (Δt_{ign}) are shown, plotted as columns. Each image is a different ensemble, therefore no two images correspond to the *same* kernel. The ensemble mean energy up-

stream of the ignition optic is $\langle E_3 \rangle \approx 55$ mJ and the laser is focused from above for all images. At $\Delta t_{ign} = 10$ μs, the kernel is elongated in the direction of the laser path. A strong, outwardly propagating blast wave appears just outside of the kernel. At $\Delta t_{ign} = 30$ μs, the kernel size has decreased slightly, a consequence of relaxation from the ignition overdrive. The kernel appears rounder, if not actually elongated in the direction perpendicular to the laser path. The blast wave has completely moved out of the field of view. The hot gases have taken on an outwardly-propagating cylindrical shape and a small amount entrained fresh gas can be seen funneling from the bottom side into the core of the kernel. By $\Delta t_{ign} = 60$ μs, the kernel has significantly elongated in the direction perpendicular to the laser path. The funnel of on-axis entrained gas is clearly visible, as are some perturbations along the top surface of the kernel. At $\Delta t_{ign} = 120$ μs, the kernel is significantly larger. The funnel of entrained gas is also larger and a new feature, a third lobe oriented towards the laser axis, has appeared. The blast wave, which had traveled away from the kernel, has reflected off the tunnel walls and now appears right above/below the kernel. These images are qualitatively similar to previous breakdown studies [28, 137].

A more quantitative comparison can be made by comparing the evolution of laser breakdown kernels to extract information about the kernel size. Three parameters: the area, perimeter, and maximum width can easily be extracted from edge-detected images (Chapter 2.1.5 and Appendix B.2 discuss the edge detection algorithm). Figure 3.2 shows an evolution of the average kernel perimeter, $\langle P \rangle$, compared to the work of Mulla et al. [30]. Several details of their work are different from this one. For example, they used the third harmonic of a Nd:YAG (355 nm) for ignition and the incident energy was much higher (128 mJ). Also, they used a premixed Bunsen burner with no windows and the flow velocity was substantially slower. These differences may seem extreme, however, several details suggest that the differences may not be so large.

Galilean invariance suggests that once the energy is deposited, the mean velocity should have no impact on the kernel development unless the local flow structure causes an initial

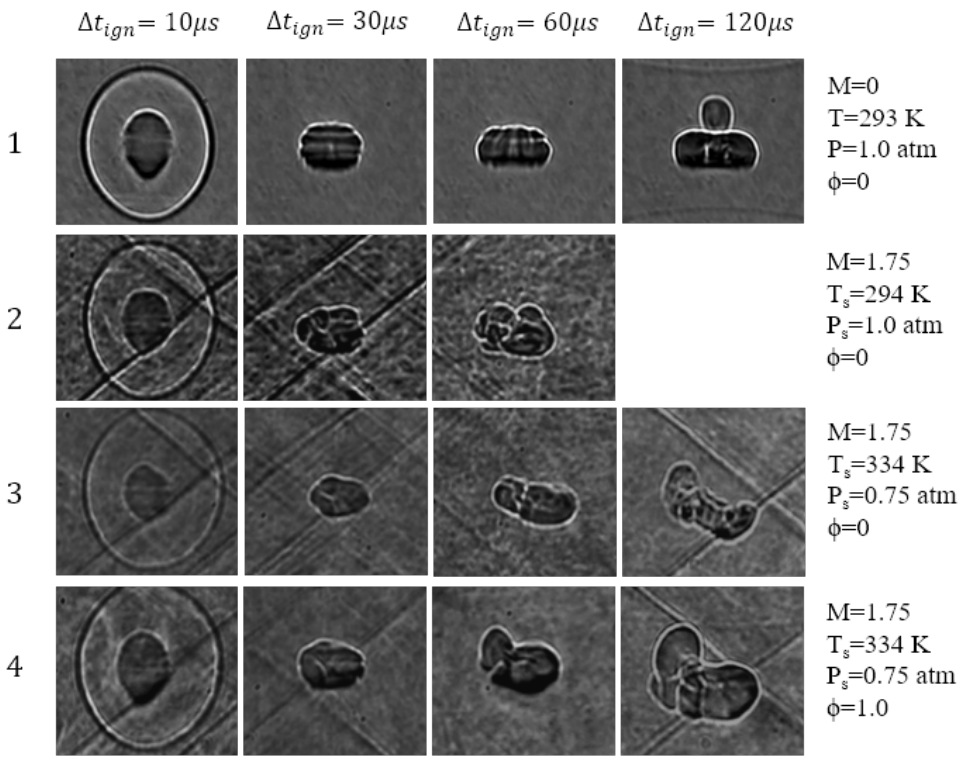

Figure 3.1: Laser breakdown and ignition kernels for a variety of conditions (rows) and time delays (columns). Row 1 corresponds to the quiescent condition, row 2 corresponds to an un-fueled M=1.75 case where the static pressure and temperature match atmospheric conditions, row 3 is an un-fueled M=1.75 case where the static pressure and temperature are matched to those used in the flame speed experiments, and row 4 corresponds to a $\phi = 1.0$ version of row 3.

change in the kernel structure. Given the same Δt_{ign}, the evolution should be similar. In addition, the tunnel windows mainly have an impact on the amount of incident energy available for ignition through the transmissive qualities of the glass. The transmission coefficient is rather high at $\epsilon_w \approx 0.93$, therefore the windows should have a very minimal impact on the ignition process. Having a reflective boundary condition does allow the blast wave to interact with the kernel, but the strength of the wave is quite weak by the time they first interact. Therefore, the reflected blast wave likely has a negligible effect on the kernel. Looking at Figure 3.2, it would appear that the evolution of $\langle P \rangle$ is indeed quite similar between both works. The early time growth is larger in the Mulla *et al.* [30] work, probably due to the larger deposited energy. This suggests that the ignition process

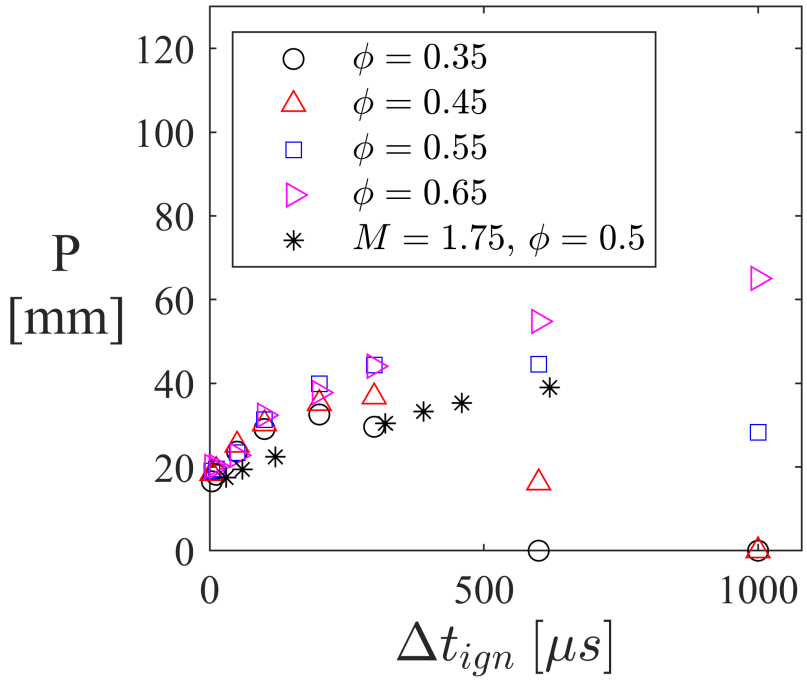

Figure 3.2: Evolution of ensemble averaged kernel perimeter $\langle P \rangle$ versus time from laser ignition pulse (Δt_{ign}). Open symbols are from the work of Mulla *et al.* [30] with $\langle E_3 \rangle = 128$ mJ. Stars correspond to $M = 1.75$, $\phi = 0.5$ kernels of this work with $\langle E_3 \rangle = 55$ mJ.

is similar despite the difference in E_3 and M. These results lend credibility to this work and motivates extension of the results to the fueled condition, which is discussed next.

3.2 Breakdown and Ignition Probability

Before discussing the flowing ignition results, a quick comment about breakdown and ignition probability is made. Figure 3.3 shows IP versus E_d and E_3 for the $M = 1.75$, $\phi = 1.0$ case. Approximately 200-350 images are used for each point in Figure 3.3. Interestingly, achieving 100% ignition is a simple enough task as long as the deposited or incident energy are large enough. The IP trend with respect to E_d shows a drastic drop off in IP as E_d is reduced below approximately 12 mJ, and IP approaches 0 as E_d approaches zero. IP also reduces with E_3, but in contrast to the E_d trend, the drop off is much more gradual and it does not appear to approach 0 as E_3 approaches 0. This is not surprising because the energy measured in E_d is much closer to the actual energy deposited into the kernel. The IP trend

with respect to E_3 also has an inflection point around $E_3 \approx 25$ mJ, whereas the trend with E_d does not. This indicates that the process through which incident energy is deposited into the kernel is non-linear. This is also not surprising because the breakdown process itself is not linear; a critical amount of incident energy is required before breakdown can occur. At the opposite extreme, we would also suspect that increasing E_3 indefinitely will not increase E_d indefinitely because in a non-thermal breakdown process the plasma can only receive energy until the electronic transitions are filled, after which the remaining energy should transmit through or be scattered by the plasma. Similarly, if the optics are damaged or poorly aligned, breakdown may not occur at all, even if E_3 is quite large. Clearly, E_3 is an inferior quantity because it is not directly related to kernel energy. Unlike IP, BP is 100% at all but the lowest incident energy levels. However, even at $E_3 = 15$ mJ, BP is still 88%, which indicates that breakdown is much easier than ignition. All of the above results are highly sensitive to the ignition optics alignment and laser settings.

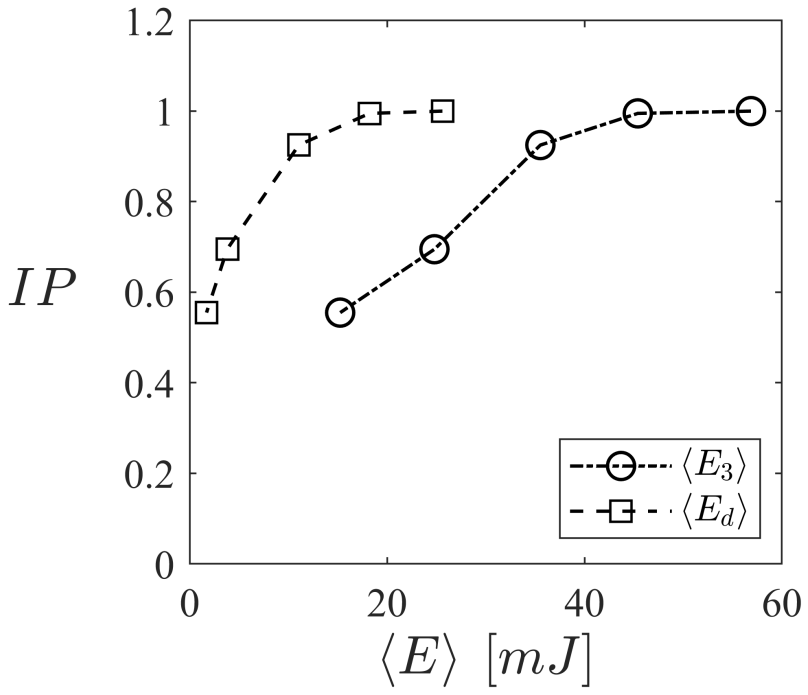

Figure 3.3: Ignition probability as a function of E_d or E_3 at $\Delta t_{ign} = 680\ \mu s$.

3.3 Non-Resonant Laser Breakdown and Ignition Process in Supersonic Flow

An example $M = 1.75$ laser breakdown kernel is shown in Figure 3.1, row 2. In this case, the stagnation pressure and temperature are set such that the static conditions are matched to atmospheric conditions. Other than some turbulent perturbations and weak shocks, the overall shape and size are fairly similar to the quiescent breakdown kernels (row 1). Also shown in Figure 3.1, row 3 is an un-fueled $M = 1.75$ case where the static pressure and temperature are matched to those used in flame speed experiments. Under these conditions, the static density is approximately 2/3 the atmospheric density and the resulting kernel is smaller. The small size at the early times suggests that less energy is deposited into the kernel. Indeed, for row 2 $E_d = 32.3\,mJ$ and for row 3 $E_d = 21.4\,mJ$, even though the incident energy is the same for both cases ($\langle E_5 \rangle \approx 46\,mJ$). Clearly the density plays an important role in the breakdown propensity and the evolution of the resulting kernel.

When the density is lower, it is harder for energy to be absorbed by the gas; a larger portion of the energy is transmitted/scattered. This can be problematic for calibration of the laser measurement system because the system cannot be calibrated on-condition (with the tunnel running supersonic) for safety reasons. The calibration of the transmitted photodiode, in particular, is sensitive to the density because the energy transmitted, and hence the calibration, depend on the density. The error may be small, however, because the calibration is linear when using the peak photodiode voltage (see Chapter 2.1.4). Therefore, measurements at the edge of the calibration may be reasonable. Nonetheless, a density-matching procedure was developed to further mitigate this calibration error; this is discussed next. The tunnel must be preheated to raise the stagnation temperature to the appropriate level. If the calibration is performed hot, then the temperature will be quite high, high enough in fact to match the on-condition density. For example, for $M = 1.75$ runs, the tunnel air is preheated to approximately 450 K and has a density of approximately 0.783 kg/m^3. In comparison, the on-condition (at $M = 1.75$) static density is 0.791 kg/m^3, which

is very similar to the conditions during preheat. By performing the calibration during preheat (low flow conditions), the calibration error is negligible. At $M = 1.5$ and $M = 2.0$, the preheat temperatures are slightly lower/higher, respectively. Therefore, the calibration error is slightly larger in those cases.

During ignition (fueled) studies, the kernel is larger than the un-fueled case, as expected. Figure 3.1, row 4 shows kernel evolution for the $M = 1.75$, $\phi = 1.0$ case. At early times, the kernel is equivalent in size to the quiescent and density-matched cases (row 1 and 2), but quite a bit larger than the un-fueled flowing case (row 3). However, by $\Delta t_{ign} = 120$ μs the kernel is larger than any of the other cases. The outline of the kernel is also sharper than the un-fueled case, which suggests that temperature discontinuities are stronger in the reacting case. Apparently the flame is beginning to self-propagate outward; maintaining the temperature discontinuity. The kernel in this situation is deemed a flame kernel because the flame structure is maintained as the kernel grows (even though the growth is still partly driven by the ignition event). One interesting feature of the flame kernel is that the third lobe is offset from the laser axis. The same general shape is also seen in the un-fueled case, which suggests that the offset is due to fluid dynamic phenomena rather than a chemical phenomena. Interestingly, Mulla *et al.* [30] also observed a deviation in the laser axis for their flowing subsonic flame kernels (see Figure 3.4), which may suggest that this may be a universal observation in subsonic and supersonic laser ignition alike. However, evidence presented in Section 3.5 suggests otherwise.

Measuring the deposited energy (rather than simply the incident energy) drastically increases the ignition system complexity. However, there is a clear benefit that necessitates the added complexity. The breakdown process, being partly stochastic, does not depend solely on the incident energy. As such, there is weak correlation between the kernel size and incident energy. Figure 3.5 shows the kernel radius (R) versus incident energy (E_5) and deposited energy (E_d). While correlation with R is evident for both E_5 and E_d, the correlation with E_d is clearly stronger, which makes sense because E_d more closely represents

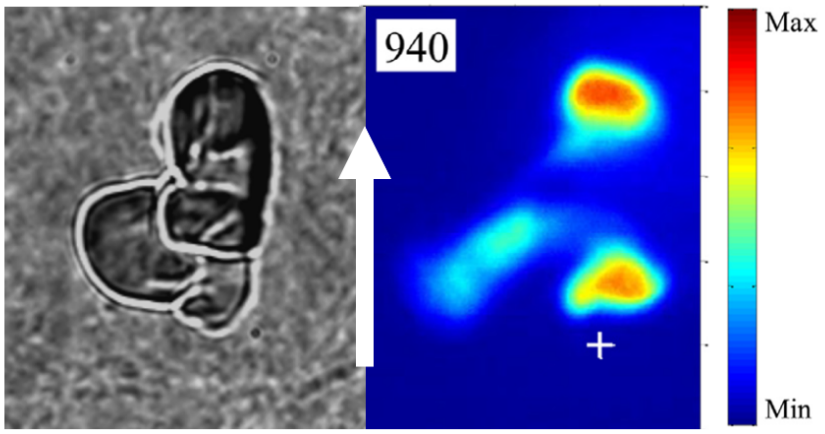

Figure 3.4: Flowing ignition kernels showing deformed third lobe structure. (Left) Schlieren image of $M = 1.75$, $\phi = 1.0$ kernel at $\Delta t_{ign} = 160\ \mu s$. (Right) OH PLIF of $U = 9.4$ m/s, $\phi = 0.6$ kernel at $\Delta t_{ign} = 600\ \mu s$ from Mulla *et al.* [30]. Flow direction is indicated by the white arrow.

the energy actually deposited into the kernel. This further supports the notion presented in Section 3.2 that E_d is a more useful quantity than incident energy.

Despite its superiority over E_5, the trend with respect to E_d is still fairly scattered, having a correlation coefficient of 0.75 (compared to 0.45 for E_5). The scatter in Figure 3.5 is due to randomness in the ignition process and early kernel growth. As Δt_{ign} increases, the scatter grows because the flame-expansion and flame-turbulence interactions are also stochastic processes. Figure 3.6 (left) shows the kernel radius versus E_d for $\Delta t_{ign} = 60\ \mu$s and $\Delta t_{ign} = 460\ \mu$s with a third order polynomial curve fit. Clearly the correlation is very tight at early times, having correlation values as high as 0.95. As Δt_{ign} increases, the correlation value decreases because the flame-growth is partially stochastic due to turbulence.

In general, the kernel size grows with time and laser energy. Figure 3.6 (left) shows two third-order polynomial curve fits to the data (red lines), which track the data quite well between $E_d = 5$ and 25 mJ, and perform moderately well outside that range. As Δt_{ign} increases, the curves shifts upward, as expected. Figure 3.6 (right) shows four such curves corresponding to $\Delta t_{ign} = 60$, 160, 460, and 680 μs; the kernel radius increases monotonically with Δt_{ign}. The same information can be displayed more compactly by extending

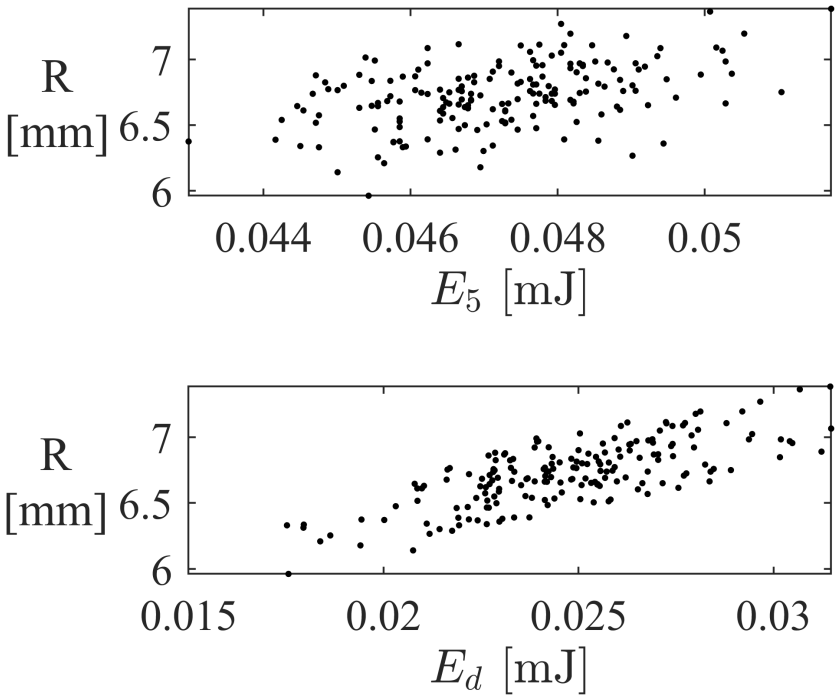

Figure 3.5: Kernel radius versus (top) incident energy, E_5 and (bottom) deposited energy, E_d for $M = 1.75$, $\phi = 1.0$ kernels at $\Delta t_{ign} = 320\ \mu s$.

time into a third axis. For example, Figure 3.7 shows the kernel radius dependent on Δt_{ign} and E_d. Again, R increases monotonically with both Δt_{ign} and E_d and the scatter increases with Δt_{ign}, as previously discussed. Evidently, the kernel radius is not independent of E_d within the time frame reported. Also shown in Figure 3.7 is a third-order-mixed polynomial surface fit of the form:

$$\begin{aligned} R\left(\Delta t_{ign}, E_d\right) = \; & a + b\Delta t_{ign} + cE_d + d{\Delta t_{ign}}^2 + e\Delta t_{ign}E_d \\ & + f{E_d}^2 + g{\Delta t_{ign}}^3 + h{\Delta t_{ign}}^2E_d + i\Delta t_{ign}{E_d}^2 \\ & + j{E_d}^3 \end{aligned} \tag{3.1}$$

Similarly to the 1D third-order polynomial fit above, the surface fit is strong when away from the lower boundaries owing to a rather small shot to shot variation of radius. For example, at $\Delta t_{ign} = 10\ \mu$s, $\langle R \rangle = 2.99$ mm and $\sigma_R = 0.062$ mm. Even at later times when

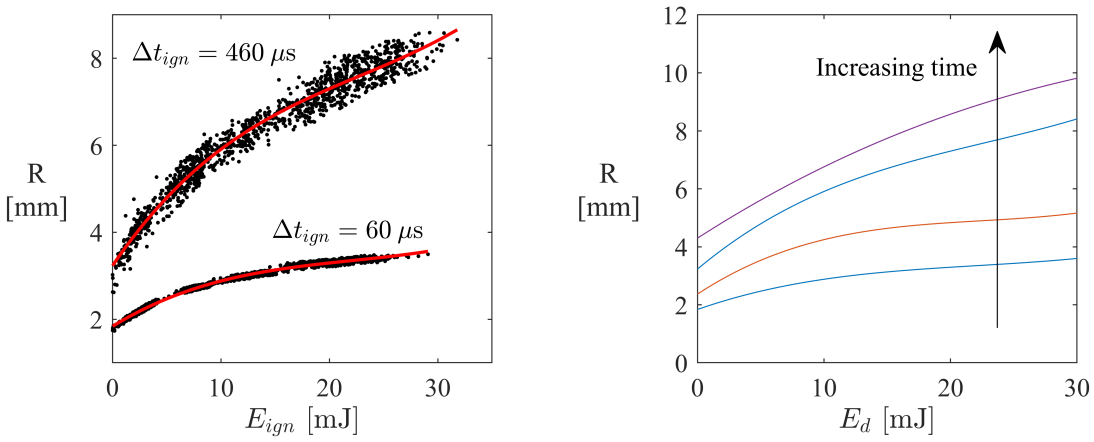

Figure 3.6: Trend of kernel radius, R versus deposited laser energy, E_d. Solid lines are third order polynomial curve fits at (left) the indicated time delays from ignition (Δt_{ign}) and (right) $\Delta t_{ign} = 60$, 160, 460, and 680 μs from bottom to top.

turbulence causes randomness in R, the variation is still quite small (e.g. at $\Delta t_{ign} = 460\,\mu$s, $\langle R \rangle = 7.28$ mm and $\sigma_R = 0.486$ mm). Low variation in the underlying data enables a curve fit with very tight confidence bounds. In fact, the upper and lower surface bounds are so tight that they cannot be displayed on Figure 3.7 because the difference to the surface fit is too small. For example, the predicted value of R at $E_d = 25$ mJ and $\Delta t_{ign} = 620$ μs is $R = 8.78$ mm with a 95% confidence bound of 8.26 - 9.30 mm, approximately a 0.5 mm difference from the prediction. Clearly the chosen surface fit tracks the data quite well, a consequence no doubt of the extreme number of data points used to create it (over 10,000 kernel ensembles appear in Figure 3.7). However, at low Δt_{ign} and E_d the curve fit deviates from the data slightly. In particular, the surface does not track the low E_d shape very well. At low E_d, the radius decays rapidly, and as $E_d \to 0$ the surface overestimates R, which may appear concerning. However, the error at low Δt_{ind} and E_d are unimportant when considering the analyses that follow, which aim to establish minimum values of Δt_{ign} and E_d for independent flame growth. It will be shown that $\tau_{ign} \sim 500$ μs and $E_{ign} \sim 25$ mJ. Therefore, how well the surface tracks the data at low Δt_{ign} or E_d is inconsequential.

Following a similar procedure for the kernel width and perimeter gives Figure 3.8. The same general trends exist for W and P. As Δt_{ign} and/or E_d increase, W and P increase

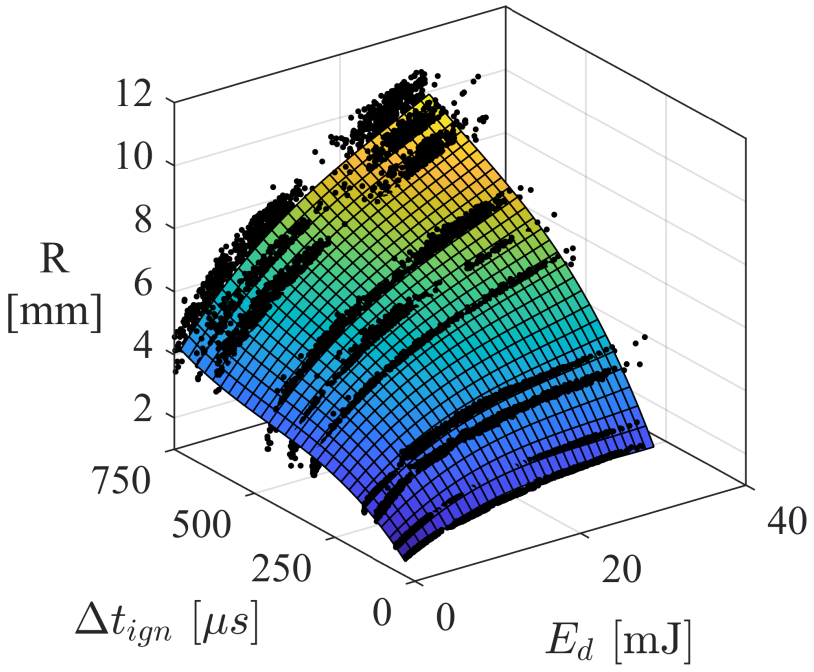

Figure 3.7: R versus E_d and Δt_{ign} for $M = 1.75$, $\phi = 1.0$ kernels. Each point corresponds to a single ensemble. The surface is a 2D polynomial curve fit (see Equation (3.1)) colored by the value of R.

as well. The scatter in W and P increases as Δt_{ign} increases. However, the perimeter has scatter at latter times, which is an expected result of flame wrinkling. Also, there is lower confidence in the edges detected by the Canny edge algorithm, especially on the windward side of the kernel where reactant entrainment weakens the density discontinuities resulting in spurious edges. Failure of the edge detection algorithm causes some additional error (and scatter) in the measured perimeter at late times. The surface fit for W and P appears more accurate as Δt_{ign} and E_d increase. Curve fit coefficients for R, W, and P are shown in Appendix D (Table D.1).

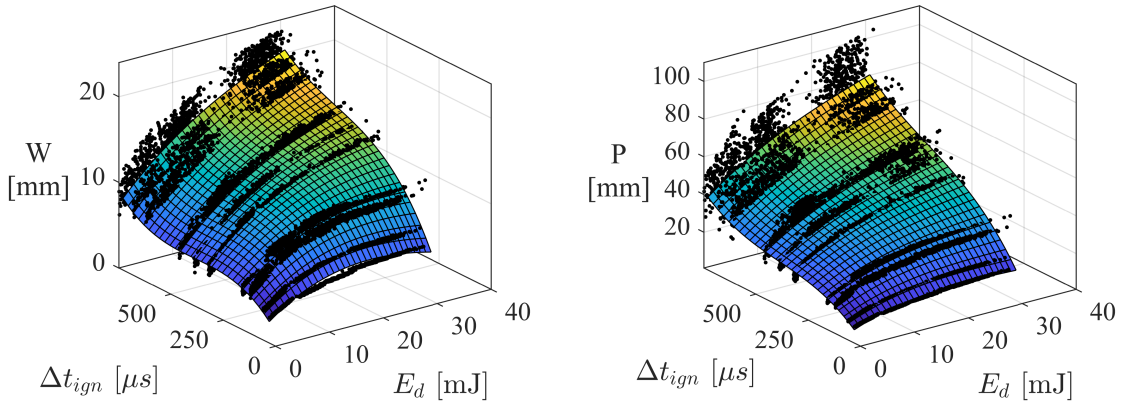

(a) Kernel width, W.

(b) Kernel perimeter, P.

Figure 3.8: Dependence of W and P on E_d and Δt_{ign} for $M = 1.75$, $\phi = 1.0$ kernels. Each point corresponds to a single ensemble. The surface is a 2D polynomial curve fit (see Equation (3.1)) colored by the value of W or P.

3.4 Transition to Self-Propagating Flames

The goal of this section is to identify the independence time, τ_{ind}, and minimum ignition energy, E_{ign}, required for independence of kernel growth from the ignition event. The minimum ignition energy is an important parameter because as will be shown, at low incident energy levels, the kernel size and growth are strong functions of the deposited energy (as seen in Figures 3.7 and 3.8). Thus, when $E_d < E_{ign}$, flame speed measurements can be drastically affected if the growth of every kernel ensemble is considered equally.

It is tempting to define τ_{ind} as the time when un-fueled kernels begin to dissipate. Hence, kernels would grow because of the ignition overdrive and dissipate, presumably, when the ignition event no longer influences the kernel. Mulla *et al.* [30] show that their un-fueled kernels increase in size until about $\Delta t_{ign} = 200 - 300\,\mu$s, after which the size decreases. Figure 3.9 shows results from this work, which are similar to the Mulla *et al.* [30] work, but for supersonic kernels and with a different ignition system. As Δt_{ign} increases, the kernels grow at first, then shrink. At late times, the data are very scattered because the temperature discontinuity is weak and the kernel edge is hard to identify. Here, the kernels

begin to dissipate at $\Delta t_{ign} \approx 250$ μs, which is similar to the Mulla *et al.* [30] results. The question remains whether this dissipation time is equivalent to τ_{ind}.

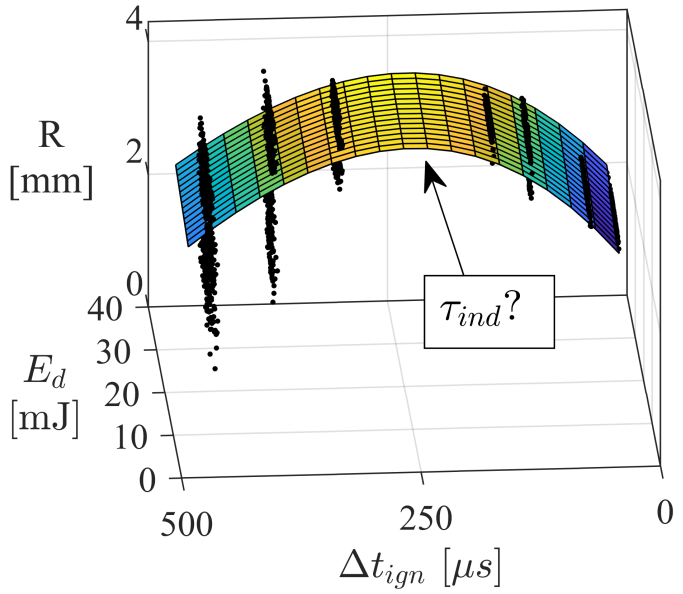

Figure 3.9: Dependence of R on E_d and Δt_{ign} for $M = 1.75$, $\phi = 0$ kernels. Each point corresponds to a single ensemble. The surface is a 2D polynomial curve fit (see Equation (3.1)) colored by the value of R.

In order to investigate τ_{ind}, we'll need to look at the reacting case, where kernel growth is partly governed by the ignition event and partly by flame propagation. The independence time is related to kernel growth rather than size, and growth eventually becomes independent of the ignition process. Hence, at $\Delta t_{ign} = \tau_{ind}$, the growth should be independent of ignition system settings such as E_d. In other words, when $\Delta t_{ign} = \tau_{ind}$, $dR/dt \neq f(E_d)$. In order to investigate this requirement, the surface fit of R is compressed into a 2D contour plot. Figure 3.10 shows the contour plot of R for the $M = 1.75$, $\phi = 1.0$ kernels. Besides being more compact, the data in Figure 3.10 are identical to the data in Figure 3.7: the radius is small at low Δt_{ign} and E_d and grows as Δt_{ign} and/or E_d increases. Looking at Figure 3.10 it becomes obvious that the conditions $\Delta t_{ign} \geq \tau_{ind}$ and $E_d \geq E_{ign}$ define a rectangular region, within which flame speed is independent of the ignition process.

It is hard to discern the dependence of dR/dt on E_d in Figure 3.10 without additional

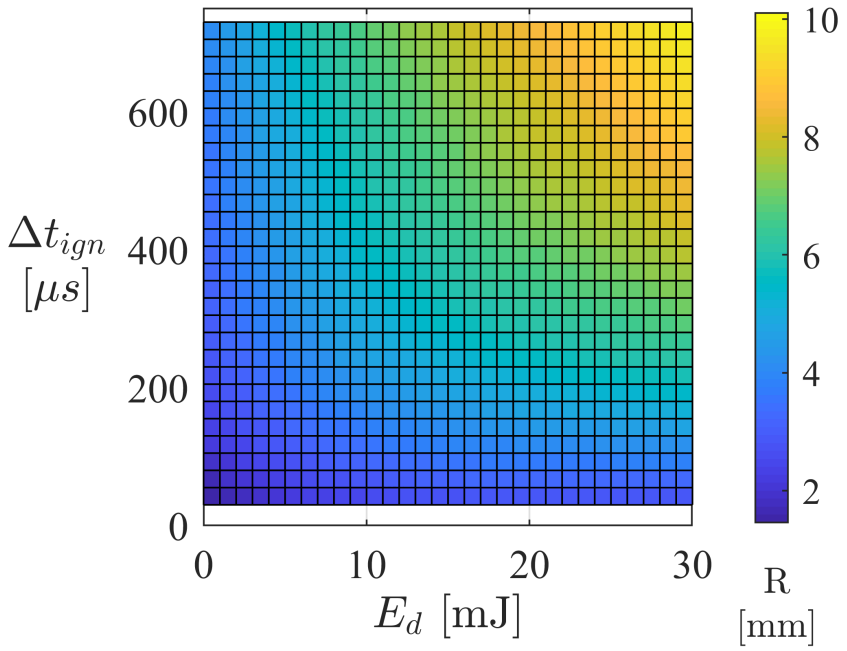

Figure 3.10: Surface plot of R versus E_d and Δt_{ign} for $M = 1.75$, $\phi = 1$ kernels.

analysis. In order to expose the dependence, the surface fit of Equation (3.1) is processed to yield $\frac{\partial R}{\partial t}$ by simply taking the partial derivative with respect to time of the surface fit. Figure 3.11a shows a contour plot of $\frac{\partial R}{\partial t}$ versus Δt_{ign} and E_d. The growth rate, being related to $\frac{\partial R}{\partial t}$, decreases with time up to about $\Delta t_{ign} = 500 - 600\,\mu s$, after which it increases slightly within the limit of the experimental times measured. The ignition overdrive causes the kernel to rapidly expand in order to reach mechanical equilibrium with the surroundings. When the overdrive effect decays, the growth naturally slows. As the flame kernel becomes self propagating, hydrodynamic instability (discussed in Chapters 4 and 5) and turbulence cause the flame to wrinkle, resulting in the observed re-acceleration.

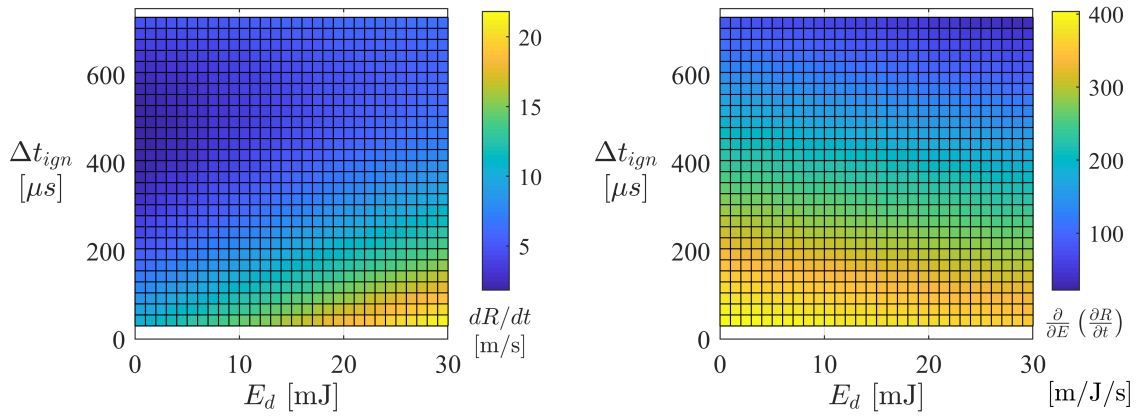

(a) $\frac{\partial R}{\partial t}$ (b) $\frac{\partial}{\partial E}\left(\frac{\partial R}{\partial t}\right)$

Figure 3.11: Surface plots of $\frac{\partial R}{\partial t}$ and $\frac{\partial}{\partial E}\left(\frac{\partial R}{\partial t}\right)$ versus E_d and Δt_{ign} for $M = 1.75$, $\phi = 1$ kernels.

The growth $\left(\frac{\partial R}{\partial t}\right)$ also appears to be a strong function of E_d in Figure 3.11a, especially at early times. As E_d increases, the overdrive effect becomes stronger resulting in large $\frac{\partial R}{\partial t}$ at early times. In fact, the dependence of $\frac{\partial R}{\partial t}$ on E_d easily continues into the middle times ($\Delta t_{ign} = 300 - 500\ \mu s$). To investigate this dependence further, the mixed second order partial derivative of R can be constructed from the surface fit. Figure 3.11b shows a contour plot of $\frac{\partial}{\partial E}\left(\frac{\partial R}{\partial t}\right)$ versus Δt_{ign} and E_d. Overall, the dependence of $\frac{\partial R}{\partial t}$ on E_d decreases as Δt_{ign} and E_d increase. However, the variation of $\frac{\partial}{\partial E}\left(\frac{\partial R}{\partial t}\right)$ with Δt_{ign} is much stronger than the variation with E_d. These observations suggest that increasing E_d has a small influence on decoupling $\frac{\partial R}{\partial t}$ from E_d, and that $\frac{\partial R}{\partial t}$ naturally decouples from E_d as time progresses, as expected. At the latest times measured, $\frac{\partial}{\partial E}\left(\frac{\partial R}{\partial t}\right)$ is nearly zero.

The above analysis might lead one to believe that $\Delta t_{ign} \geq \tau_{ind}$ is the only condition required for kernel growth to be independent of the ignition process. This notion is incorrect, however, because the relative size of $\frac{\partial R}{\partial t}$ should be taken into account when analyzing the data in Figure 3.11. By normalizing $\frac{\partial}{\partial E}\left(\frac{\partial R}{\partial t}\right)$ with $\frac{\partial R}{\partial t}$, the relative importance of E_d on the flame growth can be exposed. The quotient $\Delta_{\partial R/\partial t} = \frac{\partial}{\partial E}\left(\frac{\partial R}{\partial t}\right)/\frac{\partial R}{\partial t}$ represents the fractional change in $\frac{\partial R}{\partial t}$ per mJ of deposited laser energy (multiplying by 100 gives the % change per

mJ). When the flame growth is independent of the ignition event, $\Delta_{\partial R/\partial t} \to 0$.

Figure 3.12 shows $\Delta_{\partial R/\partial t}$ as a function of time for $E_d = 4$ mJ. Clearly $\Delta_{\partial R/\partial t}$ approaches zero as time increases, however, $\Delta_{\partial R/\partial t} = 0$ is not realized within the experimental window. Based on the asymptotic approach, it would likely take several milliseconds for the kernel growth to be completely independent of the ignition event. This is an important conclusion in supersonic flows where the flow through time is on the order of one millisecond. With this in mind, we mathematically define τ_{ign} to be the time it takes for $\Delta_{\partial R/\partial t}$ to reduce below a certain threshold value, say 2.5%/mJ. It is important to define τ_{ind} in this way because at low E_d the error is very large, mainly due to $\frac{\partial R}{\partial t}$ being small (see the left plot in Figure 3.11). The value 2.5%/mJ indicates that increasing or decreasing the deposited energy by 1 mJ would impart a 2.5% change on $\partial R/\partial t$, which is quite small; although, how over-driven the kernel is at 2.5%/mJ is not directly obvious. However, combined experimental and numerical radii trends presented in Chapter 4 suggest that these τ_{ign} (calculated using the 2.5%/mJ cutoff criteria) are reasonable.

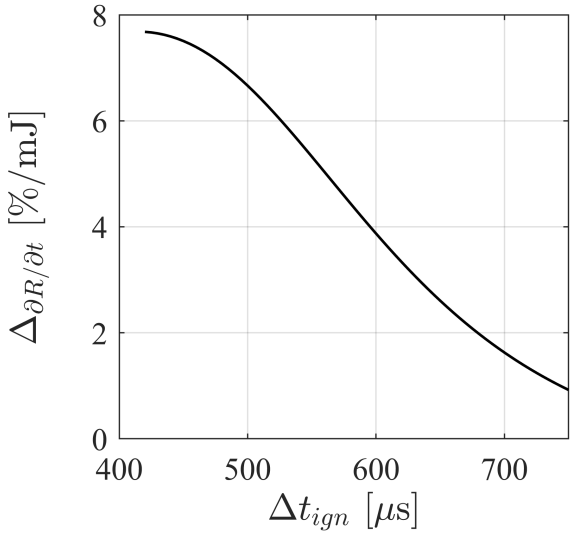

Figure 3.12: Change in $\frac{\partial R}{\partial t}$ due to variation in the deposited laser energy as a function of Δt_{ign}.

The previous analysis can be extended to identify τ_{ind} (using a plot like Figure 3.12) for every E_d. Next, E_{ign} can be defined as the minimum E_d where the error falls below

2.5%/mJ for all Δt_{ign}. Figure 3.13 shows a contour plot of $\partial R/\partial t$ with isocontour regions of $\Delta_{\partial R/\partial t}$ superimposed. The region of $\Delta_{\partial R/\partial t} \leq 2.5\%$/mJ is not a simple box as previously mentioned, but instead spreads across all E_d. Given enough time, flame growth will eventually become independent from the ignition event. However, it is still advantageous to define the independence region as being bounded by E_{ign} and τ_{ind} because, below E_{ign} the ignition process heavily influences the growth within a significant portion of the times measured. The requirement $\Delta_{\partial R/\partial t} \leq 2.5\%$/mJ requires $E_{ign} \approx 26.2$ mJ and $\tau_{ind} \approx 395\,\mu$s for the $M = 1.75$, $\phi = 1.0$ kernels.

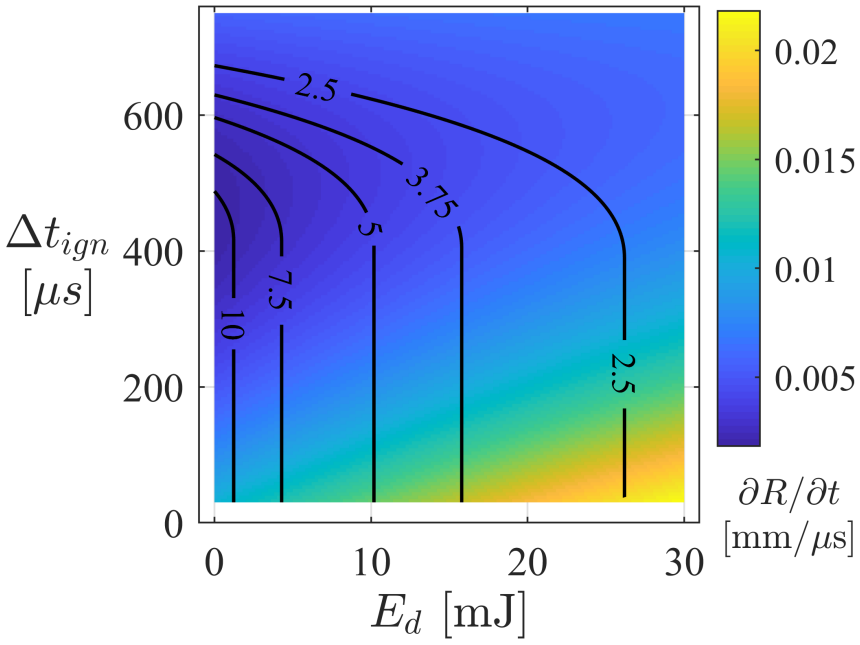

Figure 3.13: Contour plot of $\partial R/\partial t$ versus E_d and Δt_{ign} for $M = 1.75$, $\phi = 1$ kernels with regions of % change of $\partial R/\partial t$ per mJ of deposited energy overlaid with black lines.

3.5 Role of Mach Number and Equivalence Ratio

Section 3.4 discusses how independence time and ignition energy are calculated and gives an example for the $M = 1.75$, $\phi = 1.0$ kernels. The analysis is repeated here to explore the effect of Mach number and equivalence ratio. In each analysis, two additional datasets

are presented and compared to the $M = 1.75$, $\phi = 1.0$ baseline case. Therefore, four new cases are shown: two additional Mach numbers at $\phi = 1.0$, and two additional equivalence ratios at $M = 1.75$. The static temperature and pressure are matched across all cases by varying the stagnation conditions. In order to make data collection feasible for the new cases, data are collected only for $\langle E_3 \rangle = 55$ mJ.

Figure 3.14 shows schlieren snapshots arranged to highlight Mach number trends. The $M = 1.75$, $\phi = 1.0$ baseline kernels are generally larger when Δt_{ign} and/or E_d increase. Figure 3.15a and b shows that $M = 1.5$ and $M = 2.0$ kernels follow the same general trend. Despite having the same incident energy, $M = 1.5$ kernels have a larger deposited energy than $M = 2.0$ kernels. This observation could be the result of beam steering and defocusing, if a compression wave were in the vicinity of the ignition location. Another possibility is that the mean flow velocity affects the ignition process. There is a difference in the deposited energy when comparing across the three Mach numbers. Given the same value of $\langle E_5 \rangle \approx 47$ mJ, $\langle E_d \rangle = 30.6$, 21.2, and 22.9 mJ for $M = 1.5$, 1.75, and 2, respectively. The relatively different value for $M = 1.5$ is most likely an anomaly of the experiment caused by flow field differences such as turbulence level, isotropy, and flow angle (weak shocks and expansions). The offset third lobe observed in the $M = 1.75$ case is also observed in $M = 2.0$, but is harder to discern at $M = 1.5$. This suggests that fluid dynamic phenomena (shock structure, turbulence isotropy, etc.) are also partially responsible for third lobe formation. Clearly, the third lobe offset is not a universal feature of convecting ignition kernels, but rather depends on the specifics of the local flow field.

The equivalence ratio effects are shown in Figure 3.15c and d and schlieren snapshots of the different equivalence ratio conditions are shown in Figure 3.16. The $\phi = 0.75$ case is similar to the $\phi = 1.0$ case, which is shown in Figure 3.7. The measured radii are slightly smaller, but otherwise the trend is matched within the E_d range studied. In contrast, the $\phi = 0.5$ case does not closely match the $\phi = 1.0$ case. The radii are similar at early times but are significantly smaller than in the $\phi = 1.0$ case at late times. In all $\phi \geq 0.75$ cases,

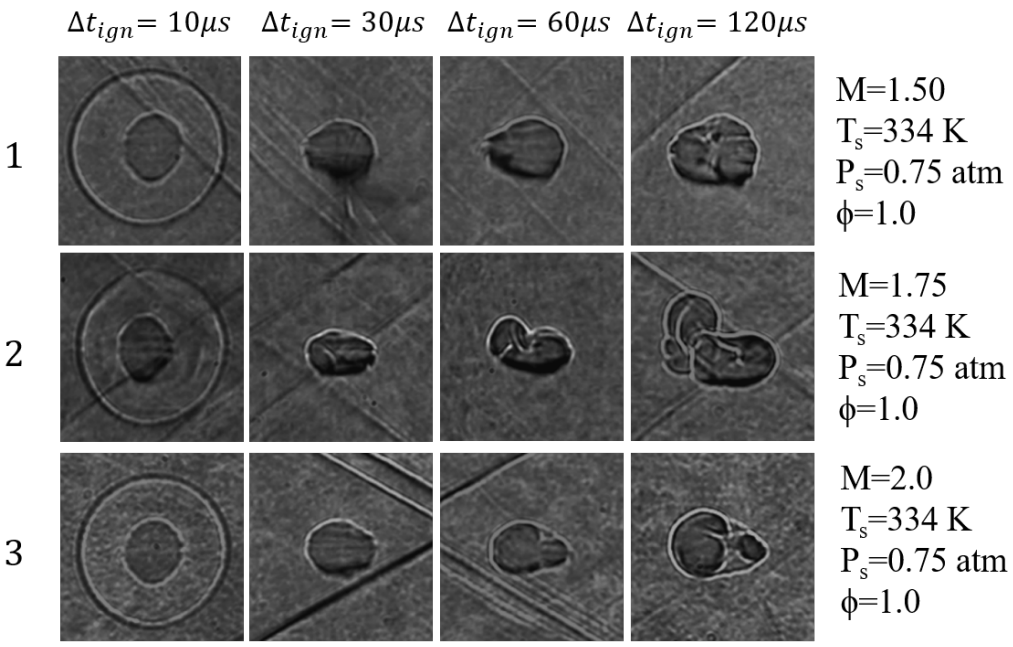

Figure 3.14: Laser ignition kernels for a variety of conditions (rows) and time delays (columns). Row 1 corresponds to $M = 1.5$, row 2 corresponds to $M = 1.75$, and row 3 corresponds to $M = 2.0$.

there appears to be an acceleration at late times (the surface curves upward); however, for $\phi = 0.5$ the flame does not accelerate. The lack of late-time acceleration in this case is not surprising because the flame is below the flammability limit at these conditions. This situation is similar to that shown in the unfueled case (Figure 3.9), where the flame grows until $\Delta t_{ign} \approx 250\ \mu s$, then dissipates. Whether the flame will grow or dissipate cannot be determined with the data presented because the elapsed time is insufficient to make the determination. Figure 3.15d suggests that adding fuel increases the dissipation time for kernels that are not self-propagating.

The form of Equation (3.1) is once again used to fit a 2D surface to data in Figure 3.15. Model coefficients are given in Appendix D for the $M = 1.5$ and $M = 2.0$ kernels (Table D.1) and for the $\phi = 0.75$ and $\phi = 0.5$ kernels (Table D.2). The surface fit is used to produce $\frac{\partial R}{\partial t}$ and $\frac{\partial}{\partial E}\left(\frac{\partial R}{\partial t}\right)$, from which $\Delta_{\partial R/\partial t}$ as a function of Δt_{ign} (for each E_d) is established. Finally, the independence area is shown for each case in Figure 3.17.

Figure 3.17 shows contour plots of $\partial R/\partial t$ versus E_d and Δt_{ign}. The images in Figure

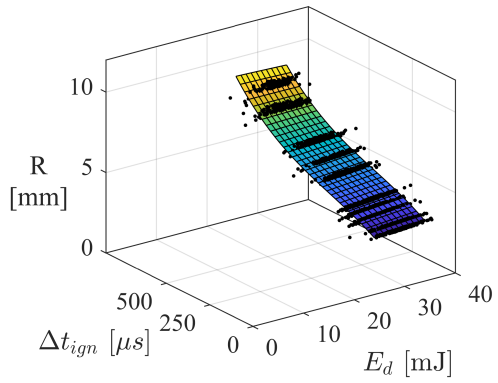

(a) $M = 1.5$, $\phi = 1.0$.

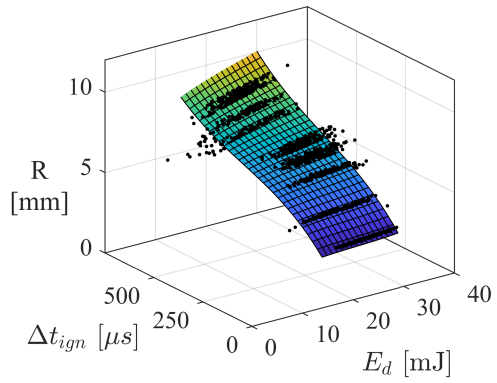

(b) $M = 2.0$, $\phi = 1.0$.

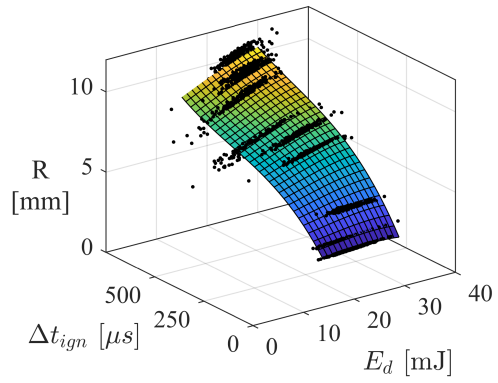

(c) $M = 1.75$, $\phi = 0.75$.

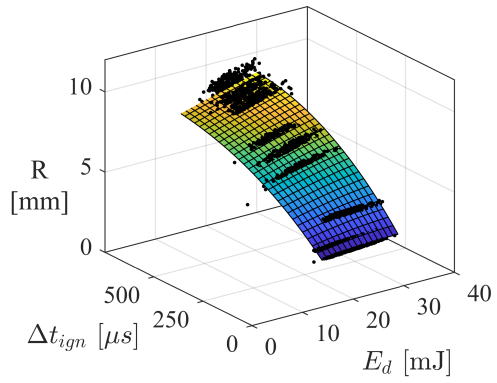

(d) $M = 1.75$, $\phi = 0.5$.

Figure 3.15: Dependence of R on E_d and Δt_{ign} at the indicated conditions.

3.17 are arranged to highlight the effect of M and ϕ. For some of the cases, the independence region is undefined because either the available data were insufficient to determine the region, or the flame does not achieve self-propagation and therefore the independence region is meaningless. For $M = 1.5$, $\phi = 1.0$, the deposited energies are too high to identify a minimum value of E_{ign} because $\Delta_{\partial R/\partial t}$ is less than 2.5%/mJ over the entire range of E_d and Δt_{ign} shown. Therefore, E_{ign} is taken as being at least 24 mJ and the independence time is undefined. For $M = 2.0$, $\phi = 1.0$, the 2.5%/mJ isocontour defines the independence region and the graph suggests $E_{ign} = 20$ mJ and $\tau_{ind} = 485$ μs. For the low fuel case, $\phi = 0.5$, the contour plot clearly shows that $\partial R/\partial t$ decreases monotonically with time. In this situation the flame is not self-sustaining and therefore independence of flame

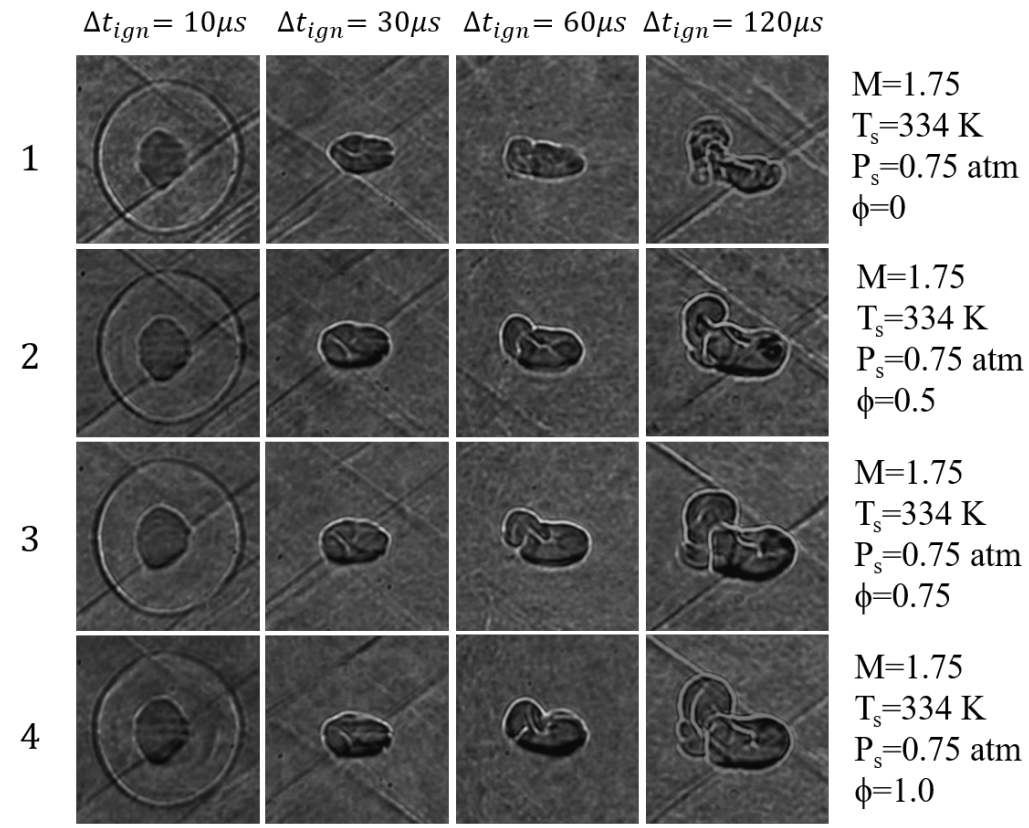

Figure 3.16: Laser ignition kernels for a variety of conditions (rows) and time delays (columns). Row 1 corresponds to $\phi = 0$, row 2 corresponds to $\phi = 0.5$, row 3 corresponds to $\phi = 0.75$, and row 4 corresponds to $\phi = 1.0$.

growth from the ignition event is not a meaningful concept. In contrast, $\phi = 0.75$ shows a re-acceleration at late time and an independence region bounded by $E_{ign} = 22.4$ mJ and $\tau_{ind} = 345$ μs.

3.6 Laser Ignition Summary

The question regarding the required laser settings and minimum time for independent flame growth can now be answered. Table 3.1 shows a summary of E_{ign} and τ_{ind} for all cases. Overall, $E_d = 25$ mJ and $\Delta t_{ign} = 500$ μs appear to be reasonable values to guarantee independence in the flame growth over all of the conditions studied. The reported value for the independence time is roughly two times larger than the value estimated by the dissipation of fuel-free kernels, which highlights the importance of examining the amount

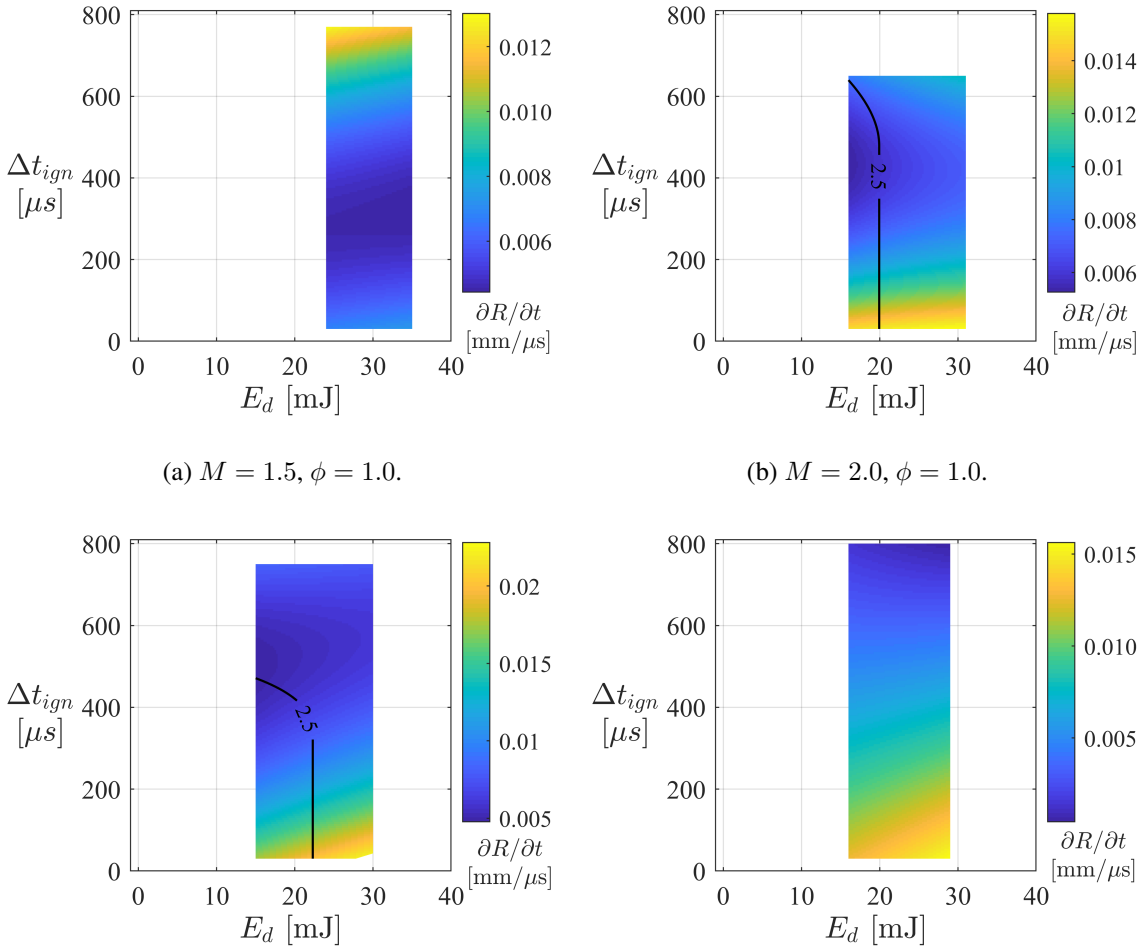

(a) $M = 1.5$, $\phi = 1.0$.

(b) $M = 2.0$, $\phi = 1.0$.

(c) $M = 1.75$, $\phi = 0.75$.

(d) $M = 1.75$, $\phi = 0.5$.

Figure 3.17: Contour plot of $\partial R/\partial t$ versus E_d and Δt_{ign} for various cases with regions of % change of $\partial R/\partial t$ per mJ of deposited energy overlaid with black lines..

by which $\partial R/\partial t$ (rather than R) varies with laser settings. It should be noted that the independence time defined in this way does not correspond to a region that is completely independent of the ignition event. Even at the latest times measured, the flame growth is still slightly dependent on E_d, and therefore has a memory of the ignition event. It would likely take several milliseconds for complete independence, which is is an impossibly long timescale for supersonic flows but would not be unreasonable in subsonic laser-ignited flame studies.

Table 3.1: Summary of independence time and ignition energies required for free flame growth for various cases. [1] indicates that all of the data satisfy the requirement $\Delta_{\partial R/\partial t} \leq 2.5\%$/mJ, therefore the minimum recorded value of E_d is used for E_{ing}.

Case		E_{ign}	τ_{ind}
$M = 1.75$	$\phi = 0.50$	-	-
$M = 1.75$	$\phi = 0.75$	22.4	345
$M = 1.75$	$\phi = 1.00$	26.2	395
$M = 1.50$	$\phi = 1.00$	24[1]	-
$M = 2.00$	$\phi = 1.00$	20	485

CHAPTER 4

EXPERIMENTAL OBSERVATIONS AND NUMERICAL VALIDATION

Experimental results of flame kernel studies and numerical validations are discussed in this chapter. Here, the emphasis is on the characteristics of freely propagating flame kernels traveling through a mean expansion. The flame topology and statistical flame growth are two particular details of interest. Schlieren and PIV are the main tools used to probe the flame and flow field. Both schlieren, being a line of sight diagnostic, and PIV, being a planar one, yield limited information. Therefore, this chapter primarily serves to demonstrate the supersonic flame kernel problem, gives observations, and offers several hypotheses. Figure 4.1 shows the Borghi-Peters diagram [49] with the conditions in this work overlaid. All of the flames studied fall within the thin reaction zone. Validated numerical simulations, which are discussed in Chapters 5 and 6, are used to expand upon the observations and evaluate the hypotheses presented here. This chapter starts with flow field characterization of the different facility nozzles and turbulence generators. Next, the growth of supersonic kernels is discussed, followed by observations and hypotheses about the kernel topology and flame speed. Finally, the end of this chapter is dedicated to numerical simulation validation.

The experimental details are discussed in Chapter 2, therefore only a few relevant details are repeated here. Premixed CH_4-air flame kernels are initiated in a supersonic channel using laser ignition. Eight experimental cases, spanning three Mach numbers, three turbulence settings, and four equivalence ratios are presented (see Table 2.3). In contrast to the supersonic ignition work, here the ignition laser is focused from the side window, rather than the top. Following the conclusions of Chapter 3, the average incident energy, $\langle E_3 \rangle$, is set to 55 mJ across all eight cases. Based on the independence time findings of Chapter 3, the turbulent flame speeds presented in this chapter are slightly in error because the ker-

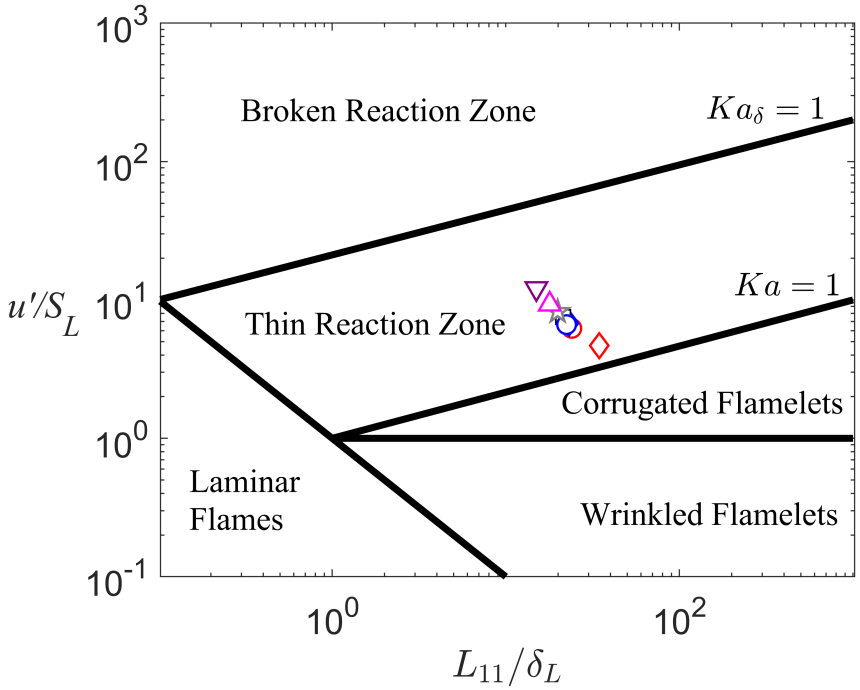

Figure 4.1: Borghi-Peters diagram [49] showing the flame regime of the experimental conditions in this study. Symbols are defined in Table 2.3.

nel has a long lasting memory of the ignition event. This is especially problematic when $\Delta t_{ign} \leq 500\ \mu s$.

4.1 One Dimensional Model and Tunnel Velocity Characterization

The non-reacting flow field is characterized using PIV post-processed into the mean velocity and RMS velocity fluctuation. Figure 4.2 shows the mean velocity versus the axial distance from the point of ignition (Δx_{ign}). The blue, black, and red symbols represent the ensemble mean x-component velocity (U) for M = 1.5, 1.75, and 2.0, respectively. The experimental data in Figure 4.12 are sub-sampled to improve visualization. Generally, U increases with Δx_{ign} due to acceleration imposed by the mean flow expansion. Also, U increases as M increases, which is also expected.

A 1D isentropic flow model was fit to the mean velocity measured experimentally. Assuming a thermally perfect gas and isentropic flow, mass continuity yields a relation for

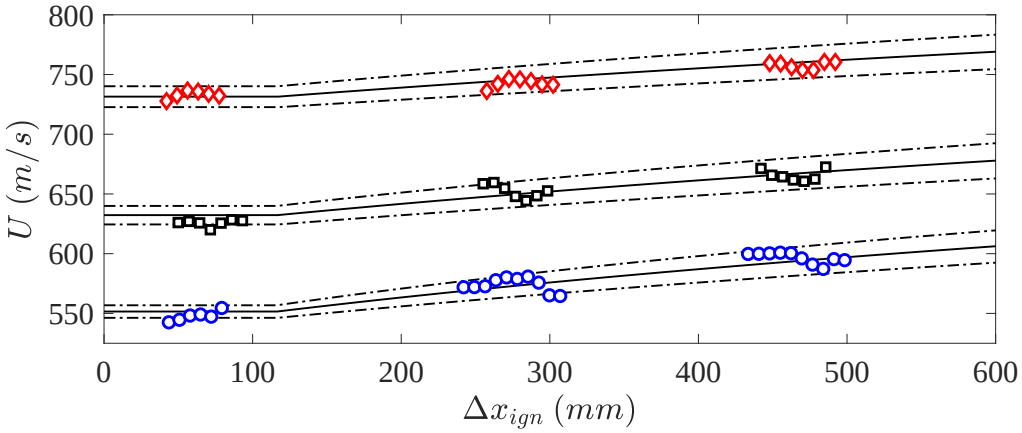

Figure 4.2: Centerline mean axial velocity ($U_{y=0\pm10mm}$) versus distance from ignition point. Case 4 ($M_0 = 1.5$): blue circles, case 3 ($M_0 = 1.75$): black squares, case 5 ($M_0 = 2.0$): red diamonds. For each Mach number the solid black line represents the 1D isentropic solution. The upper/lower dashed lines represent data boundaries constructed using, respectively, the highest/lowest recorded temperature and a 0.1° thinner/thicker boundary layer. One out of every 30 axial data points are shown to improve visualization.

the local Mach number (M_l):

$$M_l(x)\left(1+\frac{\gamma-1}{2}M(x)^2\right)^{-(\gamma+1)/2(\gamma-1)} = \frac{A^*}{A(x)}\left(\frac{\gamma+1}{2}\right)^{-(\gamma+1)/2(\gamma-1)} \tag{4.1}$$

A^* is the throat area. Assuming a simple linear BL growth:

$$A(x) = 0.0025 + 0.1\Delta_{x,tc}\,tan(\psi) \tag{4.2}$$

where $\Delta_{x,tc}$ refers to the axial distance from the turning corner and ψ to the flow turning angle. A distinction is made between ψ and the geometric turning angle (ψ_0), which differ due to BL growth. The local axial mean velocity (U_l) is only a function of M_l, the local area (A_l), the mixture properties and T_0:

$$U_l = M_l\sqrt{\gamma R}\,T_0{}^{1/2}\left(1+\frac{\gamma-1}{2}M_l^2\right)^{-1/2} \tag{4.3}$$

Similarly, the local static pressure and temperature are:

$$P_{s,l} = P_0\left(1 + \frac{\gamma - 1}{2}M_l^2\right)^{-\gamma/(\gamma-1)} \tag{4.4}$$

$$T_{s,l} = T_0\left(1 + \frac{\gamma - 1}{2}M_l^2\right)^{-1} \tag{4.5}$$

The flow turning angle is varied to fit the experimental data, resulting in best fit turning angles of 0.55°, 0.575°, and 0.6° for $M_0 = 1.5, 1.75,$ and 2.0, respectively. These turning angles correspond to average boundary layer growth angles of 0.45°, 0.425°, and 0.4° for $M_0 = 1.5, 1.75,$ and 2.0, respectively. A comparison between the model and mean flow data is shown in Figure 4.2. The modeled velocities (solid lines) clearly match the data quite well. Also shown in Figure 4.2 are dot-dashed lines for upper and lower data bounds that correspond to a 0.1°thinner/thicker BL and the highest/lowest recorded temperature for each dataset. Over 90% of the measured mean velocities fall within these two data bounds.

A limited set of stereo-PIV measurements, performed for case 3, indicates $u_2 \approx u_3$. Hence, two-component planar PIV is used for turbulence measurements and the relationship $u' = \sqrt{\frac{1}{3}(u_1^2 + 2{u_2}^2)}$ is used instead of $u' = \sqrt{\frac{1}{3}(u_1^2 + {u_2}^2 + {u_3}^2)}$ for the characteristic RMS turbulent velocity. Here, u_1, u_2, u_3 are the RMS turbulent velocity fluctuations in the x, y, and z directions, respectively. Figure 4.3 shows the RMS velocity, u', and isotropy ratio, u_1/u_2, versus Mach number and Figure 4.4 shows them versus the turbulence generator. Overall, u' decreases slightly downstream due to the natural decay of turbulent kinetic energy. In contrast, u_1/u_2 increases downstream, which is caused by the tendency of anisotropic flows to return to isotropy. The turbulence generator is located upstream of the CD nozzle where it creates nearly isptropic turbulence [138]. The isotropy is reduced when the flow travels through the CD nozzle due to non-uniform vortex stretching [139], ω_x increases while ω_y and ω_z decrease. Given enough time the flow field will return to isotropy; however, the experimental domain is not long enough for this realization. There

appears to be a weak dependence of both u' and u_1/u_2 on M.

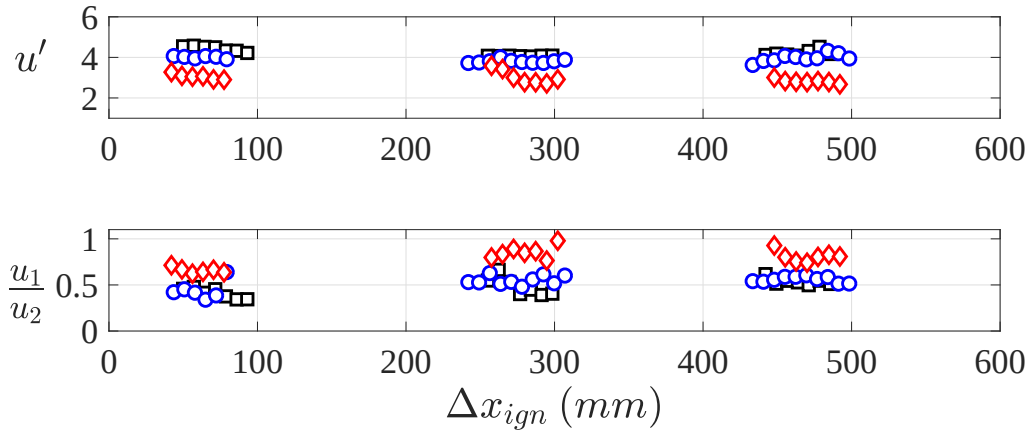

Figure 4.3: Centerline RMS turbulent velocity and isotropy versus distance from ignition point and Mach number. Case 4 ($M_0 = 1.5$): blue circles, case 3 ($M_0 = 1.75$): black squares, case 5 ($M_0 = 2.0$): red diamonds.

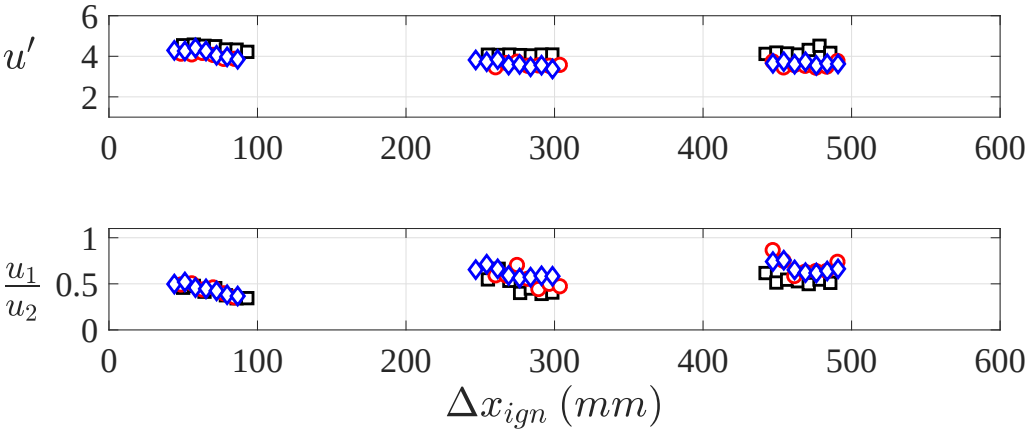

Figure 4.4: Centerline RMS turbulent velocity and isotropy versus distance from ignition point and turbulence grid. Case 1 (No Grid): red circles, case 2 (Biplanar Grid): blue diamonds, case 3 (Hole Grid): black squares.

4.2 Morphology of Supersonic Flame Kernels

It is not clear *a priori* how self-propagating supersonic flame kernels grow due to combined effects of turbulence and compressibility. Nor is it obvious if flame kernels yield a useful canonical experiment in which to study supersonic flames. To investigate these questions, this section discusses the structure, growth and viability of supersonic flame kernels.

Perhaps one of the more important questions is whether supersonic flame kernels grow and if, as expected, they become more wrinkled with time. For example, if hydrodynamic instability were too strong the flame could extinguish. To answer these questions, the average progress variable ($\bar{c}$) map and its derived quantities are investigated. A distinction is made here between the progress variable (c), which represents how much of a particular reactant has been consumed (or product produced) versus the average progress variable ($\bar{c}$), which can be thought of as the likelihood of finding an instantaneous flame at some location within the turbulent flame brush. More on this distinction and some implications are given in Chapter 5.3. Figure 4.5 shows the $\bar{c}$-map evolution for cases 3, 4, and 5. Only the difference versus M is plotted for brevity. Clearly the kernel size grows with time for all cases (this trend is consistent for the other cases not shown). Kinks, which also appear in the instant schlieren images (see Figure 2.14), can be seen in the $\bar{c}$-map. These appear after interaction with weak shocks and, once deformed, the kernels retain their new shape.

The ensemble mean flame radius, $\langle R \rangle$, was already defined in Chapter 1.4 and is a function of the flame volume and hence an important measure of flame growth. Figure 4.6 shows the evolution of $\langle R \rangle$ for every case with the data organized to highlight the effect of M, u' and ϕ. Across all cases, $\langle R \rangle$ appears to overshoot at early times due to ignition overdrive, then decrease slightly before increasing again at later times. The analysis in Chapter 3 suggests that this late time acceleration coincides with the transition to self-propagating flames. Interestingly, ϕ appears to have little effect on kernel size during ignition overdrive, but has a much greater and expected effect on $\langle R \rangle$ after $\Delta t_{ign} \approx 500\,\mu$s. Further, the flame kernels become more wrinkled with time, i.e., the $\bar{c}$-map grows thicker as Δt_{ign} increases, which is clearly obvious in Figure 4.5. These observations suggest that supersonic flame kernels are indeed self-propagating and wrinkle in response to turbulence.

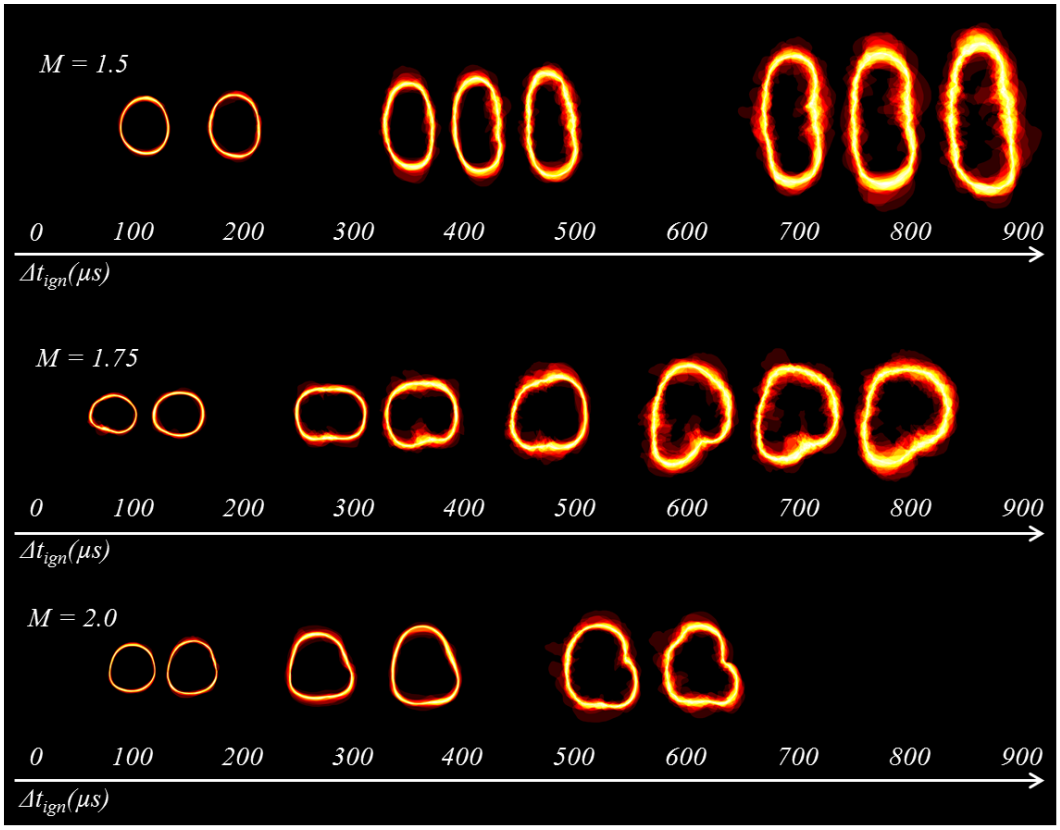

Figure 4.5: Time evolution of progress variable map for Mach = 1.5 (top), M = 1.75 (middle), and M = 2.0 (bottom) flame kernels. C-maps were formed from 30 schlieren images. Maps are colored black at both $\bar{c} = 0$ and $\bar{c} = 1$; white corresponds to the $\bar{c} = 0.5$ contour. Some horizontal positions are displaced slightly to fit images that would otherwise overlap.

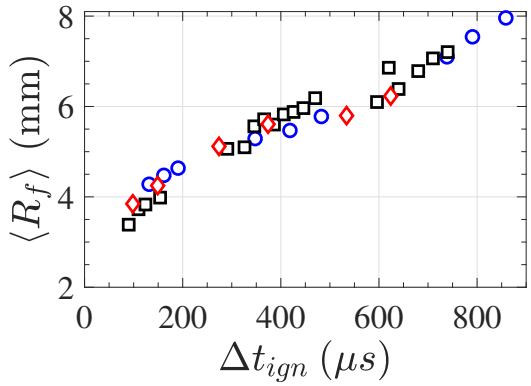

(a) Effect of M_0.

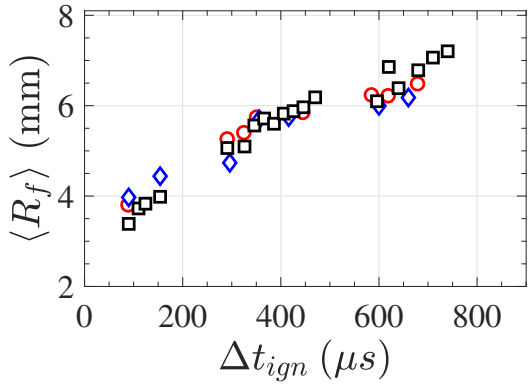

(b) Effect of u'.

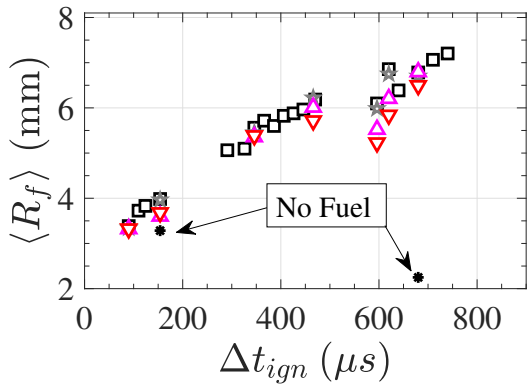

(c) Effect of ϕ.

Figure 4.6: Average flame radii versus time from ignition showing the effect of Mach number, turbulence intensity and equivalence ratio. Symbols are defined in Table 2.3. Case 1 ($M = 1.75$, $\phi = 1.0$, No Grid): red circles, case 2 ($M = 1.75$, $\phi = 1.0$, Biplanar Grid): blue diamonds, case 3 ($M = 1.75$, $\phi = 1.0$, Hole Grid): black squares, case 4 ($M = 1.5$, $\phi = 1.0$, Hole Grid): blue circles, case 5 ($M = 2.0$, $\phi = 1.0$, Hole Grid): red diamonds, case 6 ($M = 1.75$, $\phi = 0.9$, Hole Grid): gray stars, case 7 ($M = 1.75$, $\phi = 0.8$, Hole Grid): magenta upward triangles, case 8 ($M = 1.75$, $\phi = 0.7$, Hole Grid): red downward triangles. Approximately 30 ensembles are used to form statistics at each time.

The horizontal ($\mathcal{L}_\mathcal{H}$) and vertical flame extents ($\mathcal{L}_\mathcal{V}$) of the $\bar{c}$-map (1/2 of the maximum horizontal/vertical extent of the $\bar{c} = 0.5$ contour, respectively), are used to describe the kernel shape. A quick investigation of the $\bar{c}$-map data in Figure 4.5 suggests that the average $\mathcal{L}_\mathcal{H}$ and $\mathcal{L}_\mathcal{V}$ have Mach number dependencies. For $M = 1.5$ kernels, and to a lesser extent for $M = 1.75$ kernels, the average shape is elongated vertically, i.e. $\mathcal{L}_\mathcal{V}$ grows faster than $\mathcal{L}_\mathcal{H}$ downstream. While for $M = 2.0$ kernels, there is no perceptible difference between $\mathcal{L}_\mathcal{V}$ and $\mathcal{L}_\mathcal{H}$ versus time. To elucidate these effects, the normalized kernel aspect ratio (AR/AR_0) is plotted in Figure 4.7, where $AR = \mathcal{L}_\mathcal{V}/\mathcal{L}_\mathcal{H}$ and AR_0 is the initial kernel aspect ratio. Clearly, the kernels are vertically extended at lower Mach numbers and are more circular at higher Mach numbers. At the extremes, $M = 1.5$ kernels are twice as tall as they are wide (at $860\ \mu s$) while the aspect ratio of $M = 2.0$ kernels is invariant with time. This result is interesting when comparing $\langle R \rangle$ in Figure 4.6a, which shows only slight differences in the overall flame radius versus Mach number[1]. There are several potential explanations for this phenomena. First, this observation could be the result of non-spherical kernel topology if, for example, the cross-sectional area and effective radius are not representative measures of the overall kernel growth. Second, different turbulence characteristics could be responsible for the observation if the AR is a function of one or more turbulence parameters. However, the turbulence characteristics presented in Table 2.1 show that u', u_1/u_2, and L_{11} are similar for $M = 1.5$ and 1.75. Additionally, the lateral integral scale L_{22} is smallest for $M = 1.5$ and therefore unlikely to be responsible for the lateral elongation. Third, the Mach number could explain the difference through the change in the local Mach angle, which varies from $\approx 42° - 30°$ as M varies from $1.5 - 2.0$. The kernel expands through waves oriented at the local Mach angle, and so the Mach number could have an affect on the kernel shape.

Varying the turbulence intensity apparently has a smaller influence on the overall flame growth within the range studied. Figure 4.6b shows that increasing u' by changing the

[1] $M = 2.0$ kernels are slightly smaller than $M = 1.75$ kernels and this is most likely due to the smaller turbulence intensity in that case (see Table 2.1).

turbulence generator results in smaller initial kernel size and slightly faster growth. At $\Delta t_{ign} = 90\,\mu s$, the hole-grid turbulence generator (black squares) produces kernels that are 11-15% smaller than the other two generators and at late times the kernels are $\approx 7\%$ larger than the other two. In addition, Figure 4.7 shows that the choice of turbulence generator has a direction-dependent effect on AR. In comparison to the nominal case, the aspect ratio growth is slightly smaller for the no grid case and slightly larger for the biplanar grid case. These differences are quantifiable but minor when compared to the overall growth of the flame. Perhaps this is unsurprising when comparing $u'/S_{L,0}$, which varies only a small amount between these cases $(6.23 - 7.52)$. The weak dependence of kernel size on turbulence intensity is not surprising considering the large scale eddies are nearly frozen and are of the same scale as the kernel diameter or larger. As a result, they are primarily responsible for convecting the entire kernel rather than wrinkling it, especially at early times.

At first glance, one may consider the effect of turbulence on kernel growth negligible, however the situation is slightly more complicated for several reasons. For example, u' and L_{11} are not sufficient to describe the influence of turbulence on the flame. In general, the flame can respond with differing sensitivity to the entire range of wavenumber content. A simple solution to this problem can be found in Abdel-Gayad *et al.*'s [33] introduction of the effective RMS velocity, which integrates the wavenumber spectra from the smallest measurable scales to the largest scales expected to influence the flame. The smallest scales are limited by the PIV spatial resolution, hence we integrate the wavenumber spectra from the spatial resolution limit to the kernel radius when calculating u'_{eff}. For case 3, u'_{eff} increases from $\approx 0.9 - 1.8$ m/s, meaning the flame is exposed to a broader range of scales as it travels downstream. In addition, the eddy turnover time for the smaller scales are easily an order of magnitude smaller than the large scales ($\tau_e = L_{11}/u' \approx 2.2$ ms for the large scales) and, hence have sufficient time to interact with the flame. Finally, Figure 4.5 shows a very repeatable ignition event (thin flame brush) followed by an ever more

wrinkled flame downstream (growing flame brush thickness). Hence, kernels are exposed to a turbulent field that does indeed wrinkle the flame and modify the average growth rate. However, the growth appears to be driven predominately by another phenomena.

A larger variation in $u'/S_{L,0}$ can be achieved by varying ϕ. Figure 4.6c shows the effect of reducing ϕ from 1.0 (black squares) to 0.7 (red downward triangles). Unsurprisingly, at $\Delta t_{ign} = 90$ μs, reducing ϕ has very little effect on the kernel size because the size and shape are almost entirely driven by the ignition process at that time, and hence the kernel size is nearly independent of the fuel concentration. At $\Delta t_{ign} = 154$ μs, ϕ begins to have an affect on the flame kernel size, with the size decreasing slightly with ϕ. Although even under non-fueled conditions ($\phi = 0$, black star), the plasma kernel is still quite large. Later, ϕ has a larger effect: the flame kernel size decreases by 14.3% as ϕ drops from 1.0 to 0.7 at $\Delta t_{ign} = 595$ μs. As an extreme example, at $\Delta t_{ign} = 680$ μs and for non-fueled conditions ($\phi = 0$), a thermal edge can still be found in schlieren images but those edges are faint and the kernel size is small. Under those conditions the hot spot is 1/3 the size of its reacting counterpart on average, and in 30% of the images no edge could be found. Therefore, the kernel growth is clearly strongly dependent on the fuel content. Further, reducing ϕ has little effect on AR in Figure 4.7. These results suggest that the overall effect of reducing ϕ is a reduction in the flame kernel size with no preferred direction.

The observations above lend proof to the idea that supersonic flame kernels are self-propagating and respond to the equivalence ratio and turbulence intensity in expected ways. Interestingly, the 2D kernel shape appears to have a Mach number dependency. The most likely explanations for this dependency are 1. a morphology difference due to the Mach number effect on the Mach angle and/or 2. complex flame topology which cannot be discerned in line of sight (LOS) schlieren images.

4.3 One-Dimensionally Expanded Flame Kernels: Baroclinicity and The Reacting Vortex Ring

In the previous section, it is shown that supersonic flame kernels exposed to a mean flow expansion are self propagating and have a Mach number dependent shape. However, it is not clear how the flame interacts with expansion waves to produce these observations nor is it obvious through which mechanism the Mach number affects the shape. Without confinement, the Navier-Stokes equations are Galilean invariant [140] therefore we may expect subsonic and supersonic kernels to propagate in a similar fashion[2], i.e., with a comparable growth rate under identical (local) turbulence and chemical conditions. However, the supersonic situation is unique because the diverging wall boundary condition induces vorticity modification through dilatation and baroclinic torque (second and third terms on the RHS of Equation (1.18), repeated below for convenience. In this section we discuss how these interactions form a reacting vortex ring, modify the AR, and ultimately enhance flame surface growth.

$$\frac{D\boldsymbol{\omega}}{Dt} \approx (\boldsymbol{\omega}\cdot\boldsymbol{\nabla})\boldsymbol{u} - \boldsymbol{\omega}(\boldsymbol{\nabla}\cdot\boldsymbol{u}) + \frac{\boldsymbol{\nabla}\rho\times\boldsymbol{\nabla}P}{\rho^2} \tag{1.18}$$

The expansion wave interaction is modeled with a one-dimensional isentropic solution applied separately to the reactants and products. This simple model, already described in Section 4.1 for the mean flow velocity, requires mechanical equilibrium for a meaningful definition of the local static temperature and pressure after interaction with an expansion wave. Mean flow expansion occurs over pairs of Prandtl-Meyer expansion fans emanating from the turning corners. The expansion fans reflect off of the walls, hence, the flame interacts with several discrete expansion waves as it convects downstream. When a wave

[2]While the NS are Galilean invariant, the boundary conditions are not. However, utilizing fairly simple arguments, one can easily see that supersonic inflow and outflow boundary conditions cannot influence the flame. Therefore, there should be very little difference between freely propagating subsonic and supersonic flame kernels given similar chemical and flow conditions and given that the kernels are sufficiently far from the walls.

encounters the flame surface, it reflects and refracts upon interaction with the interface due to the acoustic impedance mismatch between products and reactants [141]. The interaction can be simplified by assuming that a plane acoustic wave, having a form that is itself a solution of the linear acoustic equations, encounters a planar interface between the fluids. Next, the internal boundary conditions of matched normal particle velocity and matched total pressure are imposed at the interface. Then the pressure-amplitude reflection coefficient $\mathcal{R}$, which is defined as the ratio of the Fourier transform of the reflected to incident wave, is given by [141]:

$$\mathcal{R} = \frac{Z_b - Z_u}{Z_b + Z_u} \tag{4.6}$$

where Z refers to the acoustic impedance ($Z = \rho a$), a is the speed of sound and the subscripts u and b refer to the unburned and burned gases. A value of $|\mathcal{R}|$ less than one indicates that part of the acoustic energy is transmitted into the products. Alternatively, the pressure amplitude transmission coefficient $\mathcal{T}$ is given by $\mathcal{T} = 1 + \mathcal{R}$. In these studies $\mathcal{T} \approx 0.57$ for typical reactant and burned gas conditions, and since $\mathcal{T} < 1$, the kernel is under-expanded with respect to the reactants and must expand further to achieve mechanical equilibrium. In general, this is a rate-process, requiring some time to reach equilibrium. However, if the reverberation time, $\tau_r = \langle R \rangle / a_b$ [83], is much smaller than the convective time between expansion waves, $\tau_c = \Delta x_{exp}/U$, then the kernel will reach mechanical equilibrium quickly between expansions and can be considered in quasi-mechanical equilibrium with the reactants. Here, Δx_{exp} is the distance between expansion waves (calculated using the tunnel geometry and the expansion wave angle, equal to the local Mach angle) and U is the local reactant velocity. In these studies, $\tau_r \approx \tau_c/15$ and hence, the assumption of instant mechanical equilibrium between expansions appears valid.

With mechanical equilibrium established, we now return to the 1D isentropic model. The solution will be used to predict the result of flame kernel-expansion interaction. As the fluid convects downstream, the local static pressure/temperature drop and velocity in-

Table 4.1: Predicted flame-reactant velocity slip at $\Delta x_{ign} = 460$ mm.

Conditions	$U_{f,l} - U_l$
$M = 1.50$, $\phi = 1.0$	65.5 m/s
$M = 1.75$, $\phi = 1.0$	57.5 m/s
$M = 2.00$, $\phi = 1.0$	48.9 m/s
$M = 1.75$, $\phi = 0.9$	50.5 m/s
$M = 1.75$, $\phi = 0.8$	43.4 m/s
$M = 1.75$, $\phi = 0.7$	35.0 m/s

creases due to expansion. The local product velocity ($U_{f,l}$) and local reactant velocity (U_l) are estimated via Equation (4.3) using γ and R specific to the products and reactants, respectively. Owing to the differences in γ and R between the reactants and products and to a larger stagnation temperature in the flame, the difference $U_{f,l} - U_l$ is greater than zero and increases in the downstream direction. The predicted velocity slip ($U_{f,l} - U_l$) at 480 mm is shown in Table 4.1. The slip depends on M and ϕ, decreasing slightly as M increases and decreasing more so as the product temperature is reduced (i.e lower ϕ). Apparently the flame kernel experiences a rather large impulse that sets it into motion with respect to its surroundings.

The 1D model does not take into account the kernel shape nor the fact that it is surrounded by slower, unreacted fluid. Clearly, the faster moving products will lose momentum to the surrounding reactants. Hence it would not be surprising if the model over predicts the velocity slip. Figure 4.8a shows a single reacting PIV image from case 3 ($M = 1.75$, $\phi = 1.0$) at $\Delta t_{ign} = 710$ μs and $\Delta x_{ign} \approx 460$ mm. The reactant velocity is $U_l \approx 660$ m/s, which is nearly identical to the value predicted by the 1D model. The kernel velocity is not uniform so it is hard to define the kernel velocity. However, at a maximum the velocity slip is $U_{f,l} - U_l \approx 30$ m/s, which is still 27.5 m/s smaller than the value predicted by the model. Two explanations for the discrepancy are available: (a) the flame is not adiabatic and temperature loss results in smaller product acceleration and/or (b) the veloc-

ity slip is diminished through hydrodynamic action. Chen [142] showed that the radiative loss in laminar spherical flames was as large as 200 K in one case, which is large enough to cause a significant reduction in the predicted velocity slip. In his study, heat loss occurred over 10's of ms. However, the flow-through time in this study is less than 1 ms. Therefore it is unlikely that supersonic flame kernels experience anywhere close to this level of radiative heat loss. Furthermore, in order to bring the 1D model into agreement with the observation requires ≈ 500 K loss. This is unlikely based on the previous discussion so, it is reasonable to conclude that heat loss does not cause the observed difference.

To further explore the idea that fluid dynamics inside the kernel are responsible for the difference between the predicted and observed reactant-product velocity slip, the vector field is shown overlaid on the flame kernel in Figure 4.8a and a simplified sketch is shown in Figure 4.8b. There is an acceleration on the windward (left) side of the kernel and deceleration on the leeward (right) side. Upstream, velocity-slip induces reactant entrainment into the kernel core. Downstream, the burned gas imparts momentum to the slower moving reactants, resulting in momentum loss and flow divergence. At the top and bottom reactant-product interfaces, the velocity slip induces vorticity. A counter-rotating vortex pair (CRVP), the result of this induced vorticity, appears at the top and bottom interfaces, slightly skewed towards the windward side. This result is qualitatively similar to the classic shock-helium bubble interaction, but in this case the bubble moves quicker than the surroundings[3] [83, 100, 143, 144]. While non-reacting, the kernel development is similar to these studies because the Atwood number ($At = (\rho_1 - \rho_2)/(\rho_1 + \rho_2)$), a parameter that drives the growth rate of impulsively accelerated interfaces [145], is matched. Further, in one of Haas and Sturtevant's cases the pressure change across the shock is roughly equal to the reciprocal of the total pressure change in these studies ($1/(P_2/P_1) \approx 1.28$); therefore, we should expect similar kernel (bubble) evolution. Clearly the 1D model, while useful

[3]Most shock-bubble studies use a stationary bubble and moving shock. With a simple change of reference frame, one can easily see that this situation is exactly opposite the expansion accelerated kernel used in this study.

for predicting the magnitude of the velocity slip, cannot capture the complex three dimensional velocity field within the flame kernel. It is not surprising, therefore, that the model overpredicts the experimentally observed velocity slip. Incidentally, the dependence of AR on M is most likely due to the dependence of expansion wave angle on M and the resulting differences in the internal fluid dynamics of $M = 1.5$, 1.75, and 2.0 flame kernels.

When the kernel (or bubble) travels through an expansion it is impulsively accelerated. Figure 4.9 shows a cartoon comparison of flame kernels with and without a mean pressure gradient. Vorticity is deposited at the surface and an instantaneous velocity slip imparted. A CRVP is formed on the top and bottom side of the kernel. While not directly observed, previous studies [83, 100, 143, 144] suggest that the CRVP is a 2D observation resulting from a large-scale 3D vortical motion (vortex ring) that feeds off of the velocity slip. A vortex ring cannot be experimentally observed with the diagnostics used, however, Chapter 5 will explore this idea and definitively shows that kernels exposed to mean expansion do indeed become reacting vortex rings. The theoretical model under predicts the velocity slip because it does not account for the transfer of axial momentum into the cross-stream directions. The overall effect is entrainment of reactants into the flame zone and fine scale wrinkling at the surface. These effects will no doubt have an effect on the turbulent flame speed, as is discussed below.

4.4 Flame Speed Scaling for Supersonic Flame Kernels

Whether or not turbulent flame speeds derived from supersonic flame kernel growth match well established correlations for subsonic flames is of primary importance to the more general problem of identifying supersonic flame regimes and quantifying how supersonic flames scale with flow field and chemical parameters. In this section we investigate whether the Chaudhuri [64] scaling, shown in Equation (1.10), is a reasonable relation for supersonic flame kernels exposed to a mean expansion. Several compressibility-specific corrections to the flame growth rate are needed, however, before making this comparison.

Mean flow compressibility modifies the thermodynamic variables so that derived properties such as S_L or δ_L become a function of the axial location. For the specific case of steady mean flow expansion, the local static temperature and pressure drops, resulting in reduced S_L, larger δ_L, and a positive dilatation on the flame area. The later appears as an artificially enhanced growth rate and should therefore be corrected prior to calculating S_{TD}. The 1D isentropic flow model has already been shown to properly capture the velocity change in the reactants where S_L and δ_L are defined. Therefore, to account for the change in S_L and δ_L, the 1D model is again used to calculate the local static mixture properties in the reactants. Cantera solutions for S_L and δ_L are tabulated over the range of possible static temperature and pressure conditions. A least squares quadratic curve fit is used to identify the functional dependence of the derived parameters on temperature and pressure. The local S_L and δ_L are then formed using the local thermodynamic conditions and the curve fit. S_L and δ_L vary approximately 10% from the inlet to exit. A similar procedure is followed for $\delta_{M,b}$, but with one caveat: archived data for $\delta_{M,b}$ do not exist for the exact conditions in these studies. Therefore, a least squares quadratic curve fit to the data in Gu *et al.* [121] is used with T_s, P_s and ϕ as independent variables; a linear extrapolation was required for P_s because its value in these studies ($50 - 75\ kPa$) is outside the range used in Gu *et al.* [121] ($100 - 1000\ kPa$).

The apparent increase in the flame radius due to mean flow dilatation can be corrected through a simple mass conservation argument. The products within the kernel have a well defined edge at the flame and, as the density drops due to expansion, the kernel volume dilates to satisfy mass continuity, i.e., $\rho_1 \mathcal{V}_{b,1} = \rho_2 \mathcal{V}_{b,2}$. Here, the subscripts 1 and 2 refer to the conditions before and after an expansion and $\mathcal{V}_b$ refers to the burned/product volume. Assuming a spherical kernel, $\mathcal{V}_b = 4/3\pi\langle R\rangle^3$. Rearranging for $\langle R_2\rangle$ yields:

$$\langle R_2\rangle = \langle R_1\rangle \sqrt[3]{\frac{\rho_1}{\rho_2}} \tag{4.7}$$

The density ratio is calculated using the 1D isenstropic flow model applied to the kernel.

At the latest times, the correction reduces the radius by less than 7%.

With the proper modifications to flame radius and thermodynamic mixture properties made, the turbulent flame speed can now be compared to Chaudhuri *et al.*'s [64] flame bomb data. The normalized global displacement speed, S_{TD}, is calculated using Equation (1.17), repeated below for convenience:

$$\frac{S_{TD,0.5}}{\overline{S_L}} = \frac{2\Theta}{\Theta+1}\frac{1}{\overline{\overline{S_{L,b}}}}\frac{\left\langle R_0 \right\rangle^2}{\left\langle R_{0.5} \right\rangle^2}\frac{d\left\langle R_0 \right\rangle}{dt} \tag{1.17}$$

The ratio of radii at $c = 0.5$ and $c = 0$: $\left\langle R_0 \right\rangle / \left\langle R_{0.5} \right\rangle = 4/3$ is suggested by Bradley *et al.* [53] and is adopted here. To account for flame stretch in the denominator of the RHS of Equation (1.17), the simple linear model originally proposed by Markstein is used [65]:

$$S_L = S_{L,0}\left[1 - \delta_M \kappa_g\right] \tag{4.8}$$

where the ensemble averaged global curvature for spherical flames of size $\langle R \rangle$ is given by:

$$\kappa_g = \frac{1}{\langle R \rangle} \tag{4.9}$$

At each location, the local turbulent properties (see Chapter 4.1) are used for the correlation. The following analysis considers the global displacement speed as given by Chaudhuri *et al.* [54]. Their derivation requires the assumption of a mean spherical flame. Hence, an underlying assumption is no preferential direction for flame growth, and therefore the flame speed can be directly related to the average radius growth. Other flame speed definitions were explored in this work (for example those based on growth of kernel width and height); however, no meaningful trends were found using these definitions. This is due, in part, to the complex and evolving flame topology that expanded supersonic kernels exhibit (which are beginning to take on a toroidal shape at the latest times). Hence, using the definition in Chaudhuri *et al.* [54] is questionable. However, a more consistent definition would require an understanding of the 3D kernel topology which is not readily available from the

line of sight and planar diagnostics used in these experiments. Therefore Equation (1.17) is adopted, despite the limitations and potential bias. This definition essentially averages the growth rate in the x-y directions, but ignores any enhancement or impairment of the global displacement speed due to complex three dimensional flame topology. This topic is revisited in Chapter 6 where the full three dimensional flame topology becomes available using validated numerical simulations.

Figure 4.10 shows S_{TD} versus ${Re_T}^{1/2} = \left[\frac{u'_{eff}}{S_{L,b}}\frac{\langle R \rangle}{\delta_{M,b}}\right]^{1/2}$ for the various conditions listed in Table 2.3. For any given condition, the normalized displacement speed appears to be constant versus ${Re_T}^{1/2}$. This is due to the nature of the curve fit performed on the $\langle R \rangle$ data that was previously shown in Figure 4.6. The data are too sparse to discern any higher order functional dependency, therefore, a linear curve fit is selected. Hence, both $d\langle R \rangle/dt$ and S_{TD} are constant. Further, the thermal expansion, Θ, is also constant. Therefore, $S_{TD,0.5}/\overline{S_L}$ only varies as $\overline{S_{L,b}}$ varies downstream. The evolution of $\overline{S_{L,b}}$ is nearly constant as well because, as the stretch rate reduces downstream, $\overline{S_{L,b}}$ increases, but the temperature drops, reducing $\overline{S_{L,b}}$. Therefore, $S_{TD,0.5}/\overline{S_L}$ does not very much for any given dataset. This becomes problematic when trying to discern the effects of M, ϕ, and u'. However, if all of the data are considered as being part of a single dataset, then it appears as though $S_{TD,0.5}/\overline{S_L}$ scales linearly with ${Re_T}^{1/2} = \left[\frac{u'_{eff}}{S_{L,b}}\frac{\langle R \rangle}{\delta_{M,b}}\right]^{1/2}$. This description has a clear disadvantage because the effect of Mach number on the turbulent flame speed scaling cannot be discerned. This limitation is resolved in Chapter 6 using validated simulations.

The well-established atmospheric methane-air flame data from Chaudhuri *et al.* [64] (orange dots) is also shown in Figure 4.10. The Chaudhuri *et al.* data have a linear dependence on ${Re_T}^{1/2}$, as would be expected within the thin reaction zone. If the Chaudhuri *et al.* data are extrapolated to lower turbulent Reynolds number for the conditions in this study, then the correlation takes the value $S_{TD,0.5}/S_L \approx 2-3$, which corresponds to $S_{TD,0.5} \approx 1.2-1.8$ m/s. This suggests that the kernel growth, if only considering the effect of turbulence-flame interaction, would only be 0.71 - 1.1 mm after the ignition transient.

Therefore, pure turbulent-flame interaction is responsible for at least part of the overall growth of the flame kernel. However, the supersonic flame speed appears larger for all conditions compared to the flame bomb data. The likely explanation for the discrepancy, and the one already discussed in the previous section, is that interaction with mean expansion, producing vorticity at the flame interface, modifies the growth rate of supersonic kernels. If this is the case, then another scaling related to the velocity or size of the vortex ring, may better collapse the subsonic and supersonic data.

Assuming the vortex ring is responsible for the differences in S_T, a different hydrodynamic scale could be introduced in Equation (1.10) to improve the collapse. The kernel radius is the obvious choice for the length scale so attention is turned to the velocity scale. Upon interaction with an expansion wave, the burned mass is impulsively accelerated. The impulse velocity is short-lived and not particularly relevant to the flame development except, of course, for its responsibility in setting the kernel into motion. Vortex rings propagate with a velocity that is, in part, a function of the initial impulse velocity [146]. This vortex ring propagation velocity (U_T) is, at the vortex edge, the best measure of the velocity slip at the reactant-product interface, which produces additional flame surface through the Kelvin-Hemholtz instability [147]. The vortex propagation velocity is also likely related to the global entrainment of reactants into the kernel at the windward flame surface. Therefore, replacing u'_{eff} with U_T in the flame speed scaling is investigated next.

Data on the formation of vortex rings from steady acceleration of flame kernels are not available, but for a thick vortex ring formed with a piston driven system, U_T is [148]:

$$\frac{U_T}{U_p} = \frac{3+\pi}{4\pi} - \frac{3+\pi}{3\pi^2}\frac{D}{L} \tag{4.10}$$

where U_p is the driving velocity, and D/L are the piston diameter and length. This equation is applied to the supersonic kernels with the assumptions $D/L = 1$ (assuming a spherical kernel) and the driving velocity is equal to the experimentally derived slip velocity (≈ 30 m/s for $M = 1.75$, $\phi = 1.0$ at 710 μs). With these assumptions, $U_T \approx 8.4$ m/s for case 3.

Reacting PIV data are not available for the remaining cases, so $U_T \approx 8.4$ m/s was used for all eight cases with the understanding that the value of U_T could vary from case to case and from time to time. Validated simulations, where the time dependent propagation velocity is available for all cases, are discussed in Chapter 6.3. Replacing u' with U_T in Equation (1.10) results in:

$$\frac{S_T}{S_L} \propto \left[\frac{U_T}{S_{L,b}} \frac{\langle R \rangle}{\delta_{M,b}} \right]^{\frac{1}{2}} \tag{4.11}$$

Figure 4.11 shows the new flame speed scaling using U_T. The supersonic data now appear to collapse on top of the low speed data. This may be fortuitous given the rough approximation of U_T above. However, a more important point is that the slope roughly matches the subsonic data suggesting a universal scaling may be possible.

Universal scaling of the turbulent flame speed in supersonic flows apparently requires several corrections for flame-compressibility interaction. In the case of a flame kernel exposed to a mean expansion, the flame growth is driven predominantly by the ensuing vortex ring motion and flame-turbulence interaction plays a secondary role. Hence the appropriate hydrodynamic scales for supersonic flame kernels interacting with a mean expansion are the flame radius and vortex ring propagation velocity. The propagation velocity is a function of the velocity slip, which itself is a function of the Mach number and expansion rate. Therefore, when supersonic kernels are exposed to mean flow expansion, the scaling for S_{TD}/S_L has a pseudo Mach number dependence that must be accounted for. Several points of caution are offered here. First, it was assumed that the velocity slip data were similar between case 3 and the others. This assumption is required when only considering the experimental data because reacting PIV was only collected for case 3. More data for other M and ϕ cases would be required to confirm this observation. Numerical simulation presented in Chapter 6 support the assumption that U_T is nearly constant across cases. Second, U_T may not be an inappropriate velocity scale for flame kernels. Additional data with differing expansion strengths would help answer this question. Finally, even if U_T is an

appropriate velocity scale, it does not guarantee universality in the scaling. The notion of universal scaling is further explored in Chapter 6.

4.5 Experimental-Numerical Comparison and Validation

This section discusses validation of numerical results against available experimental data. The validations presented here should not be confused with verification of the numerical methods and grid convergence, which were already discussed in Chapter 2.2. Three parameters are identified for comparison. These are the flow field mean and turbulence statistics, flame growth parameterized by the radius versus time, and flame-induced vorticity. If the three parameters match reasonably well between experiments and simulations, then the numerical results will be considered validated. Numerical simulations are performed for cases 3, 4, 5, and 8, which spans three Mach numbers and two equivalence ratios. The numerical conditions are specified in Table 2.4.

As brief recap for the large eddy simulations follows. A formally fourth-order-accurate explicit scheme is selected (see Section 2.2.3), where the inviscid flux is discretized using a ninth-order-accurate WENO scheme [125], and a fourth-order-accurate central scheme is used for the viscous terms. The time integration is performed using a low-storage version of the explicit fourth-order-accurate Runge-Kutta scheme. The SGS momentum and energy fluxes are closed using a subgrid eddy viscosity (ν_t) model, which is obtained using the local grid filter Δ and the subgrid kinetic energy k^{sgs} through: $\nu_t = C_\nu \sqrt{k^{\text{sgs}}} \Delta$. Here, C_ν is a model coefficient and k^{sgs} is obtained by solving an additional transport equation. The localized dynamic evaluation procedure is used to obtain C_ν and all other model coefficients [127, 128]. The SGS scalar fluxes are closed using an eddy-diffusivity ($D_t = \nu_t / Sc_t$, with Sc_t being the turbulent Schmidt number) based approach. The SGS turbulence-chemistry interaction is modeled using the algebraic partially stirred reactor (PaSR) [129]. A reduced four-step, eight-species methane-air mechanism [130, 131] is used to account for finite-rate kinetics. The mixture-averaged transport properties, the finite-rate kinetics source terms,

Case	M	ϕ	u'/S_{L0}	L_{11}/δ_L	$S_{L0}\ [m/s]$	$\delta_L\ [m]$
3n	1.75	1.0	7.42	20.8	0.60	4.8E-4
4n	1.50	1.0	7.42	20.8	0.60	4.8E-4
5n	2.00	1.0	7.42	20.8	0.60	4.8E-4
8n	1.75	0.7	13.0	14.3	0.34	7.0E-4

Table 2.4: Simulation parameters for the cases considered in this study.

and the thermally perfect gas based thermodynamic properties are obtained using Cantera [132].

The domain is discretized into approximately 300 million hexahedral cells with a nominal size of approximately (116 μm)^3. The inflow velocity boundary conditions were set to match the PIV results at window 1 for each Mach number. Hence, the mean velocity specified at the inlet matches the experimental mean velocity by default. However, the spatial evolution of the mean velocity could be different than experiments because the numerical domain is slightly different than the physical domain. In particular, the divergence angle is smaller in the numerical domain (see Figure 2.5). The simplification that leads to this angle reduction was already discussed in Chapter 2.2 and the accuracy of this simplification depends on how well the boundary layer thickness is estimated (using the 1D model discussed in Section 4.1). The kernel is initialized as a laminar spherical flame by mapping the 1D flame solution to spherical coordinates. Table 2.4 shows the numerical cases simulated.

Capturing the expansion strength and mean velocity is important in this problem because the pressure-density misalignment is one of the main drivers for flame growth. Therefore, if the spatial evolution of the mean velocity is not captured, then the flame growth and flame-generated vorticity will likely be inaccurate as well. Section 4.1 shows that the boundary layer grows at 0.45°, 0.425°, and 0.4° for $M_0 = 1.5, 1.75,$ and 2.0, respectively. These boundary layer thicknesses correspond to turning angles of 0.55°, 0.575°, and 0.6°. However, a consistent turning angle is desired to facilitate direct comparison between the

various numerical cases and to avoid the uncertainties that would arise if three different grids were used. Hence, 0.5° is selected for all numerical cases. A single turning angle may cause the mean velocity to differ from the experimental results, therefore, the spatial evolution of the mean velocity is checked to ensure that it is not significantly different from the experimental results. Figure 4.12 shows the evolution of the mean axial velocity comparing PIV and numerical results. The experiments and simulations are reasonably similar, and so we conclude that the estimated expansion angle is well selected.

Unlike the mean velocity, the turbulence properties set at the inflow purposely differ from the experiments in two ways. First, the RMS velocity fluctuation (u') is constant for all numerical cases; which facilitates comparison across those cases. The inflow u' is set to match the experimental value for case 3. Second, the isotropy is set to unity for all numerical cases, which is significantly different than the experimental cases. It has already been suggested here, and will be shown again in Chapters 5 and 6, that turbulence plays a secondary role to flame-generated vorticity when considering flame growth. Therefore, these changes should have little effect on the flame growth. Figure 4.13 shows u' and the isotropy u_1/u_2, both of which vary significantly across the PIV cases. Indeed, in all PIV cases there is significant anisotropy caused by the turbulence generation strategy. Turbulence is generated via a grid upstream of the converging-diverging nozzle, and it is well known that strong axial dilatation will transfer axial turbulent kinetic energy to the transverse directions [149]. Therefore, the experimental turbulent anisotropy is not surprising.

Flame growth is arguably the best statistic to compare numerical results because the rate of change of kernel size is directly related to the flame speed. Here, we consider the effective radius as defined in Equation (1.12). Experimentally, $\langle R_{c=0} \rangle$ is computed by ensemble averaging the 2D flame area from LOS schlieren measurements. The numerical results are first processed to yield numerical LOS schlieren images, which are then handled similarly to the experimental data. The output depends weakly on the numerical LOS technique used. In this analysis, the LOS binarized 460 K isocontour is picked because

it yields the most robust flame radius trend. Justification for this choice and investigation of other techniques is given in Appendix B.2. Figure 4.14 shows the kernel evolution for each numerical case. Similar to experimental schlieren images (shown in Figure 2.14), the numerical kernels grow downstream, are smaller for smaller ϕ, and appear to have Mach number dependent aspect ratios.

A comparison of the experimental and numerical effective flame radius versus Δt_{ign} is shown in Figure 4.15. The experimental data grow rapidly in the first 250 μs, a result of the ignition overdrive (discussed in depth in Chapter 3), which is not reproduced in the numerical data. At $\Delta t_{ign} > 250 \mu s$, there is very reasonable agreement between experiments and simulations, which suggests that the ignition overdrive most affects the flame within the first few hundred microseconds after ignition. As time increases, $\langle R_{0.05} \rangle$ increases for all cases, growing by approximately a factor of 2 before leaving the domain. The expected growth dependence on ϕ, i.e., that $\phi = 0.7$ kernels grow more slowly than $\phi = 1.0$ kernels, is also captured well in the numerical results. A small difference between $M = 1.5$ and $M = 1.75/2.0$ kernels can be seen in the numerical results, with $M = 1.5$ showing a slightly faster growth. However, this trend is not obvious when only considering the experimental data, which are more sparse.

It has already been shown in Section 4.3 that the kernel develops a counter rotating vortex pair (CRVP) in the reacting PIV images. Dissecting a vortex ring yields a CRVP and so the existence of the CRVP in experiments and simulations is a necessary condition for the existence of a vortex ring. Further, the CRVP, and vortex ring in general, act to increase the flame surface area, which in turn increases the flame speed. Therefore, the simulations must capture this feature of flame kernels flowing in a supersonic expanding flow field. Figure 4.16 shows a comparison between PIV and simulations for case 3 at $\Delta t_{ign} \approx 700$ μs. The results are post processed for spanwise vorticity (ω_z), and the 460 K isocontour is overlaid on the numerical result to indicate the flame position. While the experimental data are more noisy, the two results are quite similar. The upper and lower

flame edge are easy to identify in the experimental vorticity field because ω_z is maximized and minimized here, respectively. However, the windward and leeward flame edges are harder to identify because there is very little vorticity generated in those locations. Hence the experimental flame shape is difficult to identify, but it does appear to be qualitatively similar to the numerical result in that the flame is taller than it is wide and has a kidney-bean shape. A counter rotating vortex pair (CRVP) appears in both. Further, the vorticity magnitude is $\approx 6.5 \times 10^4 / s$ in both the experiments and simulations, showing a quantitative agreement for the flame-induced vorticity.

4.6 Summary of Flame Kernel Experiments

In this chapter, experimental results of turbulent premixed flames in supersonic flows with mean expansion are shown. This new premixed flame configuration is unique in that a well defined expansion (or compression if using a shock generator) can be imposed on the flame, which allows the flame-compressibility interaction to be systematically studied. These results demonstrate the feasibility of generating self-propagating flame kernels in a supersonic flow. Further, it is shown that this is an effective configuration for flame speed studies. Upon interacting with an expansion wave, the flame kernel produces a counter rotating vortex pair, which enhances the mass burning rate. It is not possible to discern the flame topology using the results presented, but evidence is presented to suggest the flame evolves into a reacting vortex ring. This idea is further explored in Chapter 5 using the validated simulation results.

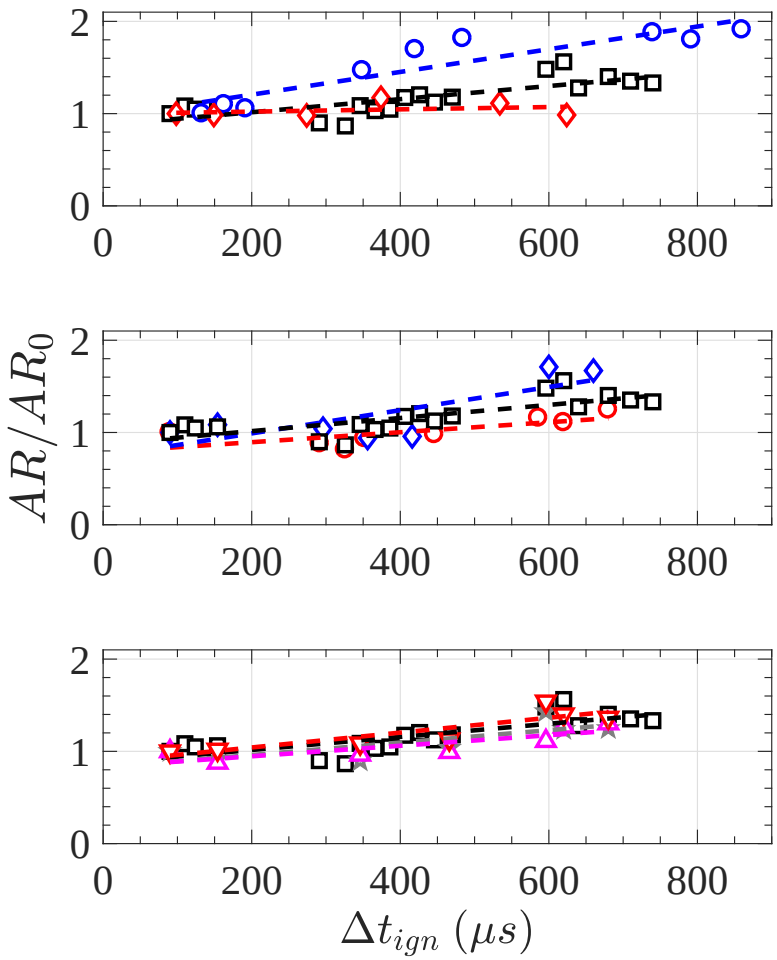

Figure 4.7: Time evolution of kernel aspect ratio normalized by the value at the earliest Δt_{ign}. (Top) effect of Mach number, (Middle) effect of turbulence condition, (Bottom) effect of ϕ. Case 1 ($M = 1.75$, $\phi = 1.0$, No Grid): red circles, case 2 ($M = 1.75$, $\phi = 1.0$, Biplanar Grid): blue diamonds, case 3 ($M = 1.75$, $\phi = 1.0$, Hole Grid): black squares, case 4 ($M = 1.5$, $\phi = 1.0$, Hole Grid): blue circles, case 5 ($M = 2.0$, $\phi = 1.0$, Hole Grid): red diamonds, case 6 ($M = 1.75$, $\phi = 0.9$, Hole Grid): gray stars, case 7 ($M = 1.75$, $\phi = 0.8$, Hole Grid): magenta upward triangles, case 8 ($M = 1.75$, $\phi = 0.7$, Hole Grid): red downward triangles. Corresponding case data are defined in Table 2.3.

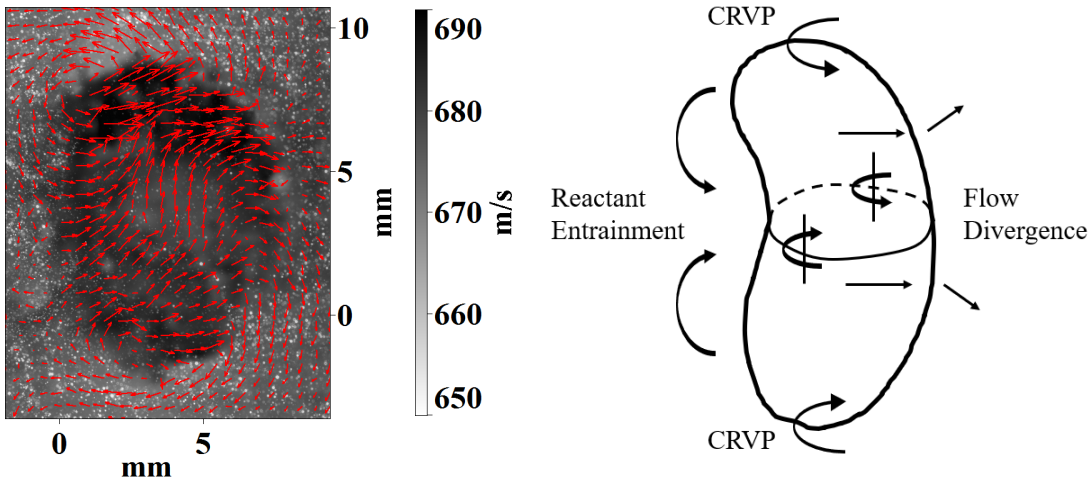

(a) Instantaneous PIV image of flame kernel.

(b) Cartoon of flame kernel

Figure 4.8: Reacting PIV and cartoon image for a single flame kernel exposed to mean flow expansion. Reacting PIV was for a single $M_0 = 1.75$, $\phi = 1.0$ flame kernel with $U_{f,l} \approx 690$ m/s in a $U_l \approx 660$ m/s flow. Vectors are superimposed on the raw Mie scattering image with reversed velocity color mapping (light to dark) for easier viewing. Vectors are plotted relative to the average. $\Delta t_{ign} = 720$ μs, $\Delta x_{ign} \approx 460$ mm.

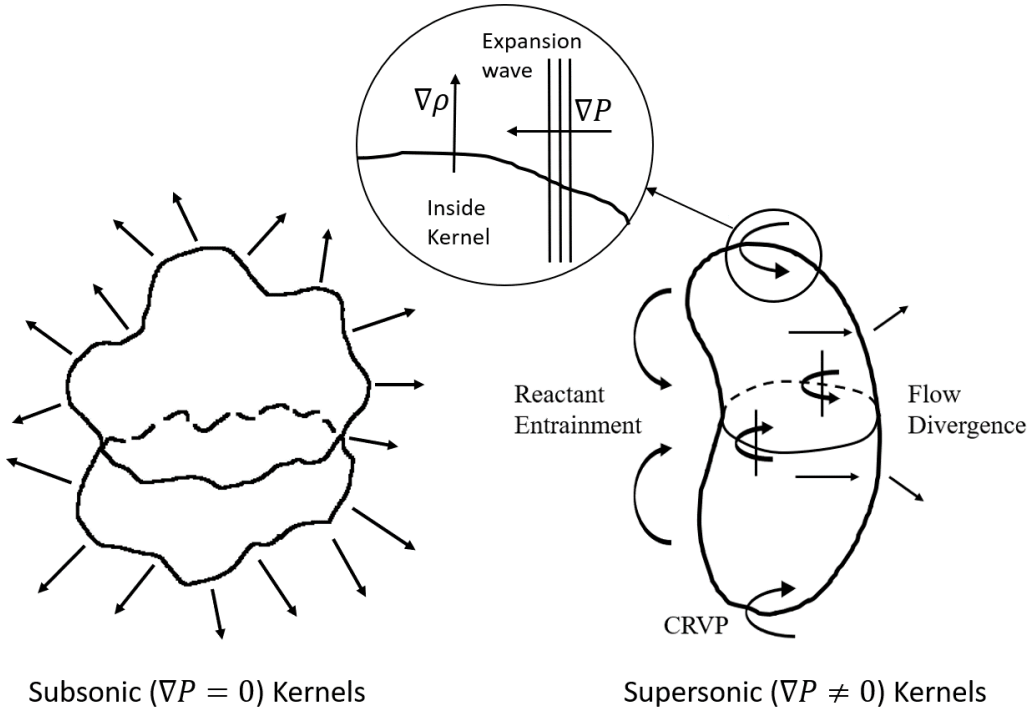

Figure 4.9: Comparison of flame kernel shape in a pressure gradient free flow versus flows with a mean pressure gradient, such as supersonic flow with mean expansion.

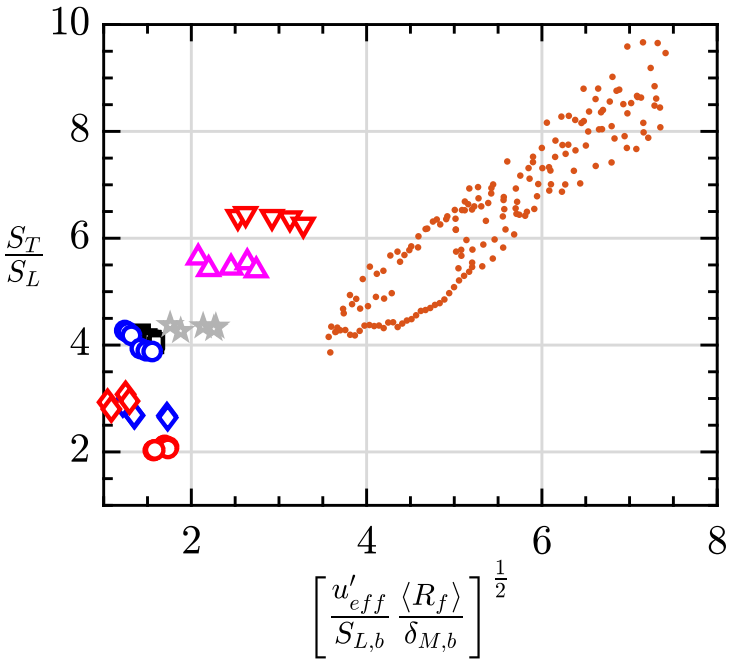

Figure 4.10: Normalized turbulent flame speed versus turbulent Reynolds number. Orange dots: $\phi = 0.9$, 1 atm flame bomb data of Chaudhuri *et al.* [64]. Refer to Table 2.3 for experimental conditions.

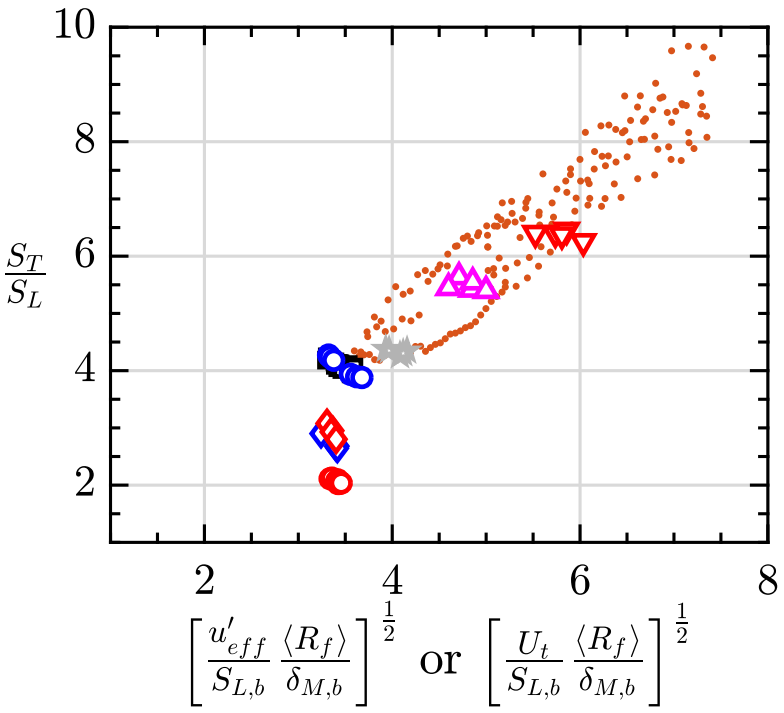

Figure 4.11: Normalized turbulent flame speed versus turbulent Reynolds number. Orange dots: $\phi = 0.9$, 1 atm flame bomb data of Chaudhuri *et al.* [64]. The velocity scale is the vortex ring propagation velocity U_T for this work and u'_{eff} for Chaudhuri *et al.*'s data. Refer to Table 2.3 for experimental conditions and symbol definitions.

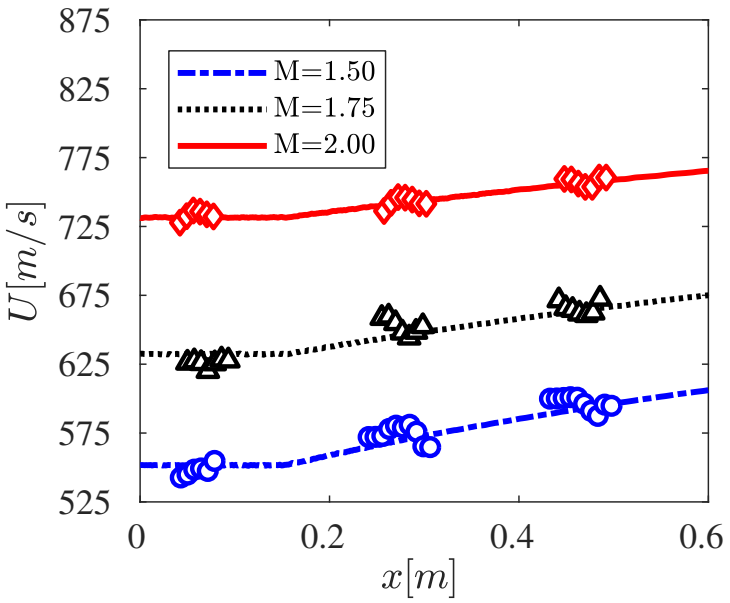

Figure 4.12: Evolution of mean axial velocity U along the axial (x) direction. Lines are simulation results and symbols are time averaged center line PIV data. PIV data are sub sampled to improve visualization.

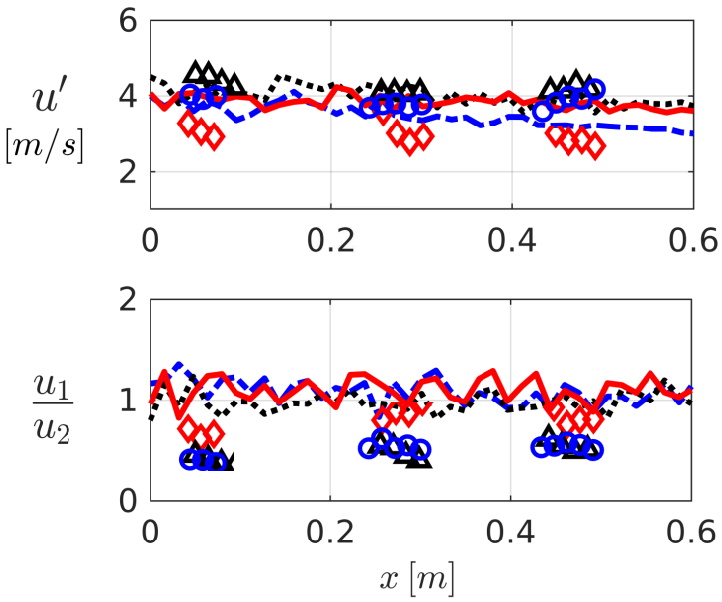

Figure 4.13: RMS velocity (u') and isotropy velocity statistics along the axial (x) direction. Lines are simulation results and symbols are time averaged center line PIV data. Case 3 ($M = 1.75$, $\phi = 1.0$, Hole Grid): black upward triangles, case 4 ($M = 1.5$, $\phi = 1.0$, Hole Grid): blue circles, case 5 ($M = 2.0$, $\phi = 1.0$, Hole Grid): red diamonds.

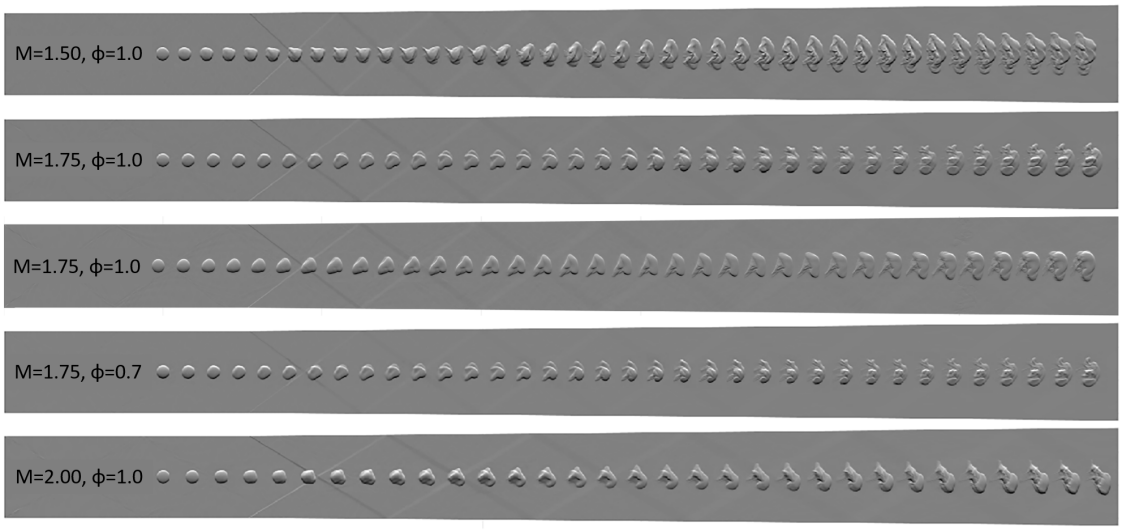

Figure 4.14: Numerical schlieren for cases 4n, 3n(a), 3n(b), 8n, and 5n (top to bottom).

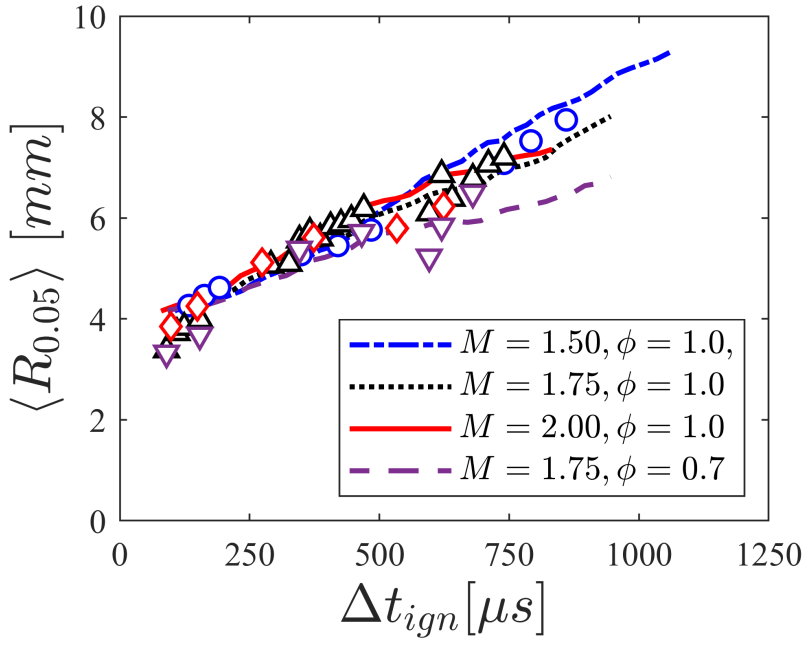

Figure 4.15: Effective kernel radius versus Δt_{ign} derived from schlieren images for experiments (symbols) and simulations (lines).

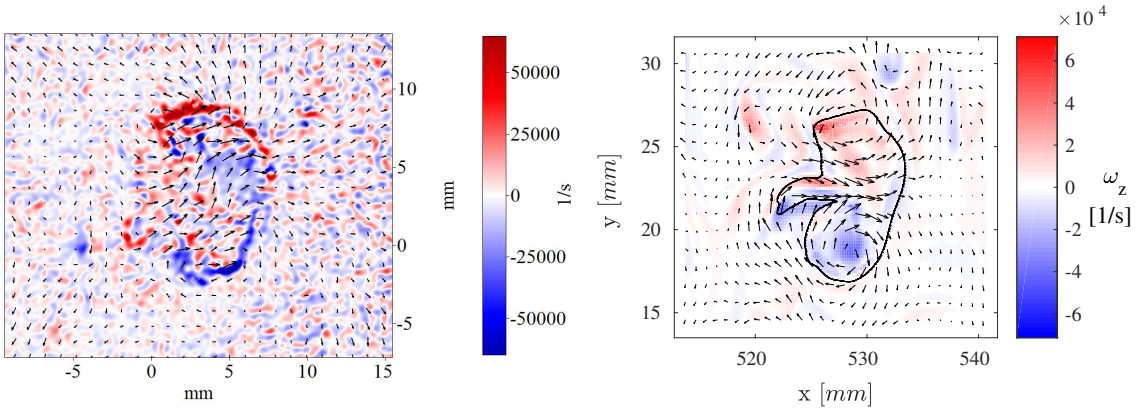

(a) Reacting PIV.

(b) Numerical results.

Figure 4.16: Instantaneous spanwise (ω_z) vorticity and relative velocity vector field from experiment (left) and simulation (right) at $\Delta t_{ign} \approx 700\ \mu s$ for case 3.

CHAPTER 5
TOPOLOGY AND EVOLUTION OF SUPERSONIC FLAME KERNELS EXPOSED TO MEAN EXPANSION

Experimental observations of supersonic premixed flame kernels were presented in Chapter 4. Several hypothesis about how flame kernels evolve when interacting with mean compressibility were offered. In this chapter, the hypothesis that flame kernels morph into reacting vortex rings is explored using theoretical and numerical analyses. Sufficient evidence is given to support the reacting vortex ring hypothesis.

Once the reacting vortex ring is established, the numerical data are used to further scrutinize the burned volume growth. The definition of the flame edge is discussed, including the effect of the progress variable (c) and line of sight (LOS) versus volumetric measurements. The numerical data show that the diagnostic technique can greatly impact the calculated flame size.

5.1 The Role of Baroclinic Torque

The density discontinuity across the flame can generate vorticity when interacting with a pressure wave through the baroclinic torque term on the right hand side of the compressible vorticity equation:

$$\frac{D\boldsymbol{\omega}}{Dt} \approx (\boldsymbol{\omega}\cdot\boldsymbol{\nabla})\boldsymbol{u} - \boldsymbol{\omega}(\boldsymbol{\nabla}\cdot\boldsymbol{u}) + \frac{\boldsymbol{\nabla}\rho\times\boldsymbol{\nabla}P}{\rho^2} \tag{1.18}$$

In order to ascertain if the 2D vortex pair identified in the planar reacting PIV images (Figure 4.8) is a counter-rotating vortex pair (CRVP) or 2D slice of a vortex ring, the magnitude and direction of the baroclinic torque is estimated for a hypothetical spherical density discontinuity interacting with a single pair of $M_0 = 1.75$ expansion waves. Expanding the

baroclinic torque term yields:

$$\begin{aligned}\frac{\nabla\rho\times\nabla P}{\rho^2} =& \frac{\hat{i}}{\rho^2}\left(\frac{\partial\rho}{\partial y}\frac{\partial P}{\partial z}-\frac{\partial\rho}{\partial z}\frac{\partial P}{\partial y}\right)- \\ & \frac{\hat{j}}{\rho^2}\left(\frac{\partial\rho}{\partial x}\frac{\partial P}{\partial z}-\frac{\partial\rho}{\partial z}\frac{\partial P}{\partial x}\right)+ \\ & \frac{\hat{k}}{\rho^2}\left(\frac{\partial\rho}{\partial x}\frac{\partial P}{\partial y}-\frac{\partial\rho}{\partial y}\frac{\partial P}{\partial x}\right)\end{aligned} \tag{5.1}$$

The partial derivatives of density are calculated assuming a laminar spherical flame with a density discontinuity of $(\rho_1 - \rho_0)$ over the laminar flame thickness (δ_L). The subscripts 1 and 0 refer to the burned and unburned conditions, respectively. The density discontinuity is directed normal to the surface and positive outward (because the products are lighter than the reactants). The pressure discontinuity is set equal to the pressure change across the turning corner over a thickness estimated from the tunnel geometry by using the pressure rise across a Prandtl-Meyer expansion fan. One pressure wave emanates from the top turning corner and another from the bottom. The waves are oriented at the local Mach angle, therefore, the pressure waves are 2D planar waves in the $\hat{i}-\hat{j}$ plane.

Equation (5.1) is used to estimate the magnitude of the baroclinic torque term for a $M = 1.75$, $\phi = 1.0$ laminar spherical flame traveling in the axial direction. Figure 5.1 shows the result for the three components of the rate of change of the vorticity at the kernel surface. Interestingly, there is no net ω_x deposited by the interaction of the hypothetical flame and expansion waves. Looking closer at ω_x, only the second term of $\frac{\hat{i}}{\rho^2}\left(\frac{\partial\rho}{\partial y}\frac{\partial P}{\partial z}-\frac{\partial\rho}{\partial z}\frac{\partial P}{\partial y}\right)$ is maintained because $\frac{\partial P}{\partial z} = 0$. Given the remaining term, it becomes obvious that the positive going wave ($\frac{\partial P}{\partial y}$) always cancels the negative going wave. Hence, ω_x must equal zero when the waves are of equal strength and when the density discontinuity has a uniform spherical shape. In contrast, the terms for ω_y and ω_z do not cancel, resulting in a significant production of ω_y and ω_z during the interaction. Furthermore, ω_y and ω_z are of similar magnitude. If a cut were made through the $\hat{i}-\hat{j}$ plane and ω_z plotted, the result would look

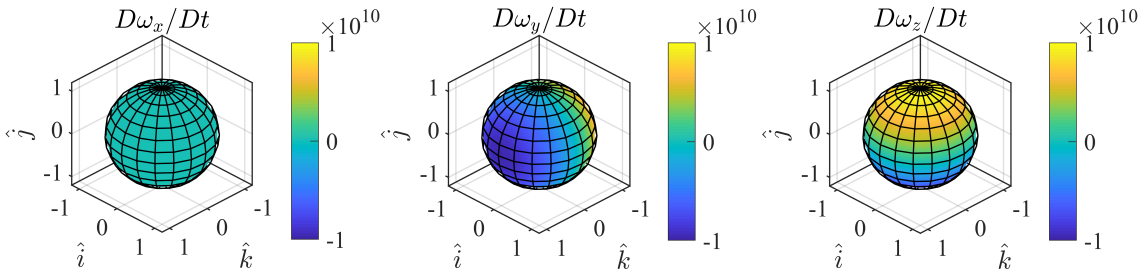

Figure 5.1: Deposition rate of baroclinic vorticity across a hypothetical spherical inhomogeneity traveling in $M_0 = 1.75$ flow and interacting with a pair of expansion fans angled at the local Mach angle.

very similar to the 2D reacting PIV previously discussed. Judging by the magnitude and direction of ω_y and ω_z, it is highly probable that the CRVP in Figure 4.8 is a 2D slice of a 3D vortex ring. When the flame interacts with compressibility, vorticity is deposited all along the periphery, which causes the flame to fold in on itself forming a reacting vortex ring. In the next section, numerical simulations are leveraged to show the reacting vortex ring.

5.2 The Reacting Vortex Ring

The following analyses consider only numerical data, which enables investigation of physical phenomena that are not observable in the experiments. Using experimental observations, it was hypothesized that the kernels form reacting vortex rings due to misalignment of the density and pressure gradients, and this idea is further confirmed by investigating the magnitude and direction of the baroclinic torque terms. Here, the numerical simulations are leveraged to show how the reacting vortex ring develops.

The kernel is initialized using a 1D laminar spherical flame solution for the temperature and species that is then mapped onto a spherical shape. The kernel interacts with turbulence as it travels downstream, distorting it slightly. Figure 5.2a shows the kernel (for case 3n), visualized by the 460 K isocontour, at $\Delta t_{ign} = 145\,\mu$s. Clearly the initially spherical kernel is only weakly wrinkled due to turbulence. After traveling into the channel divergence, baroclinic torque deposits vorticity and the kernel begins to morph into a vortex ring. Figure

5.2b shows the kernel at $\Delta t_{ign} = 445$ μs. The geometry is still fairly spherical, but the flame zone has been stretched upstream from the core of the kernel in thin tail-like structures. These tails are most likely initial vortex ejections and are produced when the vorticity forces the windward side of the flame to fold in on itself, pinching off some of the flame zone. The effects of baroclinic torque are clearly evident in Figure 5.2b, but the vortex ring is still not visible.

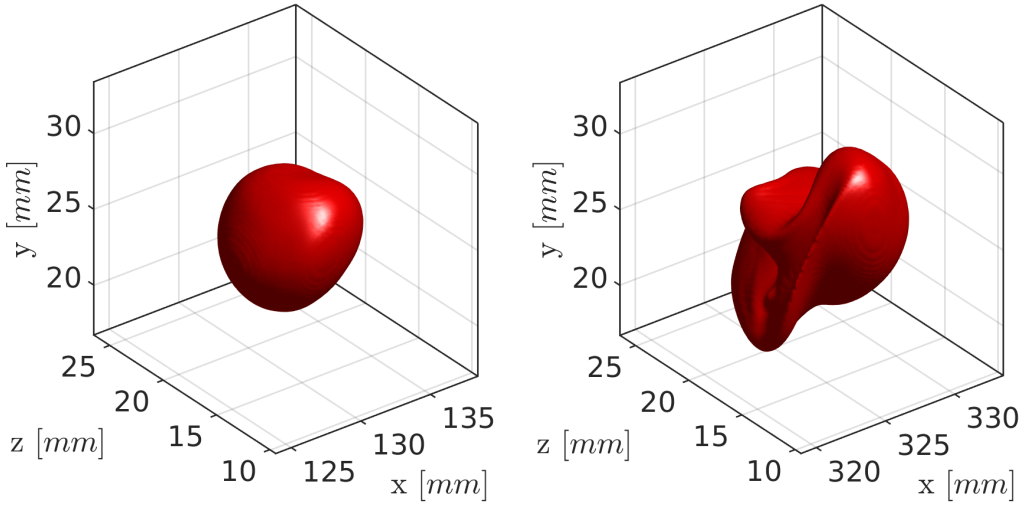

(a) $\Delta t_{ign} = 145$ μs. (b) $\Delta t_{ign} = 445$ μs.

Figure 5.2: Evolution of kernel topology visualized using the 460 K temperature isocontour. Data are for case 3n at the indicated times.

When the kernel morphs into a reacting vortex ring, the windward topology should completely invert and vortex ejections should be seen trailing the kernel. Figure 5.3 shows the kernel at $\Delta t_{ign} = 771$ μs. While the kernel appears roughly spherical externally, it has clearly taken on a partially closed torroidal shape internally. Vortex ejections are indeed seen trailing the kernel. These offer evidence that the kernel has fully morphed into a vortex ring, which proves the previous vortex ring hypothesis.

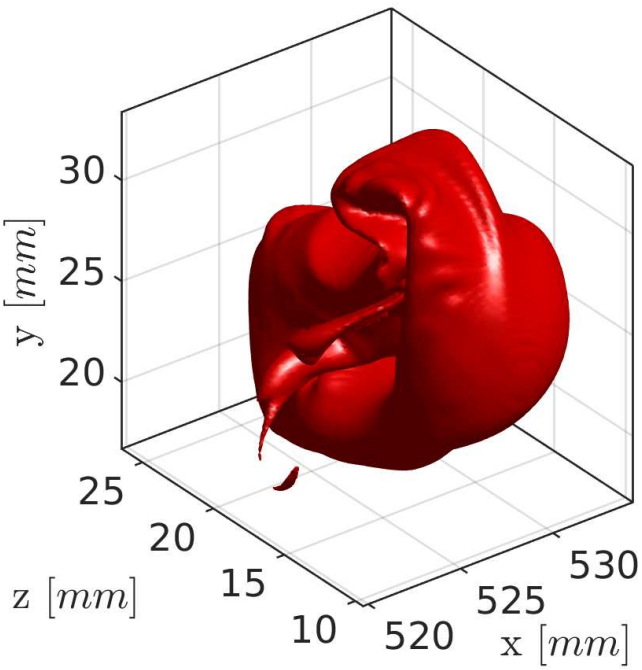

Figure 5.3: Kernel topology visualized using the 460 K temperature isocontour. Data are for case 3n at $\Delta t_{ign} = 771$ μs.

5.3 Growth of Supersonic Flame Kernels: Relationship Between Flame Radii Based on Different Progress Variable Isocontours and/or Diagnostic Techniques

Next, the relationship between the LOS estimate of the burned volume and actual burned volume is explored. However, before discussing this relationship, it is important to make a quick note on the definition of the progress variable. The average 2D flame area is typically measured in experiments by averaging LOS or planar images. The resulting image is often incorrectly referred to as the progress variable (c) map. The correct terminology is the average progress variable ($\overline{c}$) map, which ranges from 0 to 1. At any given point, the value $\overline{c} = 0$ indicates that, from ensemble to ensemble, flames are never present at that point, while $\overline{c} = 1$ indicates that flames are always present at that point. Incidentally, $\overline{c}$ would be more appropriately referred to as a flame location probability because its value is related to the average flame front location rather than to the progress variable isocontour

measured. In fact, when considering the averaged quantities, only the value $\overline{c} = 0.5$ has any meaning because it indicates the ensemble mean position of the flame. Therefore, $\overline{c} = 0.5$ is automatically assumed in the remainder of this chapter and in Chapter 6, but the possibility for c to vary is retained.

It is obvious that flame areas from LOS integrated images will always be larger than planar ones if both diagnostics measure the same value of c. Here, we introduce the terminology $A_{2D,l/p}$ to correspond to the 2D cross-sectional flame areas from the LOS/planar diagnostics, respectively. Then, ensemble averaging $A_{2D,l/p}$ yields the average cross-sectional flame area: $\left\langle A_{2D,l/p,c=c^*} \right\rangle$. The subscripts $c = c^*$ indicates that the cross-sectional flame area is bounded by the average flame position set at an arbitrary c isocontour. Equation (1.12) is used to estimate the mean kernel radii, $\left\langle R_{l/p,c=c^*} \right\rangle$, which are directly related to the volume:

$$\left\langle R_{l,p,c=c^*} \right\rangle = \sqrt{\left\langle A_{2D} \right\rangle / \pi} \tag{1.12}$$

In addition, the real mean flame volume contained within the $c = c^*$ isocontour, denoted $\langle \mathcal{V}_{v,c=c^*} \rangle$, is directly available from the numerical results. A comparison to $\left\langle R_{l/p,c=c^*} \right\rangle$ can be made by converting $\langle \mathcal{V}_{v,c=c^*} \rangle$ into an effective mean flame radius by assuming a spherical shape: $\langle \mathcal{V}_{v,c=c^*} \rangle = 4/3 \, \pi \langle R_{v,c=c^*} \rangle^3$. For the case of nearly spherical kernels in low intensity turbulence, a planar diagnostic might yield a consistent measure of the kernel size. However, supersonic kernels naturally move in the cross stream direction, which yields inconsistencies in the cutting plane. For example, there's no consistent definition of the kernel centerline in Figure 5.3. So while $\left\langle R_l \right\rangle$ has a small variance, the variance of $\left\langle R_p \right\rangle$ is much larger. Therefore, we focus on the LOS and volumetric radii, as these definitions are valid in general for ensemble mean quantities. As discussed in Chapter 2.2.4, the ensemble mean quantities are replaced by the instantaneous value in the simulation and so the $\langle\ \rangle$'s are dropped.

Figure 5.4 shows the instantaneous kernel effective radii from simulations based on the

LOS approximation (R_l) and actual volume (R_v) evaluated at the $c = 0.05, 0.5$, and 0.95 isocontours. Radii are evaluated using temperature isocontours with a cutoff value established from progress variable-conditioned temperature trends. Clearly, Figure 5.4 shows $R_l > R_v$ for all cases, c isocontours, and times, the only exception being at very early times when the kernels are nearly spherical and $R_l \approx R_v$. At the latest times, the radii for $M = 1.5 > M = 1.75 > M = 2.0$. This is mainly due to differences in the residence time between the various cases. Slower kernels have longer to grow before exiting the domain. The radii trend with equivalence ratio ($\phi = 1.0 > \phi = 0.7$) is also repeated here. The LOS data for $c = 0.5$ and 0.95 increase non-monotonically with time. The major dips were traced back to quenching of vortex ejections which, in a LOS image, appear as substantial burned volume but are actually rather small (see Figures 5.2 and 5.3). On the other hand, the volumetric data increases monotonically with time, the only exception being for $\phi = 0.7$ and $c = 0.95$, which increases then decreases. In this case, $c = 0.95$ corresponds to approximately 1443 K, which is not significantly far from the initial kernel temperature (1858 K). This combined with cooling from the expansion results in reduction of the $c = 0.95$ radii for the second half of the dataset.

When investigating Figure 5.4, its clear that LOS and volumetric derived radii are quite different. In addition, flame radii are very dependent on the c isocontour used. Therefore, the ratio of radii could also be quite different. Here, three important quantities are considered: 1. $R_{l,c=0.05}/R_{v,c=0.5}$, which is similar to comparing schlieren and Mie scattering measurements because schlieren indicates the outer edge of the flame [71, 72] while flame edges from Mie scattering are close to $c = 0.5$ [53], 2. $R_{l,c=0.05}/R_{v,c=0.05}$, which is the error associated with LOS measurements, and 3. $R_{v,c=0.05}/R_{v,c=0.5}$, which is the ratio needed to calculate $S_{TD,0.5}$. These quantities are formed with a single ensemble, i.e. they are not statistically converged quantities. However, some considerations suggest they are reasonable estimates. In the experiments, the standard deviation of the kernel radius is < 0.1 mm and the mean radii converges rapidly. In addition, while the radii do vary from ensemble

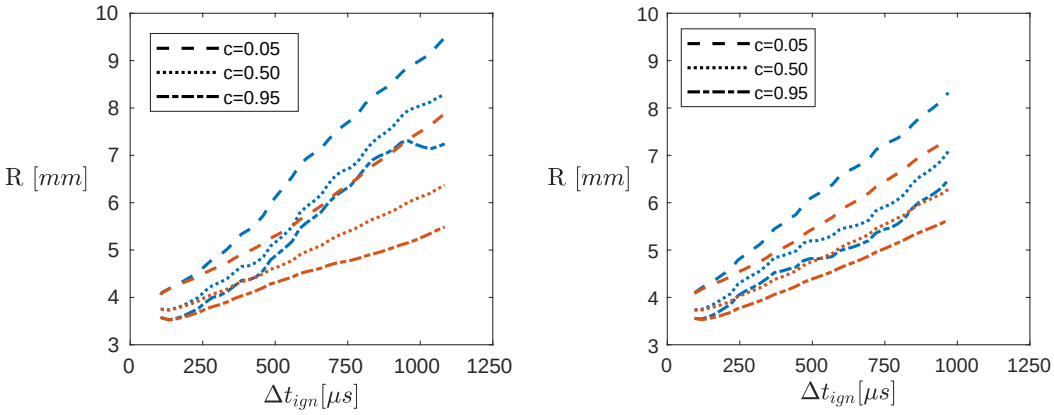

(a) Case 4n: $M = 1.50, \phi = 1.0$.

(b) Case 3n: $M = 1.75, \phi = 1.0$.

(c) Case 5n: $M = 2.00, \phi = 1.0$.

(d) Case 8n: $M = 1.75, \phi = 0.7$.

Figure 5.4: Evolution of instantaneous flame kernel effective radii. Blue corresponds to radii derived from LOS data and orange to radii derived from volumetric data, at the indicated c isocontours. Case 3n is ensemble averaged (N=2), cases 4n, 5n, and 8n have a single ensemble.

to ensemble, a physical process dictates the relationship between the various radii. For example, if in one ensemble the entire kernel is larger than average then an increase in both $R_{l,c=0.05}$ and $R_{v,c=0.05}$ would be expected. However, their ratio, $R_{l,c=0.05}/R_{v,c=0.05}$, would vary far less than either $R_{l,c=0.05}$ or $R_{v,c=0.05}$. For this reason, the ratio should converge more quickly than either the numerator or denominator would independently. Therefore, a single ensemble should give a reasonable estimate of the underlying statistical quantities in question.

Bradley *et al.* [53] compared $R_{l,c=0.05}$ to $R_{p,c=0.5}$ and found a nearly 4/3 relationship in the developed linear regime. Here we choose to explore $R_{l,c=0.05}/R_{v,c=0.5}$ instead of $R_{l,c=0.05}/R_{p,c=0.5}$ because of the previously discussed issues with planar measurements of supersonic kernels. Figure 5.5 shows $R_{l,c=0.05}/R_{v,c=0.5}$ versus Δt_{ign} for each case. The initial deviation from unity in all cases must be the caused by the difference in c, as the kernel is initially spherical and the LOS and volumetric radii should be the same. Rapid growth of $R_{l,c=0.05}/R_{v,c=0.5}$ up to $\Delta t_{ign} \approx 200\ \mu s$ is most likely also the result of the difference in c. The kernel is initialized with a 1D laminar flame solution and it takes some time for the internal structure to rearrange to the spherical flame geometry. However, after this initial development, $R_{l,c=0.05}/R_{v,c=0.5}$ continues to increase. This is most likely the result of the expansion and vortex ring topology. In this situation LOS and volumetric measurements are quite different. Cases 3n and 5n appear to asymptote to approximately 4/3, which is a reasonable expectation based on the Bradley *et al.* [53] low turbulence spherical flame results, where the planar measurement should give a reasonable estimate of the burned volume. This is not true for cases 4n and 8n, however. For case 8n we may hypothesize that the ratio is dependent on ϕ and therefore disregard the difference. However, for case 4n, which has the same ϕ as cases 3n and 5n, the difference is more puzzling. A large separation between LOS and volumetric radii for case 4n is responsible for this observation (see Figure 5.4a). For cases 3n and 5n, the LOS and volumetric based radii are more tightly grouped than those of case 4n. The LOS radii in case 4n overestimates the volumetric radii by 20% compared to 13% in cases 3n and 5n. Hence, this difference is kernel topology related. A similar observation was made in previous experimental results which showed $M = 1.5$ kernels were more vertically elongated compared to $M = 1.75$ and $M = 2.0$ kernels (see Chapter 4). The difference in kernel topology is presumably due to the expansion angle (equivalent to the Mach angle), which drops from $42°$ to $30°$ as Mach number increases from 1.5 to 2.0.

The effect of LOS measurements can be isolated from the effect of c by simply evaluat-

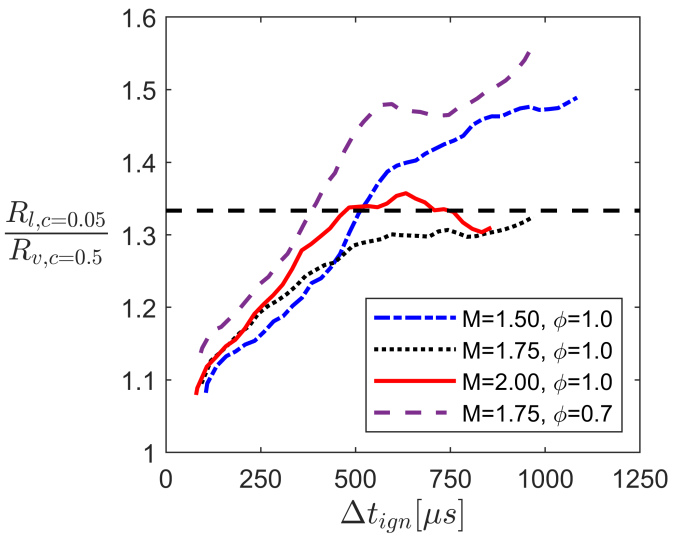

Figure 5.5: Comparison of $R_{l,c=0.05}$ and $R_{v,c=0.5}$ versus Δt_{ign}.

ing R_l and R_v at the same c isocontour. For example, Figure 5.6 shows $R_{l,c=0.05}/R_{v,c=0.05}$ versus Δt_{ign} at the $c = 0.05$ isocontour. All cases show an initial ratio of 1, consistent with the radii findings in Figure 5.4, then grow rapidly from there. Evidently LOS radii are $\geq$ volumetric radii, but the error is $\lesssim 20\%$. After $\Delta t_{ign} \approx 500\ \mu s$, cases 3n, 5n, and 8n asymptote to approximately 1.13. Case 4n once again has a larger ratio: around 1.2. This lends support to the hypothesis presented above that some phenomena in the $M = 1.5$ case causes a topology that has a larger difference between R_l and R_v when compared to the $M = 1.75$ or $M = 2.0$ cases.

The relationship between $R_{v,c=0.05}$ and $R_{v,c=0.5}$ must be known in order to evaluate the displacement speed at the $c = 0.5$ isocontour using Equation (1.17), as is common in literature. Figure 5.7 shows $R_{v,c=0.05}/R_{v,c=0.5}$ versus Δt_{ign}. There is a rapid increase up until $\Delta t_{ign} \approx 150\ \mu s$ for all cases after which the ratio assumes a constant value of ≈ 1.14 for $\phi = 1.0$ and ≈ 1.18 for $\phi = 0.7$. The dependence of $R_{v,c=0.05}/R_{v,c=0.5}$ on ϕ is due to variation in the flamelet structure with ϕ. $R_{v,c=0.05}/R_{v,c=0.5}$ is constant for a time then increases upon interaction with the expansion waves at $\Delta t_{ign} \approx 300\ \mu s$. This mirrors the observations made in Figure 5.4, which showed the ratio of radii increases with for all

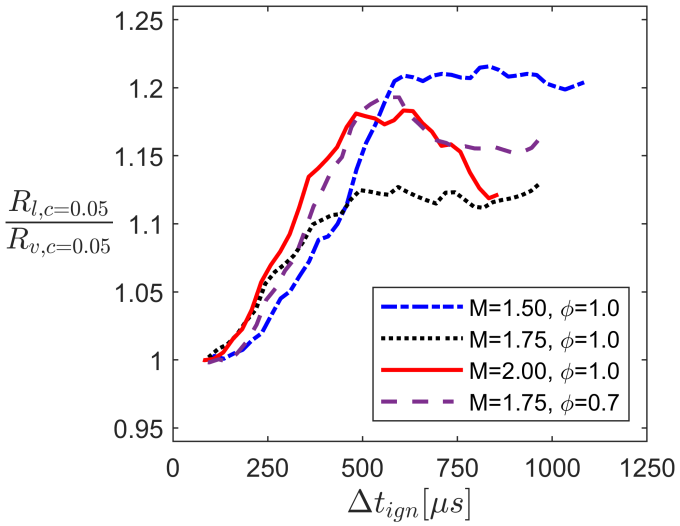

Figure 5.6: Comparison of $R_{l,c=0.05}$ and $R_{v,c=0.05}$ versus Δt_{ign}.

cases.

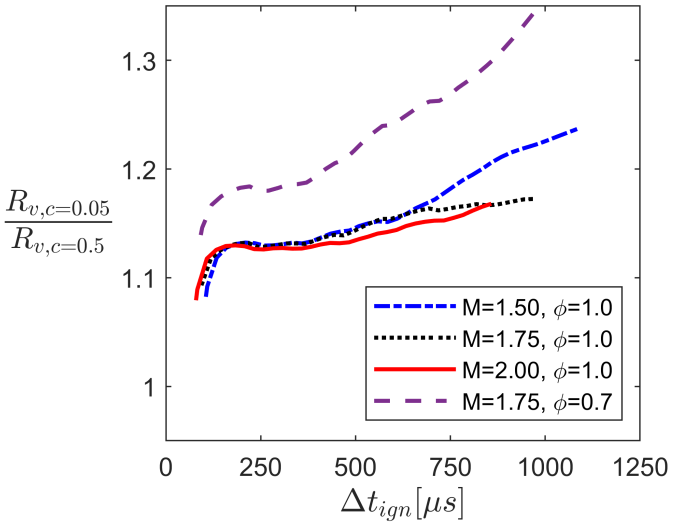

Figure 5.7: Comparison of $R_{v,c=0.05}$ and $R_{v,c=0.5}$ versus Δt_{ign}.

Evidently the time required to rearrange the 1D flamelet structure to the spherical geometry is rather short ($\simeq$ 100 μs). However the vortex ring development and subsequent difference between LOS and volumetric measurements takes much longer ($\simeq$ 500 μs).

5.4 General Trends in the Topology of Supersonic Flame Kernels

The flame interacts with mean flow compressibility to produce vorticity through baroclinic torque. For the case of an initially spherical flame, the kernel morphs into a reacting vortex ring. Hence, the flame generates its own velocity fluctuations. These fluctuations are strong enough to significantly affect the flame growth. In contrast, an unconfined flame convecting in a constant velocity flow will not experience a significant baroclinic torque. In this situation, flame-turbulence interaction would be the main flame growth driver.

When the kernel develops a vortex ring topology, line of sight measurements overestimate the actual flame volume. Therefore, diagnostics such as schlieren can produce a significantly skewed view of the flame growth. In addition, the edge produced by the diagnostic can also produce skewed results. The progress variable measured by each diagnostic must be considered when trying to compare results across various diagnostics.

CHAPTER 6

FLAME SPEEDS OF SUPERSONIC FLAME KERNELS EXPOSED TO MEAN EXPANSION

In this chapter, attention is turned to the turbulent flame speed, which is explored using numerical simulations. Three general topics are investigated: 1. how LOS error in the burned volume leads to an error in S_{TC}, 2. how well S_{TC} scales with u'_{eff} and U_T, and 3. the conditions under which $S_{TC} = S_{TD}$. Turbulent flame speeds will be estimated by a single numerical ensemble for cases 4n, 5n, and 8n and with a N=2 ensemble average for case 3n. The single-ensemble arguments made in Chapters 2 and 5.1 also apply here, and as such the calculated S_T/S_L is probably a reasonable estimate. However, it should be kept in mind that calculated flame speeds are unconverged estimates. Complete convergence would take many more ensembles, which is unfeasible considering the cost of each numerical simulation (see Chapter 2.2).

6.1 Error Associated with LOS Estimate of the Turbulent Flame Speed

In Chapter 5.3, it was shown that LOS-based radii overestimate the volumetric-based radii when comparing at the same c isocontour. Here, we expand on the previous analysis and explore how S_T is affected by LOS measurements. An additional subscript, l/v, is added to S_T to indicate that the flame speed is based on LOS or volumetric data. Evaluating Equation (1.13) for $S_{TC,l,c=0.05}$ and $S_{TC,v,c=0.05}$ and assuming A_f is available for the LOS measurement, one can arrive at:

$$\frac{S_{TC,l,c=0.05}}{S_{TC,v,c=0.05}} = \frac{A_{v,c=0.05}}{A_{l,c=0.05}} \tag{6.1}$$

Equation (6.1) suggests that the ratio of the LOS to volumetric flame speed is equivalent

to the ratio of the volumetric to LOS equivalent average spherical area. Figure 6.1 shows $\frac{S_{TC,l,c=0.05}}{S_{TC,v,c=0.05}}$ versus Δt_{ign}. The flame speed ratios start with a value of 1, quickly decrease, then approach relatively constant values. The LOS measure is reasonable prior to expansion wave interaction at $\Delta t_{ign} \approx 200\ \mu s$, with an error of $< 5\%$. Kernel topology changes rapidly after entering the expansion causing the LOS technique to under predict the flame speed by as much as 32%. Correction for these errors are not trivial as there appears to be a Mach number effect on the required correction factor. Clearly, flame speed results from experimental schlieren measurements should be considered carefully.

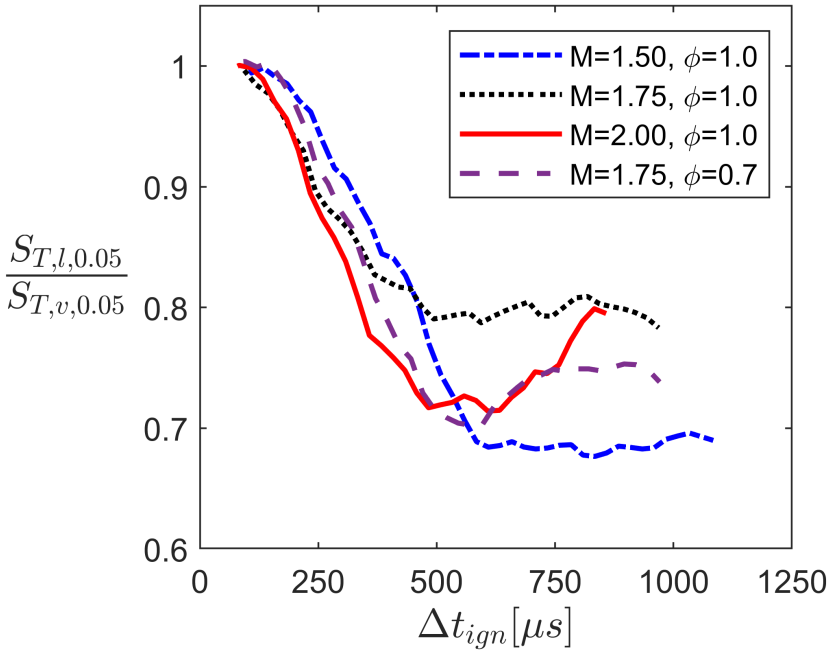

Figure 6.1: Comparison of turbulent consumption speed based on line of sight and volumetric data, both evaluated at the $c = 0.05$ isocontour.

Previous work has shown that the turbulent flame speed is dependent on the isocontour of the measured value of the progress variable [52]. In fact, some relations already exist to convert between isocontours [54]. However, these conversions usually mix progress variable differences with geometric differences (LOS, or planar), and therefore are potentially in error. Diagnostic limitations and the fact that the flame is not infinitely thin are

responsible for this error. Given the nuisance required to match the turbulent flame speed, one may consider it of limited relevance and be tempted to throw it away. However, the turbulent flame speed is still a valuable quantity when used to compare flames in the same configuration (spherical flame, Bunsen flame, etc) and when using the same diagnostics. Under those circumstances, there has been success in collapsing flame speeds over a range of macroscopic parameters [64, 94]. Therefore, the turbulent flame speed is a relevant parameter to compare experimental and numerical results when the diagnostics and flame configuration are consistent. The following sections show some of these comparisons.

6.2 Turbulent Flame Speed versus u'_{eff}

The turbulent intensity is a driving parameter for flame growth of low speed kernels and therefore should have some role in supersonic flames. Here, Equation (1.13) is used to examine the normalized turbulent consumption speed $S_{TC,v,c=0.05}/\overline{S_L}$, which is evaluated by measuring the flame surface area and volumetric-based equivalent spherical area at $c = 0.05$ for each case/time:

$$\frac{S_{TC,0.05}}{\overline{S_L}} = \frac{\langle A_{f,0} \rangle}{\langle A_0 \rangle} \tag{1.13}$$

It has been extensively shown that $S_{T,v,c=0.05}/\overline{S_L}$ scales linearly with ${Re_T}^{1/2}$ [56, 62, 63, 54]. Therefore, we examine the relationship $S_{TC,v,c=0.05}/\overline{S_L}$ versus ${Re_T}^{1/2}$ using u' as the velocity scale:

$$\frac{S_{TC,v,c=0.05}}{\overline{S_L}} \propto \left[\frac{u'}{S_L} \frac{\langle R \rangle}{\delta_L} \right]^{\frac{1}{2}} \tag{6.2}$$

Equation (6.2) is a slightly modified version of Equation (1.10), which was presented in Chapter 1. This relationship requires the flame surface-averaged laminar flamelet velocity which is readily available from the numerical solution and is given by: $\overline{S_L} = \frac{\dot{m}_b}{\rho_{c=0.05}\, A_{f,c=0.05}} = \frac{1}{\Theta A_{f,0.05}} \frac{d\mathcal{V}_{0.05}}{dt}$, where $\frac{d\mathcal{V}_{0.05}}{dt}$ is calculated from the numerical solution using

a power law fit of the burned volumes. Figure 6.2 shows the evolution of $\overline{S_L}$ for each case and time. Figure 6.2 also shows dashed lines for the unstretched 1D laminar flame speed at $\phi = 1.0$ ($\overline{S_{L0}} = 0.58\,m/s$) and $\phi = 0.7$ ($\overline{S_{L0}} = 0.33\,m/s$). $\overline{S_L}$ differs from $\overline{S_{L0}}$ because of flame stretch and differences in the mass and thermal diffusion of the mixture. The stretch effect always reduces $\overline{S_L}$ for outwardly propagating flame kernels because the flame surface is positively stretched as it propagates outward. Likewise, the thermodiffusive instability results in a reduction of $\overline{S_L}$ for $\phi = 1.0$ because the mixture is thermodiffusively stabilizing. At $\phi = 0.7$, however, the thermal and mass diffusion coefficients are equal for methane-air mixtures, resulting in no modification of $\overline{S_L}$. In Figure 6.2, the flame speed increases because the stretch rate initially reduces as kernels grow. The previously discussed flamelet structure modification within the first $200\,\mu s$ also contributes to this initial growth. The flame speed never reaches the unstretched value, although the $\phi = 0.7$ case comes closer. After interaction with the expansion, flame speeds drop due to increased flame stretch caused by emergent vortex ring topology and reduction in S_{L0} due to temperature and pressure loss through mean flow expansion.

Figure 6.3 shows the normalized turbulent consumption speed with several variants of the scaling parameter using either $\overline{S_L}$ or $\overline{S_{L,b}}$ and δ_L or $\delta_{M,b}$. The δ_L is calculated as an average through the flame via: $\delta_L = (T_1 - T_0)/(dT/dR)_{max}$ and $\delta_{M,b}$ is estimated from Gu *et al.* [121]. Overall $S_{TC,v,c=0.05}/\overline{S_L}$ increases independent of the scaling parameter used, but the variation appears larger when using $\delta_{M,b}$ as a scaling parameter instead of δ_L. This is especially true for $\phi = 0.7$. This could be caused by the necessary pressure and temperature extrapolation of the Gu *et al.* [121] data to the conditions in this study. However, it is not surprising that $\delta_{M,b}$ produces a wide variation in $S_{TC,v,c=0.05}/\overline{S_L}$ because it is not a physical length scale of the system. Instead, $\delta_{M,b}$ is a parameter that relates S_L to S_{L0} and κ, and happens to have units of $[m]$. Any fortuitous collapse using $\delta_{M,b}$ would more likely be due to the compression of the axis. Since $\overline{S_L}$ is calculated directly from flame topology data, the effects of flame stretch and thermodiffusive instability are accounted for directly and

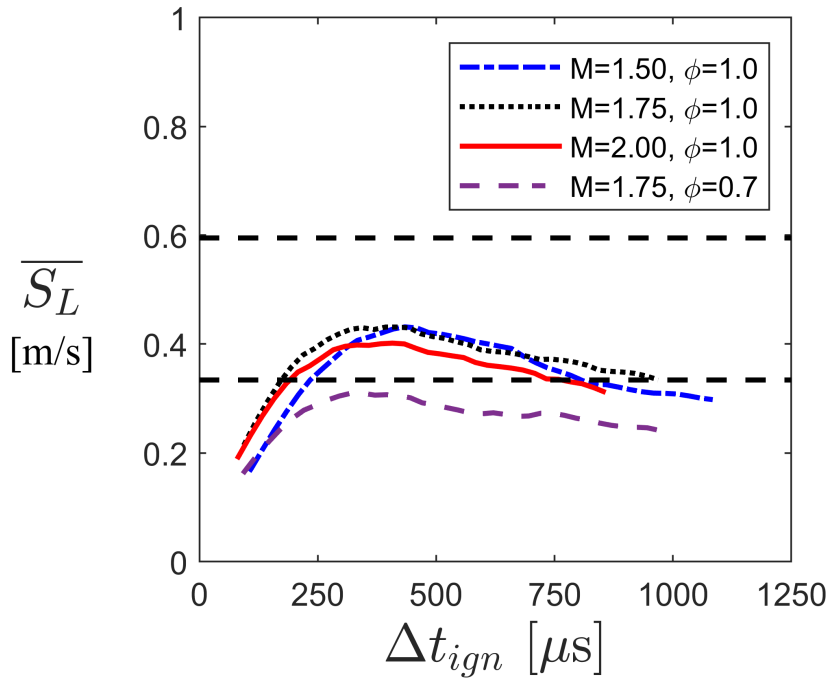

Figure 6.2: Flame surface averaged laminar flame speed versus Δt_{ign}.

$\delta_{M,b}$ is not needed. Therefore, in the remainder of this paper $\delta_{M,b}$ will be disregarded as a flame speed scaling parameter.

The difference between $\overline{S_L}$ and $\overline{S_{L,b}}$ $(= \Theta\overline{S_L})$ as a scaling parameter is rather small. The gas expansion ($\Theta = \rho_{0.05}/\rho_{0.95}$) varies from 4 to 5 for $\phi = 0.7$ to $\phi = 1.0$, which is a rather small difference when inside the square root. It can be shown that Θ should not appear in the scaling by exploring the effect of Θ on S_T. Imagine two flames with equal S_L but disparate values of Θ, one many times larger than the other. In a spherical geometry, it is obvious that the flame surface area and spherical-equivalent average flame surface area both grow more rapidly for the case with larger Θ. Now, $\overline{S_L} = \frac{\dot{m}_b}{\rho_{c=0.05} A_{f,c=0.05}}$ suggests that the mass consumption rate must increase to balance the flame surface growth in order to maintain $\overline{S_L}$. If the increase in $A_{c=0.05}$ is proportional to the increase in $A_{f,c=0.05}$, then $\dot{m}_b = \rho_{0.05} A_{c=0.05} S_{TC,0.05}$ suggests that $S_{TC,0.05}$ remains unchanged. Therefore, $S_{TC,0.05}/\overline{S_L}$ is unchanged by Θ. This explains the similarity between scaling with $\overline{S_L}$ versus $\overline{S_{L,b}}$. Any scaling improvement is due to compression of the axis. $\overline{S_L}$ is the proper scaling parameter.

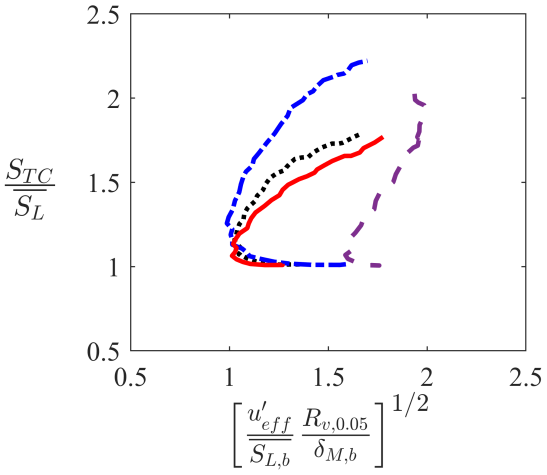

(a) $\overline{S_{L,b}}$ and $\delta_{M,b}$

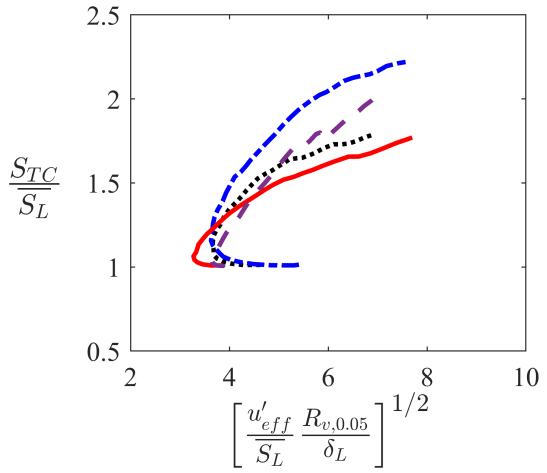

(b) $\overline{S_L}$ and δ_L

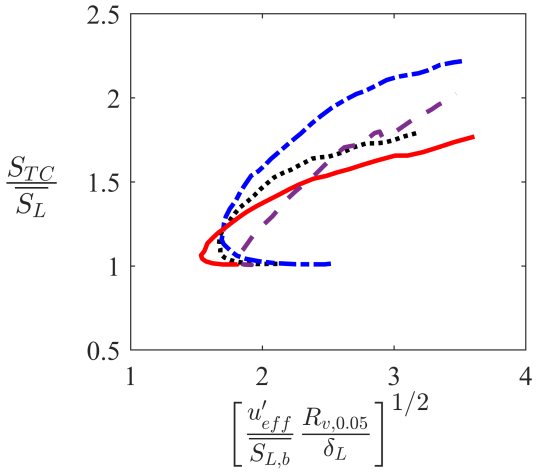

(c) $\overline{S_{L,b}}$ and δ_L

Figure 6.3: Normalized turbulent consumption speeds based on volumetric data at the $c = 0.05$ isocontour plotted against various scalings.

Overall, Figure 6.3 shows a poor collapse when u'_{eff} is used as the scaling parameter. The supported linear scaling observed in low speed flame kernels apparently is not evident in supersonic kernels traveling through a mean expansion when using u'_{eff}. Clearly $u'_{eff} \cdot R$ is not a sufficient diffusion coefficient to fully describe the growth of supersonic kernels exposed to mean expansion.

6.3 Turbulent Flame Speed versus U_T

The hypothesis that the vortex propagation velocity, U_T, is the main parameter driving kernel growth is investigated next. Upon interaction with an expansion wave, the kernel is set into motion with respect to the reactants. The kernel moves at a speed of U_T in the reactant-centered reference frame and the velocity difference, U_T, creates a shear layer between reactants and products, which transfers momentum to the slower moving reactants. This momentum transfer is accomplished over a spatial distance equivalent to the kernel radius. Therefore, $U_T \cdot R$, which has units of [m^2/s], acts to spread momentum much like the turbulent diffusivity[1]. This vortex ring diffusion stretches the flame surface which increases the reactant mass consumption rate, and therefore, the turbulent burning velocity. Vorticity in the shear layer wrinkles and stretches the flame and ultimately morphs the kernel into a reacting vortex ring. Therefore, it is a reasonable hypothesis that kernel growth would scale with the velocity difference, U_T .

The kernel velocity is calculated by tracking the kernel location versus time. Ideally the center of mass would be used in the calculation, however the center of mass varies inconsistently in time due to upstream vortex ejections which rapidly quench and disappear. Quenching of these ejections makes the kernel centroid appear to accelerate and decelerate rapidly, which results in large variation in U_T. To fix this problem, the kernel leading edge (identified by the 460 K isocontour) is used instead of the center of mass. Then, the

[1] $U_T/2$ may be a more appropriate scaling as this corresponds to the standard deviation of a step function. The difference is somewhat immaterial as the constant would simply transfer through the square root to modify the slope of the scaling. The linearity, or lack thereof, would be preserved.

kernel velocity is defined as the rate of change of the leading edge position. Figure 6.4 shows the kernel velocity for cases 3n, 4n, and 5n (case 8n is missing because it overlaps with case 3n). Overall the kernel velocity variation along the streamwise direction is fairly similar for the different cases, which is a reasonable conclusion considering that expansion strength is geometry dependent and the same geometry is used in all cases. When the kernel travels through an expansion, its velocity increases momentarily then begins to drop due to momentum transfer and viscous losses. This process repeats indefinitely downstream, weakened only by the reduction in available internal energy.

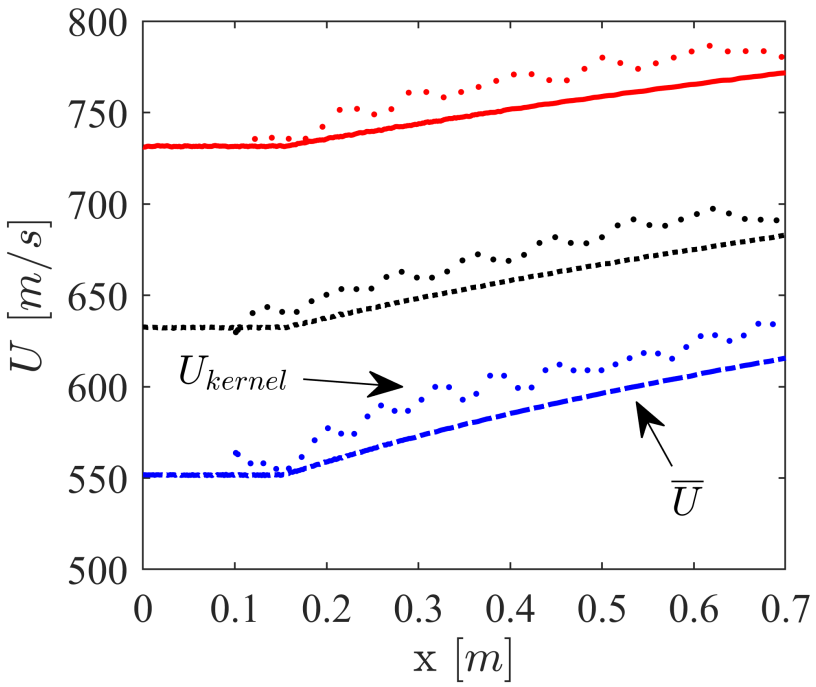

Figure 6.4: Mean axial flow velocity (lines) and kernel velocity (dots) versus distance for $M = 1.5$ (blue), $M = 1.75$ (black), and $M = 2.0$ (red).

A power law of the form $U_{kernel}(x) = C(x - x_0)^{\alpha} + U_0$ fits the kernel velocity quite well, having a minimum coefficient of determination (r^2) of 0.95 across all cases. Table 6.1 shows the best fit power law coefficients for each case. Using this fit and subtracting the mean axial velocity yields the kernel propagation velocity U_T. Figure 6.5 shows U_T versus downstream distance. Prior to interaction with the expansion waves, which act like

Table 6.1: Kernel velocity power law fit: $U_{kernel}(x) = C(x - x_0)^{\alpha} + U_0$.

Case	C	α	x_0	U_0	r^2
3n	92.1	0.57	0.157	632.4	0.96
4n	111.0	0.54	0.154	551.6	0.97
5n	76.9	0.554	0.154	731.5	0.95
8n	90.2	0.59	0.158	632.4	0.97

a constant driving force, $U_T = 0$. Upon entering the expansion, the kernel accelerates until this driving force is counterbalanced by momentum transfer into the y and z direction and viscosity. At a maximum, U_T is approximately 15 m/s with a variation of a few m/s across all cases. Then U_T decreases further downstream because the kernel temperature drops resulting in a weaker driving force. The $\phi = 0.7$ case, which is the coldest, has the lowest U_T. There is also a small difference between $M = 1.5$ and $M = 1.75$/2.0. This is similar to Figure 5.5 and is most likely due to the differences in kernel topology in those cases: $M = 1.5$ is flatter than $M = 1.75$/2.0 which are more spherical. Interestingly, the assumption of constant U_T made in Chapter 4.4 is fairly reasonable.

Figure 6.6 shows $S_{TC,v,0.05}/\overline{S_L}$ using U_T in the scaling. Two interesting observations are noted. First, $S_{TC,v,0.05}/\overline{S_L} \rightarrow 1$ as $\left[(U_T R_{v,0.05})/(\overline{S_L}\delta_L)\right]^{1/2} \rightarrow 0$, which is an expected result but is surprisingly uncommon and difficult to achieve in experimental analyses. Second, the collapse is significantly improved over Figure 6.3b. There is a tight grouping across Mach number and equivalence ratio over a significant portion of the data. In addition, the scaling appears linear over a large range of the data. A difference appears between $\phi = 1.0$ and $\phi = 0.7$ cases at late times (large $\left[\frac{U_T}{S_{L,b}}\frac{\langle R \rangle}{\delta_{M,b}}\right]^{\frac{1}{2}}$), which could be the result of over expanding in the $\phi = 0.7$ case. In this situation, the $\phi = 0.7$ flame is pushed too close to the extinction limit, potentially resulting in the non-linear behavior seen in Figure 6.6. A small kink is also seen for case 3n which is due to a sudden topology change (quenching of vortex ejections) experienced in one the numerical ensembles. These results suggest that

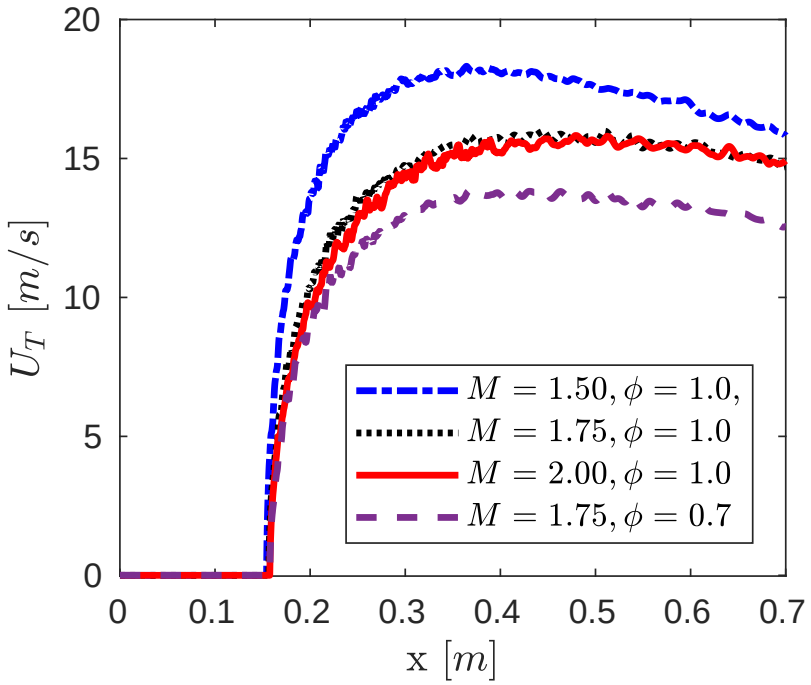

Figure 6.5: Kernel propagation velocity, U_T, versus axial distance, x.

the $Re^{1/2}$ scaling is accurate as long as an appropriate velocity scale for mixing is selected and the resulting flame falls within the thin reaction zone.

These results are not entirely conclusive because only a single ensemble is presented, however Figure 6.6 does demonstrate a relationship between U_T and S_T, i.e. $S_T/S_L = f(U_T, R, S_L, \delta_L)$. Further, U_T depends on the gas properties: P, T, and ϕ and on the mean compressibility of the gas: the Mach number and the expansion angle (α), all of which are known. Therefore, a relationship between flame speed and Mach number/compressibility has essentially been established through U_T. It would be a simple matter to relate the burning rate to the Mach number and mean flow compressibility, i.e. $S_T/S_L = f(M, \alpha, R, S_L, \delta_L, etc.)$, however data at different expansion angles would be required. This is an interesting topic left for future work.

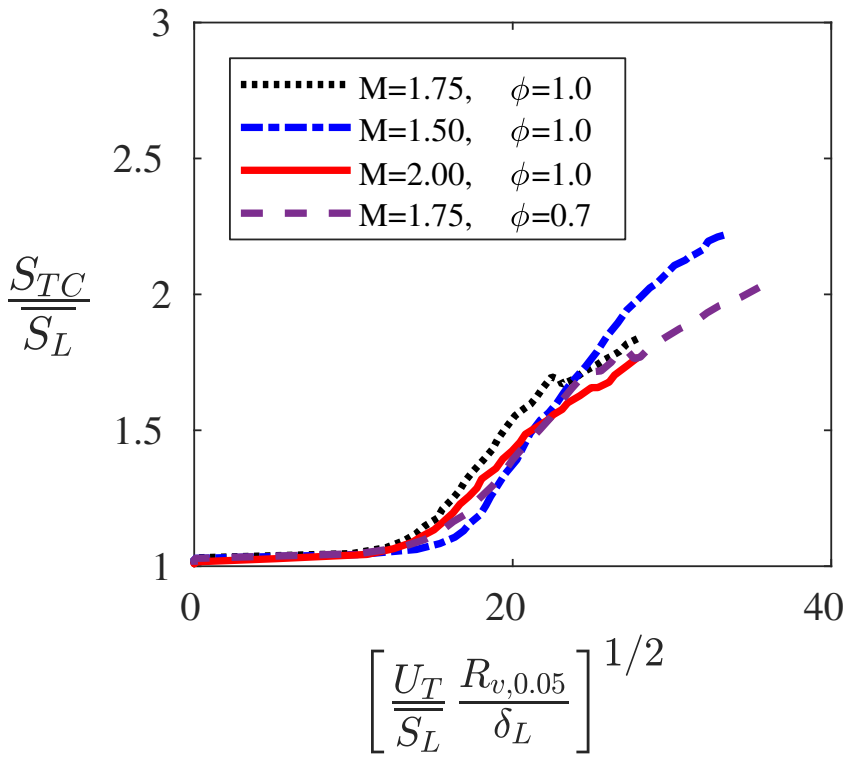

Figure 6.6: Normalized turbulent consumption speeds based on volumetric data at the $c = 0.05$ isocontour plotted against $\left[\frac{U_T}{\overline{S_L}}\frac{R_{v,0.05}}{\delta_L}\right]^{1/2}$.

6.4 Comparison of Consumption and Displacement Speeds

Here, we compare the normalized consumption speed, Equation (1.13), and the normalized displacement speed, Equation (1.16) which are different because of the ambiguity in the burned volume definition due to finite flame thickness. Equation (1.16) is repeated below for convenience.

$$\frac{S_{TD,0}}{\overline{S_L}} = \frac{1}{\overline{S_{L,b}}}\frac{d\langle R_0\rangle}{dt} \tag{1.16}$$

Evaluating the displacement speed at different c, which is equivalent to evaluating the term dR/dt at some other c isocontour, yields different results. By comparing Equations (1.13) and (1.16) and using the single ensemble estimate, a relationship between the two flame

speeds can be established:

$$\frac{S_{TD}}{S_{TC}} = \frac{\frac{1}{\overline{S_{L,b}}}\frac{dR_{v,c=c^*}}{dt}}{A_{f,c=0.05}/A_{c=0.05}} \tag{6.3}$$

Again, A_f is the instantaneous flame surface area, A is the equivalent spherical flame surface area, and $c = c^*$ indicates that the derivative is evaluated at different c isocontours. Figure 6.7 shows this quotient for the $c = 0.5$ and 0.05 isocontours. After some initial development time, the calculated displacement speed under estimates the consumption speed by 40% for cases 3n, 4n, and 5n and 65% for case 8n at the $c = 0.5$ contour. An under estimate in the flame speed is equivalent to an under estimate of the mass burning rate when using Equation (1.15). This prediction is not surprising considering that the flame has a finite thickness and that a significant amount of the burned mass is outside of the $c = 0.5$ contour. Perhaps a different isocontour would yield a better estimate of the burned volume, and one obvious choice is $c = 0.05$ because it contains more of the burned mass. Indeed, Figure 6.7b shows that the ratio of displacement and consumption speeds are much improved for all of the cases. In addition, the $\phi = 0.7$ case appears to collapse with the $\phi = 0.7$ at $S_{TD}/S_{TC} \approx 0.8$. These results suggest that diagnostics that measure the $c = 0.05$ may yield a better measure of the turbulent consumption rate. However, the most important conclusion is that consistency between the definitions of displacement and consumption speeds is paramount when comparing the two. In particular, the definition of burned volume and its displacement is critical, especially when considering flames with broadened preheat zones where the outer flame edge could be pushed quite far away from the region where products are created.

Due to simulation costs, these results are subject to some limitations because only a single ensemble was available in cases 4n, 5n, and 8n. However, the arguments presented in Chapter 2.2.4 and the overall trends in Figure 6.7 suggest that the accuracy of certain experimental measures of the flame speed could be improved by considering which isocontour/diagnostic pair is chosen. Along those same lines, it is important to consider the

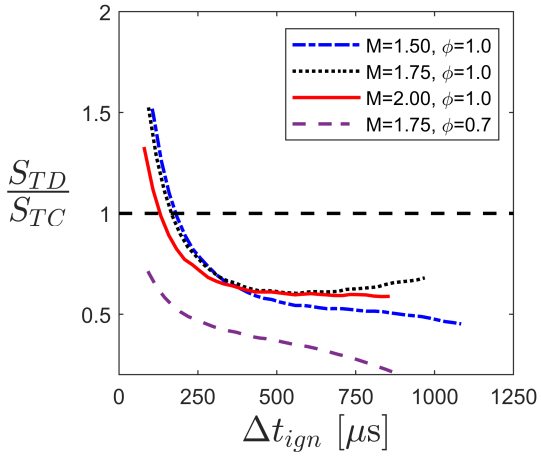

(a) $c = 0.5$

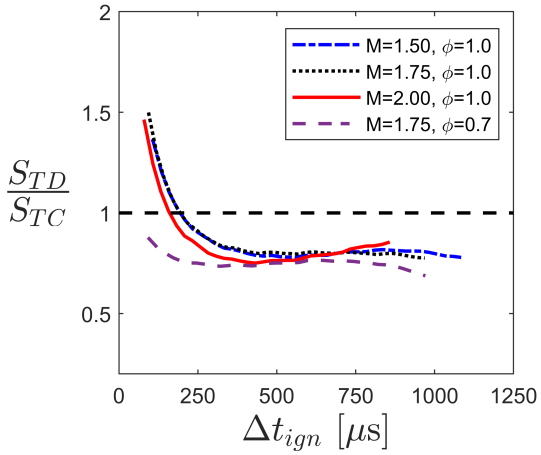

(b) $c = 0.05$

Figure 6.7: Turbulent displacement versus turbulent consumption speeds evaluated at (a) $c = 0.5$ and (b) $c = 0.05$ versus Δt_{ign}.

style of diagnostic used (planar, LOS, volumetric) when calculating the turbulent flame speed because this choice can have a drastic effect on the flame speed when the flame topology is complex.

CHAPTER 7
CONCLUSIONS AND FUTURE WORK

7.1 Conclusions

A new configuration for studying the propagation of turbulent premixed flames in supersonic flows is presented. The experiment is designed to produce a well-defined flame-compressibility interaction using a uniform area expansion. Methane-air flame kernels are initiated via laser-induced spark ignition and convect downstream with the local velocity. The flame kernels are self-propagating and grow in the downstream direction. The configuration in this study is a subclass of flame kernel problems where confining boundary conditions influence flame growth. Upon interaction with expansion waves, the pressure-density misalignment results in vorticity deposition via baroclinic torque. The interaction causes a velocity slip between the reactants and flame and results in the formation of a kernel-wide vortex ring motion. Three major studies are presented, including laser ignition experiments, flame speed and kernel topology experiments, and numerical simulations. The experimental results cover three Mach numbers, three turbulence conditions, and cover the range $\phi = 0 - 1.0$. A detailed comparison between the experiments and simulations is conducted by processing numerical results in a similar fashion to experimental results. The validated numerical results yield 3D information that is inaccessible in the experimental results, enhancing the interpretation of experimental data.

Supersonic laser ignition and the last lasting effect of the ignition event on flame growth were explored for the first time in a fully premixed supersonic flow field without the disruptive influence of a flame holder. It was shown that several features of supersonic laser ignition are similar to subsonic ignition. For example, qualitative agreement of the kernel shape with previous studies is shown out to 300 μs. Notable subsonic features, including

kernel eccentricity and third lobe formation, also appear in supersonic laser ignited kernels. However, kernel shape and third lobe location appear to depend on the baseline flow field upon which initial dieletric breakdown occurs. In addition, quantitative agreement is shown for the kernel perimeter between these studies and those of Mulla *et al.* [30]. The agreement occurs despite a difference in optical technique and reactivity of the mixture. After 300 μs, deviation in the kernel perimeter occurs at quiescent conditions. In the reacting, but non-ignitable mixture, the kernel grows for a longer time before finally beginning to dissipate. These observations suggest that similar to subsonic laser ignited flames, kernel growth is strongly driven by the ignition event out to $\approx$ 200-300 μs, after which, transition to a self propagating flame occurs over some time frame. Because the laser pulse timescale (< 10 ns) is so quick with respect to the flow field, much of the previous low speed laser ignition work is directly applicable to supersonic flows as long as the initial flow field is well characterized. Consequently, Mach number has little effect on kernel growth and transition to a self propagating flame.

The laser ignition event has a long lasting effect on the kernel radius, and more importantly, on the kernel growth. An analysis is conducted to investigate the dependence of the flame growth on the ignition event. It is shown that changes in the laser settings, such as the incident energy, can significantly effect flame growth, especially at early times. This fact is exploited by identifying when the flame growth no longer changes with respect to the laser settings. Values for the minimum deposited energy and minimum time from ignition of $E_d = 25$ mJ and $\Delta t_{ign} = 500\ \mu s$ are suggested to reduce the transition time to a fully self-propagating and independent flame. However, the independence time does not correspond to a region that is completely independent of the ignition event. Even at the latest times measured, flame growth is still slightly dependent on E_d, and therefore has a memory of the ignition event. Based on independence time trends, it would likely take several milliseconds for complete independence, which is an impossibly long timescale for supersonic flows but would not be unreasonable in subsonic laser-ignited flame studies.

Also, this analysis assumes that the ignition overdrive can be detected by varying the laser settings. If this is not the case, i.e. if the overdrive continues to influence kernel growth but the effect of E_d on the growth is negligible, then these results may be misleading. These conclusions are important to consider in a scramjet environment where flow through times are typically shorter than the amount of time it would take for full independence. This fact is likely a universal truth for any ignition technique is supersonic flows.

The morphology of supersonic flame kernels exposed to mean acceleration has been explored for the first time. It was shown that flame kernels in expanding supersonic flow have similar features to classical shock-bubble and shock-flame interactions. Upon interaction with expansion waves, the kernel is impulsively accelerated with respect to the surrounding reactants. This interaction results in a reacting vortex ring. Development of the vortex ring and the resulting kernel shape are shown to be Mach number dependent, and the Mach angle is most likely responsible for this dependence. The reacting vortex ring was hypothesized based on 2D observations from experimental studies but could not be confirmed with the limited experimental diagnostics alone. Access to the full 3D flame topology (using numerical simulations) confirms that the flame kernel morphs into a reacting vortex ring upon interaction with the mean flow expansion. Simulations also show that LOS measurements over estimate the calculated flame radii by as much as 20% because of reacting vortex ring topology. Relationships between LOS and volumetric derived radii show reasonable agreement with some previous experimental observations [53]. Line of sight measurements under predict the turbulent flame speed by up to 30%.

Two corrections to the turbulent flame speed are necessary due to some unique features of the supersonic flow field. These are: (1) a correction to the laminar flame speed, the Markstein length, and the burned to unburned density ratio, which vary with the local thermodynamic conditions, and (2) a correction to the flame radius to remove artificial growth due to mean expansion. S_T/S_L has a linear dependence on $Re_T^{1/2}$ as would be expected of flames in the thin reaction zone. However, S_T/S_L is larger than previous flame

kernel studies suggesting that compressibility interaction increases the flame speed.

Growth of supersonic flame kernels in a mean expansion is predominately influenced by hydrodynamic instability. Expansions force the kernel into motion with respect to the reactants. This process generates shear between the products and reactants. The flame-compressibility interaction generates its own turbulence, acting like a flame surface source. The turbulent flame speed does not collapse when scaled against u' because the shear induced by baroclinic torque influences the flame more than turbulence.

Utilizing the vortex ring propagation velocity, a refinement to the flame speed scaling is suggested. This can be thought of as adding a pseudo Mach number dependence to the S_T/S_L scaling. A partially linear regime is present when the turbulent flame speed is scaled against the vortex propagation velocity, U_T. With some caution, the new scaling is shown to collapse the supersonic flame kernel data with previous low speed results. These observations lend support to the idea that turbulence plays a secondary role to the hydrodynamic instability in this problem. The proposed flame speed scaling should be able to predict the consumption rate in supersonic combustors, even if the flame is anchored, as long as the flow field is expanding, fuel is injected far enough upstream such that the burning mode is premixed, and if the flame is within the thin reaction zone.

The turbulent displacement and consumption speeds are compared and the conditions for equivalence are demonstrated. The nature of the diagnostic used (LOS, planar, or volumetric) and the progress variable isocontour measured greatly affect the calculated flame speed. Numerical results suggest that the $c = 0.05$ isocontour should be used when experimentally measuring the turbulent displacement speed for $\phi = 1.0$ supersonic kernels in an expanding flow. The flame has a finite thickness and the displacement speed results depend heavily on the definition of the flame edge. This is a fact often overlooked in experimental analyses, which simply calculate the rate of change of the flame edge using some diagnostic technique. Equivalence in the definitions of the consumption and displacement speed requires careful consideration of the definition of the flame edge.

The numerical results demonstrate the utility of combined physical and numerical experiments. The simulations qualitatively and quantitatively matched experiments for the flow field statistics, flame growth, and internal flame structure. The validated numerical results enable several analyses which are not available in the experiments alone: 1. identification of the vortex ring topology, 2. estimating the error associated with line of sight measurements such as schlieren, 3. investigating the dependence of the flame speed on the progress variable isocontour measured, and 4. directly calculating the consumption speed. In turn, the experimental results lend credibility to all of the above conclusions. The numerical results demonstrate the utility of the supersonic kernel problem as a canonical validation case for supersonic simulations. This is a useful test case for the supersonic combustion modeling because complexity of the flow field often shadows numerical errors, but the simplicity of this problem enables easy identification of those errors.

7.2 Future Work

One of the main assumptions in the laser ignition study is that the dependence of the flame speed on the ignition event can be identified by examining how sensitive the flame growth is to the deposited ignition energy. This condition is a necessary condition for independence because the flame growth should be independent of all ignition system settings when independence occurs, the deposited energy being a function of the ignition system settings. However, the incident energy is just one parameter of the ignition system that could affect the results. In other words, the flame growth being independent of the deposited energy is not necessarily a sufficient condition for independence. It would be useful to investigate how the late time flame speed varies with other ignition system settings. For example, the flame speed may have a long-time dependence on the focal length, style of the ignition optic, or the beam profile. Time resolved measurements of the kernel temperature, pressure or species, might also yield useful information for determining the influence of the ignition overdrive on the turbulent flame speed.

The kernel propagation velocity scaling presented in this work isn't exclusive to supersonic flows. Flame kernels in low speed flows with strong pressure gradients would also experience an acceleration and develop into reacting vortex rings. If the flame-compressibility interaction generates strong vorticity, then the kernel propagation velocity should be the most relevant velocity scale for flame growth. Therefore, the scaling should apply to any flow with a moderately strong pressure gradient. It would be interesting to extend these findings to the subsonic realm by laser igniting kernels in a low speed flow with a superimposed expansion or compression.

For the cases presented in this work, the kernel propagation velocity is approximately four times the RMS turbulent velocity. Therefore, it is not surprising that the flame induced vorticity has a stronger impact on flame growth than turbulence. It is not obvious what would happen if the flame-turbulence and flame-compressibility interactions were of similar strength. One important question is whether the flame-turbulence and flame-compressibility scalings could be collapsed, perhaps using a modified velocity scale. Additional studies with a larger range of turbulence intensity and with varying expansion strength are required to contribute to answer this question. A similar question arises when considering extreme turbulence levels where the velocity fluctuations themselves are instantaneously compressible, i.e. compressible turbulence. It's not clear if the $\mathrm{Re}^{1/2}$ scaling extends to the compressible turbulence realm or if another scaling is required. Compressible turbulence may be realizable in a cavity flame holder or supersonic jet in cross flow, therefore, studies investigating a flame kernel interacting with these flow features could help answer these questions. Some preliminary studies of a supersonic premixed CH_4 kernel interacting with a premixed jet have already been conducted, however, the kernel quenches upon traversing the jet. A more reactive fuel may be required.

The reactivity of the fuel is another interesting parameter which could be explored further. In these studies, CH_4 reacts relatively slowly, which permits sufficient time for the flame to roll up into a reacting vortex ring, with a torroidal-like shape. If the fuel

were significantly more reactive (i.e. a replacement fuel like hydrogen or much higher static temperature), then the flame speed may be large enough to modify the vortex ring structure. It's not clear if the vortex ring would be sustained as the reactivity increases. Nonetheless, baroclinic torque would still generate vorticity, which in turn would modify the flame speed. How the flame speed would scale in this scenario is unknown.

The numerical and experimental data are very similar and there is high fidelity in the numerical validations presented. However, it cannot be completely guaranteed that the quantitative agreement isn't a coincidence. For example, if there are multiple competing effects which cancel, then agreement between experiments and simulations may be misleading. In order to further investigate the accuracy of the numerical validations, additional numerical simulations could be conducted in the subsonic realm and compared to well established flame bomb or low speed wind tunnel data. If simulations of the pure flame-turbulence interaction yields similar results to the experimental data, then there would be an even greater trust in the quantitative agreements presented in this work.

Whether compressibility affects the flamelet structure was not discussed heavily in this work. However, the numerical simulation data produced by this work is readily usable and available for this purpose. An analysis could be conducted to explore the effects of compressibility on the flamelet structure of turbulent premixed flames by progress variable conditioning the temperature or species fractions within the flame brush. This analysis could be enhanced further by coupling it with new simulations at different expansion strengths.

Appendices

APPENDIX A

SUPERSONIC NOZZLE DEVELOPMENT AND COORDINATES

Three supersonic nozzles were developed to achieve M =1.5, 1.75, and 2.0 tunnel conditions. The nozzles have a minimum length design, meaning the flow expansion is accomplished through a Prandtl-Meyer expansion fan from a single turn located at the nozzle throat. Nozzle geometry after the throat is selected to cancel the expansion waves, resulting in a uniform velocity profile at the nozzle exit. The region to region method of characteristics analysis presented in John (1984) [151] is adapted to drive the nozzle geometry. An example output for a 50 mm tunnel with $\gamma = 1.4$, $M = 2.0$, and 50 characteristics is shown in Figure A.1. Nozzle coordinates for the three nozzles are given in Tables A.1, A.2, and A.3. Upstream of the throat, the subsonic portion of the nozzle follows a linear profile, as shown in Figure 2.3.

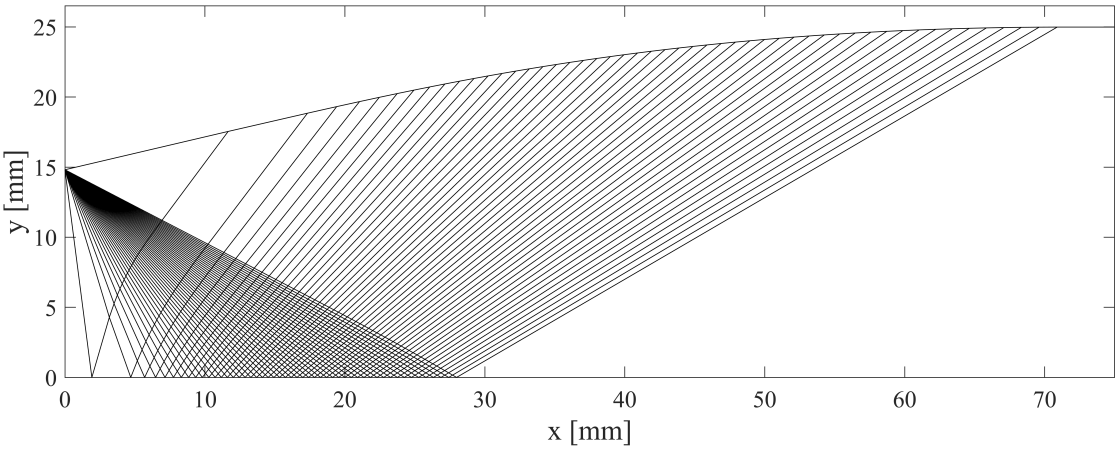

Figure A.1: Method of characteristics result for a 50 mm exit, γ=1.4, and $M = 2.0$ nozzle with 50 characteristics.

Table A.1: Nozzle coordinates for $M = 1.5$ nozzle used in these studies. y-coordinates are nozzle half-heights. Units are in millimeters.

Pos	x	y	Pos	x	y
1	0	21.255	27	37.119	24.667
2	12.361	22.544	28	37.666	24.694
3	18.098	23.130	29	38.211	24.720
4	20.034	23.324	30	38.751	24.745
5	21.483	23.466	31	39.288	24.768
6	22.689	23.582	32	39.823	24.790
7	23.746	23.681	33	40.355	24.811
8	24.702	23.769	34	40.885	24.831
9	25.583	23.848	35	41.413	24.850
10	26.409	23.920	36	41.939	24.867
11	27.190	23.986	37	42.463	24.884
12	27.935	24.048	38	42.986	24.899
13	28.650	24.107	39	43.508	24.913
14	29.341	24.161	40	44.029	24.926
15	30.010	24.213	41	44.549	24.938
16	30.662	24.262	42	45.068	24.949
17	31.298	24.308	43	45.587	24.958
18	31.920	24.352	44	46.105	24.967
19	32.531	24.394	45	46.623	24.975
20	33.131	24.434	46	47.140	24.981
21	33.721	24.472	47	47.658	24.986
22	34.304	24.508	48	48.176	24.991
23	34.879	24.543	49	48.693	24.994
24	35.447	24.576	50	49.211	24.996
25	36.009	24.608	51	49.730	24.997
26	36.566	24.638	52	50.249	25.000

Table A.2: Nozzle coordinates for $M = 1.75$ nozzle used in these studies. y-coordinates are nozzle half-heights. Units are in millimeters.

Pos	x	y	Pos	x	y
1	0	18.031	27	42.010	24.189
2	12.520	20.157	28	42.791	24.252
3	18.471	21.147	29	43.571	24.313
4	20.573	21.489	30	44.352	24.371
5	22.183	21.746	31	45.135	24.426
6	23.550	21.959	32	45.919	24.479
7	24.769	22.145	33	46.705	24.529
8	25.889	22.312	34	47.493	24.577
9	26.937	22.465	35	48.284	24.622
10	27.930	22.606	36	49.077	24.665
11	28.882	22.738	37	49.874	24.705
12	29.802	22.863	38	50.674	24.743
13	30.694	22.980	39	51.477	24.778
14	31.565	23.092	40	52.285	24.811
15	32.418	23.199	41	53.096	24.841
16	33.257	23.301	42	53.912	24.868
17	34.083	23.399	43	54.732	24.893
18	34.899	23.493	44	55.557	24.915
19	35.707	23.583	45	56.387	24.935
20	36.508	23.669	46	57.222	24.952
21	37.304	23.752	47	58.062	24.966
22	38.094	23.832	48	58.908	24.977
23	38.882	23.909	49	59.759	24.986
24	39.666	23.984	50	60.617	24.991
25	40.449	24.055	51	61.480	24.994
26	41.230	24.123	52	62.343	25.000

Table A.3: Nozzle coordinates for $M = 2.0$ nozzle used in these studies. y-coordinates are nozzle half-heights. Units are in millimeters.

Pos	x	y	Pos	x	y
1	0	14.815	27	43.870	23.500
2	11.662	17.548	28	44.868	23.611
3	17.329	18.849	29	45.874	23.718
4	19.416	19.317	30	46.888	23.821
5	21.050	19.677	31	47.910	23.920
6	22.462	19.980	32	48.942	24.015
7	23.742	20.249	33	49.984	24.107
8	24.934	20.494	34	51.036	24.194
9	26.064	20.720	35	52.098	24.278
10	27.150	20.933	36	53.172	24.357
11	28.202	21.134	37	54.257	24.432
12	29.228	21.326	38	55.355	24.503
13	30.235	21.508	39	56.465	24.569
14	31.228	21.684	40	57.588	24.631
15	32.210	21.853	41	58.724	24.689
16	33.184	22.016	42	59.873	24.742
17	34.152	22.173	43	61.037	24.790
18	35.117	22.325	44	62.215	24.834
19	36.080	22.473	45	63.408	24.872
20	37.043	22.616	46	64.616	24.905
21	38.007	22.754	47	65.840	24.934
22	38.973	22.889	48	67.080	24.956
23	39.943	23.019	49	68.336	24.974
24	40.917	23.145	50	69.609	24.985
25	41.895	23.267	51	70.900	24.991
26	42.880	23.386	52	72.110	25.000

APPENDIX B

DATA PROCESSING

B.1 Turbulent Statistics

The 2D planar PIV calculation outputs velocity vectors as a function of x-y position. The vector field is then post-processed to extract turbulent information. The mean and RMS velocity fluctuation ($\sqrt{\overline{u'^2}}$) are the simplest statistics to calculate, but, in general these quantities vary with spatial position and time. Further, these statistics are impossible to calculate experimentally in the case where the flow field statistics are non-stationary (time dependent). Therefore, during processing a stationarity test is conducted to ensure that the PIV statistics are time independent. Spatial homogeneity is harder to assume in general, especially for supersonic flows. Shock waves or other compressible features modify the statics, so special care must be taken when using the entire spatial field to create statistics; averaging is conducted over small spatial regions, but homogeneity is not guaranteed in general. The mean converges with the reciprocal of the square root of the number of independent samples [119], or PIV image pairs. 100 independent samples would normally enough to guarantee good convergence but PIV has a higher random error. Lavoie *et al.* suggest 300 independent samples for 95% convergence of the mean and 2000 samples for 95% convergence of second order moments [120]. Higher-order or more complex statistics require more samples for similar convergence. Usually around 300 high resolution image pairs are collected per condition, which is sufficient to converge the mean but more than likely insufficient to fully converge the RMS velocity fluctuation.

The next least complicated statistic calculated is the autocorrelation function R_{ij}, which is defined in Equation (B.1). R_{ij} is a measure of how strongly motion is correlated at a spatial separation of r. This function has maximum at $r = 0$, by definition. The statistic

was formed from the PIV data via the direct method; the instantaneous velocity fluctuation $u' = u - \bar{u}$ was calculated at each location (the over bar represents the time average), then the product of $u'_i * u'_j$ were ensemble averaged for each spatial separation. Finally, $R_{ij}(r,t)$ was time averaged to yield $R_{ij}(r)$. The autocorrelation is mathematically meaningful but not a meaningful turbulence quantity in an inhomogeneous field (as is the case in these studies). Nonetheless, this statistic is required to produce the integral length scales.

$$R_{ij}(r,t) = \langle u'_i(x,t) u'_j(x+r,t) \rangle \tag{B.1}$$

The integral length scale is calculated from the autocorrelation by integrating $R_{ij}(r)$, as in Equation (B.2). The integral scale is a measure of the largest size motions contained within the flow field. The variation of this statistic in the streamwise direction is an important parameter because it is necessary to initialize simulations and often reported in turbulence literature.

$$L_{ij} = \int_0^\infty R_{ij}(r) \tag{B.2}$$

The one-dimensional turbulent energy spectra is calculated via the direct FFT of the velocity fluctuation following the Welch method [152] as in Equation (B.3). The energy spectra is a statistic of much fundamental importance, although it is technically only meaningful when calculated for a homoegeneous velocity field. The spatial resolution of the PIV measurements limit the maximum wavenumber available. Therefore, high resolution (29 MP) images are used to extend the wavenumber spectra.

$$E_{11}(\kappa_1) = \frac{1}{n_d L} \sum_{i=1}^{n_d} \left| \hat{u}(\kappa_1) \right|^2 \tag{B.3}$$

B.2 Flame Edge Identification

For experimental flame edge detection, the edge detected images are binarized and centered using the centroid of each image. Next, the geometric c-map is formed at each Δt_{ign} by averaging over the centered images. The average flame area, $\langle A_f \rangle$, which is equal to the area contained within the $\bar{c} = 0.5$ contour, is converted into an effective spherical radius, $\langle R \rangle = \sqrt{\langle A_{2D} \rangle / \pi}$.

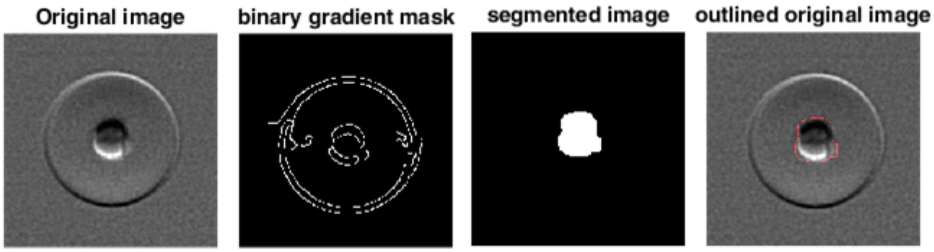

Figure B.1: Schlieren image processing routine. The original, enhanced image (left) is edge detected and masked to identify regions of the kernel and blast wave.

For the numerical simulations, the effective radius depends somewhat on the numerical Schlieren definition used. Several formulations are examined and their definitions are given in Table B.1. In Table B.1, $\sum_z$ indicates summation over z, the subscript max implies the largest value along z is chosen, and $(T > T_{crit})_{0,1}$ is a LOS binarization of the temperature field. A comparison of the numerical Schlieren techniques is shown in Figure B.2. The images are fed through algorithms to extract the 2D burned area and effective radius. Results of this process generally depend on the formulation used and a comparison of the techniques is shown in Figure B.3 for case 3. While Y-Schlieren looks most similar to a typical horizontal knife edge Schlieren, a gap in the edge appears whenever the flame surface is perpendicular to the y-direction. This causes a large error in the detected flame area. A similar problem occurs with X-Y Schlieren and hence both of these cases are excluded as potential options. Of the remaining options, all but the temperature isocontour (416 K) are problematic. Y-max under predicts at early times and over predicts at late times, X-Y mag is prone to edge detection errors, and X-Y max first over predicts and then discontinuously

Table B.1: Numerical Schlieren definitions.

Name	Definition
Y Schlieren	$\sum_z \frac{\partial \rho}{\partial y}$
X-Y Schlieren	$\sum_z \left(\frac{\partial \rho}{\partial x} + \frac{\partial \rho}{\partial y} \right)$
Temp. Isocontour	$(T > T_{crit})_{(0,1)}$
X-Y Magnitude	$\sum_z \sqrt{\left(\frac{\partial \rho}{\partial x} \right)^2 + \left(\frac{\partial \rho}{\partial y} \right)^2}$
Y Max	$\left. \frac{\partial \rho}{\partial y} \right\|_{max}$
X-Y Max	$\left. \sqrt{\left(\frac{\partial \rho}{\partial x} \right)^2 + \left(\frac{\partial \rho}{\partial y} \right)^2} \right\|_{max}$

jumps to a lower value. The temperature isocontour does not suffer from these problems, and therefore, is chosen for comparison to experiments.

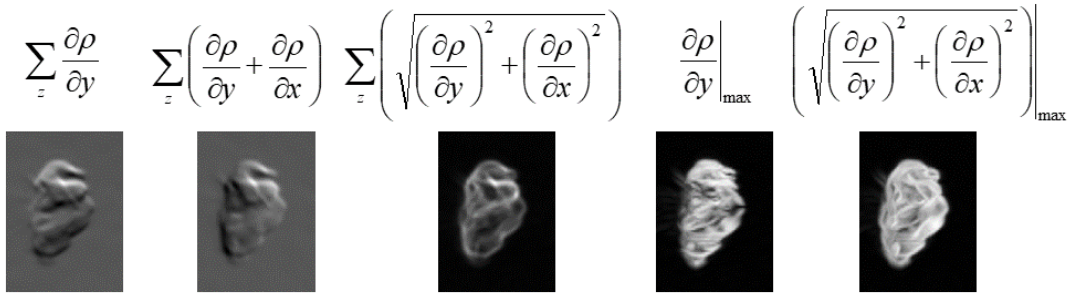

Figure B.2: Comparison of Numerical Schlieren for different edge calculation techniques.

Next, S_{TC} or S_{TD} is calculated using any of the Equations (1.13), (1.14), (1.16), or (1.17). Further, the horizontal ($\mathcal{L}_{\mathcal{H}}$) and vertical flame extents ($\mathcal{L}_{\mathcal{V}}$) of the c-map, used to describe the kernel shape, are defined as 1/2 of the maximum horizontal/vertical extent of the $\bar{c} = 0.5$ contour, respectively. Finally, the ratio of $\mathcal{L}_{\mathcal{V}}/\mathcal{L}_{\mathcal{H}}$ is defined as the kernel aspect ratio (AR).

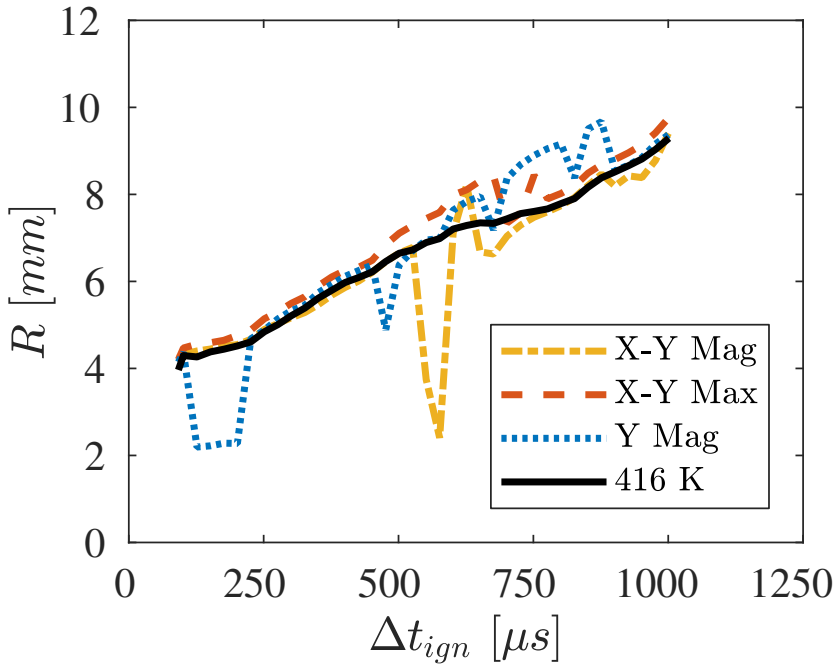

Figure B.3: Comparison of kernel radii, R, versus Δt_{ign} calculated for different edge calculation techniques.

APPENDIX C

ADDITIONAL DETAILS ABOUT QUIESCENT LASER-PLASMA BREAKDOWN

Initial studies of quiescent laser breakdown were conducted in an open environment (with windows or a test section). Kernel properties were studied versus ignition energy and focusing angle of the ignition optic. An example set of images using 19 mJ incident energy and a 100 mm plano-concave lens are shown in Figure C.1. The beam is incident on the left side of the kernel. The kernel is spherical out to 6-9 μs but then begins to change shape. Counter-rotating vortices, induced by strong outward radial motion, cause an eccentricity to develop in the kernel. This is clearly evident at 20 μs. This eccentricity is the result of line of sight imaging of the expected toroidal shape. At around 30-50 μs, the voritical motion on the back side of the toroid begins to overwhelm the forward side vorticity resulting in the formation of a third lobe. This expected shape is the result of plasma backstreaming towards the laser source. The thrid lobe becomes quite pronounced in the non-reacting case. The kernel grow out to approximately 230 μs. After 300 μs, the kernel begins to dissipate in the average, but the thermal remains of breakdown even are evident out to 1-2 ms.

A strong blast wave can be seen in the first six images. The blast is already decoupled from the plasma kernel in the first image at 1.56 μs. A plot of the blast radius, R_b, versus time is shown in Figure C.2. The blast wave velocity, $v_b = dR_b/dt$, is initially supersonic with a Mach number of 1.3, but quickly drops over the first 6 μs then remains constant. A linear fit to the data in Figure C.2, yields $v_b \approx 333$ m/s, which is very close to the speed of sound in atmospheric air, suggesting the wave is simply an acoustic pressure wave after $\approx 6\mu$s.

The shape and location of the plasma kernel is an important characteristic of the breakdown process because those parameters can have a strong effect on flame statistics when

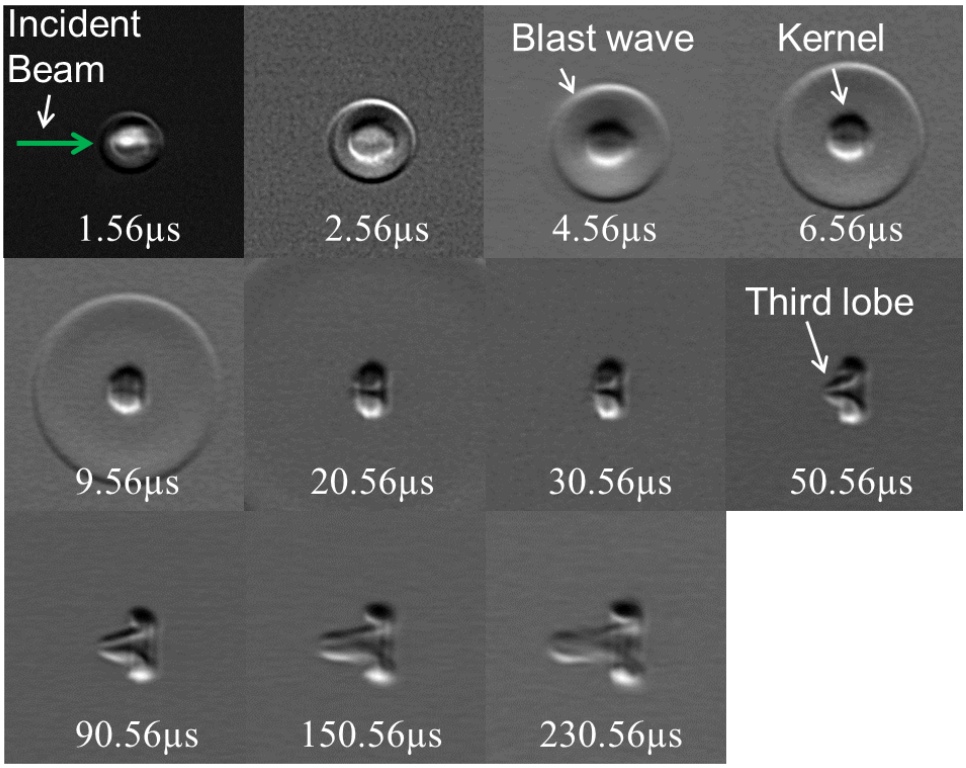

Figure C.1: Evolution of a laser breakdown plasma in quiescent air from 1.5 through 230 μs at $E_3 = 19$ mJ.

laser ignition is used. For example, if the plasma size or location are highly stoichastic for a fixed incident beam energy and setup, then derived flame statistics will have larger than actual variances. Figure C.3 shows the kernel area and position for 180 independent breakdown events at 19 mJ and 8.56 μs. Both the kernel area and position vary versus ensemble. For this case, the average area is 4.2 mm^2 with $\sigma = 0.25$ mm^2. The kernels have a relatively small variation in position with the largest extremes along the laser axis. Figure C.3b shows $< \pm 25\mu$m vertical motion (normal to the laser axis) and $< \pm 100\mu$m horizontal motion (along the laser axis). This amount of variation has a very minimal impact on flame statistics because the reacting cases are typically much larger (radii larger than 5 mm).

The kernel perimeter is plotted versus time in Figure C.4a. Also shown are the results of Mulla *et al.* [30], who use OH PLIF to derive kernel statistics on reacting flame kernels ignited using laser ignition. The data in Figure C.4a differ from those presented in Figure

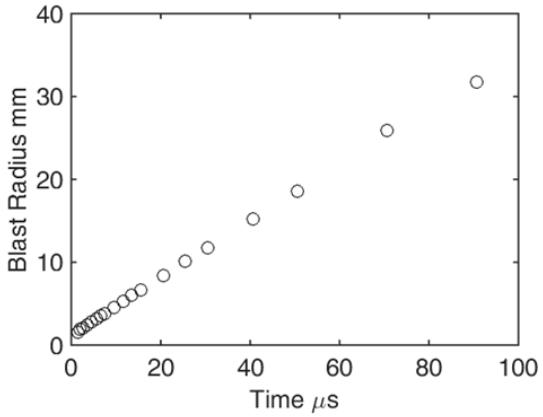

Figure C.2: Evolution of the blast radius versus time from breakdown.

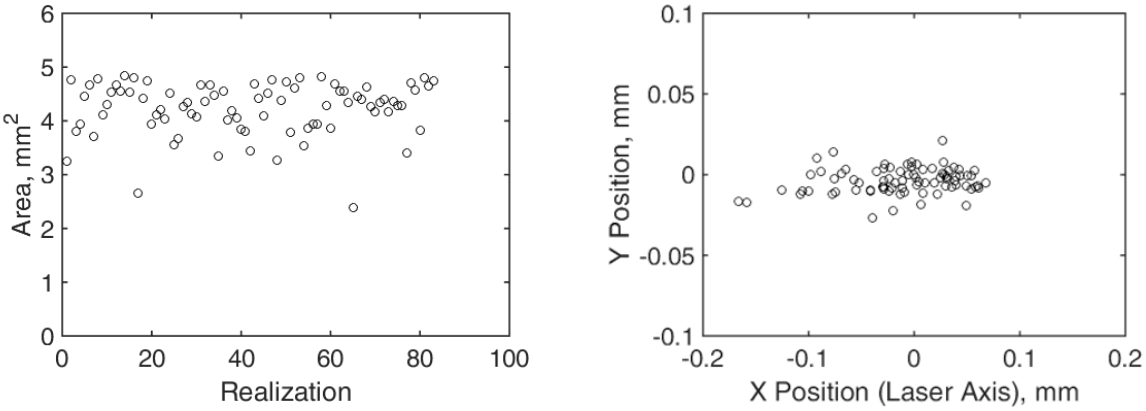

(a) Kernel area [mm^2]

(b) Location of kernel center of mass [mm].

Figure C.3: Variation of derived kernel properties with realization number.

3.2 because the ignition kernels in Figure C.4a have zero velocity, which is actually closer to the 9.4 m/s used by Mulla *et al.* [30] than the $M = 1.75$ kernels shown in Figure 3.2. The perimeter and perimeter growth rate are a strong function of ignition energy. Some of this effect can be removed by normalizing the perimeter with that of an early-time kernel; thereby removing the effect of an initially larger kernel due to greater deposited energy. Mulla *et al.* use their first kernel at 3 μs, and so all the data in Figure C.4b are normalized by the perimeter at 3 μs. Prior to 300 μs, the normalized perimeters ($P/P_{t=3\mu s}$) collapse even though 1) two different imaging techniques are used and 2) the equivalence ratio in Mulla *et al.* is $\phi = 0.6$. This suggests a universality to the early time ignition process which is independent of reaction. In addition, the perimeter growth collapses when normalized

independently of the ignition energy and imaging technique during this early development time. After 300 μs Mulla *et al.* observe a deviation in the kernels ignited using $E_{ign} = 88$ mJ, which are ultimately globally un-ignitable. This is also the period where the averaged kernels of Figure C.1 begin to dissipate.

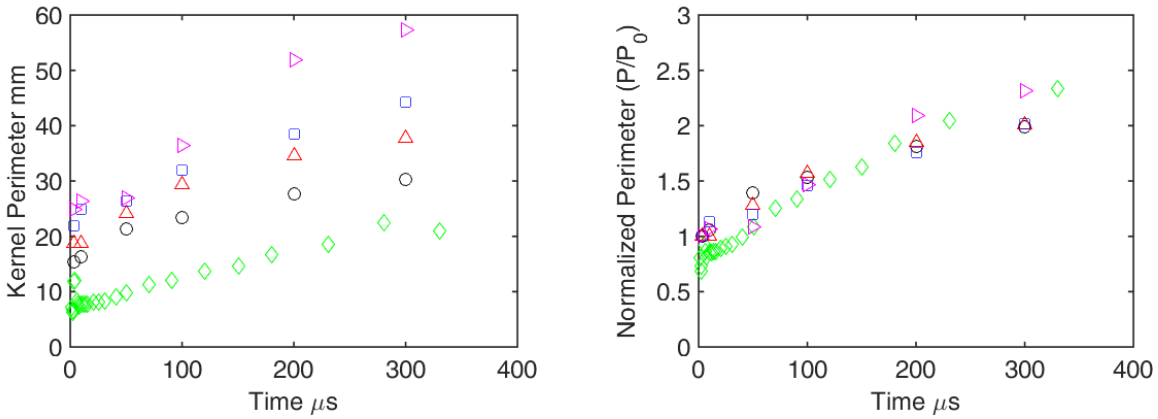

(a) Kernel perimeter [mm].

(b) Normalized perimeter, P/P_0.

Figure C.4: Growth of kernel perimeter and normalized perimeter versus time. Results of this study for $E_5 = 19$ mJ are shown with green diamonds. Results of Mulla *et al.* [30] are shown with black circles: 88 mJ, red triangles: 128 mJ, blue squares: 187 mJ, and pink triangles: 226 mJ. Data from Mulla *et al.* were produced using OH PLIF images.

APPENDIX D

LASER IGNITION SURFACE FIT COEFFICIENTS

Table D.1: Model coefficients for R, W and P surface fits: $R/W/P = a + b\Delta t_{ign} + cE_{ign} + d{\Delta t_{ign}}^2 + e\Delta t_{ign}E_{ign} + f{E_{ign}}^2 + g{\Delta t_{ign}}^3 + h{\Delta t_{ign}}^2E_{ign} + i\Delta t_{ign}{E_{ign}}^2 + j{E_{ign}}^3$. Curve fits correspond to $\phi = 1.0$ kernels at the indicated Mach number.

	$M = 1.50$			$M = 1.75$			$M = 2.00$		
Coefficient	R	W	P	R	W	P	R	W	P
a	2.03	-1.92	6.24	1.13	1.64	4.90	1.25	7.28	83.2
b	7.12E-2	8.13E-1	1.07	1.66E-1	4.64E-1	1.06	1.56E-1	-2.38E-1	-8.16
c	5.74E-3	2.45E-2	4.23E-2	1.17E-2	3.15E-2	1.12E-1	1.40E-2	4.72E-2	-5.65E-2
d	-1.65E-3	-2.67E-2	-3.06E-2	-7.47E-3	-1.68E-2	-4.23E-2	-6.78E-3	7.69E-3	3.54E-2
e	6.84E-5	-2.78E-4	1.01E-4	4.18E-4	8.34E-4	2.79E-3	1.80E-4	4.54E-4	4.63E-3
f	-6.96E-6	-5.92E-5	-4.68E-5	-2.15E-5	-8.34E-5	2.41E-4	-2.66E-5	-1.34E-4	2.68E-4
g	1.77E-5	2.98E-4	3.25E-4	1.02E-4	1.29E4	4.71E-4	1.05E-4	-6.80E-5	-5.19E-3
h	-9.60E-8	7.25E-6	2.91E-6	-8.25E-7	5.38E-6	-8.91E-7	-2.52E-6	-7.05E-6	-2.74E-5
i	-1.23E-7	-3.06E-7	-4.99E-7	-2.37E-7	-7.33E-7	-1.54E-6	7.40E-8	4.11E-7	-2.59E-6
j	1.18E-8	6.51E-8	8.31E-8	1.56E-8	7.24E-8	2.08E-7	1.95E-8	1.04E-7	-2.26E-7

Table D.2: Model coefficients for R, W and P surface fits: $R/W/P = a + b\Delta t_{ign} + cE_{ign} + d{\Delta t_{ign}}^2 + e\Delta t_{ign}E_{ign} + f{E_{ign}}^2 + g{\Delta t_{ign}}^3 + h{\Delta t_{ign}}^2E_{ign} + i\Delta t_{ign}{E_{ign}}^2 + j{E_{ign}}^3$. Curve fits correspond to $M = 1.75$ kernels at the indicated equivalence ratio.

	$\phi = 1.0$			$\phi = 0.75$			$\phi = 0.5$		
Coefficient	R	W	P	R	W	P	R	W	P
a	1.13	1.64	4.90	2.86	7.12	29.8	1.38	5.59	-36.1
b	1.66E-1	4.64E-1	1.06	-1.41E-1	-3.53E-1	-2.48	7.20E-2	-1.30E-1	6.01
c	1.17E-2	3.15E-2	1.12E-1	1.32E-2	3.53E-2	1.09E-1	1.02E-2	2.95E-2	1.83E-1
d	-7.47E-3	-1.68E-2	-4.23E-2	8.80E-3	1.81E-2	1.17E-1	-6.45E-4	9.61E-3	-2.54E-1
e	4.18E-4	8.34E-4	2.79E-3	3.88E-4	1.42E-3	3.49E-3	1.61E-4	6.74E-4	2.53E-3
f	-2.15E-5	-8.34E-5	2.41E-4	-2.44E-5	-1.12E-4	-2.38E-4	-6.92E-6	-6.87E-5	-4.76E-4
g	1.02E-4	1.29E4	4.71E-4	-1.64E-4	-2.95E-4	-1.69E-3	-1.56E-5	-1.76E-4	3.53E-3
h	-8.25E-7	5.38E-6	-8.91E-7	-2.00E-7	-1.53E-5	-5.27E-5	1.80E-6	-2.39E-6	-2.76E-5
i	-2.37E-7	-7.33E-7	-1.54E-6	-2.78E-7	-5.43E-7	8.80E-9	-1.98E-7	-5.26E-7	-7.94E-7
j	1.56E-8	7.24E-8	2.08E-7	1.91E-8	9.53E-8	1.79E-7	2.25E-9	5.94E-8	4.41E-7

REFERENCES

[1] G. B. Northam, E. Andrews, W. Guy, G. Pellett, P. Drummond, A. Cutler, and K. Rock, "An overview of hypersonic propulsion research at NASA Langley Research Center,"

[2] R. C. Rogers, D. P. Capriotti, and R. W. Guy, "Experimental supersonic combustion research at NASA Langley," *AIAA paper*, vol. 98, p. 2506, 1998.

[3] M. K. Smart, N. E. Hass, and A. Paull, "Flight data analysis of the hyshot 2 scramjet flight experiment," *AIAA journal*, vol. 44, no. 10, pp. 2366–2375, 2006.

[4] K. Matsuo, Y. Miyazato, and H.-D. Kim, "Shock train and pseudo-shock phenomena in internal gas flows," *Progress in Aerospace Sciences*, vol. 35, no. 1, pp. 33–100, 1999.

[5] E. T. Curran and F. D. Sull, "The utilization of supersonic combustion ramjet systems at low mach numbers," DTIC Document, Tech. Rep., 1964.

[6] Y. Andreopoulos, J. H. Agui, and G. Briassulis, "Shock wave-turbulence interactions," *Annual Review of Fluid Mechanics*, vol. 32, pp. 309–345, 2000.

[7] G. Briassulis and J. Andreopoulos, *Compressibility effects in grid generated turbulence*, Conference Paper, 1996.

[8] P. J. Zwart, R. Budwig, and S. Tavoularis, "Grid turbulence in compressible flow," *Experiments in Fluids*, vol. 23, no. 6, pp. 520–522, 1997.

[9] S. K. Lele, "Compressibility effects on turbulence," *Annual Review of Fluid Mechanics*, vol. 26, pp. 211–254, 1994.

[10] A. Y. Poludnenko and E. S. Oran, "The interaction of high-speed turbulence with flames: Global properties and internal flame structure," *Combustion and Flame*, vol. 157, no. 5, pp. 995–1011, 2010.

[11] A. Y. Poludnenko and E. S. Oran, "The interaction of high-speed turbulence with flames: Turbulent flame speed," *Combustion and Flame*, vol. 158, no. 2, pp. 301–326, 2011.

[12] J. Lee and R Knystautas, "Laser spark ignition of chemically reactive gases.," *AIAA Journal*, vol. 7, no. 2, pp. 312–317, 1969.

[13] B. Lewis and G. Von Elbe, *Combustion, flames and explosions of gases*. Elsevier, 2012.

[14] F. Weinberg and J. Wilson, "A preliminary investigation of the use of focused laser beams for minimum ignition energy studies," *Proceedings of the Royal Society of London. A. Mathematical and Physical Sciences*, vol. 321, no. 1544, pp. 41–52, 1971.

[15] S. Brieschenk, S. O'Byrne, and H Kleine, "Laser-induced plasma ignition sutdies in a model scramjet engine," *Combustion and Flame*, vol. 160, pp. 145–148, 2013.

[16] B. A. Ochs, T. Slais, D. E. Scarborough, S. Menon, N. R. Grady, and R. Pitz, "Characteristics of freely propagating premixed flame kernels in supersonic turbulent channel flows," *53rd AIAA Aerospace Sciences Meeting*, Kissimmee, Florida, January 5-9, 2015.

[17] B. A. Ochs, D. Fries, D. E. Scarborough, and S. Menon, "Growth rate and flame structure of turbulent premixed flame kernels in supersonic flows," in *54th AIAA Aerospace Sciences Meeting*, 2016, p. 0440.

[18] B. A. Ochs, D. Fries, D. Ranjan, and S. Menon, "Turbulent flame speeds of premixed supersonic flame kernels," *Flow Turbul Combust*, vol. 101, no. 3, pp. 927–951, 2018.

[19] S Brieschenk, H Kleine, and S O'Byrne, "Laser ignition of hypersonic air–hydrogen flow," *Shock Waves*, vol. 23, no. 5, pp. 439–452, 2013.

[20] T. X. Phuoc, "Laser-induced spark ignition fundamental and applications," *Optics and Lasers in Engineering*, vol. 44, no. 5, pp. 351–397, 2006.

[21] D. Santavicca, C Ho, B. J. Reilly, and T.-W. Lee, "Laser induced spark ignition of methane-oxygen mixtures," NASA, Tech. Rep. N91-30309, 1991.

[22] B. E. Forch and A. W. Miziolek, "Oxygen-atom two-photon resonance effects in multiphoton photochemical ignition of premixed h 2/o 2 flows," *Optics letters*, vol. 11, no. 3, pp. 129–131, 1986.

[23] B. E. Forch, "Resonant laser ignition of reactive gases," in *OE/LASE'94*, International Society for Optics and Photonics, 1994, pp. 118–128.

[24] V. Klimkin, R. Soloukhin, and P Wolansky, "Initial stages of a spherical detonation directly initiated by a laser spark," *Combustion and flame*, vol. 21, no. 1, pp. 111–117, 1973.

[25] R. W. Schmieder, "Laser spark ignition and extinction of a methane-air diffusion flame," *Journal of Applied Physics*, vol. 52, no. 4, pp. 3000–3003, 1981.

[26] J. Syage, E. Fournier, R Rianda, and R. Cohen, "Dynamics of flame propagation using laser-induced spark initiation: Ignition energy measurements," *Journal of Applied Physics*, vol. 64, no. 3, pp. 1499–1507, 1988.

[27] T. Spiglanin, A McIlroy, E. Fournier, R. Cohen, and J. Syage, "Time-resolved imaging of flame kernels: Laser spark ignition of h 2/o 2/ar mixtures," *Combustion and Flame*, vol. 102, no. 3, pp. 310–328, 1995.

[28] D Bradley, C. Sheppard, I. Suardjaja, and R Woolley, "Fundamentals of high-energy spark ignition with lasers," *Combustion and Flame*, vol. 138, no. 1, pp. 55–77, 2004.

[29] T. X. Phuoc, "An experimental and numerical study of laser-induced spark in air," *Optics and lasers in engineering*, vol. 43, no. 2, pp. 113–129, 2005.

[30] I. A. Mulla, S. R. Chakravarthy, N. Swaminathan, and R. Balachandran, "Evolution of flame-kernel in laser-induced spark ignited mixtures: A parametric study," *Combustion and Flame*, vol. 164, pp. 303–318, 2016.

[31] I. Shepherd and R. Cheng, "The burning rate of premixed flames in moderate and intense turbulence," *Combustion and Flame*, vol. 127, no. 3, pp. 2066–2075, 2001.

[32] J. F. Driscoll, "Turbulent premixed combustion: Flamelet structure and its effect on turbulent burning velocities," *Progress in Energy and Combustion Science*, vol. 34, no. 1, pp. 91–134, 2008.

[33] R. G. Abdelgayed, K. J. Alkhishali, and D. Bradley, "Turbulent burning velocities and flame straining in explosions," *Proceedings of the Royal Society of London Series a-Mathematical Physical and Engineering Sciences*, vol. 391, no. 1801, pp. 393–414, 1984.

[34] N. Peters, "The turbulent burning velocity for large-scale and small-scale turbulence," *Journal of Fluid Mechanics*, vol. 384, pp. 107–132, 1999.

[35] J. Sjöholm, J. Rosell, B. Li, M. Richter, Z. Li, X.-S. Bai, and M. Aldén, "Simultaneous visualization of OH, CH, CH_2O and toluene PLIF in a methane jet flame with varying degrees of turbulence," *Proceedings of the Combustion Institute*, vol. 34, no. 1, pp. 1475–1482, 2013.

[36] P. Tamadonfar and Ö. L. Gülder, "Experimental investigation of the inner structure of premixed turbulent methane/air flames in the thin reaction zones regime," *Combustion and Flame*, vol. 162, no. 1, pp. 115–128, 2015.

[37] B. Zhou, C. Brackmann, Q. Li, Z. Wang, P. Petersson, Z. Li, M. Aldén, and X.-s. Bai, "Distributed reactions in highly turbulent premixed methane/air flames: Part I. Flame structure characterization," *Combustion and Flame*, vol. 162, no. 7, pp. 2937–2953, 2015.

[38] Y. C. Chen and M. S. Mansour, "Investigation of flame broadening in turbulent premixed flames in the thin-reaction-zones regime," *Twenty-Seventh Symposium (International) on Combustion, Vols 1 and 2*, pp. 811–818, 1998.

[39] K. Eisazadeh-Far, F. Parsinejad, H. Metghalchi, and J. C. Keck, "On flame kernel formation and propagation in premixed gases," *Combustion and Flame*, vol. 157, no. 12, pp. 2211–2221, 2010.

[40] C. C. Huang, S. S. Shy, C. C. Liu, and Y. Y. Yan, "A transition on minimum ignition energy for lean turbulent methane combustion in flamelet and distributed regimes," *Proceedings of the Combustion Institute*, vol. 31, pp. 1401–1409, 2007.

[41] S. Kwon, M. S. Wu, J. F. Driscoll, and G. M. Faeth, "Flame surface-properties of premixed flames in isotropic turbulence- measurements and numerical simulations," *Combustion and Flame*, vol. 88, no. 2, pp. 221–238, 1992.

[42] M. T. Lim, R. W. Anderson, and V. S. Arpaci, "Prediction of spark kernel development in constant volume combustion," *Combustion and Flame*, vol. 69, no. 3, pp. 303–316, 1987.

[43] M. S. Mansour, N. Peters, and Y. C. Chen, "Investigation of scalar mixing in the thin reaction zones regime using a simultaneous ch-lif/rayleigh laser technique," *Twenty-Seventh Symposium (International) on Combustion, Vols 1 and 2*, pp. 767–773, 1998.

[44] N. Peters, *Turbulent combustion*. Cambridge: Cambridge Press, 2000.

[45] H. Pitsch, "Large-eddy simulation of turbulent combustion," *Annual Review of Fluid Mechanics*, vol. 38, pp. 453–482, 2006.

[46] T. Poinsot and D. Veynante, *Theoretical and Numerical Combustion*, illustrated. Edwards, 2001, ISBN: 1930217056, 9781930217058.

[47] M. Summerfield, S. H. Reiter, V. Kebely, and R. W. Mascolo, "The structure and propagation mechanism of turbulent flames in high speed flow," *Jet Propulsion*, vol. 25, no. 8, pp. 377–384, 1955.

[48] S. Shy, C. Liu, J. Lin, L. Chen, A. Lipatnikov, and S. Yang, "Correlations of high-pressure lean methane and syngas turbulent burning velocities: Effects of turbulent

Reynolds, Damköhler, and Karlovitz numbers," *Proceedings of the Combustion Institute*, vol. 35, no. 2, pp. 1509–1516, 2015.

[49] R Borghi, "On the structure and morphology of turbulent premixed flames," in *Recent Advances in the Aerospace Sciences*, Springer, 1985, pp. 117–138.

[50] N Peters, "Laminar flamelet concepts in turbulent combustion," in *Symposium (International) on Combustion*, Elsevier, vol. 21, 1988, pp. 1231–1250.

[51] F. Williams, "Turbulent combustion," *The mathematics of combustion*, vol. 2, pp. 267–294, 1985.

[52] D Bradley, M. Haq, R. Hicks, T Kitagawa, M Lawes, C. Sheppard, and R Woolley, "Turbulent burning velocity, burned gas distribution, and associated flame surface definition," *Combustion and Flame*, vol. 133, no. 4, pp. 415–430, 2003.

[53] D. Bradley, M. Lawes, and M. S. Mansour, "Correlation of turbulent burning velocities of ethanol-air, measured in a fan stirred bomb up to 1.2 mpa," *Combustion and Flame*, vol. 158, pp. 123–138, 2011.

[54] S. Chaudhuri, F. Wu, D. Zhu, and C. K. Law, "Flame speed and self-similar propagation of expanding turbulent premixed flames," *Physical Review Letters*, vol. 108, no. 4, p. 044 503, 2012.

[55] B Renou, A Boukhalfa, D Puechberty, and M Trinité, "Local scalar flame properties of freely propagating premixed turbulent flames at various Lewis numbers," *Combustion and Flame*, vol. 123, no. 4, pp. 507–521, 2000.

[56] G. Damköhler, "The effect of turbulence on the flame velocity in gas mixtures," *Zeitschrift Electrochem*, vol. 46, pp. 601–626, 1940(English translation, NACA TM 1112, 1947).

[57] K. Shelkin, "On combustion in a turbulent flow," *National Advisory Committee for Aeronautics*, vol. Technical Memorandum No. 1110, 1947.

[58] N Peters, P Terhoeven, J. H. Chen, and T. Echekki, "Statistics of flame displacement speeds from computations of 2-d unsteady methane-air flames," *Symposium (International) on Combustion*, vol. 27, no. 1, pp. 833–839, 1998.

[59] D Bradley, A. Lau, and M Lawes, "Flame stretch rate as a determinant of turbulent burning velocity," *Philosophical Transactions of the Royal Society of London A: Mathematical, Physical and Engineering Sciences*, vol. 338, no. 1650, pp. 359–387, 1992.

[60] H. Kido, M. Nakahara, K. Nakashima, and J. Hashimoto, "Influence of local flame displacement velocity on turbulent burning velocity," *Proceedings of the Combustion Institute*, vol. 29, no. 2, pp. 1855–1861, 2002.

[61] D. Bradley, "How fast can we burn," *Twenty-Fourth Symposium (International) on Combustion, Pittsburgh, PA*, pp. 247–262, 1992.

[62] N Peters, "A spectral closure for premixed turbulent combustion in the flamelet regime," *Journal of Fluid Mechanics*, vol. 242, pp. 611–629, 1992.

[63] S. Chaudhuri, V. Akkerman, and C. K. Law, "Spectral formulation of turbulent flame speed with consideration of hydrodynamic instability," *Physical Review E*, vol. 84, no. 2, p. 026 322, 2011.

[64] S. Chaudhuri, F. Wu, and C. K. Law, "Scaling of turbulent flame speed for expanding flames with markstein diffusion considerations," *Physical Review*, vol. 88, 2013.

[65] G. H. Markstein, "Experimental and theoretical studies of flame front stability," *J. Aero. Sci*, vol. 18, pp. 199–209, 1951.

[66] C. K. Law, *Combustion physics*. Cambridge University Press, 2010.

[67] R. G. Abdelgayed, D. Bradley, and M. Lawes, "Turbulent burning velocities: A general correlation in terms of straining rates," *Proceedings of the Royal Society of London Series A - Mathematical Physical and Engineering Sciences*, vol. 414, pp. 389–413, 1987.

[68] D. Bradley, M. Lawes, and M. S. Mansour, "Flame surface densities during spherical turbulent flame explosions," *Combustion and Flame*, vol. 158, pp. 123–138, 2011.

[69] I. Shepherd and W. T. Ashurst, *Flame front geometry in premixed turbulent flames*, Elsevier, 1992.

[70] A. Lefebvre, H. Larabi, V. Moureau, G. Lartigue, E. Varea, V. Modica, and B. Renou, "Formalism for spatially averaged consumption speed considering spherically expanding flame configuration," *Combust Flame*, vol. 173, pp. 235–244, 2016.

[71] F. Weinberg, "Location of the schlieren image in a flame," *Fuel*, vol. 34, S84–S88, 1955.

[72] D. Durox and S. Ducruix, "Concerning the location of the schlieren limit in premixed flames," *Combust Flame*, vol. 120, no. 4, pp. 595–598, 2000.

[73] D. Bradley, M. Lawes, and M. S. Mansour, "The problems of the turbulent burning velocity," *Flow Turbul Combust*, vol. 87, no. 2-3, pp. 191–204, 2011.

[74] A. Ingenito and C. Bruno, "Physics and regimes of supersonic combustion," *AIAA Journal*, vol. 48, no. 3, pp. 515–525, 2010.

[75] G. Salamandra, "Interaction between a flame and a shock discontinuity," *ARS Journal*, vol. 30, no. 1, pp. 73–76, 1960.

[76] G. Markstein, "Interaction between pressure waves and flame fronts," *Jet Propulsion*, vol. 25, pp. 173–174, 1955.

[77] G. H. Markstein, "A shock-tube study of flame front-pressure wave interaction," *Symposium (International) on Combustion*, vol. 6, no. 1, pp. 387–398, 1957.

[78] G. Markstein, "Flow disturbances induced near a slightly wavy contact surface, or flame front, traversed by a shock wave," *Journal of the Aeronautical Sciences*, vol. 24, no. 3, pp. 238–239, 1957.

[79] B.-T. Chu, "On the generation of pressure waves at a plane flame front," in *Symposium (International) on Combustion*, Elsevier, vol. 4, 1953, pp. 603–612.

[80] G. Rudinger, "Shock wave and flame interactions," in *Combustion and Propulsion, Third AGARD Colloquium*, 1958, p. 153.

[81] A. Laderman, A. Oppenheim, and P. Urtiew, "Gasdynamic effects of shock-flame interactions in an explosive gas," *AIAA Journal*, vol. 3, no. 5, pp. 876–883, 1965.

[82] J. Picone, E. Oran, J. Boris, and T. Young Jr, "Theory of vorticity generation by shock wave and flame interactions," DTIC Document, Tech. Rep., 1984.

[83] J.-F. Haas and B. Sturtevant, "Interaction of weak shock waves with cylindrical and spherical gas inhomogeneities," *Journal of Fluid Mechanics*, vol. 181, pp. 41–76, 1987.

[84] Y. Ju, A. Shimano, and O. Inoue, "Vorticity generation and flame distortion induced by shock flame interaction," in *Symposium (International) on Combustion*, Elsevier, vol. 27, 1998, pp. 735–741.

[85] G. Thomas, R. Bambrey, and C. Brown, "Experimental observations of flame acceleration and transition to detonation following shock-flame interaction," *Combustion Theory and Modelling*, vol. 5, no. 4, pp. 573–594, 2001.

[86] M. Gui, B. Fan, G. Dong, and J. Ye, "Experimental and numerical studies on interactions of a spherical flame with incident and reflected shocks," *Acta Mechanica Sinica*, vol. 25, no. 2, pp. 173–179, 2009.

[87] H. Huh, J. F. Driscoll, *et al.*, "Measured effects of shock waves on supersonic hydrogen-air flames," *AIAA Paper*, pp. 96–3035, 1996.

[88] J. Kim, Y Yoon, J. Choi, and I. Jeung, "Numerical study of hydrogen jet flame in supersonic flows: Effect of shock waves," *AIAA Journal*, 1998.

[89] C. J. Roy and J. R. Edwards, "Numerical simulation of a three-dimensional flame/shock wave interaction," *AIAA journal*, vol. 38, no. 5, pp. 745–754, 2000.

[90] A. Ratner, J. F. Driscoll, H. Huh, and R. A. Bryant, "Combustion efficiencies of supersonic flames," *Journal of Propulsion and Power*, vol. 17, no. 2, pp. 301–307, 2001.

[91] J. Watanabe and K. Takita, "Interaction between shock waves, hydrogen flame and plasma jet in supersonic flow," *AIAA Journal*, 2009.

[92] A. Kolmogorov, "The local structure of turbulence in incompressible viscous fluid for very large Reynolds numbers," *Cr Acad. Sci. URSS*, vol. 30, pp. 301–305, 1941.

[93] G. Dong, B. Fan, and J. Ye, "Numerical investigation of ethylene flame bubble instability induced by shock waves," *Shock Waves*, vol. 17, no. 6, pp. 409–419, 2008.

[94] D. Bradley, M. Lawes, K. Liu, and M. S. Mansour, "Measurements and correlations of turbulent burning velocities over wide ranges of fuels and elevated pressures," *Proceedings of the Combustion Institute*, vol. 34, no. 1, pp. 1519–1526, 2013.

[95] D. Fries, B. A. Ochs, and S. Menon, "Experimental studies of freely propagating turbulent premixed kernels with comparison to classical flame bomb studies," *54th AIAA Aerospace Sciences Meeting, San Diego, CA, January 4-8, 2016*, vol. AIAA-2306399, 2016.

[96] N. Grady, R. Pitz, B. Ochs, S. Menon, D. Scarborough, and T. Slais, "Propagation of premixed flame kernels in high speed channel flows with moderate turbulence," *53rd AIAA Aerospace Sciences Meeting*, vol. AIAA-2015-0169, 2015.

[97] N. Grady, R. Pitz, T. Slais, J. Berlette, B. Ochs, and S. Menon, *Oh plif laser diagnostics of turbulent, premixed, freely propagating flame kernels*, Conference Paper, 52nd Aerospace Sciences Meeting, National Harbor, MD, 2014.

[98] B. Renou, A. Boukhalfa, D. Puechberty, and M. Trinité, "Effects of stretch on the local structure of preely propagating premixed low-turbulent flames with various Lewis numbers," *Symposium (International) on Combustion*, vol. 27, no. 1, pp. 841–847, 1998.

[99] D. Fries, B. A. Ochs, A. Saha, D. Ranjan, and S. Menon, "Flame speed characteristics of turbulent expanding flames in a rectangular channel," *Combust. Flame*, vol. 199, pp. 1–13, 2019.

[100] D. Ranjan, J. Oakley, and R. Bonazza, "Shock-bubble interactions," *Annual Review of Fluid Mechanics*, vol. 43, pp. 117–140, 2011.

[101] N. Haehn, D. Ranjan, C. Weber, J. Oakley, D. Rothamer, and R. Bonazza, "Reacting shock bubble interaction," *Combustion and Flame*, vol. 159, no. 3, pp. 1339–1350, 2012.

[102] J. H. Niederhaus, J. Greenough, J. Oakley, D Ranjan, M. Anderson, and R Bonazza, "A computational parameter study for the three-dimensional shock–bubble interaction," *Journal of Fluid Mechanics*, vol. 594, pp. 85–124, 2008.

[103] P Krehl and S Engemann, "August toepler—the first who visualized shock waves," *Shock Waves*, vol. 5, no. 1-2, pp. 1–18, 1995.

[104] H. Draper, "On the construction of a silvered glass telescope...," *[Wash., Smithsonian inst., 1864]*, vol. 1, 1864.

[105] A. J. I. Toepler, *Beobachtungen nach einer neuen optischen methode: Ein beitrag experimentalphysik*, 157. W. Engelmann, 1906.

[106] G. S. Settles, *Schlieren and shadowgraph techniques: visualizing phenomena in transparent media*. Springer Science & Business Media, 2012.

[107] H. Schardin, "Die schlierenverfahren und ihre anwendungen," in *Ergebnisse der exakten Naturwissenschaften*, Springer, 1942, pp. 303–439.

[108] J. Canny, "A computational approach to edge detection," *Pattern Analysis and Machine Intelligence, IEEE Transactions on*, no. 6, pp. 679–698, 1986.

[109] H. N. Najm, P. H. Paul, C. J. Mueller, and P. S. Wyckoff, "On the adequacy of certain experimental observables as measurements of flame burning rate," *Combustion and flame*, vol. 113, no. 3, pp. 312–332, 1998.

[110] B. Ayoola, R Balachandran, J. Frank, E Mastorakos, and C. Kaminski, "Spatially resolved heat release rate measurements in turbulent premixed flames," *Combustion and flame*, vol. 144, no. 1, pp. 1–16, 2006.

[111] P. H. Paul and H. N. Najm, "Planar laser-induced fluorescence imaging of flame heat release rate," in *Symposium (International) on Combustion*, Elsevier, vol. 27, 1998, pp. 43–50.

[112] S. J. G. and J. C. Dutton, "Velocity measurements of a jet injected into a supersonic crossflow," *Journal of Propulsion and Power*, vol. 13, no. 2, pp. 264–273, 1997.

[113] G. Gauba, K. G. Klavuhn, J. McDaniel, K. Victor, R. Krauss, and R. Whitehurst, "Oh planar laser-induced flourescence velocity measurements in a supersonic combustor," *AIAA Journal*, vol. 35, no. 4, pp. 1678–686, 1997.

[114] C. P. Goyne, J. C. McDaneil, R. H. Krauss, and S. Day, "Velocity measurement in a dual-mode supersonic combustor using particle image velocimetry," *AIAA Paper2001-1761*, 2001.

[115] C. E. Willert and M. Gharib, "Digital particle image velocimetry," *Experiments in fluids*, vol. 10, no. 4, pp. 181–193, 1991.

[116] J. Soria, "An investigation of the near wake of a circular cylinder using a video-based digital cross-correlation particle image velocimetry technique," *Experimental Thermal and Fluid Science*, vol. 12, no. 2, pp. 221–233, 1996.

[117] J Nogueira, A Lecuona, *et al.*, "Data validation, false vectors correction and derived magnitudes calculation on piv data," *Measurement Science and Technology*, vol. 8, no. 12, p. 1493, 1997.

[118] R Mei, "Velocity fidelity of flow tracer particles," *Experiments in Fluids*, vol. 22, no. 1, pp. 1–13, 1996.

[119] L. Benedict and R. Gould, "Towards better uncertainty estimates for turbulence statistics," *Experiments in fluids*, vol. 22, no. 2, pp. 129–136, 1996.

[120] P Lavoie, G Avallone, F De Gregorio, G. Romano, and R. Antonia, "Spatial resolution of piv for the measurement of turbulence," *Experiments in Fluids*, vol. 43, no. 1, pp. 39–51, 2007.

[121] X. Gu, M. Haq, M Lawes, and R Woolley, "Laminar burning velocity and markstein lengths of methane–air mixtures," *Combustion and flame*, vol. 121, no. 1, pp. 41–58, 2000.

[122] M. P. Burke, Z. Chen, Y. Ju, and F. L. Dryer, "Effect of cylindrical confinement on the determination of laminar flame speeds using outwardly propagating flames," *Combust Flame*, vol. 156, no. 4, pp. 771–779, 2009.

[123] B. A. Ochs, R. Ranjan, D. Ranjan, and S. Menon, "Topology and flame speeds of turbulent premixed flame kernels in supersonic flows," *Combustion and Flame*, vol. 210, pp. 83–99, 2019.

[124] F. Génin and S. Menon, "Studies of shock/turbulent shear layer interaction using large-eddy simulation," *Comput. Fluids*, vol. 39, pp. 800–819, 2010.

[125] G.-S. Jiang and C.-W. Shu, "Efficient implementation of weighted ENO schemes," *J. Comput. Phys.*, vol. 126, no. 1, pp. 202–228, 1996.

[126] A. G. Smith, "Simulations of vitiated bluff body stabilized flames," PhD thesis, Georgia Institute of Technology, 2016.

[127] W.-W. Kim and S. Menon, "An unsteady incompressible Navier-Stokes solver for large eddy simulation of turbulent flows," *I. J. for Numer. Meth. Fluids.*, vol. 31, pp. 983–1017, 1999.

[128] F. Génin and S. Menon, "Dynamics of sonic jet injection into supersonic crossflow," *J. Turbul.*, vol. 11, pp. 1–30, 2010.

[129] M Berglund, E Fedina, C Fureby, J Tegnér, and V Sabel'Nikov, "Finite rate chemistry large-eddy simulation of self-ignition in supersonic combustion ramjet," *AIAA J.*, vol. 48, no. 3, pp. 540–550, 2010.

[130] N. Peters, "Reducing mechanisms," in *Reduced Kinetic Mechanisms and Asymptotic Approximations for Methane-Air Flames*, M. D. Smooke, Ed., Springer, 1991, pp. 48–67.

[131] T. M. Smith and S. Menon, "One-dimensional simulations of freely propagating turbulent premixed flames," *Combust. Sci. Technol.*, vol. 128, pp. 99–130, 1997.

[132] D. G. Goodwin, H. K. Moffat, and R. L. Speth, *Cantera: An object-oriented software toolkit for chemical kinetics, thermodynamics, and transport processes*, `http://www.cantera.org`, Version 2.1.2, 2014.

[133] R. H. Kraichnan, "Diffusion by a random velocity field," *Phys. Fluids*, vol. 13, no. 1, pp. 22–31, 1970.

[134] R. Zhang, M. Zhang, and C.-W. Shu, "On the order of accuracy and numerical performance of two classes of finite volume weno schemes," *Communications in Computational Physics*, vol. 9, pp. 807–827, 2011.

[135] H. C. Yee, N. D. Sandham, and M. J. Djomehri, "Low-dissipative high-order shock-capturing methods using characteristic-based filters," *Journal of Computational Physics*, vol. 150, pp. 199–238, 1999.

[136] E Schwarz, S Gross, B Fischer, and I Muri, "Laser-induced optical breakdown applied for laser spark ignition," *Laser and particle beams*, vol. 28, no. 1, pp. 109–119, 2010.

[137] M. Thiyagarajan and J. Scharer, "Experimental investigation of ultraviolet laser induced plasma density and temperature evolution in air," *Journal of applied physics*, vol. 104, no. 1, p. 013 303, 2008.

[138] D. Fries, B. A. Ochs, D. Ranjan, and S. Menon, "Hot-wire and piv characterisation of a novel small-scale turbulent channel flow facility developed to study premixed expanding flames," *Journal of Turbulence*, 2017.

[139] H. Tennekes, J. L. Lumley, J. Lumley, *et al.*, *A first course in turbulence*. MIT press, 1972.

[140] S. B. Pope, *Turbulent Flows*. Cambridge, UK: Cambridge University Press, 2001.

[141] A. D. Pierce, *Acoustics: an introduction to its physical principles and applications*. McGraw-Hill New York, 1981.

[142] Z. Chen, "Effects of radiation and compression on propagating spherical flames of methane/air mixtures near the lean flammability limit," *Combustion and Flame*, vol. 157, no. 12, pp. 2267–2276, 2010.

[143] D. Ranjan, J. Niederhaus, B. Motl, M. Anderson, J. Oakley, and R. Bonazza, "Experimental investigation of primary and secondary features in high-Mach-number shock-bubble interaction," *Physical Review Letters*, vol. 98, no. 2, p. 024 502, 2007.

[144] D. Ranjan, J. H. Niederhaus, J. G. Oakley, M. H. Anderson, R. Bonazza, and J. A. Greenough, "Shock-bubble interactions: Features of divergent shock-refraction geometry observed in experiments and simulations," *Physics of Fluids*, vol. 20, no. 3, p. 036 101, 2008.

[145] R. D. Richtmyer, "Taylor instability in shock acceleration of compressible fluids," *Communications on Pure and Applied Mathematics*, vol. 13, no. 2, pp. 297–319, 1960.

[146] M. Shusser and M. Gharib, "Energy and velocity of a forming vortex ring," *Physics of Fluids*, vol. 12, no. 3, pp. 618–621, 2000.

[147] J. J. Quirk and S. Karni, "On the dynamics of a shock–bubble interaction," *Journal of Fluid Mechanics*, vol. 318, pp. 129–163, 1996.

[148] M Gühler and D. W. Sallet, "The formation of vortex rings and their initial motion," *Zeitschrift fuer Flugwissenschaften und Weltraumforschung*, vol. 3, pp. 109–115, 1979.

[149] G. Comte-Bellot and S. Corrsin, "The use of a contraction to improve the isotropy of grid-generated turbulence," *Journal of Fluid Mechanics*, vol. 25, pp. 657–682, 1966.

[150] B. A. Ochs and S. Menon, "Laser ignition in supersonic channel flow," *Submitted to Combustion and Flame*, 2019.

[151] J. E. John, "Gas dynamics," 1984.

[152] J. S. Bendat and A. G. Piersol, *Random data: analysis and measurement procedures*. John Wiley & Sons, 2011, vol. 729.